HYDRODYNAMIC INSTABILITIES OF CYLINDRICAL INTERFACES

Rui-Qing Li

Department of Mining and Metallurgical Engineering
McGill University, Montreal
Sept. 1992

A Thesis submitted to the
Faculty of Graduate Studies and Research
in partial fulfilment of the requirements of
the degree of
Doctor of Philosophy

ISBN 0-315-87615-8

To my parents

ABSTRACT

This thesis consists of two parts. In the first part of the thesis, the Rayleigh-Taylor and the Kelvin-Helmholtz instabilities of a cylindrical interface between two inviscid fluids or two viscous fluids are analyzed from first principles (momentum and continuity equations). Dispersion equations, relating wavenumber, k, to growth rate, G, were derived for various conditions. Application of the dispersion equations to film boiling on a cylindrical heater and to breakup of a liquid film around a cylindrical body led to the development of mathematical models for the prediction of the dominant wavelengths formed during these processes for both inviscid and viscous fluids.

Experiments were carried out to measure the dominant unstable wavelength during the breakup of a liquid film around a cylindrical body. It was found that the dominant wavelength decreased with a decrease in the radius of the cylindrical body in agreement with the present theory and in contradiction to previously published work.

In another application of the present theory, the breakup of a cylindrical liquid-in-gas jet and a cylindrical gas-in-liquid jet was analyzed based on the Kelvin-Helmholtz instability. It was predicted that the dominant wavelength decreased rapidly with an increase in the jet velocity.

In the second part of the thesis, gas injection through a very narrow slot into a liquid is examined extensively. A modified bubble formation model is proposed taking into consideration the surface tension force and the inertial force.

When gas was injected into liquid through a very narrow slot (50-250μm), three different bubbling regimes were found as the flow rate of gas was increased. They were: *regular bubble regime* at low flow rates, *coalescence bubble regime* at medium flow rates, and *gas globe regime* at high flow rates. The gas-dispersion characteristics of each of the regimes were discussed and mathematically analyzed. In the *regular bubble regime*, the bubble formation was dominated by both surface tension force and inertial force. In the *coalescence bubble regime*, the formation of bubbles was dominated by inertial forces only. In the *gas globe regime*, due to the Rayleigh-Taylor instability, multiple bubbles were formed at separate nodes of a continuous gas blanket extending the length of the slot. The critical transition condition between the regular bubble formation regime and the coalescence bubble regime is given.

RÉSUMÉ

Cette thèse est composé de deux sections. Dans la première section, les instabilités de Rayleigh-Taylor et de Kelvin-Helmholtz pour des interfaces cylindriques entre deux fluides inviscides ou deux fluides visqueux sont analysé selon les premiers principes (équations du moment et de continuité). Les équations de dispersion, reliant le numero d'onde, k, au taux de croissance, G, sont derivées pour maintes conditions. L'application des équations de dispersion pour un film bouillant sur un radiateur cylindrique et un bris de film de liquide autour d'un corps cylindrique, a mené au developpement de modèles mathématiques pour la prédiction de la longueur d'onde dominante créer durant ces procédés avec des fluides inviscides et visqueux.

Des expériences ont été entreprises pour mesurer la longueur d'onde instable dominante durant le bris d'un film de fluide autour d'un corps cylindrique. Il a été déterminé que la longueur d'onde dominante diminuait avec la reduction du rayon du corp cylindrique, ce qui correspond avec la presente théorie et est en contradiction avec des oeuvres publiés précédemment.

Dans une autre application de la présente théorie, le bris d'un jet cylindrique d'un liquide dans un gaz et d'un jet cylindrique d'un gaz dans un liquide a été analysé selon le théorème d'instabilité de Kelvin-Helmholtz. La diminution rapide de la longueur d'onde dominante avec une augmentation de la vitesse du jet d'eau a été predite.

Dans la seconde section de cette thèse, l'injection d'un gaz par une ouverture très étrcite (50-250um) dans un liquide a été étudiée en grand détail. Un modèle modifié de formation de bulles est proposé tenant compte de la force tension de surface et des forces d'inertie.

RÉSUMÉ

Lorsque le gaz est injecté dans le liquide par une ouverture très étroite trois régimes de bulles distincts sont observables en augmentant le taux de gaz injecté. Les régimes observés sont: le régime de bulles régulier à un bas taux d'injection; le régime de coalescence des bulles à un taux d'injection moyen; et le régime de gaz en globe à un haut taux d'injection. Les caractèristiques de dispersion du gaz dans chaque regime sont discutées et analysées mathématiquement. Dans le régime de bulles régulier, la formation de bulles est dominée par la force de tension de surface et les forces d'inerties. Lors du régime de coalescence des bulles, la formation de bulles est dominée par les forces d'inertie seulement. Dans le régime de gaz en globe, a cause de l'instabilité de Rayleigh-Taylor, beaucoup de bulles sont formées à des points nodales séparées par des rideaux continues de gaz longeant la longueur de l'ouverture. Les conditions de transition critique entre le régime de bulles régulier et le régime de coalescence des bulles sont aussi fournies.

ACKNOWLEDGEMENTS

Grateful acknowledgment is hereby made of the essential contributions of many whose names do not appear on the title page. First of all, I am indebted to two people:

My supervisor, Professor Ralph Harris, for his advice, generosity, keen interest, and constant encouragement throughout the research program.

My wife, Lin Cheng, for her support, understanding and inspiration throughout the past three years, and for her sharing the excitement of raising our daughter, Cathy.

I am also indebted to Dr. A. E. Wraith for his interest, helpful suggestions and advice.

I am grateful to my colleagues, Z. Wang, J. Liu, P. Hancock, M. Kennedy, M. Ikezawa, M. Laurin, T. Schnyrenkova, M. Xu, G. Sheng and Q. Zhang for their friendship and help.

As well, I want to thank all members of the Department of Mining and Metallurgical Engineering of McGill University, and especially to Mr. Sylvain Poudrette for his carrying out the vapour condensation experiments.

TABLE OF CONTENTS

ABSTRACT i

ACKNOWLEDGEMENTS iii

NOMENCLATURE viii

LIST OF TABLES xv

LIST OF FIGURES xvi

CHAPTER 1 INTRODUCTION TO THE THESIS 1

1.1 Background of the present research 1
1.2 Objectives of the present work 2
1.3 Structure of the thesis 3

PART 1
HYDRODYNAMIC INSTABILITIES OF
A CYLINDRICAL INTERFACE 4

CHAPTER 2 LITERATURE REVIEW ON INTERFACIAL HYDRODYNAMIC INSTABILITY 5

2.1 Interfacial instabilities 5
2.1.1 Kelvin-Helmholtz instability of a planar interface 6
2.1.2 Rayleigh-Taylor instability of a planar interface 12
2.2 Hydrodynamic theory of film boiling 13
2.3 The mistakes of Lee's model 16

CHAPTER 3 RAYLEIGH-TAYLOR INSTABILITY OF A CYLINDRICAL INTERFACE: INVISCID SYSTEM . . . 21

3.1 Theory . . . 21
3.2 Application to film boiling . . . 26
3.2.1 Mathematical model . . . 26
3.2.2 Comparison with experimental results . . . 28
3.3 Breakup of a liquid film around a horizontal cylindrical body 33
3.3.1 Experiments . . . 33
3.3.2 Theoretical analysis . . . 38
3.4 Conclusions . . . 43

CHAPTER 4 RAYLEIGH-TAYLOR INSTABILITY OF A CYLINDRICAL INTERFACE: VISCOUS FLUIDS 45

4.1 Theory . . . 45
4.2 Application to film boiling . . . 55
4.2.1 Mathematical model . . . 55
4.2.2 Comparison with experimental results . . . 57
4.3 Conclusions . . . 62

CHAPTER 5 KELVIN-HELMHOLTZ INSTABILITY OF A CYLINDRICAL INTERFACE:INVISCID FLUIDS 63

5.1 Theory . . . 63
5.2 Applications of the present theory . . . 67
5.2.1 Breakup of a gas jet in liquid . . . 67
5.2.2 Breakup of a liquid jet in gas . . . 71
5.3 Conclusions . . . 73

PART 2
GAS INJECTION PHENOMENA
THROUGH A VERY NARROW SLOT . . . 74

CHAPTER 6 LITERATURE REVIEW ON BUBBLE FORMATION . . 75

6.1 Spherical bubble formation models 80
6.1.1 Constant flow bubble formation 80
6.1.2 Constant pressure bubble formation 85
6.1.3 Bubble formation under unsteady conditions 86
6.2 Non-spherical bubble formation models 88
6.3 Bubble formation at a multi-orifice plate 89
6.4 Bubble formation in liquid metals 90
6.5 Discussion on bubble formation models 91
6.6 Conclusions 93

CHAPTER 7 MODIFIED BUBBLE FORMATION MODEL WITH SURFACE TENSION AND INERTIAL FORCES 95

CHAPTER 8 GAS INJECTION PHENOMENA THROUGH A VERY NARROW SLOT: EXPERIMENTAL 99

CHAPTER 9 GAS INJECTION PHENOMENA THROUGH A VERY NARROW SLOT: RESULTS AND ANALYSIS 116

9.1 Pressure drop across a slot 116
9.2 Bubble formation in the regular bubble regime 119
9.3 Bubble formation in the coalescence bubble regime 134
9.4 Critical transition condition between the regular bubble regime and the coalescence bubble regime 137
9.5 Bubble formation in the gas globe regime 139
9.6 Conclusions 142

CHAPTER 10 CONCLUSIONS AND SUGGESTIONS FOR FUTURE RESEARCH 144

10.1 Conclusions 144
10.1.1 Hydrodynamic instabilities of a cylindrical interface . 144

10.1.2 Gas injection phenomena through a very narrow slot . . . 146
10.2 Claims for original research . . . 147
10.3 Suggestions for future research . . . 149

APPENDIX I **BESSEL FUNCTION** . . . 150

APPENDIX II **EXPERIMENTAL RESULTS FOR GAS INJECTION** . . 152

APPENDIX III **TK-SOLVER PROGRAM FOR BUBBLE FORMATION THROUGH A NARROW SLOT** . . . 175

REFERENCES . . . 178

NOMENCLATURE

Roman letters

a	constant
a_i	major axis of *i*th ellipsoidal bubble (m).
A	constant
A_o	orifice cross section (m^2)
A_1	constant
A_1''	constant
A_2''	constant
b_i	minor axis of *i*th ellipsoidal bubble (m).
B	constant
B_1	constant
B_2''	constant
c_1	constant
c_2	constant
c_3	constant
C	phase speed in Chapter 2 (m/s)
C	sonic speed in Chapter 6 (m/s)
C_∞	phase speed in the absence of flow (m/s)
$C_{\infty,c}$	minimum value of C_∞ (m/s)
C_d	drag coefficient
D	constant
D_o	tube diameter (m)
d_b	bubble diameter (m)
d_g	vapour depth (m)
d_n	neck length for determining the detachment condition of the bubble formation (m)

d_p	particle (bubble or droplet) diameter (m)
f	friction factor
f_b	frequency of bubble formation (1/s)
f_p	frequency of pressure fluctuation (1/s)
F_{nozzle}	total force acting on the bubble by nozzle surface (N)
F_k	force acting on a solid surface by a fluid (N)
g	acceleration due to gravity (m/s^2)
G	growth rate (1/s)
G_i	imaginary part of growth rate (1/s)
G_r	real part of growth rate (1/s)
h	depth of slot (m)
H	depth of liquid (m)
$I_n(X)$	modified Bessel function of the first kind
Je	$=\rho_g U_{jet}^2 d_p/\sigma$ dimensionless gas-liquid jet number
k	wave number (1/m)
K_b	constant
K_o	nozzle constant (m^{4}s/kg)
$K_n(X)$	modified Bessel function of the second kind

$$I_0'(X) = \frac{dI_0(X)}{dX} = I_1(X) \quad ; \quad K_0'(X) = \frac{dK_0(X)}{dX} = -K_1(X)$$

$$I_0''(X) = \frac{d^2 I_0(X)}{dX^2} = I_0(X) - \frac{I_1(X)}{X} \quad ; \quad K_0''(X) = \frac{d^2 K_0(X)}{dX^2} = K_0(X) + \frac{K_1(X)}{X}$$

L	length of slot (m)
m	constant (1/m)
n	constant (1/m) in Chapter 2; order of Bessel function in Chapters 3-5
N	number of the bubble sources
N_{node}	node number of an unstable interface
N_c	capacitance number
n_b	number of the bubbles for measuring the average bubble volume
P	pressure of fluid (N/m^2)
ΔP	pressure drop across a slot (N/m^2)
P_{atm}	atmosphere pressure (N/m^2)

P_b	pressure inside a gas bubble (N/m^2)
P_c	pressure inside a nozzle chamber (N/m^2)
$(P_c)_o$	initial pressure inside a nozzle chamber (N/m^2)
P^d	perturbation pressure of fluid (N/m^2)
P^t	total pressure of fluid (N/m^2)
P^t_{10}	equilibrium pressure of fluid 1 (N/m^2)
P^t_{20}	equilibrium pressure of fluid 2 (N/m^2)
ΔP_{tr}	transverse pressure (N/m^2)
Q	potential of fluid in Chapter 4 $(m/s)^2$
Q	gas flow rate in Chapters 6-10 (m^3/s)
Q_d	dimensionless gas flow rate
Q_g	gas flow rate when gas flows into bubble from nozzle chamber (m^3/s)
Q_o	gas flow rate when gas flows into nozzle chamber from gas source (m^3/s)
Q_t	total gas flow rate (m^3/s)
r	bubble radius (m)
r_{fb}	bubble radius at the end of first stage of bubble formation (m)
r_h	bubble radius of a hemispherical bubble (m)
r_o	radius of a circular orifice (m)
r, θ, z	cylindrical coordinates
R	radius of cylindrical jet (m)
R_1, R_2	principal radii of disturbed cylindrical interface (m)
R_o	radius of cylinder (m)
R_c	radius of cylinder plus the vapour depth (m)
Re	Reynolds number
s	displacement of bubble centre from orifice plate (m)
t	time (s)
t_e	time at the end of first stage of Kumar and Kuloor's model (s)
t_c	time at the end of detachment (s)
T	temperature (K)
U	velocity of fluid (m/s)
U_{jet}	superficial velocity of gas-in-liquid jet or liquid-in-gas jet (m/s)
U_r^I, U_z^I	velocity components of fluid 1 in the cylindrical coordinates (m/s)
U_r^{II}, U_z^{II}	velocity components of fluid 2 in the cylindrical coordinates (m/s)

v	upward motion velocity of bubble (m/s)
V	potential of the impressed force in Chapter 4 (m^2/s^2)
V_b	bubble volume (m^3)
V_c	nozzle chamber volume (m^3)
V_f	final bubble volume (m^3)
V_{fb}	bubble volume at the end of first stage of bubble formation (m^3)
V_h	bubble volume of hemispherical at the end of first stage of bubble formation (m^3)
V_o	initial bubble volume (m^3)
W	slot spacing (m)
We	Weber number
x, y, z	coordinates for an plane interface (m)
Y, Y_o	vertical coordinate (m)

Greek letters

ϕ	velocity potential of fluid due to perturbation (m^2/sec)
Φ	velocity potential of fluid (m^2/sec)
ξ	disturbance of an interface (m)
ζ	kR_o
ρ	density of fluid (kg/m^3)
λ	wavelength (m)
α	angle between the horizontal axis and the symmetrical axis of the cylindrical interface (degree)
α_1	ratio between zero order of modified Bessel function of the first kind and its first order derivative
α_2	ratio between minus zero order of modified Bessel function of the second kind and its first order derivative
δ_1	ratio between nth order of modified Bessel function of the first kind and its first order derivative
δ_2	ratio between minus nth order of modified Bessel function of the second kind and its first order derivative
ε_1, ε_2	ratio between the second order derivative and the first order derivative of

	the zero order modified Bessel function of the first kind
ε_3, ε_4	ratio between the second order derivative and the first order derivative of the zero order modified Bessel function of the second kind
σ	interfacial tension between fluid 1 and fluid 2 (N/m)
μ	viscosity of fluid (Kg/m/sec)
ν	kinematic viscosity (m^2/sec)
Λ	dimensionless wavelength
Π	dimensionless radius
K	dimensionless wave number
M	dimensionless liquid viscosity parameter
Ω	dimensionless growth rate
Ψ	Stokes's stream function of fluid (m^3/sec)
ϵ	perturbing amplitude of the interface wave during film boiling (m)
θ_c	contact angle (degree)
$\Delta\rho$	density difference between liquid and gas (kg/m^3)

Subscript

$_1$	fluid 1, the lower fluid for a plane interface or inner fluid for a cylindrical interface
$_2$	fluid 2, the superior fluid for a plane interface or outward fluid for a cylindrical interface
$_c$	critical wavenumber or wavelength
$_{c,\,boiling}$	critical wavenumber or wavelength during film boiling on a cylindrical body
$_{c,\,bubble}$	critical wavenumber or wavelength during bubble formation from a narrow slot
$_{c,\,droplet}$	critical wavenumber or wavelength during liquid film breakup on a cylindrical body
$_{c,\,PW}$	corrected critical wavenumber or wavelength for the breakup of a liquid film on a cylindrical body
$_{c,\,LW}$	Lienhard and Wong's critical wavenumber or wavelength for film boiling on a cylindrical body
$_{c,\,Rayleigh}$	Rayleigh's critical wavelength for a liquid column

$_{c,\,Taylor}$	critical wavenumber or wavelength for the Rayleigh-Taylor instability of a plane interface
$_{d}$	most dangerous wavenumber or wavelength
$_{d,\,boiling}$	most dangerous wavenumber or wavelength during film boiling on a cylindrical body
$_{d,\,bubble}$	most dangerous wavenumber or wavelength during bubble formation from a narrow slot
$_{d,\,droplet}$	most dangerous wavenumber or wavelength during liquid film breakup on a cylindrical body
$_{d,\,gas}$	most dangerous wavelength for a gas-in-liquid jet
$_{d,\,jet}$	most dangerous wavelength for a plane gas or liquid jet
$_{d,\,kelvin}$	most dangerous wavelength for the Kelvin-Helmholtz instability of a plane interface
$_{d,\,liquid}$	most dangerous wavelength for a liquid-in-gas jet
$_{d,\,Lee}$	Lee's most dangerous wavenumber or wavelength for the breakup of a liquid film on a cylindrical body
$_{d,\,PW}$	corrected most dangerous wavenumber or wavelength for the breakup of a liquid film on a cylindrical body
$_{d,\,LW}$	Lienhard and Wong's most dangerous wavenumber or wavelength for film boiling on a cylindrical body
$_{d,\,Rayleigh}$	Rayleigh's most dangerous wavelength for a liquid column
$_{d,\,Taylor}$	most dangerous wavenumber or wavelength for the Rayleigh-Taylor instability of a plane interface
$_{g}$	gas
$_{I}$	inner fluid for a cylindrical interface
$_{II}$	outward fluid for a cylindrical interface
$_{l}$	liquid
$_{r,\,\theta,\,z}$	cylindrical coordinates

Superscript

^{d}	perturbation
^{t}	total

$_{I}$	inner fluid for a cylindrical interface
$_{II}$	outward fluid for a cylindrical interface

LIST OF TABLES

Table 3.1 Experimental results for the breakup of liquid film.

Table 5.1 Parameters of an air jet in water.

Table 6.1 Gas injection variables.
Table 6.2 Theoretical models for bubble formation at a single submerged orifice.

Table 8.1 Some related experimental parameters.
Table 8.2 Experimental conditions for gas injection phenomena from a slot nozzle.
Table 8.3 Physical properties of liquids and gases.

Table 9.1 Dimension of each variable.
Table 9.2 Slopes and intercepts of $ln(\lambda_d/W)$-$ln(We)$ curves.
Table 9.3 Experimental determined node number for gas globe regime.
Table 9.4 Calculated dangerous wavelengths for gas globe regime.

LIST OF FIGURES

Figure 2.1 The assumed geometry of film boiling on a horizontal cylindrical heater.

Figure 2.2 The assumed geometry of gas-liquid interface during liquid film breakup on a cylindrical body.

Figure 3.1 The relationships between the heater radius and the dangerous wavelengths for isopropanol.

Figure 3.2 The relationships between the heater radius and the dangerous wavelengths for benzene.

Figure 3.3 Calculated ratio between square of dimensionless growth rate and its maximum value as a function of dimensionless dangerous wavelength at specific radius.

Figure 3.4 The relationship between the dimensionless wavelength and the dimensionless radius.

Figure 3.5 Calculated ratio between the dimensionless dangerous wavelength and the dimensionless critical wavelength as a function of dimensionless radius.

Figure 3.6 Schematic representation of the condensation of water vapour on the cold tube.

Figure 3.7 Condensation of vapour on a cooled tube.

Figure 3.8 Schematic representation of the formation and the breakup of a liquid film around a cylindrical tube.

Figure 3.9 Photograph for a liquid film breakup experiment.

Figure 3.10 Breakup of a liquid film around horizontal cylindrical stainless steel and glass tubes.

Figure 3.11 The relationship between the dimensionless most dangerous wavelength and the dimensionless radius.

Figure 3.12 Calculated ratio between the most dangerous wavelength and the critical wavelength as a function of dimensionless radius.

Figure 4.1 Calculated relationships between dimensionless wavelength and dimensionless growth rate for M=1.

Figure 4.2 Calculated relationships between dimensionless wavelength and dimensionless growth rate for M=5.4.

Figure 4.3 Calculated relationships between dimensionless wavelength and dimensionless growth rate for M=16.

Figure 4.4 Experimental dimensionless growth rate for 0.185 of dimensionless radius.

Figure 4.5 Experimental dimensionless growth rate for 0.22 of dimensionless radius.

Figure 4.6 Experimental dimensionless growth rate for 0.33 of dimensionless radius.

Figure 4.7 Experimental and calculated dimensionless wavelength for M=5.4.

Figure 4.8 Experimental and calculated dimensionless wavelength for M=16.

Figure 5.1 Schematic illustration of breakup of gas jet into fine bubbles; the wavelengths on the top surface of the jet are shorter than those on the bottom of the jet.

Figure 5.2 Calculated G_i as a function of wavelength at U_l=0 and 10 m/s for air jet in water.

Figure 5.3 Calculated dangerous wavelength as a function of superficial gas velocity for an air jet in water.

Figure 5.4 Calculated dangerous wavelength as a function of superficial liquid velocity for a water jet in air.

Figure 6.1 Gas dispersion phenomena in circular orifice (d_o=5mm) injection.

Figure 6.2 Gas dispersion phenomena in porous plug injection.

Figure 6.3 Geometrical models of bubble formation.

Figure 7.1 Geometrical assumption of modified bubble formation model.

Figure 7.2 The comparison between Kumar and Kuloor's model and modified model for bubble formation dominated by both inertial and surface tension forces.

Figure 8.1 Schematic representation of the experimental system.

Figure 8.2 Photograph of the stainless steel slot-nozzle.

Figure 8.3 Side view of the slot-nozzle.

Figure 8.4 Configuration of a slot shaped nozzle and gas-liquid interface.

Figure 8.5 Regular bubble formation pattern when helium was injected into water through a slot with W=125μm at Q_t=1.5015 slpm (top picture) and Q_t=4.575 slpm (bottom picture).

Figure 8.6 Coalescence bubble formation pattern when helium was injected into water through a slot with W=125μm at Q_t=15.16 slpm.

Figure 8.7 Gas globe formation pattern when helium was injected into water through a W=125μm slot at Q_t=65 slpm, N_{node}=5.

Figure 8.8 Regular bubble formation pattern when air was injected into water through a slot with W=50μm at Q_t=0.24 slpm (top picture) and Q_t=0.65 slpm (bottom picture).

Figure 8.9 Coalescence bubble formation pattern when air was injected into water through a slot with W=50μm at Q_t=2.5 slpm (top picture) and Q_t=4 slpm (bottom picture).

Figure 8.10 Bubble formation when air was injected into water with W=50μm at Q_t=0.65 slpm (top picture) and Q_t=0.9 slpm (bottom picture). These pictures show only a part of a slot.

Figure 8.11 Regular bubble formation pattern when helium was injected into methyl alcohol through a slot with W=50μm at Q_t=0.07 slpm (top picture) and Q_t=0.88 slpm (bottom picture).

Figure 8.12 Regular bubble formation pattern when air was injected into methyl alcohol through a slot with W=75μm at Q_t=0.4slpm (top picture) and Q_t=0.8 slpm (bottom picture).

Figure 8.13 Coalescence bubble formation pattern when air was injected into methyl alcohol through a slot with W=75μm at Q_t=2.6slpm (top picture) and Q_t=5.4slpm (bottom picture).

Figure 8.14 Gas globe formation pattern when air is injected into methyl alcohol through a slot with W=75μm at Q_t=22.8slpm; N_{node}=10.

Figure 8.15 Bubble formation pattern in "*regular bubble regime*" when helium was injected into methyl alcohol through a W=250μm slot at Q_t=7.6slpm.

Figure 8.16 Schematic representation of measuring the number of bubble sources in the regular bubble regime.

Figure 9.1 Measured pressure drop as a function of gas flow rate.

Figure 9.2 The relationship between fraction factor and Reynolds Number.

Figure 9.3 The predicted and measured bubble volume as a function of gas flow rate per bubble source for a $W=125\mu m$ slot submerged in water (from Tables A-1 and A-2).

Figure 9.4 The predicted and measured bubble volume as a function of gas flow rate per bubble source for a $W=75\mu m$ slot submerged in water (from Tables A-3 and A-4).

Figure 9.5 The predicted and measured bubble volume as a function of gas flow rate per bubble source for a $W=75\mu m$ slot submerged in methyl alcohol (from Table A-5).

Figure 9.6 The predicted and measured bubble volume as a function of gas flow rate per bubble source for a $W=50\mu m$ slot submerged in water (from Table A-6).

Figure 9.7 The predicted and measured bubble volume as a function of gas flow rate per bubble source for a $W=50\mu m$ slot submerged in methyl alcohol (from Tables A-7 and A-8).

Figure 9.8 The predicted and measured bubble volume as a function of gas flow rate per bubble source for a $W=250\mu m$ slot submerged in water (from Table A-9).

Figure 9.9 The predicted and measured bubble volume as a function of gas flow rate per bubble source for a $W=250\mu m$ slot submerged in methyl alcohol (from Tables A-10 and A-11).

Figure 9.10 The predicted and measured bubble volume as a function of gas flow rate per bubble source for a $W=175\mu m$ slot submerged in methyl alcohol (from Tables A-12 and A-13).

Figure 9.11 The predicted and measured bubble volume as a function of gas flow rate per bubble source for a $W=175\mu m$ slot submerged in water (from Tables A-14 and A-15).

Figure 9.12 Calculated ratio between dangerous wavelength and critical wavelength as a function of dimensionless radius for an axisymmetrical cylindrical interface at $\theta=0$.

Figure 9.13 The relationship between the most dangerous wavelength and dimensionless radius of cylindrical interface

Figure 9.14 Measured dimensionless distance between bubbles as a function of Weber number for first eight experiments.

Figure 9.15 Measured dimensionless distance between bubbles as a function of Weber number for last seven experiments.

Figure 9.16 The comparison between the measured and predicted dimensionless distance between the bubbles.

Figure 9.17 The relationship between coefficient, A, and the density ratio between liquid and gas, ρ_l/ρ_g.

Figure 9.18 Measured K_b values for fifteen experiments.

Figure 9.19 Measured bubble diameter as a function of total gas flow rate for the fifteen experiments.

Figure 9.20 Schematic drawing of the critical transition condition between the regular bubble regime and the coalescence regime.

Figure 9.21 The comparison between measured and predicted critical transformation condition.

Figure 9.22 Schematic drawing of the gas globe regime.

CHAPTER 1

INTRODUCTION TO THE THESIS

1.1 BACKGROUND OF THE PRESENT RESEARCH

Gas-liquid interactions occur in boiling and condensation operations, and in many chemical and metallurgical processes. The hydrodynamic instabilities of the gas-liquid interface play an important role in film boiling[1], filmwise condensation[2] and in gas bubble breakup[3]. There are two kinds of instabilities for interfaces between two fluid phases. The first derives from the character of the equilibrium of an interface between two fluids of different densities superposed one on another or accelerated towards each other; the instability of the plane interface between the two fluids, when it occurs, is called the *Rayleigh*[4]*-Taylor*[5] *instability*. The second type of instability arises when two stratified heterogeneous fluids are in relative motion; the instability of the plane interface between the two fluids, when it occurs, is called the *Kelvin-Helmholtz instability*[6,7,8].

Vapour evolution during film boiling and droplet formation during filmwise condensation are definite and highly predictable Rayleigh-Taylor instability processes. In order to understand the film boiling and the condensation on a cylindrical body rather than on a planar interface, the conventional theory of the Rayleigh-Taylor instability of a planar interface must be modified to incorporate the cylindrical curvature of the interface between gas vapour and liquid. Therefore, the first part of the thesis is concerned with the mathematical development and subsequent application of the Rayleigh-Taylor instability to a cylindrical interface between two fluids.

The theme of the second part of the thesis is the gas injection through a very narrow slot. The distribution of gas bubbles into a liquid or slurry for the purpose of mass transfer is a very often preformed operation in chemical and metallurgical engineering. Because the main purpose of this gas phase subdivision is to increase the interfacial area, it is essential to produce small size bubbies. It was found in the present research that small size bubbles could be generated through a very narrow slot (e.g., 50-250μm). When gas was injected into liquid through a very narrow slot, the dynamic gas-liquid interface along the length of the slot could be assumed as a cylindrical one due the capillary effect. Because of the instability of the cylindrical interface, the dynamic gas-liquid interface breaks-up so that small bubbles are formed separately along the slot. The mechanism of the bubble generation through a very narrow slot is similar to that of the vapour bubble formation during film boiling on a cylindrical heater.

1.2 OBJECTIVES OF THE PRESENT WORK

Bubble formation during film boiling on a cylindrical body and during gas injection through a very narrow slot results from the breakup of a cylindrical interface between liquid and gas. The breakup phenomena of a cylindrical interface between two fluid phases was attributed to the hydrodynamic instabilities. Thus, the overall objective of this investigation was to analyze the hydrodynamic instabilities of cylindrical interfaces with application to several gas-liquid interaction processes. To achieve this objective, the following studies were carried out.

1. To analyze the Rayleigh-Taylor instability of a cylindrical interface between two fluids so that:

   • a mathematical model is proposed to predict the film boiling phenomena on a cylindrical heater immersed in both inviscid and viscous liquids.

   • the breakup phenomena of a liquid film around a long, horizontal, circular cylindrical body in still air is clarified. Furthermore, the erroneous theoretical analysis and experimental result reported in the literature[9] can be corrected.

2. To examine the Kelvin-Helmholtz instability of a cylindrical interface between two moving fluids with applications to the breakup of a gas-in-liquid jet and a liquid-in-gas jet.

3. To understand the gas injection phenomena through a very narrow slot so that the bubble formation from a slot could be predicted.

1.3 STRUCTURE OF THE THESIS

This thesis consists of two parts comprising ten chapters. The first part (Chapters 2-5) covers the hydrodynamic instabilities and their applications. The second part (Chapters 6-9) presents the gas injection phenomena through a very narrow slot. Chapter 10 concludes the thesis and suggests future research.

In the first part, a literature survey on the hydrodynamic instabilities is presented and the Rayleigh-Taylor instability and the Kelvin-Helmholtz instability of a plane interface are described. Film boiling on a cylindrical heater is reviewed. Previous mistakes reported in the literature regarding the breakup of a liquid film around a cylindrical body are pointed out and are corrected.

Following this, the Rayleigh-Taylor instabilities of a cylindrical interface between two inviscid fluids and between two viscous fluids with applications to film boiling on a cylindrical heater and liquid film breakup on a cylindrical body are examined.

Finally, the Kelvin-Helmholtz instability of a cylindrical interface between two inviscid fluids with applications to the analysis of the breakup of the gas-in-liquid jet and liquid-in-gas jet is discussed.

In the second part, previous research about gas injection phenomena with emphasis of bubble formation models is first reviewed. A modified bubble formation model with consideration of surface tension and inertial forces is then proposed. Experimental phenomena and results as well as theoretical analysis on gas injection through a very narrow slot are presented.

PART 1

HYDRODYNAMIC INSTABILITIES OF A CYLINDRICAL INTERFACE

CHAPTER 2

LITERATURE REVIEW ON INTERFACIAL HYDRODYNAMIC INSTABILITY

Hydrodynamic interfacial instabilities occur through nature in an astonishing diversity of physical, chemical and engineering systems. For example:

A. *Natural phenomena*

1) Overturn of the outer portion of the collapsed core of a massive star[10].
2) The formation of high luminosity twin-exhaust jets in rotating gas clouds in an external gravitational potential[11].

B. *Technological applications*

1) Laser implosion of deuterium-tritium fusion targets[12].
2) Boiling phenomena[13].

This chapter reviews the hydrodynamic theory of interfacial instability, film boiling and condensation.

2.1 INTERFACIAL INSTABILITIES

It was Helmholtz[7] who first considered the stability of an interface of two superposed semi-infinite fluids flowing with different velocities. His work was followed by that of Kelvin[6]. The stability of an interface between two superposed fluids under the action of gravity was first investigated by Stokes[8]. In 1883, Rayleigh[4] analyzed the stability of a fluid with variable density, which was the fundamental work for the so called "Rayleigh-Taylor instability". The stability of heterogeneous fluids accelerated in the direction perpendicular to the plane of stratification can be treated by the same formalism as used by Rayleigh. Harrison[14] obtained the dispersion equation, relating the wavenumber, k, and growth rate, G, by taking into account the surface tension and viscosity. Harrison's discussion was complete from an analytical standpoint. The special case of the stability of the interface between two fluids of differing densities was also investigated by Taylor[5]. Bellman and Pennington[15] also reconsidered the problem by taking into account the surface tension and the viscosity and obtained a dispersion equation which, though very different in form, was nevertheless the same as Harrison's result, when certain of Harrison's misprints were corrected. From this point of view, the work of Taylor[5] and of Bellman and Pennington[15] was mathematically based on the work of Harrison.

The nature of the equilibrium of a cylindrical column of liquid jet in still air (zero density) was first analyzed by Rayleigh[16]. It can be considered as the first mathematical analysis of the instability of a cylindrical interface. Lamb[8] extended Rayleigh's analysis to treat circumferential waves as well as axisymmetric ones. Rayleigh concluded that for symmetry about the axis, the equilibrium is unstable for disturbances whose wavelength exceeds the circumference of the jet, and the ratio of the wavelength to the diameter of jet for the kind of disturbance which leads most rapidly to the disintegration of the cylindrical mass is equal to 4.508, i.e.,

$$\begin{aligned} \lambda_{c,Rayleigh} &= 2\pi R \\ \lambda_{d,Rayleigh} &= 4.508\,(2R) \end{aligned} \tag{3}$$

where $\lambda_{c,Rayleigh}$ and $\lambda_{d,Rayleigh}$ are the critical and dangerous wavelengths of liquid cylindrical column; R is the radius of the cylindrical jet.

The Rayleigh-Taylor instability of a spherical interface has also been analyzed by several investigators [17,18].

2.1.1 KELVIN-HELMHOLTZ INSTABILITY OF A PLANAR INTERFACE

The Kelvin-Helmholtz instability arises at the interface of two fluid layers of different densities, ρ_1 and ρ_2, flowing horizontally with velocities, U_1 and U_2, respectively.

If the effects of viscosity of the fluids are neglected, and the perturbed flow is assumed to be irrotational, the velocity potentials of the two fluids can be written, respectively, as:

$$\Phi_1 = U_1 x + \phi_1 \quad , \qquad \Phi_2 = U_2 x + \phi_2 \tag{4}$$

in which x is measured in the direction of the mean velocities; ϕ_1 and ϕ_2 are the velocity potentials for fluid 1 and 2 due to a perturbation; the subscript 1 indicates the lower fluid; and all of the Φ (ϕ)'s satisfy the Laplace equation.

If the direction of increasing y is the vertically upwards, and ξ is the displacement of the interface in the y-direction, the kinematic conditions to be satisfied at $y=0$ are:

$$\frac{\partial \xi}{\partial t} + U_1 \frac{\partial \xi}{\partial x} = \frac{\partial \Phi_1}{\partial y} \quad , \qquad \frac{\partial \xi}{\partial t} + U_2 \frac{\partial \xi}{\partial x} = \frac{\partial \Phi_2}{\partial y} \tag{5}$$

in which the quadratic terms in ξ, ϕ_1 and ϕ_2 are neglected. Other boundary conditions for ϕ_1 and ϕ_2 are, without loss of generality,

$$\phi_1 \to 0 \quad as \quad y \to -\infty \quad , \, and \qquad \phi_2 \to 0 \quad as \quad y \to \infty \tag{6}$$

which guarantee vanishing velocities at $y = \pm\infty$.

Neglecting higher than first order terms in ξ, the dynamic boundary condition at the interface is:

$$P_1^d - P_2^d = -\sigma \left[\frac{\partial^2 \xi}{\partial x^2} + \frac{\partial^2 \xi}{\partial z^2} \right] \tag{7}$$

in which z is measured in a horizontal direction normal to that x, and σ is the surface tension; P_1^d and P_2^d are the perturbation pressures. Since the flow is assumed to be irrotational, the Bernoulli equation can be used to evaluate P^d. The linearized form of it is:

$$\frac{P_1^d}{\rho_1} = -\frac{\partial \phi_1}{\partial t} - U_1 \frac{\partial \phi_1}{\partial x} - gy \tag{8}$$

and a similar formula gives P_2^d in terms of ϕ_2 and U_2. Applying the formulas for P_1^d and P_2^d to Equation (7) at $y=\xi$, one has:

$$\rho_1 \left[-\frac{\partial \phi_1}{\partial t} - U_1 \frac{\partial \phi_1}{\partial x} - g\xi \right] - \rho_2 \left[-\frac{\partial \phi_2}{\partial t} - U_2 \frac{\partial \phi_2}{\partial x} - g\xi \right] = -\sigma \left[\frac{\partial^2 \xi}{\partial x^2} + \frac{\partial^2 \xi}{\partial z^2} \right] \tag{9}$$

where g is the acceleration due to gravity.

If the perturbation is assumed to be periodic in x and z, the appropriate forms for ϕ_1, ϕ_2 and ξ are:

$$\begin{aligned} \phi_1 &= c_1 \exp[ky + i(Gt + mx + nz)] \\ \phi_2 &= c_2 \exp[-ky + i(Gt + mx + nz)] \end{aligned} \tag{10}$$

$$\xi = a \exp[i(Gt + mx + nz)] \tag{11}$$

where a, c_1 and c_2 are constants, k the wave number, and G the growth rate. It is evident that ϕ_1 and ϕ_2 satisfy the Laplace equation if:

$$k^2 = m^2 + n^2 \tag{12}$$

and that the boundary conditions at $y = \pm\infty$ are satisfied. Substituting Equations (10)-(11) into Equations (5) and (9), and then eliminating c_1, c_2 and a, yields:

$$\frac{G}{m} = -\frac{\rho_1 U_1 + \rho_2 U_2}{\rho_1 + \rho_2} \pm \left[\frac{gk}{m^2} \frac{\rho_1 - \rho_2}{\rho_1 + \rho_2} + \frac{\sigma k^3}{m^2} \frac{1}{\rho_1 + \rho_2} - \frac{\rho_1 \rho_2 (U_1 - U_2)^2}{(\rho_1 + \rho_2)^2} \right]^{1/2} \tag{13}$$

If the disturbance is two-dimensional, $n = 0$ and $m = k$, Equation (13) becomes:

$$\frac{G}{k} = -\frac{\rho_1 U_1 + \rho_2 U_2}{\rho_1 + \rho_2} \pm \left[\frac{g}{k} \frac{\rho_1 - \rho_2}{\rho_1 + \rho_2} + \frac{\sigma k}{\rho_1 + \rho_2} - \frac{\rho_1 \rho_2 (U_1 - U_2)^2}{(\rho_1 + \rho_2)^2} \right]^{1/2} \tag{14}$$

which is called *dispersion equation* and was in effect given by Lamb and Chandrasekhar[8,19]. The right-hand side of Equation (14) is the phase velocity of the disturbance. If the propagation velocity of the surface waves is expressed by C, Equation (14) can be rewritten as:

$$C = -\frac{\rho_1 U_1 + \rho_2 U_2}{\rho_1 + \rho_2} \pm \left[C_\infty^2 - \rho_1 \rho_2 \left(\frac{U_1 - U_2}{\rho_1 + \rho_2} \right)^2 \right]^{1/2} \tag{15}$$

in which,

$$C_\infty^2 = \frac{g}{k} \frac{\rho_1 - \rho_2}{\rho_1 + \rho_2} + \frac{\sigma k}{\rho_1 + \rho_2} \tag{16}$$

When the root in the expression for the wave velocity C has a nonzero imaginary part, the interfacial disturbance can grow exponentially. Hence, the flow is unstable if:

$$\frac{g}{k} \frac{\rho_1 - \rho_2}{\rho_1 + \rho_2} + \frac{\sigma k}{\rho_1 + \rho_2} < \rho_1 \rho_2 \left(\frac{U_1 - U_2}{\rho_1 + \rho_2} \right)^2 \tag{17}$$

There are several important points to be recognized in this stability criterion. First, the viscosities of the fluids are neglected; therefore, the Reynolds number plays no role in this kind of interfacial instability. The instability of the system then is governed by three effects-namely, the gravity force, surface tension force, and relative motion. The relative-motion term reflects the effect of the pressure through the Bernoulli principle. The gravity term is stabilizing only if the upper fluid is lighter than the lower fluid ($\rho_2 < \rho_1$). The surface-tension force is always stabilizing, since the flat interface has the minimum surface area, and the surface-tension force acts to resist any deformation from the equilibrium configuration. On the other hand, relative motion between the fluids is destabilizing.

The propagation velocity, C_∞, in the absence of the flows (or the left-hand side of the stability criterion) is a function of the wave number k. Therefore, as the wavelength $\lambda = 2\pi/k$ changes from zero to infinite, the wave velocity decreases to the minimum value and then increases. This minimum value of C_∞^2 is given by:

$$C_{\infty c}^2 = 2 \left(\frac{\sigma g (\rho_1 - \rho_2)}{(\rho_1 + \rho_2)^2} \right)^{1/2} \tag{18}$$

which occurs at the critical wave number, k_c:

$$k_c = \left[\frac{g(\rho_1 - \rho_2)}{\sigma} \right]^{1/2} \tag{19}$$

This corresponds to the critical wavelength λ_c:

$$\lambda_c = \frac{2\pi}{k_c} = 2\pi \left[\frac{\sigma}{g(\rho_1 - \rho_2)} \right]^{1/2} \tag{20}$$

The system is stable for small disturbances of all wavelengths if the relative velocity is sufficiently small to satisfy:

$$(U_1 - U_2)^2 < \frac{2(\rho_2 + \rho_1)}{\rho_1 \rho_2} \sqrt{\sigma g(\rho_1 - \rho_2)} \tag{21}$$

For a relative velocity larger than this limit, the system is only conditionally stable for a certain range of wavelengths. When the wavelength is large, the value of C_∞^2 in Equation (16) is mainly determined by the gravity term. Conversely, if λ is sufficiently small, the capillary force governs the wave motion.

Since the dominant wave is the one having the maximum growth rate, it is obtained by vanishing the derivative of the imaginary part of the growth rate, G, with respect to wavenumber k. From Equation (14), if $G = G_r + iG_i$, G_i is then expressed as:

$$G_i^2 = -\frac{gk(\rho_1 - \rho_2)}{\rho_1 + \rho_2} - \frac{\sigma k^3}{\rho_1 + \rho_2} + \frac{\rho_1 \rho_2 (U_1 - U_2)^2 k^2}{(\rho_1 + \rho_2)^2} \tag{22}$$

$\partial G_i^2 / \partial k = 0$ leads to:

$$-\frac{g(\rho_1 - \rho_2)}{\rho_1 + \rho_2} - \frac{3\sigma k^2}{\rho_1 + \rho_2} + \frac{2\rho_1 \rho_2 (U_1 - U_2)^2 k}{(\rho_1 + \rho_2)^2} = 0 \tag{23}$$

Furthermore:

$$\lambda_{d,Kelvin} = \frac{2\pi}{k_{d,Kelvin}} = \frac{2\pi}{\dfrac{\rho_1\rho_2(U_1-U_2)^2}{3\sigma(\rho_1+\rho_2)} + \left[\left[\dfrac{\rho_1\rho_2(U_1-U_2)^2}{3\sigma(\rho_1+\rho_2)}\right]^2 - \dfrac{g(\rho_1-\rho_2)}{3\sigma}\right]^{1/2}} \tag{24}$$

$\lambda_{d,\,Kelvin}$ is the most dangerous wavelength for the Kelvin-Helmholtz instability.

The Kelvin-Helmholtz instability plays an important role in the breakup of a jet. For a high speed gas-in-liquid jet or liquid-in-gas jet, the gravity term, the density of the gas phase and the velocity of the bulk phase in Equation (24) can be neglected, so that Equation (24) is written as:

$$\lambda_{d,jet} = \frac{3\pi\sigma}{\rho_g U_{jet}^2} \tag{25}$$

where U_{jet} is the superficial velocity of the jet and $\lambda_{d,\,jet}$ is the most dangerous wavelength of a gas-in-liquid or a liquid-in-gas jet. Because of the Kelvin-Helmholtz instability, a liquid-in-gas jet breaks up into fine droplets and a gas-in-liquid jet breaks up into fine bubbles. If the diameters of the droplets or bubbles, d_p, are of the order of the most dangerous wavelength, $\lambda_{d,\,jet}$, we then can define a very important dimensionless number, *Je*:

$$Je = \frac{d_p\rho_g U_{jet}^2}{\sigma} \tag{26}$$

where *Je* is designated as the gas-liquid jet number by the present author. In fact, it is a Weber number. The reason for the present author to define the dimensionless gas-liquid jet number, *Je*, is that the gas density to surface tension ratio dominates the droplet (or bubble) size of a high speed liquid-in-gas jet (or a gas-in-liquid jet) rather than the liquid density to surface tension ratio. Many investigators who believe that the liquid density to surface tension ratio dominates the diameters of bubbles produced from a gas jet are misled by traditionally defined Weber number, *We*:

$$We = \frac{d_p \rho_l U_{jet}^2}{\sigma} \tag{27}$$

2.1.2 RAYLEIGH-TAYLOR INSTABILITY OF A PLANAR INTERFACE

The Rayleigh-Taylor instability is the interfacial instability between two fluids of different densities that are stratified in a gravity field or accelerated normal to the interface. It is commonly observed that the interface between two stratified fluid layers at rest is not stable if the upper-fluid density ρ_2 is larger than the lower-fluid density ρ_1. Since the Rayleigh-Taylor instability leads to deformation of the interface, it is important in the formation of bubbles or droplets. In particular, the critical wavelength predicted by the related stability analysis is one of the most significant length scales for two-phase flows.

The Rayleigh-Taylor instability can be considered as a special case of the Kelvin-Helmholtz instability with zero flow and with $\rho_2 > \rho_1$. Hence the propagation velocity can be obtained from Equation (15) by setting $U_l = U_2 = 0$, i.e.,

$$C^2 \equiv \frac{G^2}{k^2} = \frac{g}{k}\frac{\rho_1 - \rho_2}{\rho_1 + \rho_2} + \frac{\sigma k}{\rho_1 + \rho_2} \tag{28}$$

The system is unstable if the root of the propagation velocity has a nonzero imaginary part. Equation (28) shows that the gravitational force is destabilizing for $\rho_2 > \rho_1$, whereas the surface tension force is stabilizing. There is a critical wavelength $\lambda_{c,Taylor}$ below which C^2 is always positive. This is given by:

$$\lambda_{c,Taylor} = \frac{2\pi}{k_{c,Taylor}} = 2\pi\left[\frac{\sigma}{g(\rho_2 - \rho_1)}\right]^{1/2} \tag{29}$$

If the wavelength of a disturbance is larger than the critical wavelength, then C^2 becomes negative and the interface is unstable. For fluids that extend infinitely in the plane of the interface, the wavelength of the disturbance can be as large as necessary; therefore such a system is always unstable. However, if the fluids are confined, the maximum wavelength is limited to twice the system dimension. This implies that a system is stable if the lateral characteristic dimension is less than half the critical wavelength $\lambda_{c,Taylor}$. For an air-water system, this characteristic dimension is 0.86 cm.

For an unstable system, any disturbance having a wavelength greater than $\lambda_{c,Taylor}$ can grow in time. However, the dominant waves, $\lambda_{d,Taylor}$, are those having the maximum growth rate [max($-G^2$)]. From Equation (28) it should be:

$$\lambda_{d,Taylor} = 2\pi\sqrt{3}\left[\frac{\sigma}{g\,(\rho_2-\rho_1)}\right]^{1/2} \tag{30}$$

This is the so-called *most dangerous* wavelength which exhibit the maximum growth rate. These unstable waves can be observed as condensed water droplets dripping from a horizontal downward-facing surface. Quite regular waveforms and generation of bubbles due to the Rayleigh-Taylor instability can be observed in film boiling. However, this instability is not limited to the gravitational field. Any interface between fluids that are accelerated normal to the interface, can exhibit the same instability. In such a case the acceleration should replace the gravity field g in the analysis.

2.2 HYDRODYNAMIC THEORY OF FILM BOILING

There exist three types of boiling, namely, nucleate, transition and film boiling. The transition from one type to another is accompanied by marked changes in the hydrodynamic and thermal states of the system. In the film boiling regime, the superheated wall and the saturated boiling (or subcooled) liquid are separated by a thin vapour film. The upper limit of the attainable heat flux in the region of film boiling is determined by the melting point of the heating material. A lower limit is given by so-called Leidenfrost point[20], where the thickness of the vapour film reaches a minimum value that is critical for stability. Relatively large vapour bubbles are periodically released from the upper side of the liquid-vapour interface in film boiling. In the neighbourhood of the Leidenfrost point, the coalescence of the individual vapour bubbles is avoided, and heat removal from the surface is assumed to be governed by the behaviour of the bubbles, which in turn should be related to the occurrence of hydrodynamic instabilities at the liquid-vapour interface.

Chang[21,22], Zuber[23], and Zuber and Tribus[24] presented mathematical model for film boiling on horizontal flat plates. These models are based on the Rayleigh-Taylor instability of the liquid-vapour interface. Capillary waves are propagated along this interface which becomes unstable if the wavelength exceeds a certain critical value. Berenson[25] improved on these theories by emphasizing the importance of the *most dangerous* wavelength, instead of the critical wavelength.

For film boiling on a horizontal cylindrical wire, the equations for the Rayleigh-Taylor instability of a plane interface must be modified to incorporate the effect of the surface tension along the curved periphery of the liquid-vapour interface normal to the axis of the wire. Lienhard and Wong [26] made an assumption regarding the shape of this cylindrical vapour-liquid interface, as shown in Figure 2.1. In this assumption, a cylindrical heater with radius R_o is immersed in liquid. The shape of the liquid-vapour interface surrounding the wire during film boiling is assumed to take a sinusoidally undulating, asymmetrical form. The vapour blanket surrounding the heater is assumed to be sufficiently thin that the smallest radius of the interface is negligibly larger than the radius of heater. The maximum perturbing amplitude, ϵ, of the dominant wave occurs at the top of the interface. The pressure due to the surface tension in the transverse direction varies between σ/R_0 in the valleys and $\sigma/(R_0+\epsilon)$ at the peaks of the wave, it has an average value of $\sigma/(R_0+\epsilon/2)$ and an amplitude of $\sigma\epsilon/(2R_0^2)$. Therefore, the transverse pressure can be expressed as[26]:

$$\Delta P_{tr} = \frac{\sigma\xi}{2R_o^2} \tag{31}$$

After considering the transverse pressure, the dynamic boundary condition (Equation (7)) at the interface is expressed as:

$$P_1^d - P_2^d = -\sigma\left[\frac{\partial^2\xi}{\partial z^2}\right] - \Delta P_{tr} \tag{32}$$

in which the curvature in the x direction is replaced by the transverse pressure, ΔP_{tr}. If a two-dimensional wave is assumed ($n = 0$), and $U_1 = U_2 = 0$ is considered, the dispersion equation (Equation (14)) becomes:

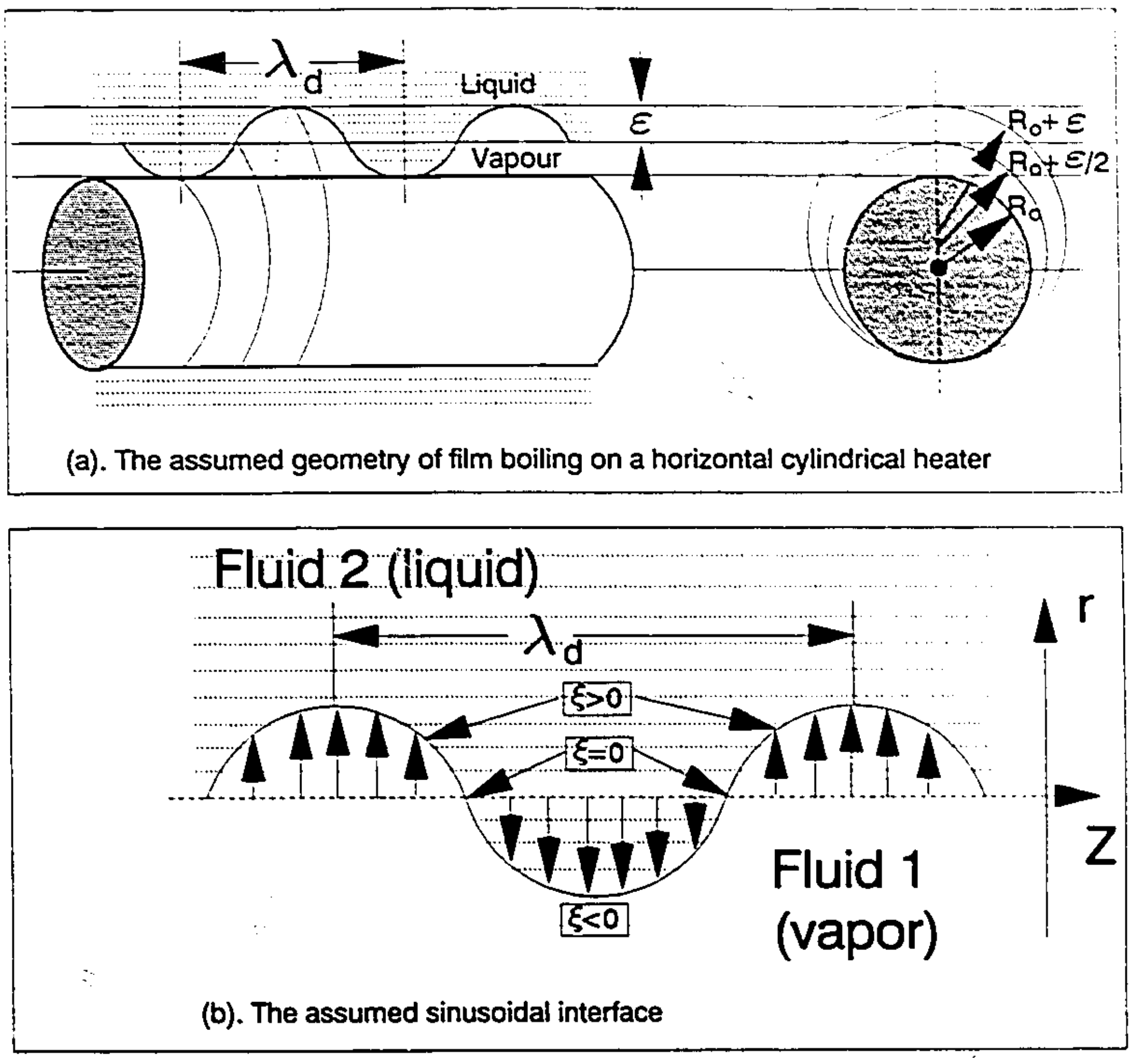

Figure 2.1 The assumed geometry of film boiling on a horizontal cylindrical heater.

$$C^2 \equiv \frac{G^2}{k^2} = \frac{g}{k}\frac{\rho_1 - \rho_2}{\rho_1 + \rho_2} + \frac{\sigma k}{\rho_1 + \rho_2} - \frac{\sigma}{2k(\rho_1 + \rho_2)R_o^2} \tag{33}$$

By setting $C = 0$ we have the critical wavelength:

$$\lambda_{c,LW} = \frac{2\pi}{\left[\frac{g(\rho_2 - \rho_1)}{\sigma} + \frac{1}{2R_o^2}\right]^{1/2}} \tag{34}$$

By maximizing the growth rate, the dangerous wavelength can be expressed as:

$$\lambda_{d,LW} = \frac{2\pi\sqrt{3}}{\left[\frac{g(\rho_2 - \rho_1)}{\sigma} + \frac{1}{2R_o^2}\right]^{1/2}} \tag{35}$$

Equations (34) and (35) were obtained by Lienhard and Wong[26] in 1964.

By assuming that the spacing between bubbles is dominated by the dangerous wavelength, Lienhard and Wong predicted and measured the distance between the bubbles forming during film boiling on cylindrical wires in isopropanol and benzene. The experimental bubble spacing exceeds the theoretical value by 25% in both isopropanol and benzene. In 1969, Lienhard and Sun[27] proposed a modified formula for the prediction of the wavelength by taking into account the minimum blanket thickness of vapour in order to overcome the under-estimation of dangerous wavelength of Lienhard and Wong's model. However, comparison to experiment showed that they still under-predicted the data. In fact, this is not surprise because they oversimplified the instability problem of the cylindrical interface due to the use of Cartesian coordinates even though they considered the eccentric circular contour of the interface on planes perpendicular to the heating wire axis. They employed velocity potentials for a flat interface (which are the solutions of the continuity equation and the momentum equations for a flat interface rather than for a cylindrical interface) to analyze the instability problem for cylindrical interface. One of the objectives of this thesis is to propose a correct model to predict the film boiling phenomena on a cylindrical heater.

In order to predict the film boiling phenomena on a cylindrical wire in a viscous system, Dhir and Lienhard[28], following the same mathematical procedure as used by Bellman and Pennington[15] but including transverse pressure term due to cylindrical curvature, obtained dispersion equation for viscous fluids similar to Lienhard and Wong's modification for a inviscid system. Again, it can only be considered as an approximation.

2.3 THE MISTAKES OF LEE'S MODEL

In contrast to film boiling on a cylindrical heater, when a horizontal cylindrical body, with infinite length and uniform circular cross section, is coated with a thin film of liquid and placed in still air, the liquid film will break away from the cylindrical body due to the Rayleigh-Taylor instability. By employing Cartesian coordinates as Lienhard and Wong did, Lee[9] presented a theoretical model to predict the dominated wavelength during the breakup of a liquid film around the cylinder. In his theoretical analysis, not only was the incorrect coordinate system used but also mistakes were made so that a completely wrong conclusion was drawn.

By assuming that the entire surface of the horizontal, infinitely long circular cylinder is covered by a layer of liquid film thin enough to be regarded as having uniform thickness while in equilibrium as shown in Figure 2.2, Lee got an expression for the exponential growth rate (Equation (21) of Lee's paper)*:

$$-G^2 = \frac{\left[g(\rho_2 - \rho_1) + \sigma\left[k^2 + \frac{1}{R_o^2}\right]\right] k}{\rho_1 + \rho_2} \tag{36}$$

Since the wave amplitude grows according to $\exp(iGt)$, $G^2 < 0$ gives unstable interface; i.e., when:

$$k^2 > \left[\frac{(\rho_1 - \rho_2)\, g}{\sigma} - \frac{1}{R_o^2}\right] \tag{37}$$

the interface is unstable. Consequently, a shorter wavelength (larger wavenumber) would produce an unstable interface, which is wrong and also in conflict with his Figure 3.

By maximizing $-G^2$, Lee obtained expressions for the dangerous wavenumber (in his paper, he called it the critical wavenumber):

* In Lee's paper, C_1 and β_1 were used to express the exponential growth rate and the wave number, respectively, i.e., $iG=C_1$ and $k=\beta_1$.

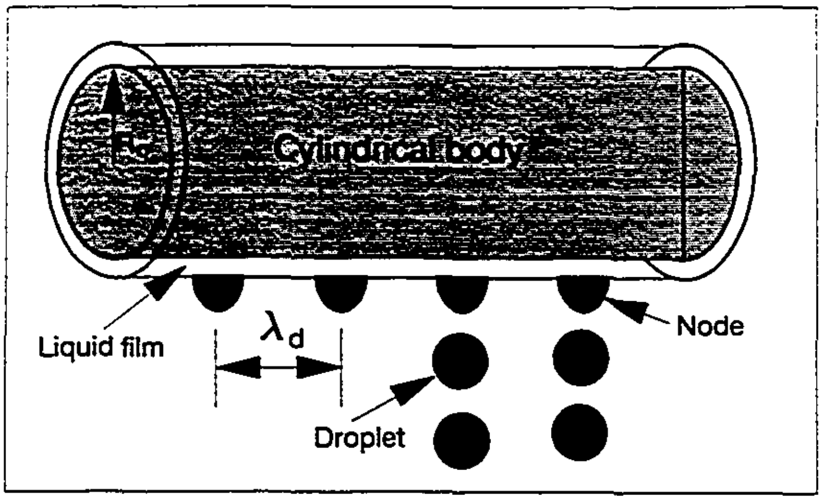

Figure 2.2 The assumed geometry of gas-liquid interface during liquid film breakup on a cylindrical body

$$k_{d,Lee} = \frac{\left[\dfrac{(\rho_1 - \rho_2)\, g}{\sigma} - \dfrac{1}{R_o^2}\right]^{1/2}}{\sqrt{3}} \tag{38}$$

and the dangerous wavelength (he called the critical wavelength):

$$\lambda_{d,Lee} = \frac{2\pi\sqrt{3}}{\left[\dfrac{(\rho_1 - \rho_2)\, g}{\sigma} - \dfrac{1}{R_o^2}\right]^{1/2}} \tag{39}$$

Thus, the dangerous wavelength increases with a decrease of the radius of the cylinder, which means that extremely thin wires give the most stable interface (from Figure 3 of Lee's paper, when the dimensionless radius $(g(\rho_1-\rho_2)/\sigma)^{1/2}R_o < 1$, the interface is stable for all wavelengths). Again, this conclusion is questionable despite Lee having experimental data to verify his theory.

Lee made several mistakes in his analysis:

(1). The expression for the curvature caused by the variation of ξ in the x direction is not correct. Equation (16) of Lee's paper should be:

$$\frac{1}{R_{(x)}} = -\frac{\partial^2 \xi}{\partial x^2} \tag{40}$$

(2). The dispersion Equation (36) (Equation (21) in Lee's paper) is wrong, it should be:

$$G^2 = \frac{\left[g(\rho_2 - \rho_1) + \sigma \left[k^2 - \frac{1}{R_o^2} \right] \right] k}{\rho_1 + \rho_2} \tag{41}$$

(3). An incorrect criterion was employed to explain the interfacial instability. Lee believed that the sign of the real part of iG determines whether the wave is amplified ($\mathrm{Re}(iG) > 0$) or damped [$\mathrm{Re}(iG) < 0$]. For $\mathrm{Re}(iG) < 0$ the corresponding flow is stable for given values of wavelength whereas $\mathrm{Re}(iG) > 0$ denotes instability. The correct criterion is whether iG is a real number or an imaginary value. If iG is a real value the disturbance grows exponentially ($\exp(iGt)$) and the system is unstable. If iG is an imaginary value, the system is stable.

From Equation (41) the critical wavelength above which the growth rate, G^2, is always negative can be expressed as:

$$\lambda_{c,PW} = \frac{2\pi}{k_{c,PW}} = \frac{2\pi}{\left[\frac{(\rho_1 - \rho_2)\, g}{\sigma} + \frac{1}{R_o^2} \right]^{1/2}} \tag{42}$$

The dangerous wavelength is obtained by maximizing $-G^2$:

$$\lambda_{d,PW} = \frac{2\pi}{k_{d,PW}} = \frac{2\pi\sqrt{3}}{\left[\frac{(\rho_1 - \rho_2)\, g}{\sigma} + \frac{1}{R_o^2} \right]^{1/2}} \tag{43}$$

Obviously, the dominant wavelength decreases with a decrease in the radius of cylinder, which is contrary to Lee's conclusion.

In fact, Equations (42) and (43) can only be considered as an approximation to the real solution due to the Lee's use of inappropriate velocity potentials. The objective of the present paper is to clarify above Rayleigh-Taylor instability phenomena by experiments and theoretical analysis.

CHAPTER 3

RAYLEIGH-TAYLOR INSTABILITY OF A CYLINDRICAL INTERFACE: INVISCID SYSTEM

3.1 THEORY

Let us consider the nature of the equilibrium of an interface between two fluids separated by $r=R_o$ *. If the fluids are inviscid, the perturbed flow can be assumed to be irrotational. We then have:

$$\nabla^2\Phi = 0 \tag{44}$$

In the Laplace equation, Φ is the velocity potential. Thus,

$$U_r = \frac{\partial\Phi}{\partial r} \quad , \quad U_\theta = \frac{1}{r}\frac{\partial\Phi}{\partial\theta} \quad , \quad U_z = \frac{\partial\Phi}{\partial z} \tag{45}$$

where U_r, U_θ and U_z are the velocity components in the cylindrical coordinates**. The Laplace equation in cylindrical polar coordinates can be expressed as:

$$\nabla^2\Phi = \frac{\partial^2\Phi}{\partial r^2} + \frac{1}{r}\frac{\partial\Phi}{\partial r} + \frac{1}{r^2}\frac{\partial^2\Phi}{\partial\theta^2} + \frac{\partial^2\Phi}{\partial z^2} \tag{46}$$

The solution of the Laplace equation can be obtained by using the method of separation of

* In the present thesis, the cylindrical interface is assumed to be horizontal; if the interface is not horizontal and has an angle α between the vertical axis and the symmetrical axis of the cylindrical interface, the acceleration due to gravity, g, in all derived equations of the present thesis should be replaced by $gCos(\alpha)$.

** In the following sections, z represents the symmetrical axis in the cylindrical coordinates.

variables[29], i.e.:

$$\Phi = R(r) \cdot \Theta(\theta) \cdot Z(z) \tag{47}$$

Furthermore, the velocity potential can be expressed as:

$$\Phi = A\, I_n(kr) \exp[i(Gt + kz)]\, Cos(n\theta) + B\, K_n(kr) \exp[i(Gt + kz)]\, Cos(n\theta) \tag{48}$$

in which, A and B are constants and n, the order of Bessel functions, is an integer so that the velocity potential has same value at $\theta=0$ and at $\theta=2\pi$. $I_n(kr)$ and $K_n(kr)$ are known as modified Bessel functions of the first kind and the second kind, respectively.

Equation (48) is the general solution of the Laplace equation and can be simplified by considering the following limits:

$$\lim_{X\to\infty} I_n(X) = \infty \qquad , \qquad \lim_{X\to 0} K_n(X) = \infty \tag{49}$$

Therefore, the velocity potentials for fluid 1 and fluid 2 (Φ_1 and Φ_2) can be expressed as:

$$\begin{aligned} \Phi_1 &= A\, I_n(kr) \exp[i(Gt + kz)]\, Cos(n\theta) \qquad r \le R_0 \\ \Phi_2 &= B\, K_n(kr) \exp[i(Gt + kz)]\, Cos(n\theta) \qquad r \ge R_0 \end{aligned} \tag{50}$$

Let the disturbance of interface ($r=R_0$) be:

$$r = R_0 + \xi(\theta,z,t) \tag{51}$$

The kinematic condition at the interface is that the radial velocity component must be continuous, and this demands:

$$\frac{\partial\Phi_1}{\partial r} = \frac{\partial\Phi_2}{\partial r} = \frac{\partial\xi}{\partial t} \qquad at\ r = R_o \tag{52}$$

From Equation (50) we have:

$$A\left[\frac{\partial I_n(kr)}{\partial r}\right]_{r=R_0} = B\left[\frac{\partial K_n(kr)}{\partial r}\right]_{r=R_0} \tag{53}$$

While,

$$\xi(\theta,z,t) = \int U_r \, dt = \int \left(\frac{\partial \Phi}{\partial r}\right)_{r=R_o} dt = \frac{1}{i\,G}\left(\frac{\partial \Phi}{\partial r}\right)_{r=R_o} \tag{54}$$

The dynamic boundary condition at the interface is:

$$P_1^t = P_2^t + \sigma\left(\frac{1}{R_1} + \frac{1}{R_2}\right) \tag{55}$$

where P_1^t and P_2^t are the total pressures of fluid 1 and 2; R_1 and R_2 are the principal radii, counted positive if the centres of curvature are toward the symmetrical axis of cylindrical interface. In the case of absence of a disturbance, Equation (55) becomes:

$$P_{10}^t = P_{20}^t + \frac{\sigma}{R_0} \tag{56}$$

where P_{10}^t and P_{20}^t are the equilibrium pressures of fluids 1 and 2.

For the disturbance, the curvature in the direction of z is:

$$\frac{1}{R_1} = -\frac{\partial^2 \xi}{\partial z^2} \tag{57}$$

while, the curvature of the surface which differs infinitely little from a circle having its centre at the origin is:

$$\frac{1}{R_2} = \frac{1}{r} - \frac{1}{r^2}\frac{\partial^2 r}{\partial \theta^2} \tag{58}$$

From Equation (51) and if the disturbance (ξ) is small, we have:

$$\frac{1}{r} = \frac{1}{R_o} - \frac{\xi(\theta,z,t)}{R_o^2} \tag{59}$$

Moreover,

$$\frac{1}{R_2} = \frac{1}{R_0} - \frac{1}{R_0^2}\left[\xi(\theta,z,t) + \frac{\partial^2\xi}{\partial\theta^2}\right] \tag{60}$$

Thus, the perturbation pressures, P_1^d and P_2^d, must satisfy the following condition:

$$P_1^d = P_2^d + \sigma\left[-\frac{\partial^2\xi}{\partial z^2} - \frac{\xi}{R_o^2} - \frac{1}{R_o^2}\frac{\partial^2\xi}{\partial\theta^2}\right] \tag{61}$$

From Equations (50) and (54), we have:

$$\frac{\partial^2\xi}{\partial z^2} = \frac{1}{iG}\left[\frac{\partial\Phi}{\partial r}\right](-k^2) = -k^2\,\xi \tag{62}$$

$$\frac{\partial^2\xi}{\partial\theta^2} = \frac{1}{iG}\left[\frac{\partial\Phi}{\partial r}\right](-n^2) = -n^2\,\xi \tag{63}$$

Thus,

$$P_1^d = P_2^d + \left[k^2 - \frac{1}{R_o^2} + \frac{n^2}{R_o^2}\right]\xi\,\sigma \tag{64}$$

From the Bernoulli equation, neglecting the second order velocity term, we have:

$$P_1^d = -\rho_1\left[\frac{\partial\Phi_1}{\partial t} + g\,\xi\,Cos(\theta)\right] \quad , \quad P_2^d = -\rho_2\left[\frac{\partial\Phi_2}{\partial t} + g\,\xi\,Cos(\theta)\right] \tag{65}$$

Substituting Equations (54) and (65) into Equation (64) and rearranging gives:

$$G^2 = \frac{\sigma\left[-k^2 + \frac{1}{R_o^2} - \frac{n^2}{R_o^2} + \frac{(\rho_2-\rho_1)\,g\,Cos(\theta)}{\sigma}\right]\left[\frac{\partial\Phi}{\partial r}\right]_{r=R_o}}{\rho_2\left(\Phi_2\right)_{r=R_o} - \rho_1\left(\Phi_1\right)_{r=R_o}} \tag{66}$$

Substituting Equations (50) and (52) into above equation, we get the required formula:

$$G^2 = \frac{\sigma k \left[k^2 - \frac{1-n^2}{R_o^2} - \frac{(\rho_2 - \rho_1) g \, Cos(\theta)}{\sigma} \right]}{\rho_1 \delta_1 + \rho_2 \delta_2} \tag{67}$$

where:

$$\delta_1 = \frac{I_n(kR_o)}{I_n'(kR_o)} \quad , \quad \delta_2 = -\frac{K_n(kR_o)}{K_n'(kR_o)} \tag{68}$$

From the approximate expressions for the Bessel functions $I_n(X)$ and $K_n(X)$ when X is large (APPENDIX I), it is quite obvious that Equation (67) becomes Equation (28) when R_o goes to infinity.

Equation (67) gives the relationship between the exponential growth rate (G) and the wave number (k) for a cylindrical interface. The nature of G governs the stability of the disturbance. If G is real, the stabilizing effect of surface tension in the axial direction will smooth out the disturbance. If G is imaginary, the force of gravity will dominate and the disturbance will increase exponentially. G passes from real to imaginary as the right-hand side of Equation (67) passes through zero. The critical wave number, k_c, and critical wave length λ_c are then obtained by equating the right-hand side to zero:

$$\lambda_c = \frac{2\pi}{k_c} = \frac{2\pi}{\left[\frac{(\rho_2 - \rho_1) g \, Cos(\theta)}{\sigma} + \frac{(1-n^2)}{R_o^2} \right]^{1/2}} \tag{69}$$

The most dangerous wave number, k_d and wave length λ_d were obtained by maximizing -G^2 by using a numerical optimization technique such as the commercial available software *TK-Solver*[30].

When the equilibrium radius R_o goes to infinity, the most dangerous wavelength can be expressed analytically, i.e., Equation (30).

Since the order of Bessel function, n, equals 0 for a cylindrical interface, the dispersion equation, Equation (67), becomes:

$$G^2 = \frac{\sigma k \left[k^2 - \frac{1}{R_o^2} - \frac{(\rho_2 - \rho_1) g \, Cos(\theta)}{\sigma} \right]}{\rho_1 \alpha_1 + \rho_2 \alpha_2} \tag{70}$$

where:

$$\alpha_1 = \frac{I_0(k R_o)}{I_0'(k R_o)} = \frac{I_0(k R_0)}{I_1(k R_0)} \;, \quad \alpha_2 = - \frac{K_0(k R_o)}{K_0'(k R_o)} = \frac{K_0(k R_0)}{K_1(k R_0)} \tag{71}$$

3.2 APPLICATION TO FILM BOILING

3.2.1 MATHEMATICAL MODEL

The dispersion equation, Equation (70), derived in Section 3.1 is applicable to a symmetric cylindrical interface in an inviscid system. As mentioned in Section 2.2, the gas-liquid interface (Figure 2.1) for film boiling on a horizontal cylindrical heater is asymmetric. Using Lienhard and Wong's geometrical assumption for the vapour-liquid interface (Figure 2.1), the term "$\xi \sigma / R_o^2$" of Equation (64) should be replaced by Equation (31). Consequently, Equation (64) becomes:

$$P_1^d = P_2^d + \left[k^2 - \frac{1}{2 R_o^2} \right] \xi \sigma \tag{72}$$

in which $n = 0$ has been assumed. Finally, the dispersion equation, Equation (70), becomes:

$$G^2 = \frac{\sigma k \left[k^2 - \frac{1}{2 R_o^2} - \frac{(\rho_2 - \rho_1) g}{\sigma} \right]}{\rho_1 \alpha_1 + \rho_2 \alpha_2} \tag{73}$$

Since bubbles are formed along the top line of the cylindrical heater during film boiling, $\theta = 0$ is used in Equation (73).

In order to express Equation (73) in a convenient dimensionless form, we define following dimensionless variables by considering $\rho_1 = \rho_g = 0$ and $\rho_2 = \rho_l$:

1). Dimensionless radius:

$$\Pi = R_o \left[\frac{\rho_l \, g}{\sigma} \right]^{1/2} \tag{74}$$

2). Dimensionless wavenumber:

$$\mathrm{K} = k \left[\frac{\sigma}{\rho_l \, g} \right]^{1/2} \tag{75}$$

3). Dimensionless growth rate:

$$\Omega = iG \left[\frac{\sigma}{\rho_l \, g^3} \right]^{\frac{1}{4}} \tag{76}$$

From Equation (75), we have the dimensionless wavelength:

$$\Lambda = \frac{2\pi}{\mathrm{K}} = \frac{2\pi}{k} \left[\frac{\rho_l \, g}{\sigma} \right]^{1/2} = \lambda \left[\frac{\rho_l \, g}{\sigma} \right]^{1/2} = 2\pi\sqrt{3} \; \frac{\lambda}{\lambda_{d,Taylor}} \tag{77}$$

Finally, combining Equations (73)-(76), Equation (73) becomes:

$$\Omega^2 = -\frac{1}{\alpha_2} \left[\mathrm{K}^2 - \frac{1}{2\Pi^2} - 1 \right] \mathrm{K} \tag{78}$$

where,

$$\alpha_2 = \frac{K_0(k R_o)}{K_1(k R_o)} = \frac{K_0(\mathrm{K}\,\Pi)}{K_1(\mathrm{K}\,\Pi)} \tag{79}$$

Equation (78) is independent of the properties of fluids. By equating Ω to zero, we get the dimensionless critical wavelength:

$$\Lambda_{c,boiling} = \frac{2\pi}{K_{c,boiling}} = \frac{2\pi}{\left[1 - \frac{1}{2\,\Pi^2}\right]^{1/2}} \tag{80}$$

Based on the above definitions of dimensionless groups, Lienhard and Wong's formula for predicting the most dangerous wavelength (Equation (35)) can be rewritten as:

$$\Lambda_{d,LW} = \frac{2\pi}{K_{d,LW}} = \frac{2\pi\sqrt{3}}{\left[1 + \frac{1}{2\,\Pi^2}\right]^{1/2}} \tag{81}$$

From Equation (80), it is obvious that when the dimensionless radius, Π, becomes large (e.g. $\Pi > 3$), the critical wavelength is independent on the radius, and so is the most dangerous wavelength.

3.2.2 COMPARISON WITH EXPERIMENTAL RESULTS

Lienhard and Wong[26] experimentally determined the dominant unstable wavelength during film boiling of isopropanol (ρ=785.5 kg/m^3, σ=23.78 dyns/cm) and benzene (ρ=876.5 kg/m^3, σ=28.89 dyns/cm) liquids on horizontal nichrome-V wires (60-650 μm) and tungsten wires (25-50 μm).

Figure 3.1 and Figure 3.2 present comparisons between measured[26] and predicted wavelengths by Lienhard and Wong's model (Equation (35)) and also by the present model (Equation (73)) for isopropanol and benzene, respectively. It is obvious that there is excellent agreement between the present model and Lienhard and Wong's experimental data. Because the surface tensions of isopropanol and benzene obtained from the CRC handbook are not the saturation values, calculations were also made for the most dangerous wavelengths based on values 25 percent less than the surface tension value given above and are also shown in Figure 3.1 and Figure 3.2. It can be seen that a 25% variation in surface tension does not change the agreement between the predicted values and the experimental data.

Figure 3.3 presents the ratio between the square of dimensionless growth rate (Ω^2)

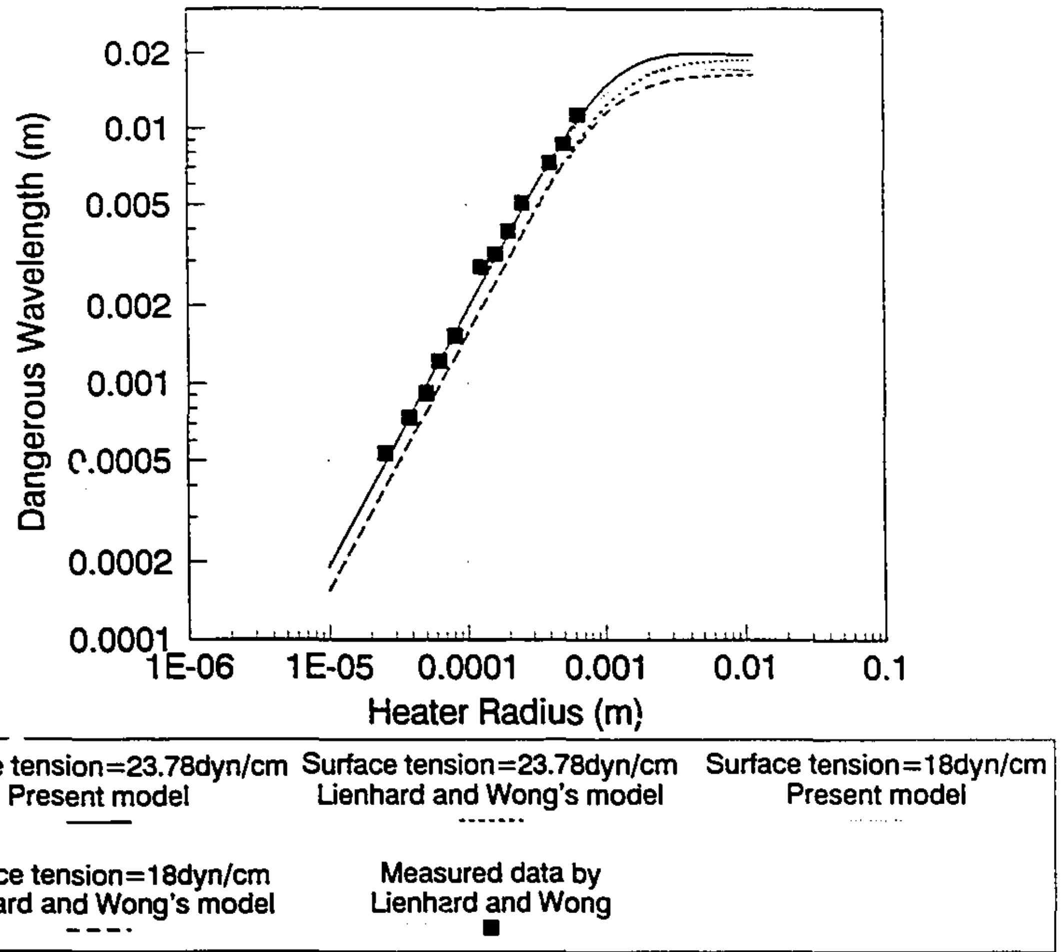

Figure 3.1 The relationships between the heater radius and the dangerous wavelengths for isopropanol.

and its maximum value ($\max(\Omega^2)$) as a function of dimensionless wavelength at specific dimensionless radii according to Equation (78). The dimensionless critical wavelength and dangerous wavelength can be read from this figure at zero dimensionless growth rate and maximum dimensionless growth rate, respectively. The curves in Figure 3.3 become flatter with increasing dimensionless radius, i.e. a broad band of dimensionless wavelengths gives growth rates with almost equal $\max(\Omega^2)$. Thus, the variability of measured dimensionless dangerous wavelength is expected to increase with increasing dimensionless radius, as pointed out by Lienhard and Sun[27].

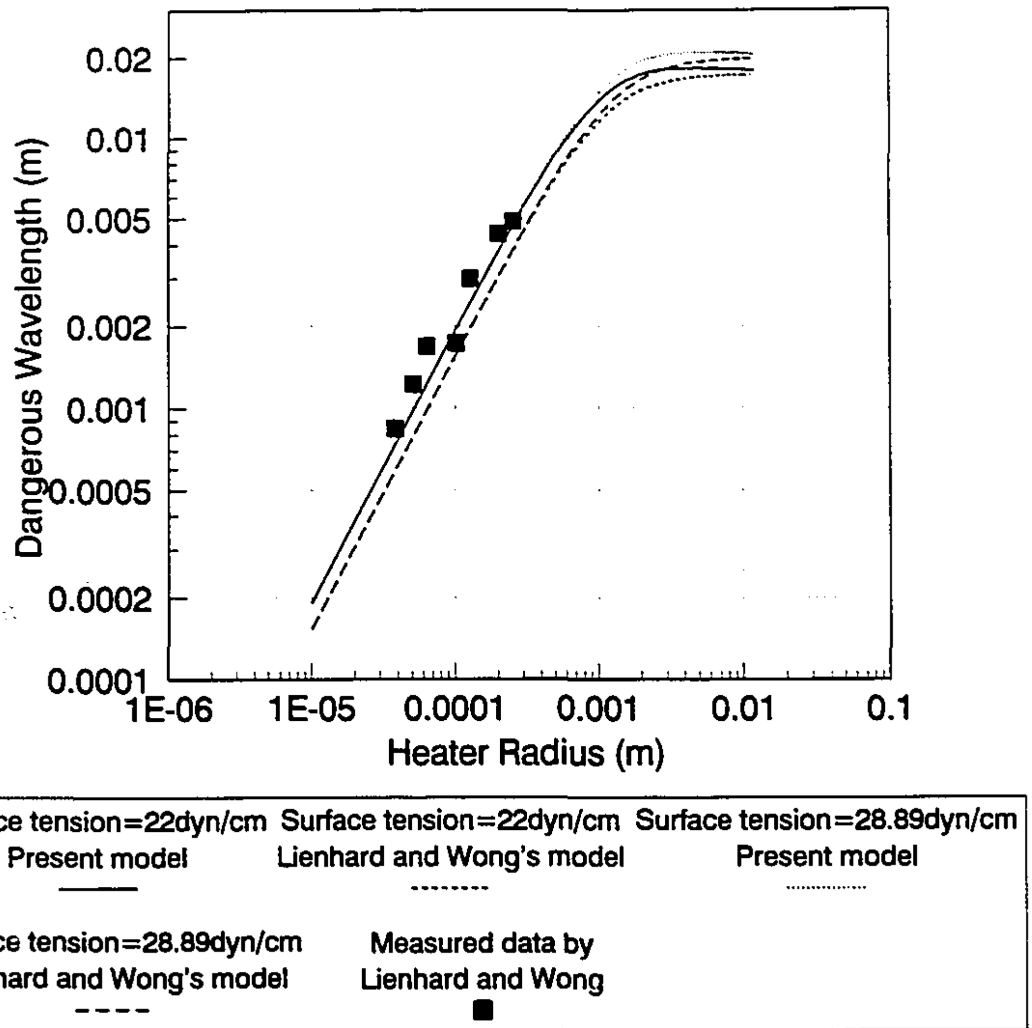

Figure 3.2 The relationships between the heater radius and the dangerous wavelengths for benzene.

Figure 3.4 shows the dimensionless dangerous wavelengths predicted by Equations (78) and (81), which should correspond to the measured average dangerous wavelengths. The measured data[27] are also presented. Evidently, the present model gives the best representation of measured average wavelength. However, in reality there is not a precise value of the wavelength; the most dangerous wavelength is that which happens at the maximum growth rate and corresponds to the measured average data. If it is assumed that the measured wavelengths corresponding to a growth rate greater than some fraction of the maximum growth rate, and setting the cut off for the wavelength at 90% of the maximum

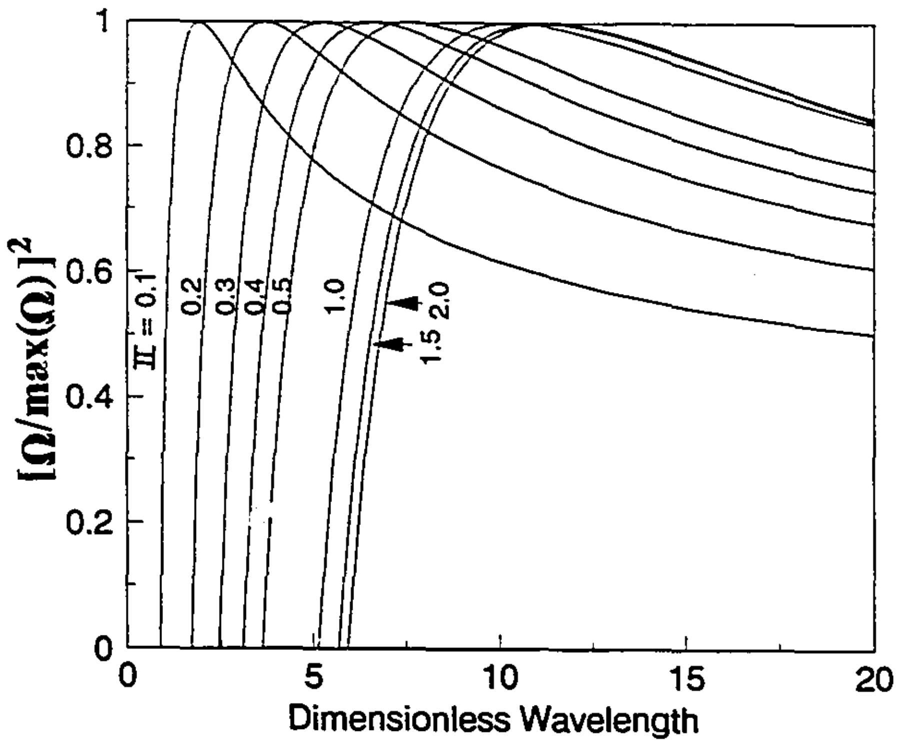

Figure 3.3 Calculated ratio between square of the dimensionless growth rate and its maximum value as a function of most dangerous dimensionless wavelength at specific radius.

growth rate, the variation in the measured data is encompassed, Figure 3.4.

Figure 3.5 shows the ratios between the calculated values of the most dangerous wavelengths and the critical wavelengths according to Equation (78). It is obvious that the ratios are greater than $\sqrt{3}$, the result of Lienhard and Wong. This is why the present model gives better correlation to the observed values than the previous models. The data shown in Figure 3.5 are fitted by Equation (82):

$$\frac{\Lambda_{d,boiling}}{\Lambda_{c,boiling}} = \frac{2.16 + \sqrt{3}\ 0.4672\ \Pi^{1.491}}{1 + 0.4672\ \Pi^{1.491}} \tag{82}$$

Equation (82) gives $\Lambda_{d,boiling}/\Lambda_{c,boiling} = \sqrt{3}$ when the dimensionless radius is infinitely large and $\Lambda_{d,boiling}/\Lambda_{c,boiling} = 2.16$ when the dimensionless radius is zero. From Equations (80) and (82), we have an expression for the dimensionless dangerous wavelength in a closed form:

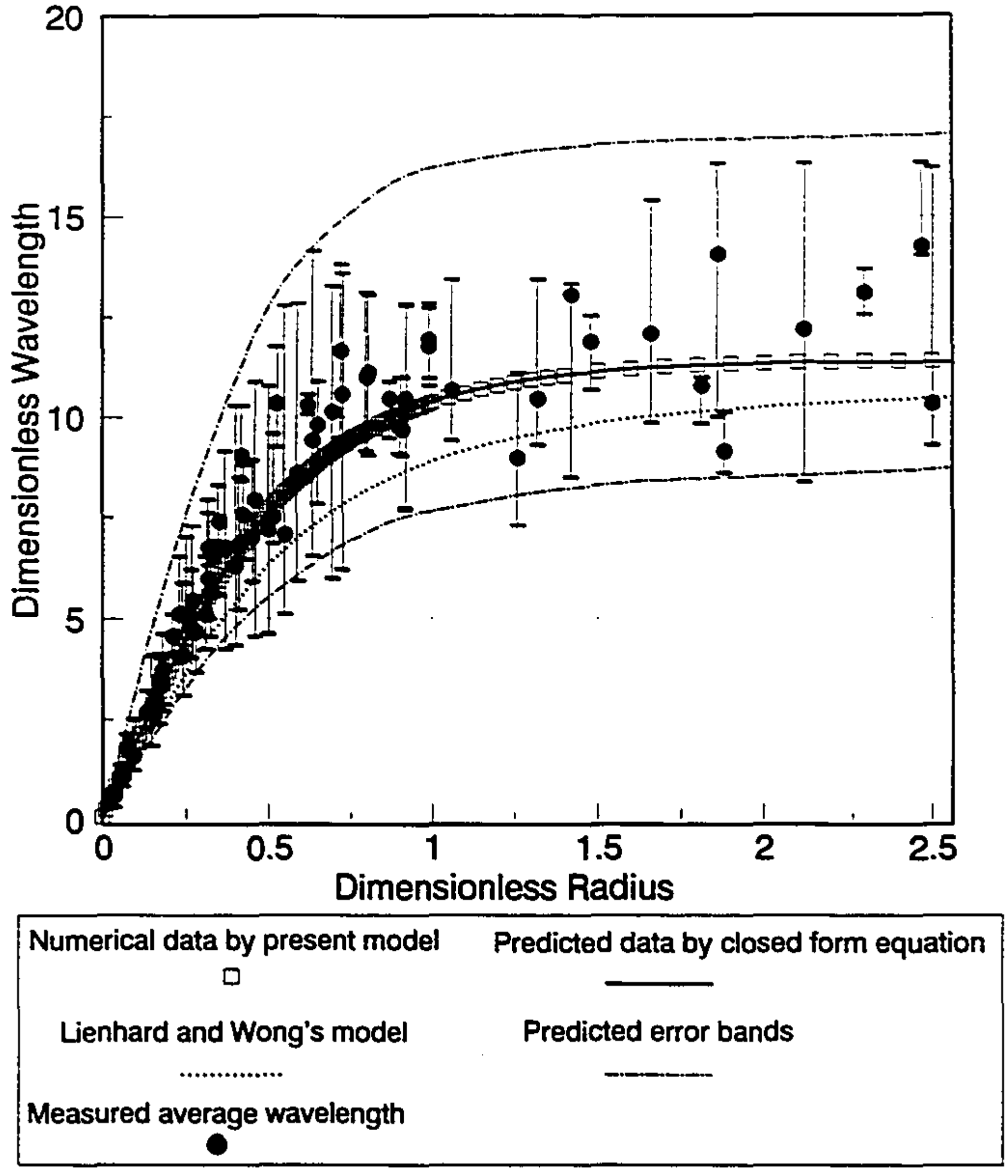

Figure 3.4 The relationship between the dimensionless wavelength and the dimensionless radius.

$$\Lambda_{d,\,boiling} = \frac{2.16 + \sqrt{3}\ 0.4672\ \Pi^{1.491}}{1 + 0.4672\ \Pi^{1.491}} \cdot \frac{2\pi}{\left[1 + \frac{1}{2\,\Pi^2}\right]^{1/2}} \tag{83}$$

The predicted dimensionless most dangerous wavelength based on Equation (83) is also

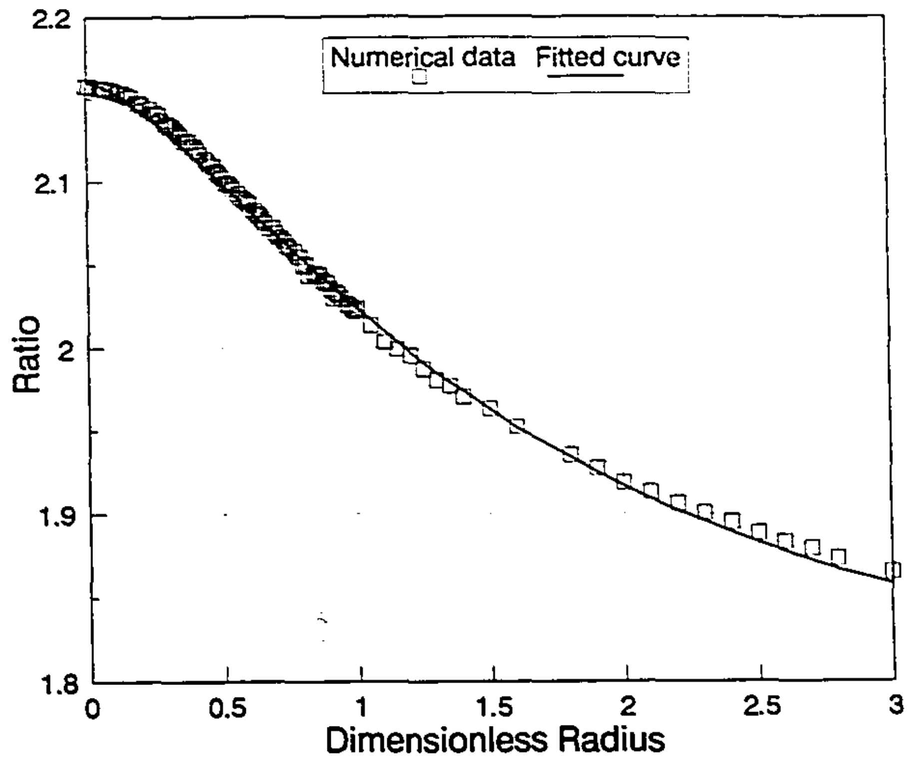

Figure 3.5 Calculated ratio between the dimensionless dangerous wavelength and the dimensionless critical wavelength as a function of dimensionless radius.

shown in Figure 3.4 by a solid line. Equation (83) predicts the dimensionless wavelength in a great success.

3.3 BREAKUP OF A LIQUID FILM AROUND A HORIZONTAL CYLINDRICAL BODY

As mentioned in Section 2.3, an incorrect conclusion was derived in previous experimental and theoretical research on the breakup of a liquid film around a horizontal cylindrical body[9]. The present section discusses new experiments and an appropriate theoretical analysis.

3.3.1 EXPERIMENTS

In order to measure the distance between the nodes of a unstable liquid film around a long, horizontal, circular cylindrical body in still air, two different kinds of experiments were carried out. The first one consisted of the condensation of water vapour on a cold cylindrical tube.

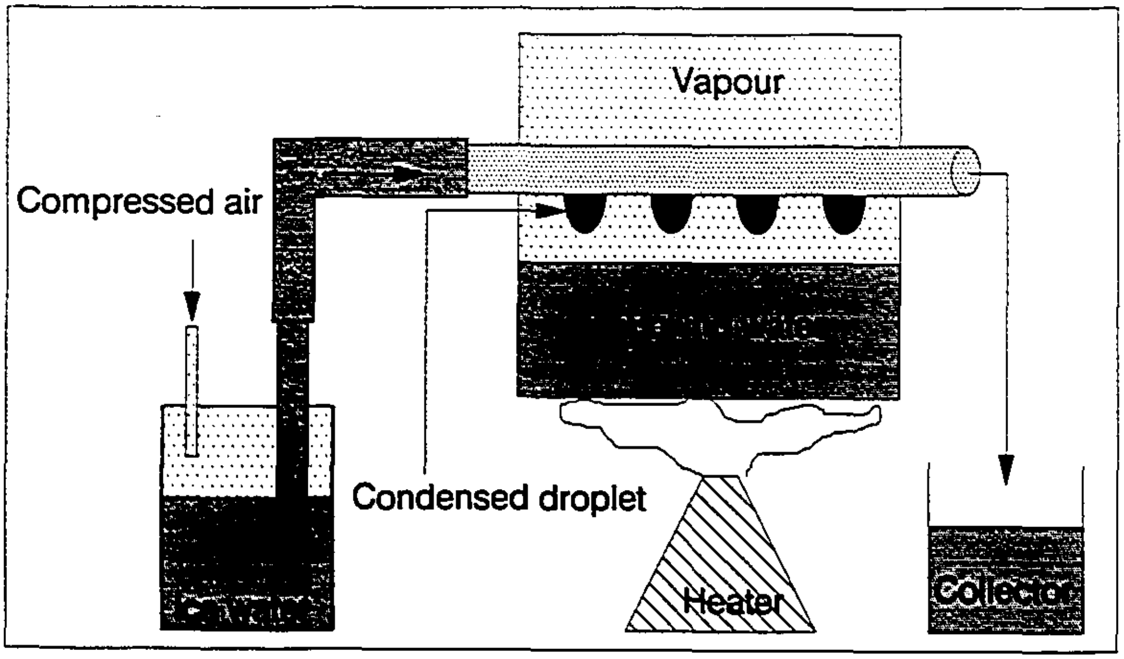

Figure 3.6 Schematic representation of the condensation of water vapour on the cold tube.

The apparatus is shown in Figure 3.6. It consisted of a wide water container heated by a gas burner, surmounted by a rectangular plexiglass box with a open bottom. Boiling water evaporated, and rose into the plexiglass box. A thin hollow tube cooled by internally flowing freezing water is positioned across the width of the box and thus condensed some of the vapour, which accumulated over its surface, eventually forming suspended droplets along its length. Stainless steel tubes were held in tension with two machined brass grips, in order to ensure their straightness. The grips are designed to gently grip the external surface of the tubes without crushing them, and be tightened against the exterior of two opposite walls of the plexiglass box. The glass tubes used were rigid and did not bend under their weight or that of the feed tubes. The diameters of the glass and the stainless steel tubes used were in the range of 0.6-8mm.

Ice water was contained in a plastic container whose cap was adapted for a compressed air inlet at 20 psi and an ice water outlet. This rudimentary pump was adequate to feed ample amounts of ice water to the tube, so that the heat transfer was limited by the thermal conductivities of the tubes. This was confirmed by the observed uniform distribution of the water droplets, with no cold spot. Photographs of the nucleation, growth and impingement of the water droplets were taken. Each tube of given size and material was tested several times, being wiped off with virgin cotton wool at the end of each test. Each test or trial consisted in observing the time evolution of the droplet pattern, and photographing it.

For each test, a photograph of the early incubation stage was taken, followed by several photographs of the slowly changing droplet pattern. Finally, one or two photographs of the impingement stage were included, if it was observed. Over 170 photographs were taken in all.

Figure 3.7 presents some key features of the condensation process. In general, each trial consisted of an incubation period, where water condensed on the surface of the tubes in small droplets. The stainless steel tube photographs show that even for the small tubes, small droplets formed over the circumference. As these small drops were spaced closer than the main ones underneath, the perturbation theory cannot be invoked to explain their presence. These droplets likely nucleate on the cold surface, and are held in position against their weight by adsorption and surface tension.

True cylindrical film formation did not occur during condensation because of the low heat conductivity of the stainless steel and glass tubes as well as the poor wetting. For all tubes there was no long term steady state droplet distribution reached. Instead, the incubation time was followed by a temporarily stable, slowly evolving droplet distribution, eventually reaching impingement and growth of favoured droplets at the expense of their neighbours. For all radii the original pattern evolved from the cleaned tube did not recreate itself, but rather slowly evolved into a group of large droplets. Thus, the condensation experiments on the cooled tube did not represent the Rayleigh-Taylor instability. In fact, This process is dropwise condensation.

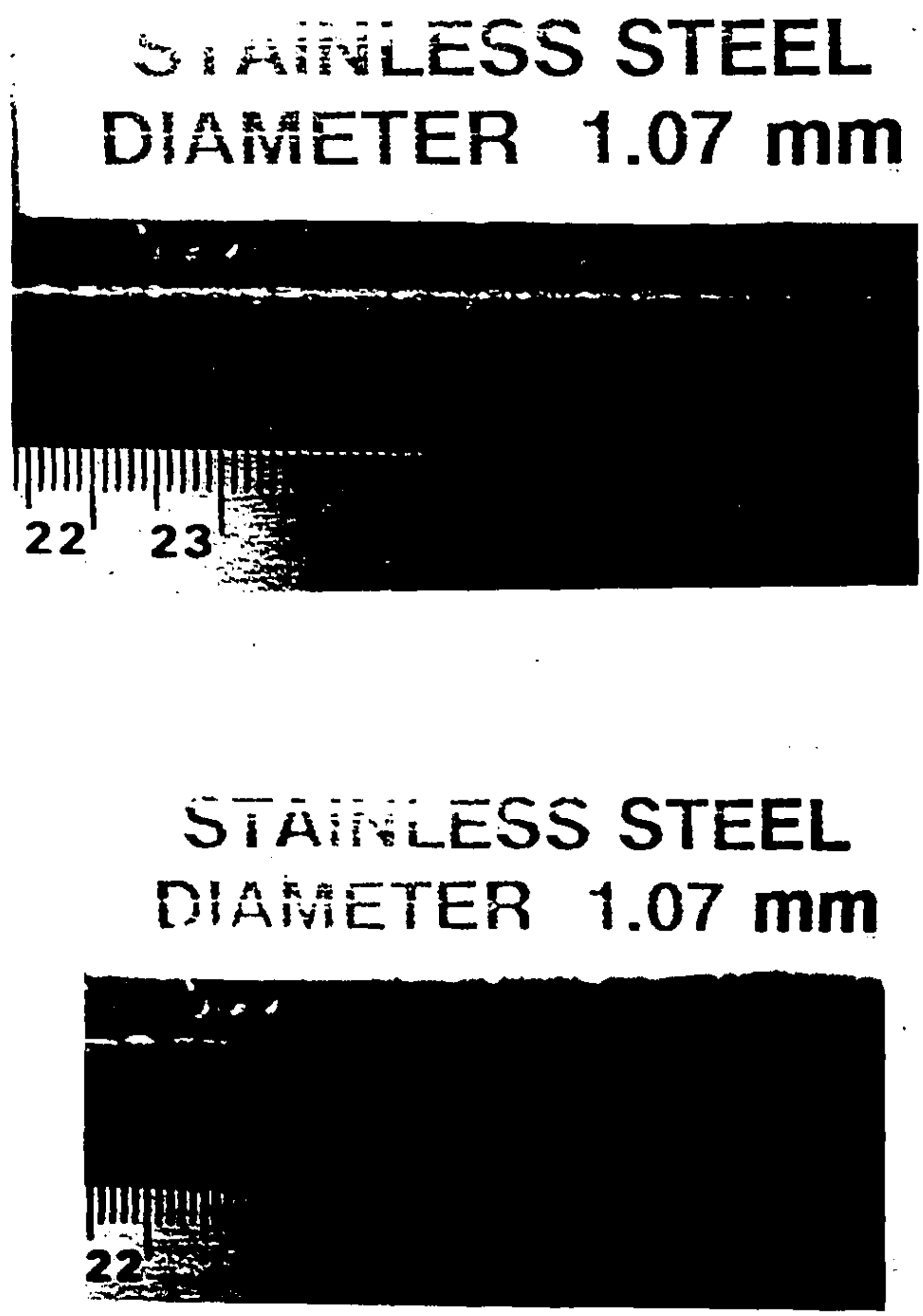

Figure 3.7 Condensation of vapour on a cooled tube (top and bottom pictures show earlier and later stages of droplet formation, respectively).

Because there is not a liquid film formed around the test tube during the present condensation experiments, a second kind of experiment was carried out, which is shown in Figure 3.8 and Figure 3.9. It consisted of a slot nozzle, a cylindrical tube attached to the slot and a spirit-level.

The spacing and length of the slot were W=120μm and L=20cm. A ruler was placed below the tube, providing a scale to measure the droplet spacing. Tap water was injected through the slot onto the cylindrical tube to form a liquid film around the test tube. The flow rate of water was maintained at the minium required to form a continuous film around the tube. The horizontal attitude of the tube was guaranteed by the spirit-level. For each of the given tube, several pictures (5-10) were taken under different liquid flow rates. The distance between the nodes from which the liquid film breaks up into droplets were measured from each of the pictures. Results are presented in Table 3.1 and Figure 3.11. In Table 3.1, D_o is the diameter of the tube, σ_{sd} is the standard deviation and S and G represent stainless steel and glass, respectively.

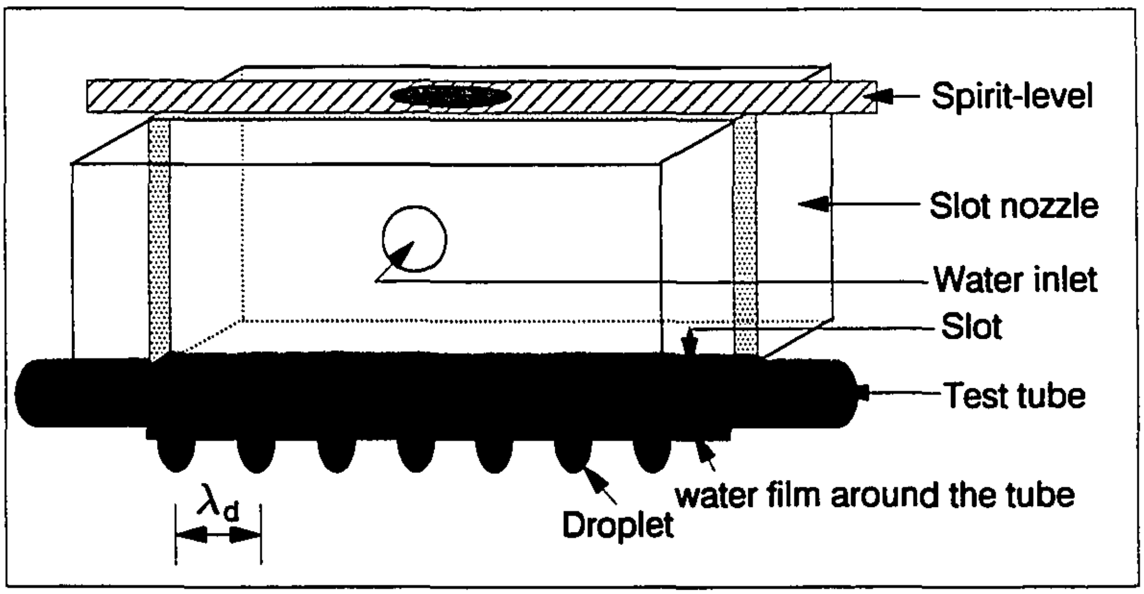

Figure 3.8 Schematic representation of the formation and the breakup of a liquid film around a cylindrical tube.

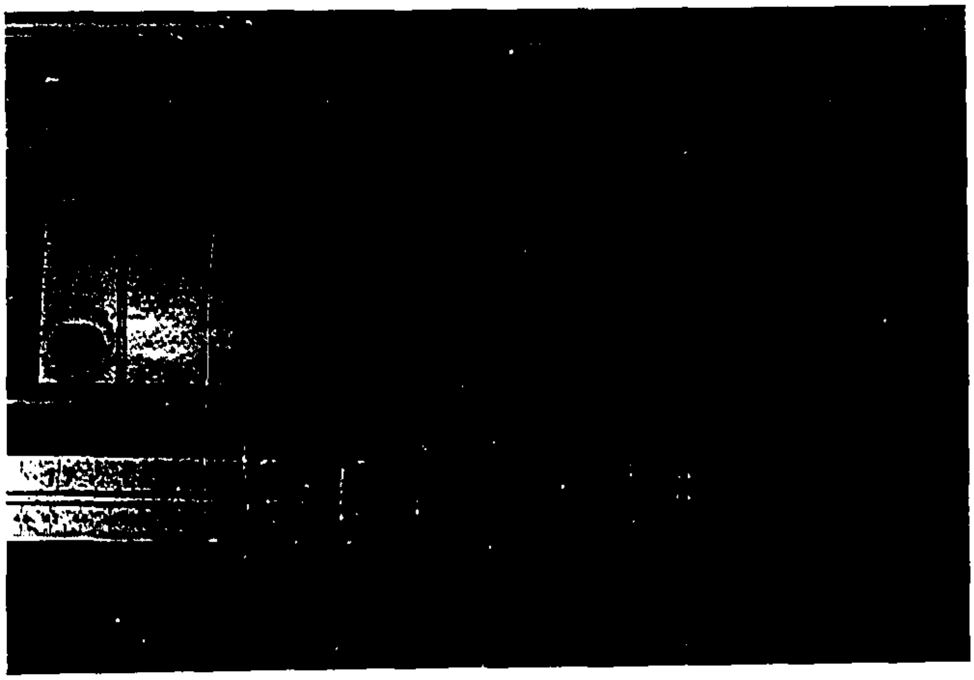

Figure 3.9 Photograph for a liquid film breakup experiment.

Figure 3.10 presents the breakup of liquid film around a cylindrical tube due to the Rayleigh-Taylor instability. The distance between the nodes decreases with a decrease in the diameter of the tube.

The diameters of the glass and the stainless steel tubes used are in the range of 0.6-8mm. Photographs were taken at 1/500s with a macrolens 35 mm camera. For each trial, the radius and material were indicated on a panel included on the photographs.

3.3.2 THEORETICAL ANALYSIS

In Section 3.1, general dispersion equation (Equation (70)), relating the wavenumber and the growth rate, for the Rayleigh-Taylor instability of a cylindrical interface was derived. For the liquid film breakup from the bottom of the test tube in still air, substituting $\theta=180^{\circ}$, $\rho_1=\rho_l$ and $\rho_2=\rho_g=0$ into Equation (70) yields:

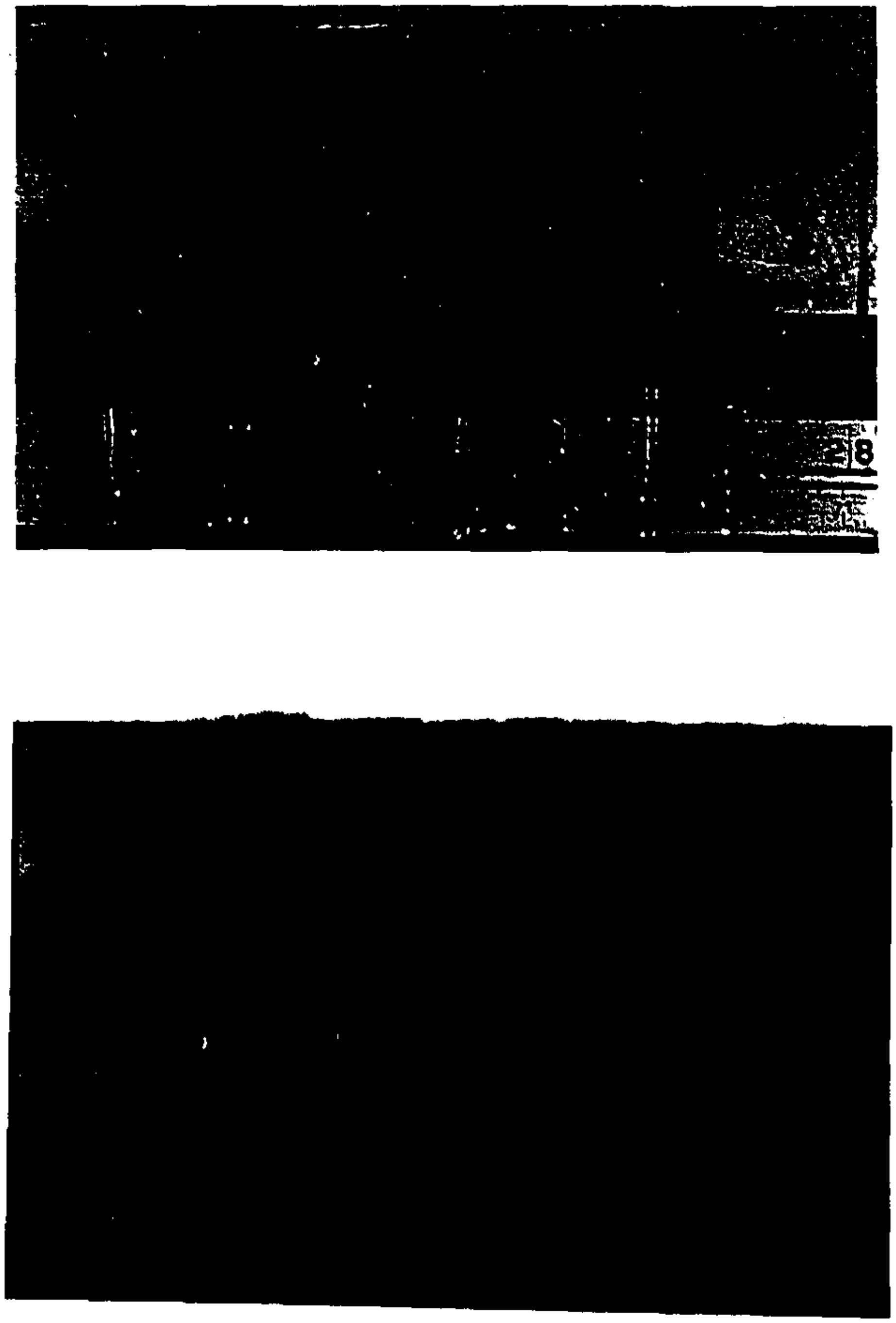

Figure 3.10 Breakup of a liquid film around horizontal glass (top picture) and stainless tubes (bottom picture).

$$G^2 = \frac{\sigma k \left\{ k^2 - \frac{1}{R_o^2} - \frac{\rho_l g}{\sigma} \right\}}{\rho_l \alpha_1} \tag{84}$$

Regarding the definitions of the dimensionless variables in Equations (74)-(77), Equation (84) can be expressed in dimensionless form:

$$\Omega^2 = -\frac{1}{\alpha_1} \left[\mathrm{K}^2 - \frac{1}{\Pi^2} - 1 \right] \mathrm{K} \tag{85}$$

where,

$$\alpha_1 = \frac{I_0(k R_o)}{I_1(k R_o)} = \frac{I_0(\mathrm{K}\,\Pi)}{I_1(\mathrm{K}\,\Pi)} \tag{86}$$

Equation (85) is independent of the properties of fluids. By equating Ω to zero, we get the dimensionless critical wavelength:

$$\Lambda_{c,droplet} = \frac{2\pi}{\mathrm{K}_{c,droplet}} = \frac{2\pi}{\left[1 + \frac{1}{\Pi^2} \right]^{1/2}} \tag{87}$$

The dimensionless most dangerous wavelength are calculated numerically from Equation (85) and are presented in Figure 3.11. Very good agreement between the experiments and the calculated values is obtained. The ratio between the most dangerous wavelength and the critical wavelength is presented in Figure 3.12. The values shown in Figure 3.12 are fitted by Equation (88):

$$\frac{\Lambda_{d,droplet}}{\Lambda_{c,droplet}} = \frac{1.435 + 0.072\sqrt{3}\,\Pi^{1.877}}{1 + 0.072\,\Pi^{1.877}} \tag{88}$$

Equation (88) gives $\Lambda_{d,droplet}/\Lambda_{c,droplet}=\sqrt{3}$ when the dimensionless radius is infinitely large and $\Lambda_{d,droplet}/\Lambda_{c,droplet}=1.435$ when the dimensionless radius is zero. Furthermore, the dimensionless dangerous wavelength is expressed in a closed form as:

Table 3.1 Experimental Results for the Breakup of Liquid Film

	Material	S	S	S	S	G	G
	D_o (mm)	15.88	9.53	5.16	3.76	7.12	3.94
	Measured distance between nodes λ_d (cm)	2.83	2	2.26	1.6	2.28	1.92
		2.3	2.7	2.08	1.91	2	1.94
		2.63	2.3	2.14	1.68	2.27	1.92
		3.6	2.5	1.63	1.91	2.16	1.75
		2.3	2.6	1.92	2.2	1.9	1.7
		2.22	2.6	1.67	1.83	1.92	1.89
		2.25	2.42	1.59	2.08	2.14	2.2
		2.2	2.7	1.6	1.5		
				1.63	1.73		
				1.88	1.5		
					1.4		
					1.4		
					1.35		
					1.61		
					1.69		
	Average, λ_d (cm)	2.54	2.48	1.84	1.69	2.10	1.90
	$\sigma_{sd}(\lambda_d)$	0.48	0.24	0.25	0.25	0.16	0.16
Dimensionless	Π	2.93	1.76	0.95	0.69	1.31	0.73
	Average, $\Lambda_{d,\mathrm{droplet}}$	9.38	9.14	6.79	6.24	7.73	7.02
	$\sigma_{sd}(\Lambda_{d,\mathrm{droplet}})$	1.78	0.87	0.93	0.94	0.58	0.59
	$\max(\Lambda_{d,\mathrm{droplet}})$	13.28	9.96	8.34	8.12	8.41	8.12
	$\min(\Lambda_{d,\mathrm{droplet}})$	8.12	7.38	5.87	4.98	7.01	6.27

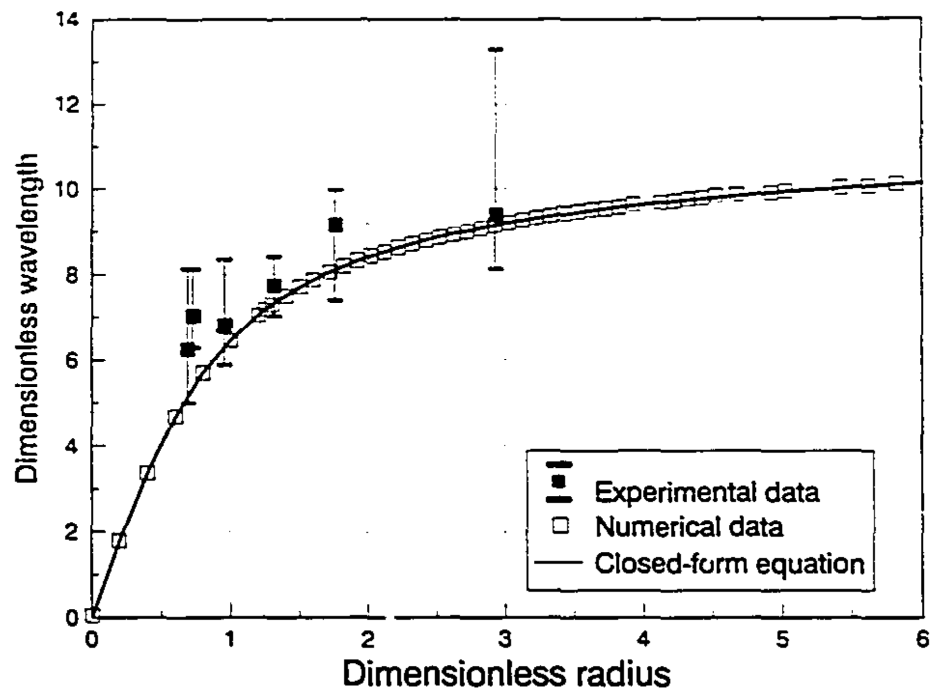

Figure 3.11 The relationship between the dimensionless most dangerous wavelength and dimensionless radius of the tube.

$$\Lambda_{d,droplet} = \frac{1.435 + 0.072\sqrt{3}\,\Pi^{1.877}}{1 + 0.072\,\Pi^{1.877}} \cdot \frac{2\pi}{\left[1 + \frac{1}{\Pi^2}\right]^{1/2}} \tag{89}$$

The predicted dimensionless most dangerous wavelength based on Equation (89) is also shown in Figure 3.11 by a solid line. Equation (89) predicts the dimensionless wavelength with a great success.

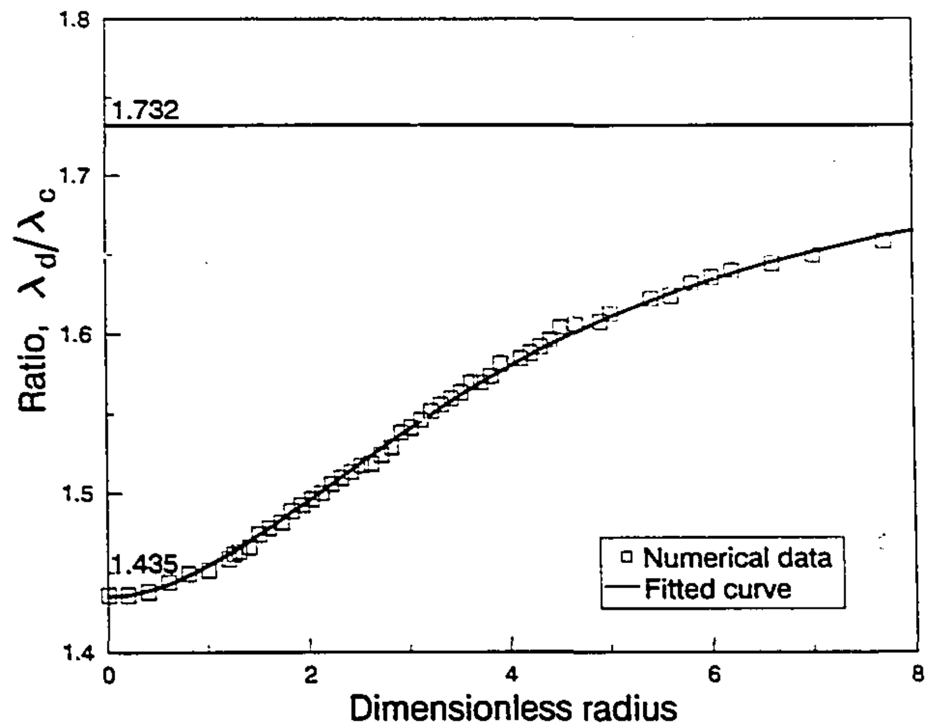

Figure 3.12 Calculated ratio between the most dangerous wavelength and the critical wavelength as a function of dimensionless radius.

3.4 CONCLUSIONS

1. A General dispersion equation, Equation (70), relating wavenumber, k, to growth rate, G, was derived for the Rayleigh-Taylor instability of a axisymmetric cylindrical interfaces between two inviscid fluids.

2. The Film boiling phenomenon on a horizontal cylindrical heater was analyzed based on the Rayleigh-Taylor instability. Several conclusions can be drawn:

(1). The dominant unstable dimensionless wavelength during film boiling on a horizontal cylinder is predicted successfully by Equation (83).

(2). The geometrical assumption made by Lienhard and Wong (Figure 2.1) is reasonable.

(3). Lienhard and Sun's conclusion[27] about the invalidity of theory below $\Pi \approx 0.1$ is also suitable for the present theory.

3. Experiments and theoretical analysis were carried out to measure and to predict the dominant wavelength during cylindrical liquid film breakup. It was found that the distance between the nodes decreases with a decrease in the radius of the test tube. The most dangerous wavelength is predicted successfully by a closed-form equation (Equation (89)).

CHAPTER 4

RAYLEIGH-TAYLOR INSTABILITY OF A CYLINDRICAL INTERFACE: VISCOUS FLUIDS

In Chapter 3 we discussed the Rayleigh-Taylor instability of a cylindrical interface between two inviscid fluids with applications to film boiling and liquid film breakup on a cylindrical body. In order to understand the Rayleigh-Taylor instability phenomena in a viscous system, the previous theory must be extended to include the viscosities of fluids.

4.1 THEORY

The linearized equations governing the motion of an incompressible, viscous fluid are:

1. Continuity equation

$$\frac{1}{r}\frac{\partial (r\,U_r)}{\partial r} + \frac{\partial U_z}{\partial z} = 0 \tag{90}$$

2. Momentum equations

$$\rho\frac{\partial U_r}{\partial t} = -\frac{\partial P}{\partial r} + \rho g_r + \mu\left[\frac{\partial}{\partial r}\left[\frac{1}{r}\frac{\partial}{\partial r}(r\,U_r)\right] + \frac{\partial^2 U_r}{\partial z^2}\right] \tag{91}$$

$$\rho\frac{\partial U_z}{\partial t} = -\frac{\partial P}{\partial z} + \rho g_z + \mu\left[\frac{1}{r}\frac{\partial}{\partial r}\left[r\frac{\partial U_z}{\partial r}\right] + \frac{\partial^2 U_z}{\partial z^2}\right] \tag{92}$$

where P is the pressure of the fluid, g_r and g_z the acceleration components due to gravity and μ the viscosity of fluid. If we define Q as:

$$Q = -\frac{P}{\rho} - V \tag{93}$$

where V is the potential of the impressed force[31], i.e.:

$$\frac{\partial V}{\partial r} = -g_r \quad ; \quad \frac{\partial V}{\partial z} = -g_z \tag{94}$$

Equations (91) and (92) can be rewritten as:

$$\frac{\partial U_r}{\partial t} = \frac{\partial Q}{\partial r} + \nu \left[\nabla^2 U_r - \frac{U_r}{r^2} \right] \tag{95}$$

$$\frac{\partial U_z}{\partial t} = \frac{\partial Q}{\partial z} + \nu \nabla^2 U_z \tag{96}$$

where,

$$\nabla^2 = \frac{\partial^2}{\partial r^2} + \frac{1}{r}\frac{\partial}{\partial r} + \frac{\partial^2}{\partial z^2} \tag{97}$$

and ν is the kinematic viscosity. From Equation (90), we can express the velocities using Stokes's stream function, i.e.:

$$U_r = \frac{1}{r}\frac{\partial \Psi}{\partial z} \tag{98}$$

$$U_z = -\frac{1}{r}\frac{\partial \Psi}{\partial r} \tag{99}$$

While:

$$
\begin{aligned}
-\frac{dQ}{\nu} &= -\frac{1}{\nu}\left[\frac{\partial Q}{\partial r}dr + \frac{\partial Q}{\partial z}dz\right] \\
&= \left[\left[\nabla^2 - \frac{\partial}{\nu\partial t}\right]U_r - \frac{U_r}{r^2}\right]dr + \left[\left[\nabla^2 - \frac{1}{\nu}\frac{\partial}{\partial t}\right]U_z\right]dz
\end{aligned}
\tag{100}
$$

Substituting Equation (98), we have:

$$
-\frac{1}{\nu}\frac{\partial Q}{\partial r} = \left[\nabla^2 - \frac{\partial}{\nu\partial t}\right]U_r - \frac{U_r}{r^2} = \frac{1}{r}\frac{\partial}{\partial z}\left[D - \frac{1}{\nu}\frac{\partial}{\partial t}\right]\Psi \tag{101}
$$

where:

$$
D = \frac{\partial^2}{\partial r^2} - \frac{1}{r}\frac{\partial}{\partial r} + \frac{\partial^2}{\partial z^2} \tag{102}
$$

Similarly,

$$
-\frac{1}{\nu}\frac{\partial Q}{\partial z} = \left[\nabla^2 - \frac{\partial}{\nu\partial t}\right]U_z = -\frac{1}{r}\frac{\partial}{\partial r}\left[D - \frac{1}{\nu}\frac{\partial}{\partial t}\right]\Psi \tag{103}
$$

By complete differential, we have:

$$
\frac{\partial}{\partial z}\left[\frac{\partial Q}{\partial r}\right] - \frac{\partial}{\partial r}\left[\frac{\partial Q}{\partial z}\right] = 0 \tag{104}
$$

Substituting the expressions for $\partial Q/\partial r$ and $\partial Q/\partial z$, Equations (101) and (103), into Equation (104) and rearranging, we obtain:

$$
D\left[D - \frac{1}{\nu}\frac{\partial}{\partial t}\right]\Psi = 0 \tag{105}
$$

Equation (105) can be satisfied by putting

$$
\Psi = \Psi_a + \Psi_b \tag{106}
$$

where:

$$D\Psi_a = 0 \tag{107}$$

and

$$D\Psi_b = \frac{1}{\nu}\frac{\partial \Psi_b}{\partial t} \tag{108}$$

In the present question, Ψ is a function of z and t and is proportional to $\exp[i(Gt+kz)]$. Thus, Equations (107) and (108) become:

$$\frac{\partial^2 \Psi_a}{\partial r^2} - \frac{1}{r}\frac{\partial \Psi_a}{\partial r} - k^2\,\Psi_a = 0 \tag{109}$$

$$\frac{\partial^2 \Psi_b}{\partial r^2} - \frac{1}{r}\frac{\partial \Psi_b}{\partial r} - k'^2\,\Psi_b = 0 \tag{110}$$

where:

$$k'^2 = k^2 + \frac{iG}{\nu} \tag{111}$$

If we let:

$$\Psi_a = \frac{r}{ik}\frac{\partial \Phi_a}{\partial r} \tag{112}$$

$$\Psi_b = \frac{r}{ik}\frac{\partial \Phi_b}{\partial r} \tag{113}$$

It is easy to show that Φ_a is the velocity potential when the flow is irrotational.

Substituting Equation (112) into Equation (109), we have:

$$\frac{\partial^2 \Phi_a}{\partial r^2} + \frac{1}{r}\frac{\partial \Phi_a}{\partial r} - k^2\,\Phi_a = 0 \tag{114}$$

Similarly,

$$\frac{\partial^2 \Phi_b}{\partial r^2} + \frac{1}{r}\frac{\partial \Phi_b}{\partial r} - k'^2 \Phi_b = 0 \tag{115}$$

However, Equations (114) and (115) have analytical solutions[29] which can be expressed as:

$$\Phi_a = A_1'' I_0(kr) + A_2'' K_0(kr) \tag{116}$$

$$\Phi_b = B_1'' I_0(k'r) + B_2'' K_0(k'r) \tag{117}$$

where A_1'', B_1'', A_2'' and B_2'' are constants. Thus, combining Equations (112) and (113) with Equations (116) and (117), and considering that Ψ is proportional to $\exp[i(Gt+kz)]$, we have the following expressions for Stokes's stream functions:

$$\Psi_a = [A_1 r I_0'(kr) + A_2 r K_0'(kr)] \exp[i(Gt+kz)] \tag{118}$$

$$\Psi_b = [B_1 r I_0'(k'r) + B_2 r K_0'(k'r)] \exp[i(Gt+kz)] \tag{119}$$

where A_1, B_1, A_2 and B_2 are constants. By considering the boundary conditions for fluid 1 and fluid 2, we have Stokes's stream functions for fluid 1 and fluid 2, i.e.,

$$\Psi_I = [A_1 r I_0'(kr) + B_1 r I_0'(k_I r)] \exp[i(Gt+kz)] \tag{120}$$

$$\Psi_{II} = [A_2 r K_0'(kr) + B_2 r K_0'(k_{II} r)] \exp[i(Gt+kz)] \tag{121}$$

where k_I and k_{II} are:

$$k_I^2 = k^2 + \frac{iG}{\nu_1} \tag{122}$$

$$k_{II}^2 = k^2 + \frac{iG}{\nu_2} \tag{123}$$

where ν_1 and ν_2 are the kinematic viscosities of fluid 1 and fluid 2, respectively.

If the disturbance of interface at $r = R_0$ is expressed by Equation (51), we then have:

$$
\begin{aligned}
\xi &= \int U_r \, dt = \int \left[\frac{1}{r} \frac{\partial \Psi_I}{\partial z} \right]_{r=R_o} dt \\
&= \frac{k}{G} \left[A_1 \, I_0'(kR_0) + B_1 \, I_0'(k_I R_0) \right] \exp[i(Gt + kz)] \\
&= \frac{k}{G} \left[A_2 \, K_0'(kR_0) + B_2 \, K_0'(k_{II} R_0) \right] \exp[(i(Gt + kz)]
\end{aligned}
\tag{124}
$$

After we have the Stokes's stream functions for fluid 1 and fluid 2 and the expression for the disturbance of the interface, the relationship between the pressure of fluid and the stream function has to be found.

Substituting Equations (101) and (103) into Equation (100) and considering Equations (107) and (108), we obtain:

$$
dQ = \frac{1}{r} \frac{\partial}{\partial z} \left[\frac{\partial \Psi_a}{\partial t} \right] dr - \frac{1}{r} \frac{\partial}{\partial r} \left[\frac{\partial \Psi_a}{\partial t} \right] dz \tag{125}
$$

From Equations (112) and (125), we have:

$$
Q = Q_0 + \frac{\partial \Phi_a}{\partial t} \tag{126}
$$

Thus, the disturbance pressure can be expressed as:

$$
P^d = -\rho \left[\frac{\partial \Phi_a}{\partial t} + g \, \xi \cos(\theta) \right] \tag{127}
$$

which is same as the Bernoulli equation for irrotational flow, Equation (65). Combining Equations (112) and (118) and considering the boundary conditions for fluid 1 and fluid 2, we have:

$$
\frac{\partial \Phi_a}{\partial t} = -A_1 \, G \, I_0(kr) \exp[i(Gt + kz)] \qquad \textit{for fluid } 1 \tag{128}
$$

$$\frac{\partial \Phi_a}{\partial t} = -A_2\, G\, K_0(kr)\exp[i(Gt+kz)] \qquad \textit{for fluid 2} \tag{129}$$

Thus, the disturbance pressures for fluid 1 and fluid 2 can be expressed as:

$$P_I^d = \rho_1 \left(A_1\, G I_0(kr)\, \exp[i(Gt+kz)] - g\,\xi\cos(\theta)\right) \tag{130}$$

$$P_{II}^d = \rho_2 \left(A_2\, G K_0(kr)\, \exp[i(Gt+kz)] - g\,\xi\cos(\theta)\right) \tag{131}$$

The boundary conditions to be satisfied at the interface are:

$$U_r^I = U_r^{II} \tag{132}$$

$$U_z^I = U_z^{II} \tag{133}$$

$$-P_I^d + 2\mu_1 \frac{\partial U_r^I}{\partial r} = -P_{II}^d + 2\mu_2 \frac{\partial U_r^{II}}{\partial r} + \sigma\left[\frac{\partial^2 \xi}{\partial z^2} + \frac{\xi}{R_0^2}\right] \tag{134}$$

$$\mu_1 \left[\frac{\partial U_r^I}{\partial z} + \frac{\partial U_z^I}{\partial r}\right] = \mu_2 \left[\frac{\partial U_r^{II}}{\partial z} + \frac{\partial U_z^{II}}{\partial r}\right] \tag{135}$$

where μ_1 and μ_2 are the viscosities of fluid 1 and fluid 2, respectively. The last two equations state the equality of the components of the stress tensor. Substitution of the expressions for U_r, U_z, P^d, and ξ in Equations (132) to (135) gives four conditions for the unknown constants A_1, A_2, B_1 and B_2. From Equation (132), we have:

$$I_0'(kR_0)A_1 + I_0'(k_I R_0)B_1 - K_0'(kR_0)A_2 - K_0'(k_{II}R_0)B_2 = 0 \tag{136}$$

From Equation (133) and Equation (136), we have:

$$kI_0''(kR_0)A_1 + k_I I_0''(k_I R_0)B_1 - kK_0''(kR_0)A_2 - k_{II}K_0''(k_{II}R_0)B_2 = 0 \tag{137}$$

From Equation (134), we have:

$$\beta_1 A_1 + \beta_2 B_1 + \beta_3 A_2 + \beta_4 B_2 = 0 \tag{138}$$

where:

$$\begin{aligned}\beta_1 &= \rho_1 \left(g k \cos(\theta)\, I_0'(kR_0) - G^2 I_0(kR_0)\right) \\ &+ \sigma \left[k^3 - \frac{k}{R_0^2}\right] I_0'(kR_0) + 2\,\mu_1\,(ik^2 G)\, I_0''(kR_0)\end{aligned} \tag{139}$$

$$\begin{aligned}\beta_2 &= \rho_1\, g\, k \cos(\theta)\, I_0'(k_I R_0) \\ &+ \sigma \left[k^3 - \frac{k}{R_0^2}\right] I_0'(k_I R_0) + 2\,\mu_1\,(ikk_I G)\, I_0''(k_I R_0)\end{aligned} \tag{140}$$

$$\begin{aligned}\beta_3 &= -\rho_2 \left(g k \cos(\theta)\, K_0'(kR_0) - G^2 K_0(kR_0)\right) \\ &- 2\mu_2\,(ik^2 G)\, K_0''(kR_0)\end{aligned} \tag{141}$$

$$\beta_4 = -\rho_2\, g k \cos(\theta)\, K_0'(k_{II} R_0) - 2\mu_2\,(ikk_{II} G)\, K_0''(k_{II} R_0) \tag{142}$$

In terms of the Stokes's stream function defined in Equations (98) and (99), Equation (135) can be rewritten as:

$$\mu_1 \left[\frac{\partial^2}{\partial r^2} - \frac{1}{r}\frac{\partial}{\partial r} + k^2\right] \Psi_I = \mu_2 \left[\frac{\partial^2}{\partial r^2} - \frac{1}{r}\frac{\partial}{\partial r} + k^2\right] \Psi_{II} \tag{143}$$

Substitution of Equations (120) and (121) in Equation (143) and simplifying according to Equations (109) and (110), Equation (143) becomes:

$$\begin{aligned}&2k^2 I_0'(kR_0)\,\mu_1 A_1 + (k_I^2 + k^2)\, I_0'(k_I R_0)\,\mu_1 B_1 \\ &-2k^2 K_0'(kR_0)\,\mu_2 A_2 - (k_{II}^2 + k^2)\, K_0'(k_{II} R_0)\,\mu_2 B_2 = 0\end{aligned} \tag{144}$$

Equations (136), (137), (138) and (144) are linear and homogeneous in A_1, B_1, A_2 and B_2. They have non-trivial solutions if and only if the determinant of the coefficient vanishes, i.e.:

$$\begin{vmatrix} I_0'(kR_0) & I_0'(k_I R_0) & -K_0'(kR_0) & -K_0'(k_{II}R_0) \\ kI_0''(kR_0) & k_I I_0''(k_I R_0) & -kK_0''(kR_0) & -k_{II}K_0''(k_{II}R_0) \\ \beta_1 & \beta_2 & \beta_3 & \beta_4 \\ 2k^2 I_0'(kR_0)\mu_1 & (k_I^2+k^2)I_0'(k_I R_0)\mu_1 & -2k^2 K_0'(kR_0)\mu_2 & -(k_{II}^2+k^2)K_0'(k_{II}R_0)\mu_2 \end{vmatrix} = 0 \quad (145)$$

Defining:

$$\varepsilon_1 = \frac{I_0''(kR_0)}{I_0'(kR_0)} = \frac{I_0(kR_0)}{I_1(kR_0)} - \frac{1}{kR_0} \quad (146)$$

$$\varepsilon_2 = \frac{I_0''(k_I R_0)}{I_0'(k_I R_0)} = \frac{I_0(k_I R_0)}{I_1(k_I R_0)} - \frac{1}{k_I R_0} \quad (147)$$

$$\varepsilon_3 = \frac{K_0''(kR_0)}{K_0'(kR_0)} = -\frac{K_0(kR_0)}{K_1(kR_0)} - \frac{1}{kR_0} \quad (148)$$

$$\varepsilon_4 = \frac{K_0''(k_{II}R_0)}{K_0'(k_{II}R_0)} = -\frac{K_0(k_{II}R_0)}{K_1(k_{II}R_0)} - \frac{1}{k_{II}R_0} \quad (149)$$

The evaluation of the determinant as defined at Equation (145) gives:

$$\left[(\rho_1-\rho_2)gk\cos(\theta)+\sigma\left[k^3-\frac{k}{R_0^2}\right]\right]\cdot\left[(k_I^2-k^2)(k_{II}\varepsilon_4-k\varepsilon_3)\mu_1+(k^2-k_{II}^2)(k_I\varepsilon_2-k\varepsilon_1)\mu_2\right]+$$
$$2iGk\left[(k_{II}\varepsilon_4-k\varepsilon_3)\left((k_I^2+k^2)k\varepsilon_1-2k^2k_I\varepsilon_2\right)\mu_1-(k_I\varepsilon_2-k\varepsilon_1)\left((k_{II}^2+k^2)k\varepsilon_3-2k^2k_{II}\varepsilon_4\right)\mu_2\right](\mu_1-\mu_2)$$
$$-G^2\rho_1\alpha_1\left(\left[(k_{II}^2+k^2)k\varepsilon_3-2k^2k_{II}\varepsilon_4+(k^2-k_{II}^2)k_I\varepsilon_2\right]\mu_2+\left[(k_I^2+k^2)(k_{II}\varepsilon_4-k\varepsilon_3)\right]\mu_1\right)$$
$$+G^2\rho_2\alpha_2\left(\left[(k_I^2+k^2)k\varepsilon_1-2k^2k_I\varepsilon_2+(k^2-k_I^2)k_{II}\varepsilon_4\right]\mu_1+\left[(k_{II}^2+k^2)(k_I\varepsilon_2-k\varepsilon_1)\mu_2\right]\right)=0 \tag{150}$$

where α_1 and α_2 are defined in Equation (71). Clearly, this equation relating G and k is in general very complicated.

When R_0 becomes to infinite (planar interface), we have the following limits:

$$\begin{aligned}&\varepsilon_1\to 1\;;\quad \varepsilon_2\to 1\;;\quad \varepsilon_3\to -1\;;\quad \varepsilon_4\to -1\\&\alpha_1\to 1\;;\quad \alpha_2\to 1\;;\quad \theta\to 0\;;\end{aligned} \tag{151}$$

By considering above limits and having regard to Equations (122) and (123), Equation (150) becomes:

$$\begin{aligned}&\left[(\rho_1-\rho_2)gk+\sigma k^3-G^2(\rho_1+\rho_2)\right]\left[\mu_1(k+k_I)+\mu_2(k+k_{II})\right]\\&\quad+4iGk\left[\mu_1k+\mu_2k_{II}\right]\left[\mu_2k+\mu_1k_I\right]=0\end{aligned} \tag{152}$$

This is the same as Bellman and Pennington's expression[15] for a planar interface.

When both fluids are inviscid, i.e. $\mu_I=\mu_2=0$ and k_I and k_{II} become infinite, Equation (150) reduces to our previous dispersion equation for an inviscid system, i.e., Equation (70).

4.2 APPLICATION TO FILM BOILING

4.2.1 MATHEMATICAL MODEL

For film boiling on a horizontal cylinder, there is only a need to treat the stability of the top of the cylindrical interface ($\theta=0$). Since the gas-liquid interface is asymmetric as shown in Figure 2.1, we have to modify the dispersion equation for the symmetrical interface, i.e., Equation (150). As in Section 3.2 for an inviscid system, we only replace the term "$\xi\sigma/R_o^2$" of Equation (134) by "$\xi\sigma/\ 2R_o^2$" of Equation (31). If the vapour depth, d_g, is considered, R_o should be replaced by $R_c = R_o + d_g$. The force balance equation (134) is rewritten as:

$$-P_I^d + 2\mu_1 \frac{\partial U_r^I}{\partial r} = -P_{II}^d + 2\mu_2 \frac{\partial U_r^{II}}{\partial r} + \sigma\left[\frac{\partial^2 \xi}{\partial z^2} + \frac{\xi}{2R_c^2}\right] \qquad (153)$$

Following the procedure of Section 4.1, the dispersion equation for film boiling becomes:

$$\begin{aligned}
&\left[(\rho_1-\rho_2)gk\cos(\theta)+\sigma\left[k^3-\frac{k}{2R_C^2}\right]\right]\cdot\left[(k_I^2-k^2)(k_{II}\varepsilon_4-k\varepsilon_3)\mu_1 + (k^2-k_{II}^2)(k_I\varepsilon_2-k\varepsilon_1)\mu_2\right]+\\
&2iGk\left[(k_{II}\varepsilon_4-k\varepsilon_3)\left((k_I^2+k^2)k\varepsilon_1-2k^2k_I\varepsilon_2\right)\mu_1-(k_I\varepsilon_2-k\varepsilon_1)\left((k_{II}^2+k^2)k\varepsilon_3-2k^2k_{II}\varepsilon_4\right)\mu_2\right](\mu_1-\mu_2)\\
&\quad - G^2\rho_1\alpha_1\left(\left[(k_{II}^2+k^2)k\varepsilon_3-2k^2k_{II}\varepsilon_4+(k^2-k_{II}^2)k_I\varepsilon_2\right]\mu_2 + \left[(k_I^2+k^2)(k_{II}\varepsilon_4-k\varepsilon_3)\right]\mu_1\right)\\
&\quad + G^2\rho_2\alpha_2\left(\left[(k_I^2+k^2)k\varepsilon_1-2k^2k_I\varepsilon_2+(k^2-k_I^2)k_{II}\varepsilon_4\right]\mu_1 + \left[(k_{II}^2+k^2)(k_I\varepsilon_2-k\varepsilon_1)\mu_2\right]\right) = 0
\end{aligned} \qquad (154)$$

Generally, for film boiling we can assume the density and viscosity of the vapour to be zero, i.e. $\rho_1 = 0$ and $\mu_1 = 0$. Thus, Equation (154) can be greatly simplified to:

$$\left[-\rho_2 g + \sigma\left[k^2 - \frac{1}{2R_c^2}\right]\right]\frac{k\rho_2}{\mu_2} - 2k\left(\varepsilon_3 k(k_{II}^2 + k^2) - 2k^2 k_{II}\varepsilon_4\right)\mu_2 + (iG)\rho_2\alpha_2(k_{II}^2 + k^2) = 0 \tag{155}$$

If we define:

$$M = \frac{\rho_2^{1/4}\sigma^{3/4}}{\mu_2 g^{1/4}} \tag{156}$$

as the dimensionless liquid viscosity parameter, and using the dimensionless variables defined in Equations (74)-(77), Equation (155) can be rewritten in dimensionless form as:

$$\begin{gathered}\left[1 - K^2 + \frac{1}{2\Pi^2}\right] + \frac{2}{M^2}\left[\varepsilon_3 K(K^{*2} + K^2) - 2K^2K^*\varepsilon_4\right] \\ - \Omega\alpha_2(K^{*2} + K^2)\frac{1}{MK} = 0\end{gathered} \tag{157}$$

where:

$$K^{*2} = K^2 + \Omega M \tag{158}$$

and

$$\begin{gathered}\varepsilon_3 = -\frac{K_0(K\Pi)}{K_1(K\Pi)} - \frac{1}{K\Pi} \\ \varepsilon_4 = -\frac{K_0(K^*\Pi)}{K_1(K^*\Pi)} - \frac{1}{K^*\Pi} = -\frac{K_0(\Pi\sqrt{K^2+\Omega M})}{K_1(\Pi\sqrt{K^2+\Omega M})} - \frac{1}{\Pi\sqrt{K^2+\Omega M}}\end{gathered} \tag{159}$$

α_2 is expressed in dimensionless form by Equation (79).

Equation (157) is the required dispersion equation, through which the dimensionless wavenumber is related to the dimensionless growth rate. We are interested in the "most dangerous" wavelength which corresponds to maximum growth rate of the disturbance. Obviously, the evaluation of "most dangerous" wavelength needs numerical calculation.

When $\Omega = 0$, we have $K = K^*$, and $\varepsilon_3 = \varepsilon_4$. Equation (157) thus reduces to:

$$K_{c,boiling} = \left\{ 1 + \frac{1}{2\,\Pi^2} \right\}^{1/2} \tag{160}$$

which is the expression for the dimensionless critical wavenumber and is the same as that of inviscid system (Equation (80)). It is independent of liquid properties and is only a function of dimensionless radius.

4.2.2 COMPARISON WITH EXPERIMENTAL RESULTS

In 1973, excellent experiments were carried out by Dhir and Lienhard[28] to observe the wavelength, its rate of growth, and the thickness of the vapour blanket surrounding a wire heater during film boiling in viscous liquids. In order to compare the experimental results and predicted data by the present model, numerical calculations were made based on dispersion equation (157) by using the commercial program TK-Solver.

Figure 4.1, Figure 4.2 and Figure 4.3 present the calculated dimensionless growth rate as a function of dimensionless wavelength at various dimensionless radii for values of the dimensionless viscosity parameter M equal to 1, 5.4 and 16. Maximum growth rate points and 98% of maximum growth rate points are shown on these curves.

By comparing Figure 4.1, Figure 4.2 and Figure 4.3, it is clear that the dispersion curves become flatter as the dimensionless viscosity parameter (M) becomes smaller. As shown in Figure 4.1 with $M = 1$, a small difference, for example 2%, from maximum dimensionless growth rate will cause very larger variation in dimensionless wavelength, 100%. Conversely, for $M = 16$ as shown in Figure 4.3, a small difference of 2% in the dimensionless growth rate only produces about 20% variation of dimensionless wavelength. Thus, it is expected that the agreement between predicted and measured dimensionless wavelength should be better for higher M values (e.g. $M = 16$) than that for lower M values (e.g. $M = 5.4$).

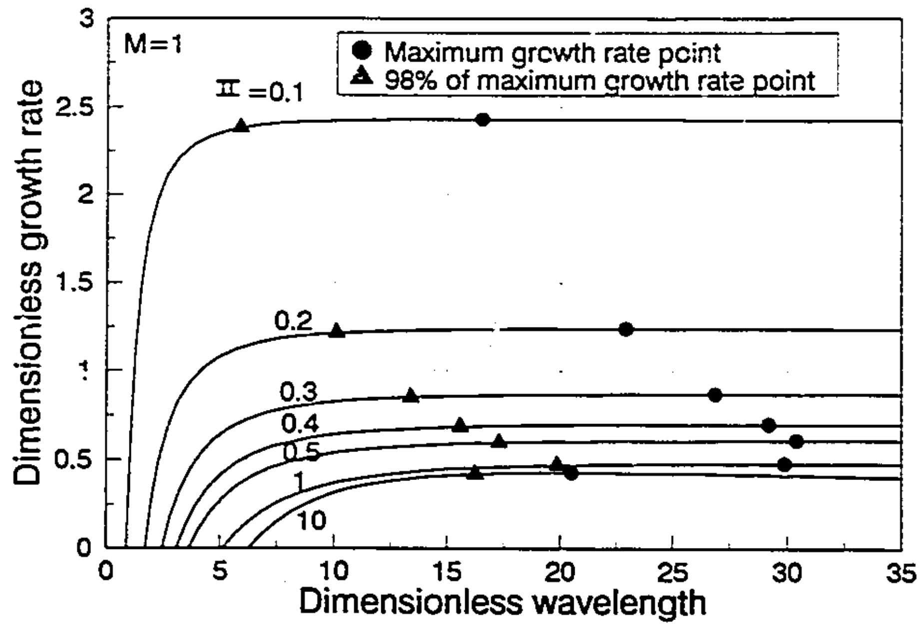

Figure 4.1 Calculated relationships between dimensionless wavelength and dimensionless growth rate for M=1.

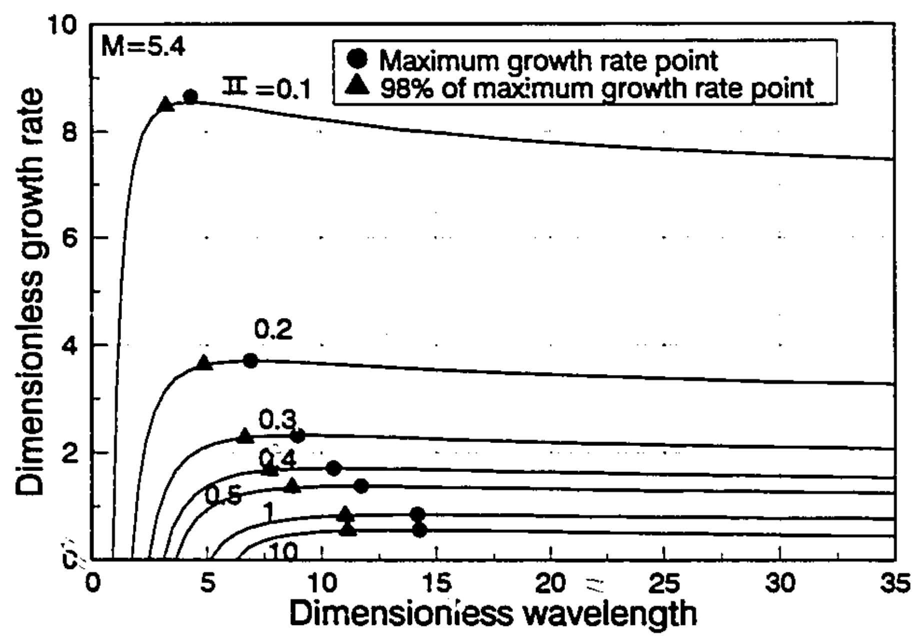

Figure 4.2 Calculated relationships between dimensionless wavelength and dimensionless growth rate for M=5.4.

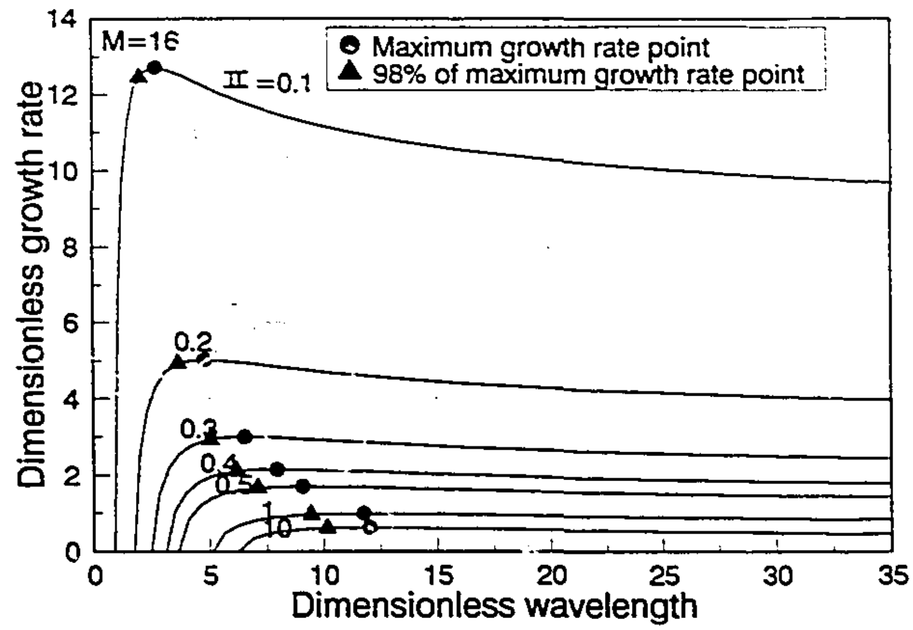

Figure 4.3 Calculated relationships between dimensionless wavelength and dimensionless growth rate for M=16.

Figure 4.4, Figure 4.5 and Figure 4.6 show the comparisons between measured and predicted dimensionless growth rates for M=16 and at three different dimensionless radii. Obviously, the observed growth rates occurred at the so called "most dangerous" wavelengths according to the present theory, that is the measured points lie in the maximum growth rate region. Dhir and Lienhard's model underestimates the dimensionless dangerous wavelength. However, the predicted growth rates by present theory are higher than that observed. Possibly, the experimental error in determining the growth rates and the small perturbation assumption which led to the linearized governing equations are responsible for the difference between predicted and observed. Figure 4.7 and Figure 4.8 present the relationship between dimensionless wavelength and radius for M=5.4 and M=16, respectively. From Figure 4.7, it is evident that the calculation based on the maximum growth rate overestimates the wavelength, and predicted data based on 98% of maximum growth rate is closer to the observed data. From Figure 4.2, this can be easily understood since the maximum points on the curves lie on a flat region. For M = 16, because the dispersion curves shown in Figure 4.3 are less flat in comparison to those of M = 5.4, good agreement between measured data and predicted data based on the maximum growth rate is expected, as mentioned above.

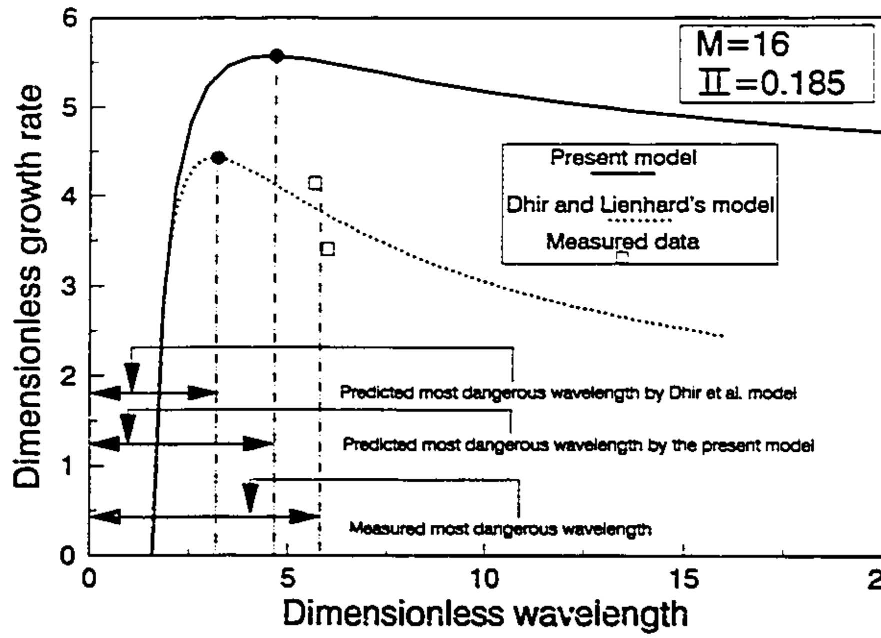

Figure 4.4 Experimental dimensionless growth rate for 0.185 of dimensionless radius.

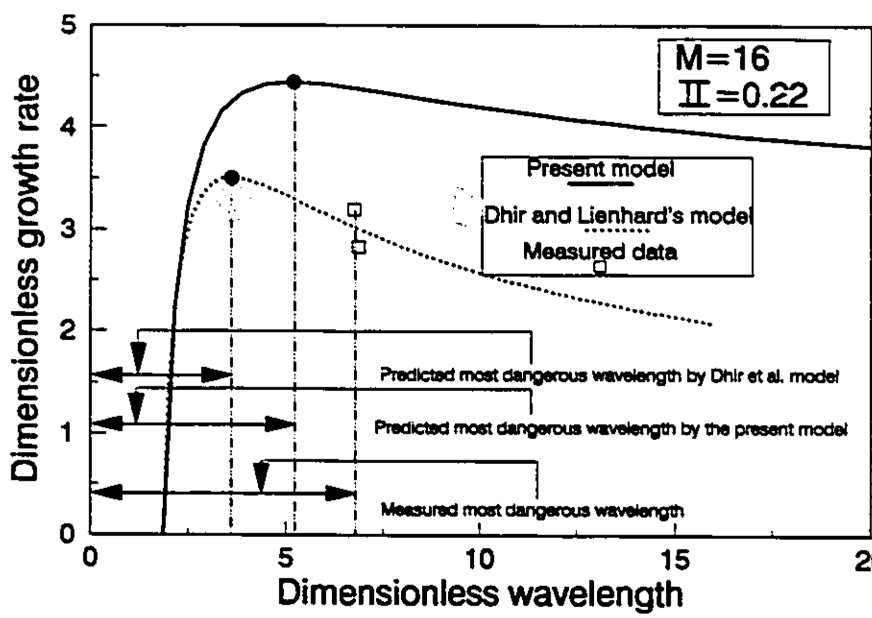

Figure 4.5 Experimental dimensionless growth rate for 0.22 of dimensionless radius.

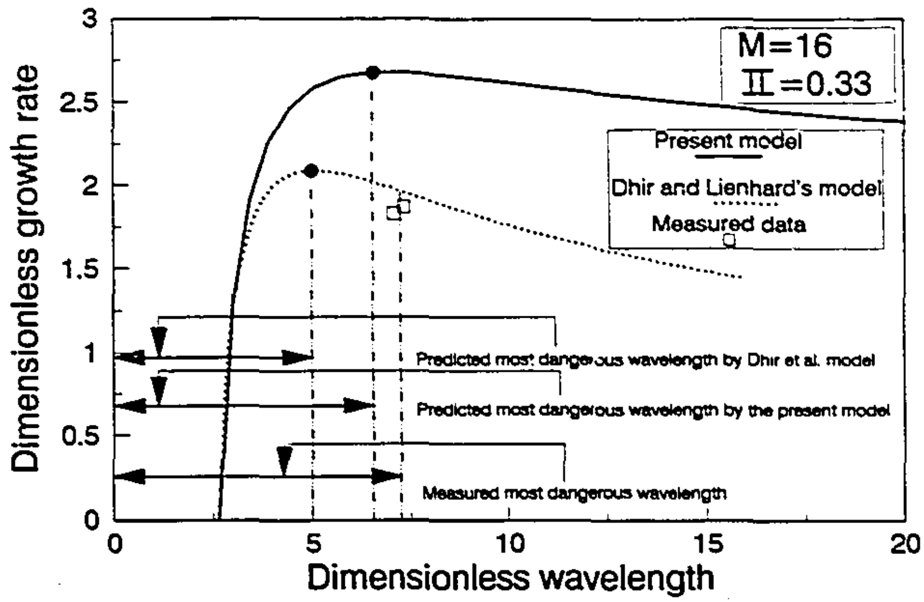

Figure 4.6 Experimental dimensionless growth rate for 0.33 of dimensionless radius.

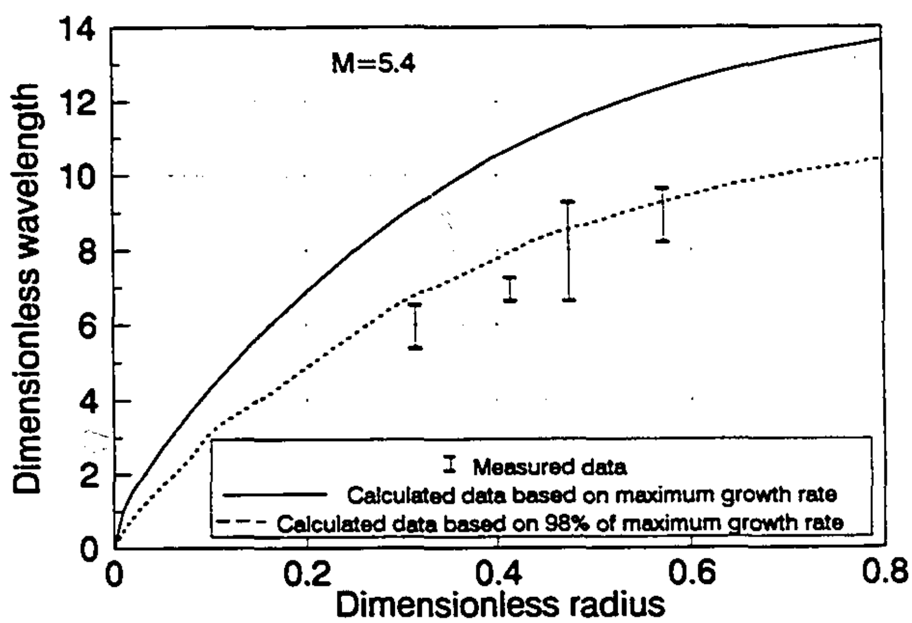

Figure 4.7 Experimental and calculated dimensionless wavelength for M=5.4.

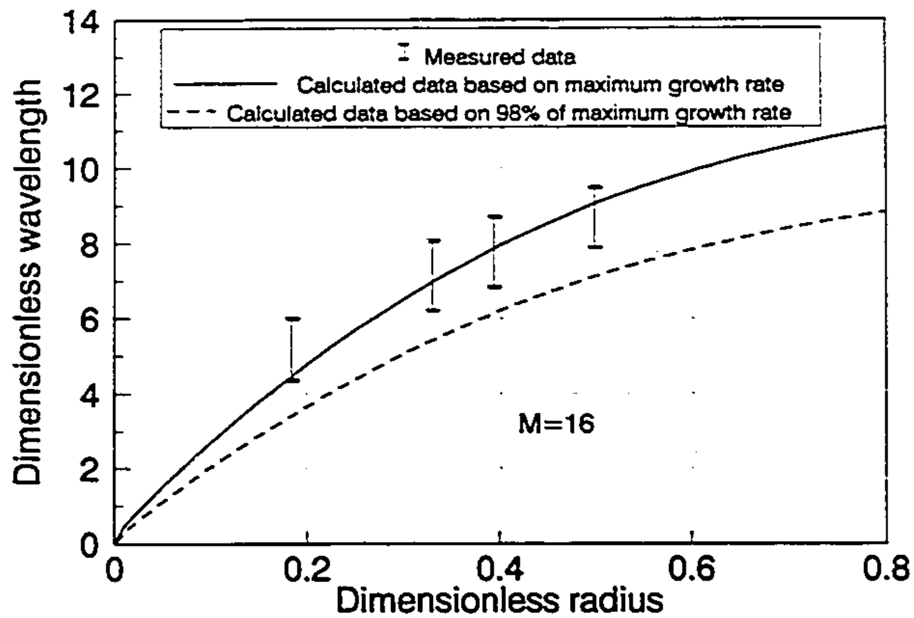

Figure 4.8 Experimental and calculated dimensionless wavelength for M = 16.

In contrast with our analysis, Dhir and Lienhard's model[28] underestimates the dimensionless wavelength for M = 16 and gives close prediction for M = 5.4, which is unreasonable. In fact, there was no explanation for their prediction in their paper.

4.3 CONCLUSIONS

1. Dispersion equations (Equation (150) and (154)) relating k to G have been derived for both axisymmetric and asymmetrical cylindrical interfaces between two viscous fluids.

2. The present theoretical model (Equation (155)) can be used to understand the film boiling phenomena on a heater wire immersed in a viscous liquid.

CHAPTER 5

KELVIN-HELMHOLTZ INSTABILITY OF A CYLINDRICAL INTERFACE:INVISCID FLUIDS

Chapter 1 mentioned that there are two kinds of instabilities for a two-phase interface, namely, *Rayleigh-Taylor instability* and *Kelvin-Helmholtz* instability. In Chapters 3 and 4 we discussed the Rayleigh-Taylor instability for inviscid and viscous fluids with applications to film boiling and liquid film breakup on a cylindrical body. When two stratified heterogeneous fluids are in relative motion (e.g., gas jet injected from a circular orifice into liquid), the stability of the interface between two fluids depends on the relative velocity of the fluids. In this chapter, the dispersion equation for the interfacial Kelvin-Helmholtz instability is derived and then some of its applications are presented.

5.1 THEORY

Let us consider a cylindrical fluid jet with radius R_o moving with velocity U_1 in direction Z. Fluid 2 is moving with velocity U_2 at the same direction. If the fluids are inviscid, and the perturbed flow is assumed to be irrotational, the velocity potentials of the two fluids can be written as Equation (161) according to Equations (4) and (50).

$$\begin{aligned}\Phi_1 &= \phi_1 + U_1\, z = A\, I_n(kr) \exp[i(Gt+kz)]\, Cos(n\theta) + U_1\, z \\ \Phi_2 &= \phi_2 + U_2\, z = B\, K_n(kr) \exp[i(Gt+kz)]\, Cos(n\theta) + U_2\, z\end{aligned} \tag{161}$$

If the disturbance of interface at $r = R_0$ is assumed to be expressed by Equation (51), the kinematic conditions to be satisfied at the interface can be expressed as:

$$\frac{\partial \xi}{\partial t} + U_1 \frac{\partial \xi}{\partial z} = \frac{\partial \Phi_1}{\partial r} , \quad \frac{\partial \xi}{\partial t} + U_2 \frac{\partial \xi}{\partial z} = \frac{\partial \Phi_2}{\partial r} \tag{162}$$

where the quadratic terms in ξ, ϕ_1 and ϕ_2 have been neglected.

Combining Equations (161) and (162) yields:

$$\frac{\partial \xi}{\partial t} = D \exp\left[i\,(Gt + kz)\right] \, Cos\,(n\,\theta) \tag{163}$$

where D is:

$$D = \frac{A\ U_2 \left[\dfrac{\partial I_n(kr)}{\partial r}\right]_{r=R_o} - B\ U_1 \left[\dfrac{\partial K_n(kr)}{\partial r}\right]_{r=R_o}}{U_2 - U_1} \tag{164}$$

Thus,

$$\xi = \frac{D}{i\,G} \exp\left[i\,(Gt + kz)\right] \, Cos\,(n\theta) \tag{165}$$

Combining Equations (161), (162) and (165) yields:

$$A = D\, \frac{1 + \dfrac{U_1\, k}{G}}{\left[\dfrac{\partial I_n(kr)}{\partial r}\right]_{r=R_o}} , \quad B = D\, \frac{1 + \dfrac{U_2\, k}{G}}{\left[\dfrac{\partial K_n(kr)}{\partial r}\right]_{r=R_o}} \tag{166}$$

If the total pressures in fluids 1 and 2 are denoted by P_1^t and P_2^t, and the equilibrium pressures of fluids 1 and 2 are represented by P_{10}^t and P_{20}^t, we have following relationships for fluid 1 from the Bernoulli equation:

In the absence of disturbance,

$$\frac{P_{10}^t}{\rho_1} + \frac{1}{2}\, U_1^2 + g\ Y_o = constant \tag{167}$$

where Y_o is vertical reference height of the interface.

In the disturbance,

$$\frac{\partial \Phi_1}{\partial t} + \frac{P_1^t}{\rho_1} + \frac{1}{2}(U_1^t)^2 + g\ Y = constant \tag{168}$$

where U_1^t is the total velocity of fluid 1 due to both the fluid motion and the disturbance, Y is the vertical coordinate of the interface relative to Y_o.
In Equation (168),

$$(U_1^t)^2 = U_z^2 + U_r^2 + U_\theta^2$$
$$= U_1^2 + 2\ U_1 \left[\frac{\partial \phi_1}{\partial z}\right]^2 + \left[\frac{\partial \phi_1}{\partial z}\right]^2 + \left[\frac{\partial \phi_1}{\partial r}\right]^2 + \frac{1}{r^2}\left[\frac{\partial \phi_1}{\partial \theta}\right]^2 \tag{169}$$
$$\approx U_1^2 + 2\ U_1 \left[\frac{\partial \phi_1}{\partial z}\right]^2$$

Combining Equations (167) to (169), we obtain the expression for the perturbation pressure of fluid 1, P_1^d,

$$P_1^d = P_1^t - P_{10}^t = -\rho_1 \left[\frac{\partial \phi_1}{\partial t} + U_1 \frac{\partial \phi_1}{\partial z} + g\,\xi \cos(\theta)\right] \tag{170}$$

Similarly for fluid 2,

$$P_2^d = -\rho_2 \left[\frac{\partial \phi_2}{\partial t} + U_2 \frac{\partial \phi_2}{\partial z} + g\,\xi \cos(\theta)\right] \tag{171}$$

Substituting Equations (170) and (171) into Equation (64) and rearranging gives:

$$\rho_2 \left[\frac{\partial \phi_2}{\partial t} + U_2 \frac{\partial \phi_2}{\partial z}\right] - \rho_1 \left[\frac{\partial \phi_1}{\partial t} + U_1 \frac{\partial \phi_1}{\partial z}\right]$$
$$+ g\ \xi\ (\rho_2 - \rho_1)\cos(\theta) = \left[k^2 - \frac{1 - n^2}{R_o^2}\right] \xi\ \sigma \tag{172}$$

Combining Equation (172) with Equations (161), (165) and (172) and rearranging, we have:

$$\begin{aligned}&\left[\rho_1\,\delta_1 + \rho_2\,\delta_2\right]\frac{G^2}{k} + 2\left[\rho_1\,\delta_1\,U_1 - \rho_2\,\delta_2\,U_2\right]G\\ &+\left[\rho_1\delta_1 U_1^2 + \rho_2\delta_2 U_2^2\right]k = \left[k^2 - \frac{1-n}{R_o^2} - \frac{(\rho_2-\rho_1)g\cos(\theta)}{\sigma}\right]\sigma\end{aligned} \tag{173}$$

where δ_1 and δ_2 are defined in Equation (68). Rearranging Equation (173) gives:

$$\begin{aligned}\frac{G}{k} &= -\frac{\rho_2\,\delta_2\,U_2 + \rho_1\,\delta_1\,U_1}{\rho_1\,\delta_1 + \rho_2\,\delta_2}\\ &\pm\left[-\frac{\rho_1\rho_2\delta_1\delta_2(U_1-U_2)^2}{(\rho_1\delta_1+\rho_2\delta_2)^2} + \frac{\left[k^2 - \frac{(1-n^2)}{R_o^2} - \frac{(\rho_2-\rho_1)g\cos(\theta)}{\sigma}\right]\sigma}{(\rho_1\delta_1+\rho_2\delta_2)k}\right]^{1/2}\end{aligned} \tag{174}$$

Equation (174) is the required dispersion equation for the Kelvin-Helmholtz instability of a cylindrical interface. The right-hand side of Equation (174) is the phase velocity of the disturbance. The first term on the right hand side is a weighted (by the density and Bessel function) mean velocity of the two streams.

If the root in the expression for the wave velocity (right-hand side of Equation (174)) has a nonzero imaginary part, then the interfacial disturbance can grow exponentially, i.e., the flow is unstable. If the root of right-hand side of Equation (174) is a real number, the interface is stable. The "most dangerous" wave number, k_d, or wavelength, λ_d, which dominates the breakup of a gas or liquid jet, can be predicted by maximizing the imaginary part of growth rate, G. If the imaginary part is denoted by G_i (i.e., $G=G_r+iG_i$), we have:

$$G_i^2 = \frac{\rho_1\rho_2\alpha_1\alpha_2(U_1-U_2)^2k^2}{(\rho_1\alpha_1+\rho_2\alpha_2)^2} - \frac{\left[k^2 - \frac{1}{R_o^2} - \frac{(\rho_2-\rho_1)g\cos(\theta)}{\sigma}\right]\sigma k}{(\rho_1\alpha_1+\rho_2\alpha_2)} \tag{175}$$

where n, the order of the Bessel function, has been assumed to be zero, and δ_1 and δ_2 have been replaced by α_1 and α_2 which are expressed in Equation (71). By maximizing G_i, the dangerous wavelength can be determined.

It is obvious that when $R_0 \to \infty$ Equation (174) reduces to Equation (14). If $U_1 = U_2 = 0$, Equation (174) becomes Equation (67), which is the dispersion equation of Rayleigh-Taylor instability for a cylindrical interface.

5.2 APPLICATIONS OF THE PRESENT THEORY

5.2.1 BREAKUP OF A GAS JET IN LIQUID

It is common practice in the metallurgical industry that gases are injected into liquid metals at high velocities in order to carry out the refining reactions quickly. As shown in Figure 5.1, the gas jet breaks into fine bubbles on the surface of the jet due to both Rayleigh-Taylor and Kelvin-Helmholtz instabilities. Since the interface between the gas jet and liquid can be approximated as a cylindrical one, above theoretical analysis can be employed to understand this phenomenon.

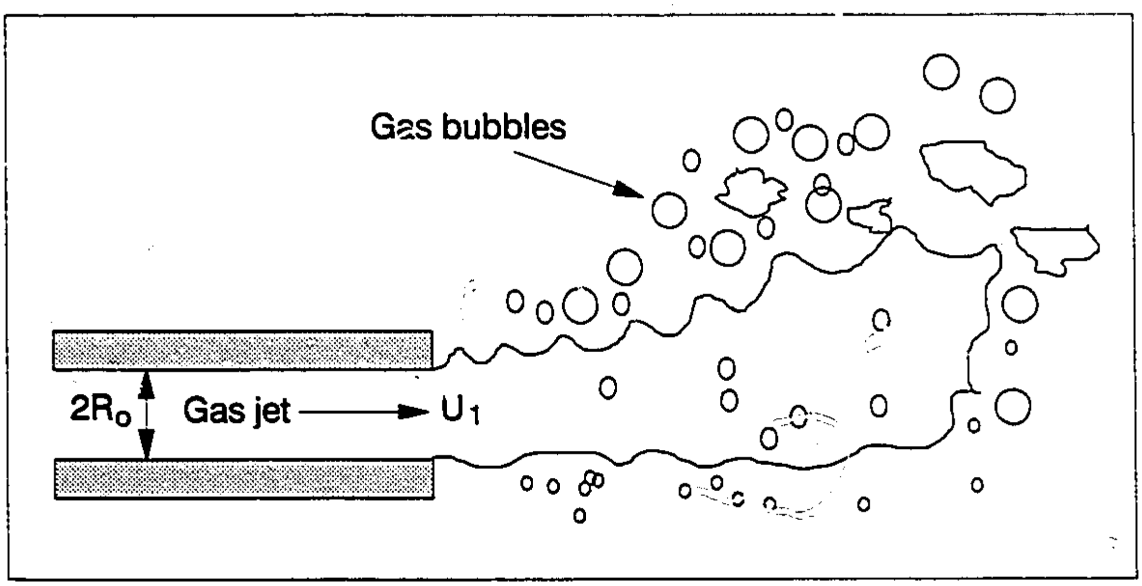

Figure 5.1 Schematic illustration of breakup of gas jet into fine bubbles; the wavelengths on the top surface of the jet are shorter than those on the bottom of the jet.

For the breakup of a gas jet in liquid, the density of gas is much smaller than that of the liquid, i.e., $\rho_1 \ll \rho_2$ and the velocity of the liquid can be assumed to be zero, $U_2 = 0$. Therefore, Equation (175) can be greatly simplified and be rewritten as:

$$G_i^2 = \frac{\rho_1 \alpha_1 U_1^2 k^2}{\rho_2 \alpha_2} - \frac{\left[k^2 - \frac{1}{R_o^2} - \frac{\rho_2 g \, Cos(\theta)}{\sigma}\right] \sigma k}{\rho_2 \alpha_2} \tag{176}$$

By maximizing G_i according to Equation (176), we can find the most dangerous wavelength which dominate the breakup of a gas jet into fine bubbles. Clearly, the most dangerous wavelength is a function of superficial velocity of the gas, the jet radius, R_o, the density of liquid, ρ_2, and the cylindrical coordinate, θ.

As an example, let us consider a horizontal air jet injected into water through a circular orifice with diameter 1cm. Table 5.1 gives the required parameters for a air jet in liquid water.

Table 5.1 Parameters of an Air Jet in Water

Density of air	Density of water	Surface tension	Radius of orifice
1.29 kg/m^3	1000 kg/m^3	0.072 N/m	5 mm

Figure 5.2 presents the relationship between the growth rate, G_i, and the wavelength, $\lambda = 2\pi/k$ at specific gas velocities, which was calculated by commercially available software, *Tk-solver*. It is clear that there is only one maximum on each curve. When the velocity of gas is very small ($U_1 \approx 0$), the top surface ($\theta = 0$) of the air jet is more unstable (higher growth rate, G_i and smaller dangerous wavelength) in comparison to the surface at $\theta = 90°$. However, the bottom of the jet ($\theta = 180°$) is stable at $U_1 \approx 0$ ($G_i^2 < 0$ according to Equation (175)). For the air jet at high velocity (e.g. 10 m/s), the instability of interface is mainly dominated by relative motion of fluids so that the maximum growth rates, G_i, are almost same for θ=0, 90 and 180°.

Figure 5.3 represents the calculated most dangerous wavelengths as a function of superficial gas velocity for θ = 0, 90 and 180°. The dangerous wavelength decreases

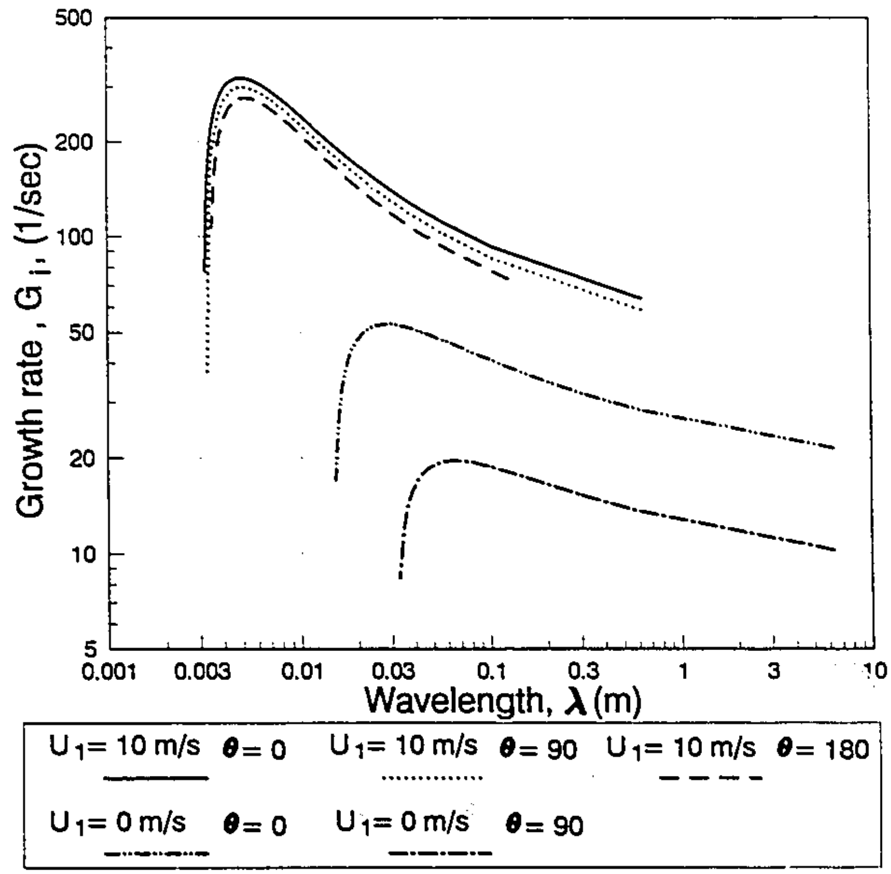

Figure 5.2 Calculated G_i as a function of wavelength at $U_1=0$ and 10 m/s for air jet in water.

greatly with an increase in the gas velocity, i.e., the first term of the right hand side of Equation (176) can not be neglected although the density of gas is very small in comparison to that of liquid. Because the top surface ($\theta = 0$) of the air jet is unstable from both the Rayleigh-Taylor and Kelvin-Helmholtz instabilities, it has the smallest dangerous wavelength. The bottom ($\theta = 180°$) of the air jet is stable from the Rayleigh-Taylor instability so that it has largest dangerous wavelength which becomes infinite when the velocity of the gas jet is less than 3~4 m/s. The middle curve in Figure 5.3 is calculated without considering the gravity term of Equation (176) ($\theta = 90$, $Cos(\theta) = 0$). It can also be considered as a relationship between the dangerous wavelength and the gas superficial velocity for a vertical gas jet. Beyond 10 m/s of gas velocity all curves for θ=0, 90 and 180° give the same dangerous wavelength, which means that the dangerous wavelength is dominated by relative motion or the Kelvin-Helmholtz instability, and the gravity term in

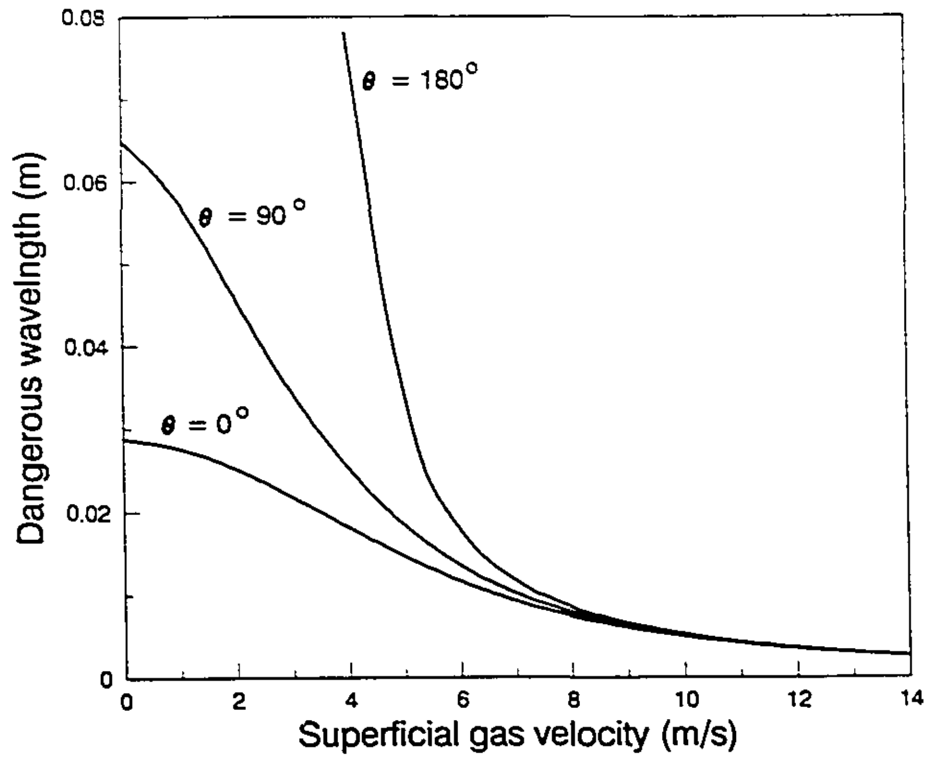

Figure 5.3 Calculated dangerous wavelength as a function of superficial gas velocity for air jet in water.

Equation (176) becomes negligible.

When the velocity and radius of the gas jet are very small, the velocity and gravity terms of the right hand side of Equation (176) can be neglected. Then Equation (176) is simplified as:

$$G_i^2 \left[\frac{\rho_2 R_o^3}{\sigma}\right] = (1 - \zeta^2)\, \zeta \, \frac{K_1(\zeta)}{K_0(\zeta)} \tag{177}$$

where $\zeta = kR_o$. Numerical calculation shows that the right hand side of Equation (177) reaches a maximum value at $\zeta = 0.484$, which is independent of the gas jet physical parameters. Therefore, the dangerous wavelength at $U_1 \approx 0$ and $R_o \approx 0$ can be expressed as:

$$\lambda_{d,gas} = \frac{2\pi}{k} = \frac{2\pi R_o}{\zeta} = \frac{2\pi R_o}{0.484} = 6.49(2R_o) \tag{178}$$

i.e., the ratio of dangerous wavelength to diameter of gas jet is equal to 6.49.

5.2.2 BREAKUP OF A LIQUID JET IN GAS

In contrast to a gas jet in liquid, the breakup of a liquid jet in gas (e.g., air) uses the subscript 1 to indicate the liquid. The density of gas is much smaller than that of liquid, i.e., $\rho_2 \ll \rho_1$ and velocity of gas can be assumed to be zero, $U_2 = 0$. Therefore, Equation (175) can be greatly simplified and be rewritten as:

$$G_i^2 = \frac{\rho_2 \alpha_2 U_1^2 k^2}{\rho_1 \alpha_1} - \frac{\left[k^2 - \frac{1}{R_o^2} + \frac{\rho_1 g\, Cos(\theta)}{\sigma} \right] \sigma k}{\rho_1 \alpha_1} \tag{179}$$

By maximizing G_i according to Equation (179), we obtain the dangerous wavelength which dominates the breakup of a liquid jet into fine droplets.

Consider the example of the breakup of a water jet with 1cm diameter in air. The required parameters are given in Table 5.1. Figure 5.4 presents the calculated most dangerous wavelength as a function of superficial liquid velocity for $\theta = 0$, 90 and 180°. The dangerous wavelength decreases greatly with an increase in the liquid velocity, i.e., the first term of the right hand of Equation (179) can not be neglected although the density of gas is very small in comparison to that of liquid. In contrast to an air jet in liquid, the top surface ($\theta = 0$) of the liquid jet is stable from the Rayleigh-Taylor instability point of view, it has the largest dangerous wavelength. The bottom of the liquid jet ($\theta = 180°$) has smallest dangerous wavelength. Again, the middle curve can be considered as a vertical liquid jet since the gravity term is equal to zero ($\theta = 90$, $Cos(\theta) = 0$). At high liquid velocity (10 m/s) all curves for $\theta = 0$, 90 and 180° give the same dangerous wavelength, and the dangerous wavelength is dominated by the Kelvin-Helmholtz instability.

When the velocity and radius of the liquid jet are very small, the velocity and gravity terms of the right hand side of Equation (179) can be neglected, and then Equation

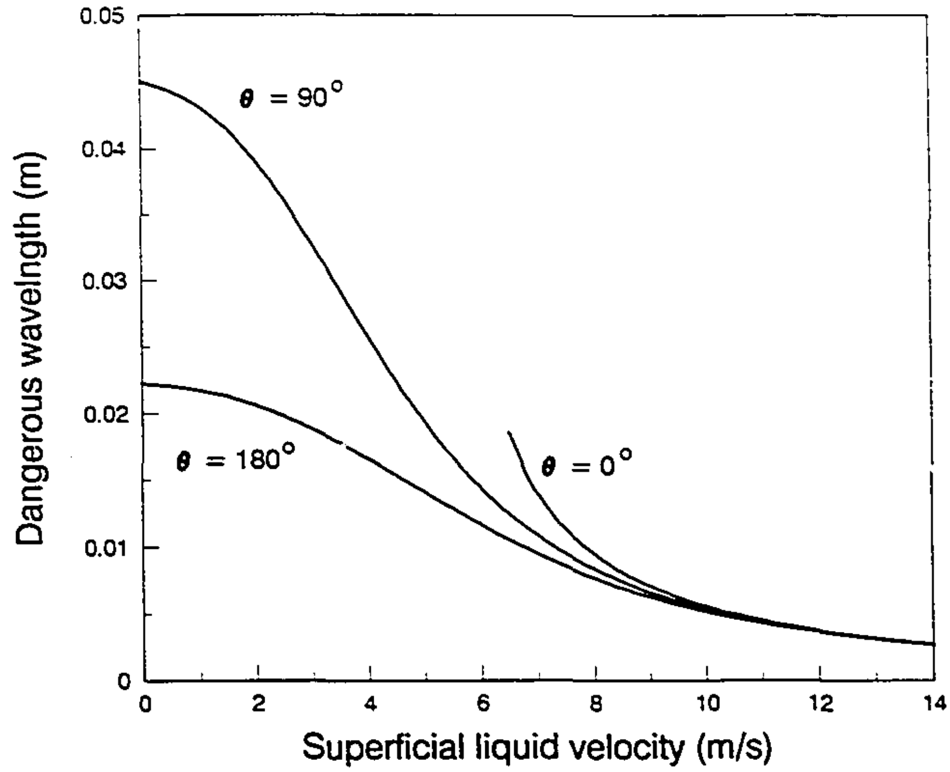

Figure 5.4 Calculated dangerous wavelength as a function of superficial liquid velocity for a water jet in air.

(179) is simplified as:

$$G_i^2 \left[\frac{\rho_1 R_o^3}{\sigma}\right] = (1 - \zeta^2)\,\zeta\,\frac{I_1(\zeta)}{I_0(\zeta)} \tag{180}$$

The right hand side of Equation (180) has the maximum value at $\zeta = 0.698$. The dangerous wavelength at $U_1 \approx 0$ and $R_o \approx 0$ can be expressed as:

$$\lambda_{d,liquid} = \frac{2\pi}{k} = \frac{2\pi R_o}{\zeta} = \frac{2\pi R_o}{0.698} = 4.5(2R_o) \tag{181}$$

which is the classic Rayleigh's result for a liquid jet (Equation (3)).

5.3 CONCLUSIONS

1. The general dispersion equation (Equation (175)) relating k and G_i has been derived, from which the dangerous wavelengths of an unstable interface can be predicted as a function of relative velocity of fluids and properties of fluids.

2. Simplified dispersion equations (Equations (176) and (179)) are given for gas jet breakup in liquid and liquid jet breakup in gas.

3. The most dangerous wavelength of a gas jet in liquid or a liquid jet in gas depends greatly on the jet velocity. It decreases rapidly with an increase of jet velocity.

4. At $U_1 \approx 0$ and $R_o \approx 0$, the ratio between dangerous wavelength and diameter of jet is 6.49 for a gas jet in liquid and 4.5 for a liquid jet in air.

5. For relatively high speed jets, e.g. 5 m/s for an air-liquid jets from a R_o = 5 mm orifice, conclusion 4 would no longer be valid and the full analysis would be required.

PART 2

GAS INJECTION PHENOMENA THROUGH A VERY NARROW SLOT

CHAPTER 6

LITERATURE REVIEW ON BUBBLE FORMATION

Submerged gas injection into liquid metal baths is playing an increasingly important role in high temperature metallurgical processes such as hot metal pretreatment, steelmaking and metal refining processing[32]. The objectives of gas injection into high temperature metallurgical baths are as follows:

- supply of reactant such as O_2 or CO;
- mixing;
- increase mass transfer rates or chemical reaction rates;
- impurity removal and degassing.

The gas injector elements conventionally employed in the metallurgical industry fall into two main categories: those based upon the porous plug and those based upon the single circular orifice. Figure 6.1 and Figure 6.2 show gas dispersion phenomena from a single circular nozzle and from a porous plug, respectively. The main problems concerning gas injection through traditional circular nozzles mounted on the bottom of the bath are: (a) the erosion of nozzle refractory due to the jet action, (b) the clogging of orifices by freezing metal inside the nozzles and (c) the large bubbles formed in the liquid metal due to the large size of orifices or due to the coalescence of bubbles inside the circular plume. A good nozzle should create the shortest mixing time for the bath, the lowest splashing and spitting, the highest mass transfer rate, and the maximum bubble surface area by using the minimum amount of injection gas.

Previous research on gas injection through non-circular nozzles into a liquid suggested that the back-attack effect which is evident when bubbles form at a circular

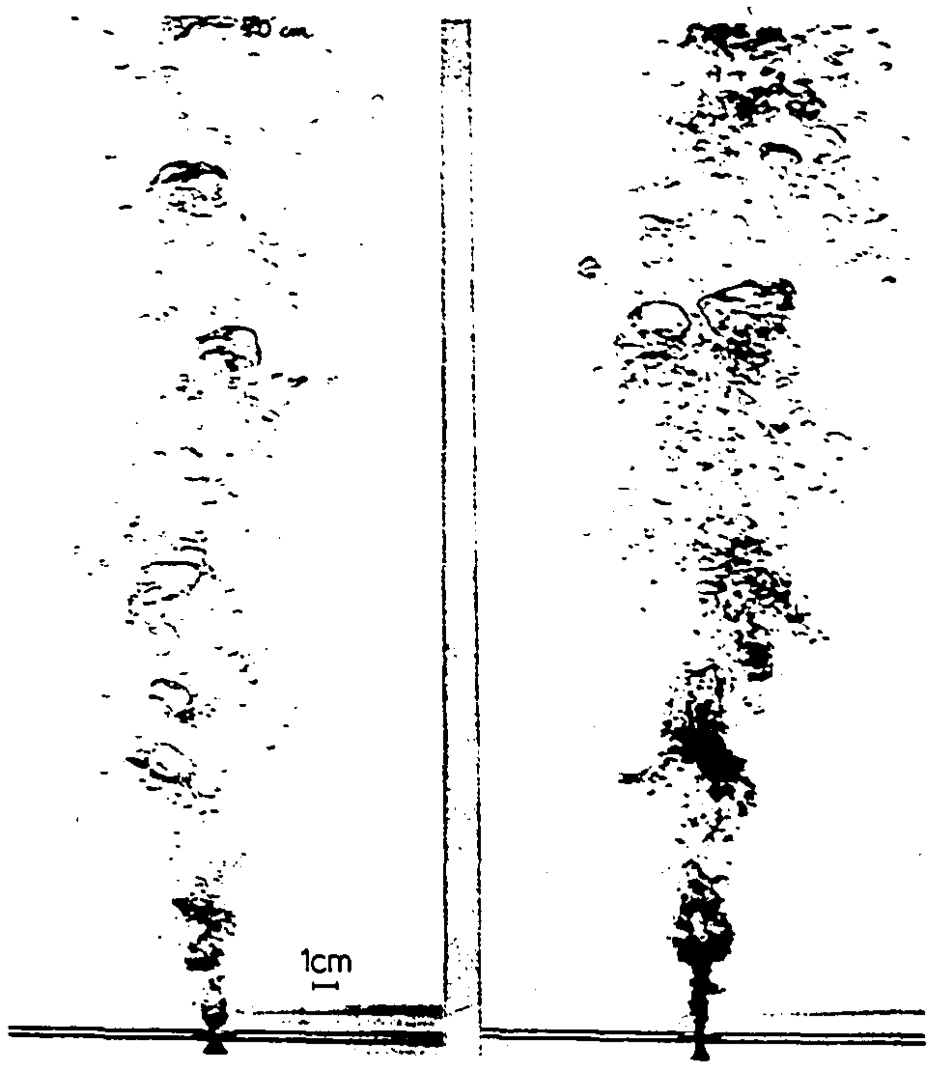

Figure 6.1 Gas dispersion phenomena in circular orifice (d_o=5mm) injection.

nozzle may be reduced by changing the shape of the nozzle towards a slot-shape or rectangular section with an appropriate aspect ratio[33]. When slot-shaped nozzles were explored for injecting different gases (nitrogen or carbon dioxide) at different stages during a steelmaking process in China, the blockage effect was largely reduced[34]. Based upon the above reason, a nozzle consisting of a very narrow single rectangular slot was designed for the present study. This kind of nozzle may prevent the liquid metal from flooding into it. It also produces a bubble wall instead of the circular plume generated by a circular nozzle. A bubble wall consists of widely distributed bubbles and provides an effective

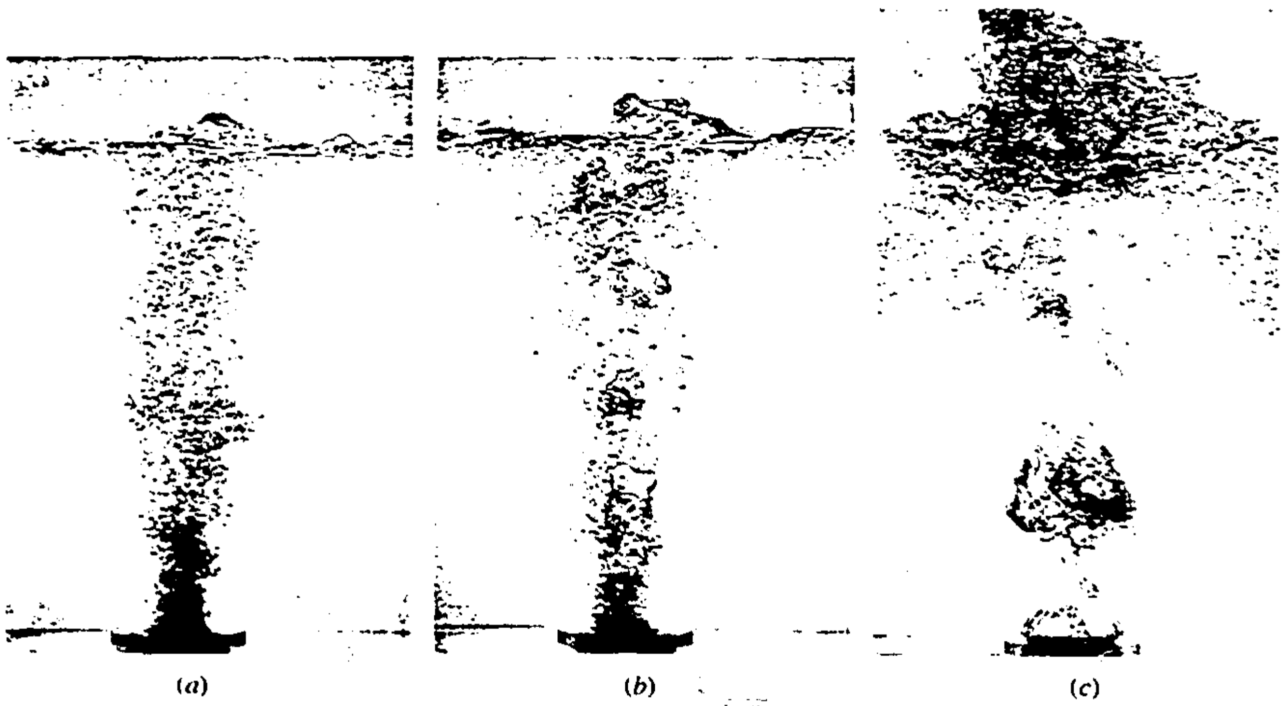

Figure 6.2 Gas dispersion phenomena in porous plug injection.

means of promoting agitation and/or chemical reaction through transfer processes at the liquid/gas interfaces. There has been little discussion of gas bubble formation and behaviour of gas injection through a narrow slot. Consequently, it is significant to understand the flow phenomenon of gas injection through submerged very narrow rectangular slots into high temperature metallurgical baths by studying their aqueous or metallic analogues and to apply this understanding to high temperature metallurgical processes.

The understanding of the complicated phenomena of gas injection into liquid needs research into (a) the behaviour of gas dispersion in the liquid and (b) the transport phenomena in gas/liquid systems, such as bubble formation, bubble motion, bubble coalescence and breakup, bubble distribution in liquid, bubbling-jetting transition, mass transfer, and momentum transfer as well as nozzle design and its erosion and blockage. There has been a great deal of work carried out on the development of gas injection. A state of the art summary of this field was given recently[32]. The application of gas injection in steelmaking process was reviewed by Lange[35,36].

Table 6.1 Gas Injection Variables

	Variable	Major Effects
Equipment Variable	chamber volume	fluctuation of flow rate and pressure
	orifice size	velocity of gas through the orifice; bubble volume at low flow rate
	orifice constant	pressure drop across the orifice
System Variable	surface tension	bubble volume at low flow rate
	liquid density	bubble volume at low flow rate and large viscosity
	liquid viscosity	bubble volume, bubble shape and motion in liquid
	gas density	bubble shape, disintegration and volume
	contact angle	bubble volume and bubble formation
	velocity of sound in gas	fluctuation of flow rate and pressure
Operating Variable	gas flow rate	dispersion regime; bubble volume at high flow rate
	liquid depth	dispersion regime at low liquid depth
	liquid motion	bubble volume, motion and disintegration; bubble shape
	operating temperature	bubble volume

Since the present research is mainly concerned with the bubble generation through a very narrow slot-shaped nozzle, the literature review is limited to bubble formation.

Bubble formation at the point of gas injection into a liquid is a highly complex phenomenon involving a variety of system and operating variables as listed in Table 6.1. A number of models which describe the bubble growth and predict the bubble volume and frequency are summarized in Table 6.2. Although a number of investigators summarized the models of bubble formation[37,38,39,40,32], no critical review has been given. Model studies of the formation of bubbles usually involve simplifying assumptions to isolate variables of relatively less significance in the process of interest. For ease of analysis and experimentation, most of the models consider gas flow through a single orifice, usually of circular geometry and located at the bottom plate of a tank of liquid.

The mechanics of bubble formation at the submerged orifice depend strongly on the flow properties of the gas phase. The pressure in a growing bubble decreases under the combined effects of diminishing hydrostatic and surface tension pressure components, thus inducing an increasing amount of gas flow into the expanding bubble and correspondingly decreasing the pressure in the source tank. Bubble formation, therefore, ordinarily occurs under unsteady conditions of varying system pressure and gas flow rate. However, the presence of a large pressure drop between the gas reservoir and the orifice, such as a long capillary, can swamp the influence of bubble-growth pressure fluctuation and produce a stable condition of "constant flow" gas injection[41]. Similarly, if the volume of the reservoir or "plenum chamber" upstream of the orifice is very large by comparison with the volume of bubbles being formed, the varying gas effux will not significantly change the pressure in the chamber[41]. For conditions intermediate between the limits of constant flow and constant pressure, the chamber volume must be taken into account. Spells and Bakowski[42] were the first to recognize the importance of the chamber volume as a variable. Hughes et al.[43] suggested quantitative criteria for constant flow and constant pressure gas injection on the basis of the system capacitance number, N_c, given by

$$N_c = \frac{\Delta\rho\, g\, V_c}{\rho_g A_o C^2} \tag{182}$$

where $\Delta\rho=\rho_l-\rho_g$ is the density difference between liquid and gas, g the acceleration due to gravity, V_c the chamber volume of nozzle, A_o the nozzle cross area, and C the sonic speed. The gas injection system is considered to operate at constant flow when $N_c<1$ and at constant pressure if $N_c > 9$.

The bubble formation models can be divided into spherical and non-spherical ones according to the assumption of the shape of the bubbles. The spherical models can be classified into constant flow, constant pressure and time dependent flow and pressure models corresponding to different conditions. All proposed models for bubble formation at a single circular orifice are summarized in Table 6.2.

6.1 SPHERICAL BUBBLE FORMATION MODELS

6.1.1 CONSTANT FLOW BUBBLE FORMATION

Under the constant flow conditions, the mechanism of bubble formation depends on the gas flow rate. At low gas flow rates which normally require capillary injection to minimise nozzle flooding, the bubble volume is determined by a balance of the upward force acting on the bubble (buoyancy force) and surface tension forces, giving:

$$V_b = \frac{2\pi r_0 \sigma Cos(\theta_c)}{\Delta\rho g} \tag{183}$$

where r_o is the radius of the circular orifice, V_b the bubble volume and θ_c the contact angle. Equation (183) is widely known as "Tate's Law". At high flow rates, the buoyancy force is balanced by the downward inertial force. Davidson and Schuler[44] have proposed a diffuse point-source model for deriving the volume of a bubble growing at a submerged orifice under constant flow conditions. The geometrical model is shown in Figure 6.3. A closed-form solution was obtained for the case of an inviscid liquid by considering that the surface tension force becomes negligible in comparison with the inertia of the bubble, so that:

$$V_b \Delta\rho g = \frac{d}{dt}\left[V_b\left[\rho_g + \frac{11}{16}\rho_l\right]\frac{ds}{dt}\right] \tag{184}$$

Table 6.2. Theoretical Models for Bubble Formation at a Single Submerged Orifice

	Condition	Reference	Geometrical Assumption	Force included*
spherical	constant flow	44	Model I of Figure 6.3	B, Ia
		45	Model I of Figure 6.3	B, Da, Ia
		46	Model I of Figure 6.3	B, Ib
		47	Model II of Figure 6.3	B, Ia
		48	Model III of Figure 6.3	B, Ia
	constant pressure	44	Model I of Figure 6.3	B, Ia
		45	Model I of Figure 6.3	B, Da, Ia
		49	Model II of Figure 6.3, but no detachment stage	B, Dc, I, P, S
		50	Model II of Figure 6.3	B, S, Da, Ia
		51	Model IV of Figure 6.3	B, Ia
	varying flow rate and pressure	52	Model II of Figure 6.3	B, Db, Ia, S
		53	Model II of Figure 6.3, but forces acting on the bubble were calculated by pressure distribution	B, I
		54	Model II of Figure 6.3, considering the wake behind the bubble	B, Ib, W
		55	Model IV of Figure 6.3	B, Ia, M
		56,57,58	Model II of Figure 6.3	B, Ia, Db
nonspherical	varying flow rate and pressure	59	shape varies, finite difference	B, Ic, S
		60	modification of Kupferberg and Jameson's[53] model, finite difference	B, Ia
		61	modification of Marmur and Rubin's model[59]. Apply for wetting and non-wetting liquid	B, Ia
	constant flow	62	based on continuity and motion equations	
		63	based on assumption of a prolate ellipsoidal shape of the bubbles	B, Db, I, M

*. B: buoyancy; D: drag (a: stokes: b: empirical expression: c: kept as constant to fit data); I: inertia (a: C = 11/16: b: C = 1/2: c: kept as constant to fit data); M: gas momentum; P: excess pressure term; S: surface tension force; W: wake effect from previous bubble.

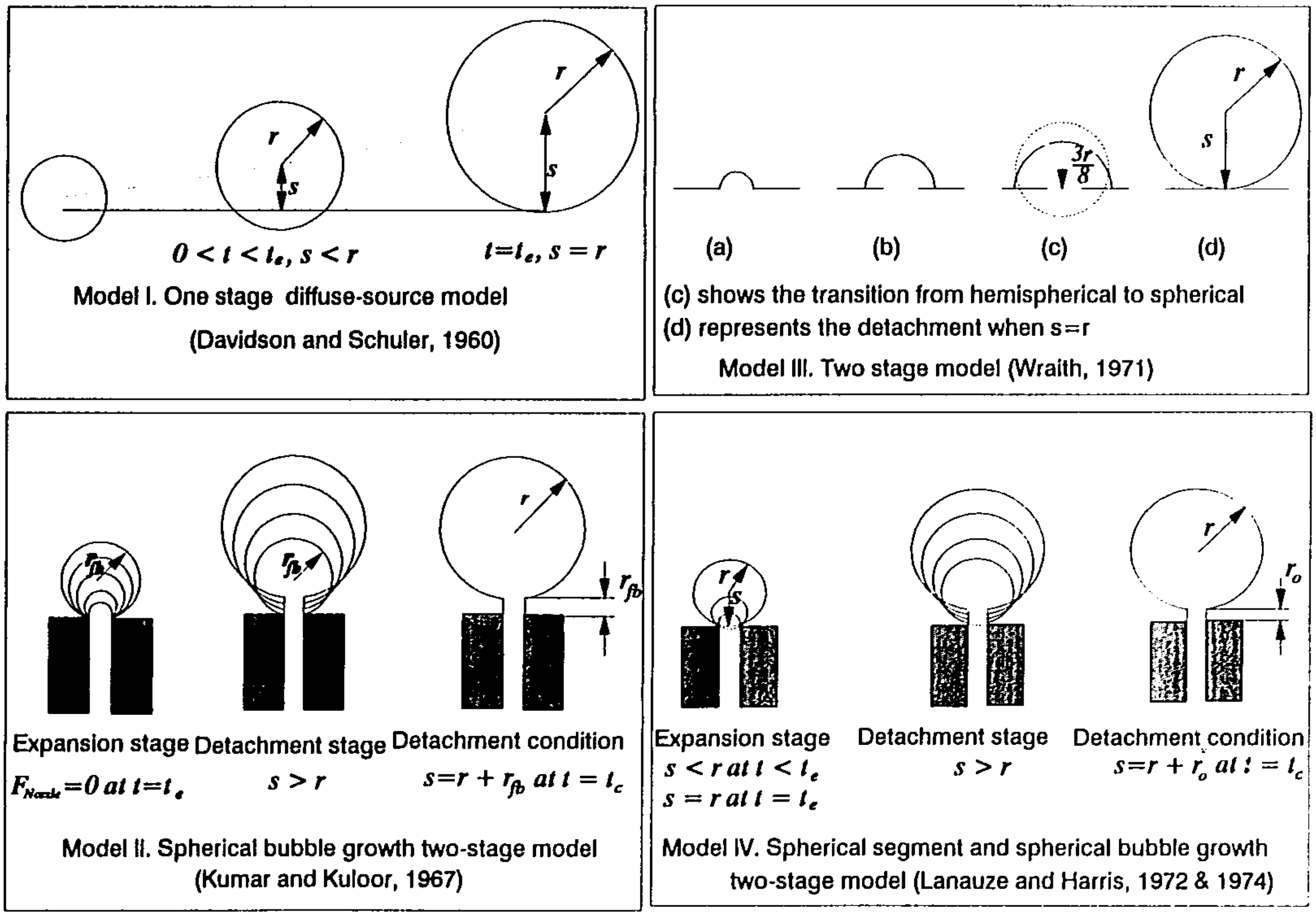

Figure 6.3 Geometrical models of bubble formation

where s is the displacement of the bubble centre from orifice plate, t the time, ρ_g and ρ_l the densities of gas and liquid. Bubble is assumed to be spherical throughout the period of growth; hence the hydrodynamic mass coefficient, 11/16, corresponds to a submerged sphere moving away from a solid surface[64]. The gas is assumed to be incompressible so that $V_b = Qt$; and the density of the gas is negligible in comparison with that of the liquid. Davidson and Schuler assumed that the upward force acting on the bubble (buoyancy force), is always balanced by the downward force (inertia) during bubble formation, and the bubble growth is terminated when its radius r equals s the distance travelled. Thus, Equation (184) can be solved readily by a double integration, with the initial conditions, $s = ds/dt = 0$ at $t = 0$. The final bubble volume is:

$$V_b = \frac{1.378\, Q^{6/5}}{g^{3/5}} \qquad (185)$$

Davidson and Schuler's model represents the first classical solution for the bubble volume at a submerged orifice in a constant flow system. Davidson and Schuler's model does not recognise the physical presence of the orifice plate and also the detachment condition ($s=r$) is improbable. However, it closely predicts many experimental results. The reason will be discussed later.

The physical limitation of Davidson and Schuler's model was overcome by a two-stage model of Kumar and Kuloor[47], Figure 6.3. In this model, bubble formation was assumed to take place in two stages, that is, a first or expansion stage, and a second or detachment stage. During the first stage the spherical bubble expands while its base remains attached to the orifice, whereas in the second stage the bubble base moves away from the orifice, while the bubble itself remains in contact with the orifice through a neck as shown in Figure 6.3. The first stage is assumed to end when the net downward force (i.e., the sum of the viscous drag force, the surface tension force, and the inertial force) is equal to the upward force, namely, the buoyancy force, so that Newton's second law of motion is used as follows:

$$V_{fb}\, \Delta\rho\, g = \frac{d}{dt_e}(M v_e) \qquad (186)$$

where:

$$M = \left[\rho_g + \frac{11}{16}\rho_l\right] Q t_e \tag{187}$$

$$v_e = \frac{dr}{dt_e} = \frac{Q}{4\pi r^2} \tag{188}$$

and V_{fb} is the bubble volume at the end of first stage of bubble formation; t_c is the time at the end of the first stage. By solving Equations (186)-(188) with the assumption of negligible gas density, the bubble volume at the end of the expansion stage ($t = t_c$) is expressed as:

$$V_{fb} = 0.160 \frac{Q^{6/5}}{g^{3/5}} \tag{189}$$

The equation during the second stage is the same as Equation (184) with initial conditions: $t = 0$, $r = s = r_{fb}$, $V_b = V_{fb}$, $ds/dt = dr/dt = v_e$. The end of the detachment stage is assumed when the length of the bubble neck is equal to the radius of the bubble from the first stage, r_{fb}, i.e., $t = t_c$, $s = r + r_{fb}$, so that the subsequent expanding bubble does not coalescence with it. With some simplifications and approximate treatment, the final bubble volume is expressed as:

$$V_b = 0.976 \frac{Q^{6/5}}{g^{3/5}} \tag{190}$$

In order to account the effect of deformed bubble base at the orifice plate, a modified version of Davidson and Schuler's model was proposed by Wraith[48], where the formation of a bubble at a plate orifice submerged in an inviscid liquid consists of two stages. The first stage corresponds to the growth of a hemispherical bubble pressed to the plate by the inertial force generated at the expanding bubble surface. The equilibrium equation for the expanding hemisphere (the end of the first stage) can be established at once by setting equal to zero the sum of the reactive force, F_{Nozzle}, due to the plate. By potential theory the bubble volume at the end of the first stage is expressed as:

$$V_h = 0.194 \frac{Q^{6/5}}{g^{3/5}} \tag{191}$$

Since the 'centre of mass' of a hemisphere is located at a polar height $(3/8)r_h$ above the base, the equation during the second stage is also the same as Equation (184) with initial conditions, $t = t_h$, $s = (3/8)r_h$, $ds/dt = (3/8)dr_h/dt$ and $V_b = V_h$. The end of the detachment stage is assumed when $t = t_c$, $s = r$. The final bubble volume is:

$$V_b = 1.090 \frac{Q^{6/5}}{g^{3/5}} \tag{192}$$

6.1.2 CONSTANT PRESSURE BUBBLE FORMATION

The formation of bubbles under constant chamber pressure is presumed in system of large capacitance as determined by Equation (182). In practice this corresponds to a system with a subnozzle gas chamber more than about a litre in volume[37]. The bubble volume under constant pressure conditions can still be determined by means of force balance similar to the case of a constant flow system, provided the gas flow rate, Q, is related to the steady chamber pressure P_c, through the so-called orifice equation:

$$Q = \frac{dV_b}{dt} = K_o \left[P_c - \rho_l g (H-s) - \frac{2\sigma}{r} \right]^{1/2} \tag{193}$$

where K_o is the orifice constant, determined experimentally for a steady-state flow of gas through the orifice in the absence of the liquid phase, H the depth of liquid and s the displacement of bubble centre from orifice plate. By solving Equation (184) and Equation (193) numerically with different initial conditions and different detachment conditions for varies models in Figure 6.3, the bubble volume is predicted.

In the one stage diffusion source model of Davidson and Schuler[44], Equation (184) and (193) are solved simultaneously under the following initial conditions at $t = 0$:

$$s = 0, \quad \frac{ds}{dt} = 0, \quad V_b = \frac{4}{3}\pi r_o^3 \tag{194}$$

The bubble is assumed to detach when $s = r + r_o$.

In Satyanarayan, Kumar and Kuloor's [50] two-stage model, the procedure is the same as constant flow condition of Kumar and Kuloor's model[47]. During the expansion stage, Equation (193) can be used to predict the bubble growth with time. The termination of the expansion stage is when the sum of the reactive force, F_{Nozzle}, due to the orifice is equal to zero, that is the force balance Equation (186) is applied. During the detachment stage, Equations (184) and (193) can be solved simultaneously under the following initial conditions:

$$t = t_e, \quad r = r_e, \quad \frac{dr}{dt} = \frac{ds}{dt} = \frac{dr}{dt_e}, \quad s = r_e \tag{195}$$

The detachment condition is the same as the constant flow model of Kumar and Kuloor[47].

Lanauze and Harris[51] developed a two-stage model to describe the bubble formation under the constant pressure conditions, as shown in Figure 6.3. In their model, during the first stage the spherical segment of bubble which is above the plane of the orifice was considered. The upward motion of the bubble centre was determined by a balance between buoyancy and inertia, which was the same as Davidson and Schuler's treatment, except that the spherical segment was considered in the equations for the bubble volume, surface tension pressure, etc. The end of the first stage was assumed to happen when $s=r$. During the second stage, which was the same as the procedure of Satyanarayan, Kumar and Kuloor[50], the upward motion of spherical bubble was described by solving simultaneously Equations (184) and (193), the detachment condition was experimentally found as $s = r + r_o$.

6.1.3 BUBBLE FORMATION UNDER UNSTEADY CONDITIONS

Bubble formation at a submerged orifice can in practice occur under conditions where both gas flow rate and chamber pressure are unsteady, for instance, where the chamber volume is small but the orifice constant is relatively large. Khurana and Kumar[52] considered that the bubble was formed in the same two stages as under the constant flow condition and the constant pressure condition. At the end of the first stage, a force balance equation was obtained by equating the buoyancy force with the sum of the inertial, surface tension and viscous drag forces:

$$\rho_l V_b g = \frac{d(M v_e)}{dt} + 2\pi r_o \sigma \, Cos(\theta_c) + C_d \pi r^2 \frac{(\rho_l v_e^2)}{2} \tag{196}$$

Where M and v_e are expressed in Equations (187) and (188); C_d is the drag coefficient. During the second stage bubble growth, Newton's second motion law is applied, i.e.,

$$\frac{d(Mv)}{dt} = \rho_l V_b g - C_d \pi r^2 \frac{\rho_l v^2}{2} \tag{197}$$

where v is the upward motion velocity of the bubble. The bubble detaches at $s = r + r_{fb}$.

Kupferberg and Jameson[53] developed a two stage model based on the orifice equation:

$$Q = \frac{dV_b}{dt} = K_o (P_c - P_b) \tag{198}$$

The chamber pressure equation was obtained by assuming adiabatic gas behaviour:

$$P_c = (P_c)_0 + \frac{\rho_l C^2}{V_c}(V_b - V_o - Qt) \tag{199}$$

and the bubble pressure equation was derived from potential theory:

$$P_b = P_{atm} + \rho_l \left[g(H-s) + r\frac{d^2 r}{dt^2} + \frac{3}{2}\left[\frac{dr}{dt}\right]^2 \right] + \frac{2\sigma}{r} \tag{200}$$

in which $(P_c)_o$ is the initial chamber pressure and P_{atm} the atmospheric pressure. During the first stage (growing stage) the net force calculated by the pressure distribution around the bubble acts downwards causing a reaction on the surface of the plate and since the bubble is in direct contact with the plate during this stage, s is equal to r. The condition for the termination of the growing stage is that the net force acting on the bubble equals to zero. For the second stage (elongating stage) the buoyancy force and inertial reaction are in equilibrium but $s > r$. Obviously, Kupferberg and Jameson's bubble formation mechanism is similar to that of Kumar and Kuloor[47] as shown in Figure 6.3.

Based on the same model as (Model IV in Figure 6.3) in the constant pressure condition, Lanauze and Harris[55] employed the motion equation (Equation (184)), orifice equation (Equation (198)) and the chamber pressure equation (Equation (199)) to describe the bubble formation under elevated system pressure.

Similar to Kupferberg and Jameson's model, a two-stage model (Model II of Figure 6.3) was proposed by Tsuge and Hibino[56]. In their model, the chamber pressure is expressed as:

$$\frac{dP_c}{dt} = \frac{\gamma P_c}{V_c}(Q_g - Q_o) \tag{201}$$

where γ is the specific heat ratio. During the expansion stage, Equations (198), (200) and (201) are solved simultaneously under the initial conditions,

$$r=r_o, \quad \frac{dr}{dt}=0, \quad P_c=P_{atm} + \rho_l g H + \frac{2\sigma}{r_o} \tag{202}$$

The termination of the expansion stage is when the force balance equation similar to Equation (184) holds. In the detachment stage, Equations (184), (198), (200) and (201), are solved simultaneously under the following initial conditions:

$$r = s = r_e, \quad \frac{dr}{dt} = \frac{ds}{dt} = \frac{dr}{dt_e}, \quad P_c=(P_c)_e \tag{203}$$

The detachment condition is when the length of bubble neck equals to the diameter of the orifice, $s = r + 2r_o$, which is different from that of Kumar and Kuloor's model.

6.2 NON-SPHERICAL BUBBLE FORMATION MODELS

All of the spherical bubble formation models have been forced to use an empirical or semi-empirical criterion for determining the instant of detachment. However, the bubble is not spherical during its formation and the moment of the detachment is determined by the varies of the bubble shape. A non-spherical bubble formation model was first proposed by Marmur and Rubin[59] for predicting continuously the instantaneous shape of bubble during its growth, using simplified equations of motion for the liquid, and thermodynamic relationships for the gas in the bubble and the chamber volume. For such a model, there is no need for a two stage formation mechanism nor for an empirical detachment criteria, because the instant of detachment comes out naturally as the time when the neck, which develops during the formation, attains zero width. Liow and Gray[61] modified the Marmur and Rubin's model to describe the bubble formation in wetting and non-wetting liquids.

6.3 BUBBLE FORMATION AT A MULTI-ORIFICE PLATE

The bubble formation at a multi-orifice plate is more complicated than at a single orifice. The system comes to an equilibrium between the mean pressure drop across the orifice, the bubble frequency, f_b, the pressure fluctuation frequency, f_p, the bubble size and the number of holes bubbling per pressure cycle (f_b/f_p). Kupferberg and Jameson[65] assumed that the bubbles were uniform in size and that there was negligible interaction between neighbouring bubbles during formation. Furthermore, they assumed that the mean diameter of bubbles formed on the multi-orifice plate was the same as that the bubbles formed at a single orifice above a gas chamber of volume $V_c/(f_b/f_p)$ by a gas rate of $Q/(f_b/f_p)$. The major unknown in this model was the relationship between the bubbling frequency and the pressure fluctuation frequency. Titomanlio, Rizzo and Acierno[66] pointed out that for bubbles growing from a multiple-orifice plate feed from a single chamber, the orifice plate works discontinuously at low gas flow rates and as the number of the orifices increases "simultaneous bubbling" becomes more difficult. They carried out experimental research for gas bubble formation in water from a two-orifice plate. They concluded that the volume of bubbles outcoming from a single orifice approximated that of simultaneous bubbles growing from a chamber which had double the capacitance and was fed by double the flow rate.

Miyahara, Matsuba and Takahashi[67] investigated experimentally the size of the bubbles in bubble column, which was generated from perforated plates. They showed that the size of the bubbles formed at a single orifice is strongly influenced by the gas-chamber volume, but this effect weakens as the number of holes is increased, and disappears when there are more than 15 holes. For conditions in which the chamber volume has no effect on the bubble size, the behaviour depends on whether the ratio of the pitch to the hole diameter is above or below eight.

Spells and Bakowski[42] studied experimentally the bubble formation at a single slot submerged vertically in water. In their research, the slot widths varied between 2 and 10 mm. They pointed out that the phenomenon of bubbling of air through a slot submerged vertically in water might be regarded as being a periodic one, with irregularities superimposed. Hobler and Pawelczyk[68] investigated the interfacial area in bubbling through a slot. Recently, the gas injection phenomenon through a narrow, submerged horizontal slot mounted in a vertical wall was studied by Kozlowski and Wraith[69].

6.4 BUBBLE FORMATION IN LIQUID METALS

A number of studies have been carried out on bubble formation in liquid metals. Sano et al.[70,71,72,73] employed curved tubes of silica, alumina and glass as free-standing nozzles in liquid metal. By injecting air into mercury and into molten silver, argon into molten iron and nitrogen into mercury, they obtained the bubble size by bubble frequency measurements and concluded that the correlations for bubble volume in aqueous systems were generally valid for liquid metals provided the outer diameter of the nozzle was substituted for the inner diameter to account for the non-wettability of liquid metal. Andreini, Foster and Callen[74] bubbled argon into tin, lead and copper melts under conditions of constant pressure and orifice laminar flow, using quartz capillary tubes set at 30 deg to the horizontal. The bubble size was determined from the frequency of noise generated by bubble expansion.

Guthrie et. al.[75,76,77] used X-ray cinematographic techniques and bubble frequency measurements to study the bubbling of inert gases into molten metals. In the injection of argon into pig iron, they employed higher flow rates, orifice sizes, chamber volumes and nozzle submergence than Sano's, but the results still confirmed the earlier observations, i.e., bubble formation in liquid metals was based on the outer diameter of the nonwetted nozzle. It was found that the bubble size was uniform at low gas flow rates but increased with increasing gas flow rate beyond a critical range, that the bubble size in liquid metal depended strongly on the Capacitance Number. The experimental results were confirmed by mathematical model predictions of Liow and Gray[61] for bottom injection, which took both slip and contact angle of the bubble into consideration.

Hoefele and Brimacombe[78] injected air, argon and helium through a horizontal tuyere into mercury at even higher flow rates, up to 3000 cm^3/s. The bubble volume was measured by a high speed cinematography, made possible by a 'half-tuyere' arrangement, and found to be marginally higher than corresponding measurements in water and zinc chloride solution but still in agreement with the Davidson and Schuler equation (Equation (185)), but with coefficient 1.57 instead of coefficient 1.378 for liquid metals.

6.5 DISCUSSION ON BUBBLE FORMATION MODELS

Basically, there are four different geometrical models for the spherical bubble formation models, as shown in Figure 6.3. Among them, Model II and III are similar, since in these the termination of the first stage is when the net force acting on the bubble equals zero (the force balance equation between the buoyancy force and inertia, viscous forces etc. can be used only at the end of the first stage), and during second stage the spherical bubble moves upward a certain distance before detachment. Therefore, rather similar expressions for the bubble volume (Equation (190) and Equation (192)) were obtained. Strictly, Equation (190) expresses the bubble volume at detachment after the base of bubble moves upward some distance (r_{fb}) and Equation (192) represents the bubble volume when the base of the bubble is in tangential contact with the orifice, as shown in Figure 6.3. If the neck length defined in Model II of Figure 6.3 was considered in the Wraith's theory, the bubble volume predicted using Wraith's geometrical assumption would be much larger than that of either Davidson and Schuler's model (Equation (185)) or Kumar and Kuloor's model (Equation (190)). From this point of view, it is worth noting that although Equation (192) is almost the same as Equation (190), and that both Equations

(190) and (192) are widely used to predict the bubble volume under constant flow conditions, the models developed by Kumar and Kuloor and by Wraith are different in concept.

As mentioned before, Davidson and Schuler's model has been accepted by many investigators, and close prediction of experimental results has been seen, even though an improbable physical model (Model I of Figure 6.3) was used. Such agreement arises because the single stage bubble formation used by Davidson and Schuler is similar to the second stage in two-stage models[47,48], and because the bubble volume at the end of the first stage in two-stage models (Equation (189)) is too small in comparison with the final bubble volume (Equations (190) and (192)).

In response to the literature, Lanauze et al.[79] believed that the net force acting on the bubble due to the buoyancy, inertia etc. is always zero during bubble growth and the end of the first stage is when the base of bubble is in tangential contact with the orifice plate. Lanauze et al. thought that Kumar and Kuloor's model was not correct since Kumar and Kuloor used the so called force balance equation at, and only at, the end of the first stage of bubble formation. In fact, Lanauze et al. may have misinterpreted Kumar and Kuloor's model since this model is really a dynamic growth model, i.e., at each moment, the forces acting on bubble are in balance. This includes the period of the first stage of bubble growth. The force acting on the bubble due to the orifice plate is larger than zero during first stage and is equal to zero at the end of the first stage. To help explain this, imagine that there is a uninflated balloon on a desk. The balloon doesn't rise because the upward force, i.e. buoyancy force acting on the balloon is much smaller than the downward force, i.e. gravity on the balloon. Although the gravity force is not balanced by the buoyancy, you cannot say that the balloon is not in force balance since there is an upward force acting on the balloon due to the desk. If helium is introduced into the balloon, the balloon expands gradually so that the buoyancy force acting on the balloon increases. Once the buoyancy force overcomes the gravity force, the balloon will rise. A similar phenomenon is at play when a bubble grows from a nozzle.

Lanauze et al. also pointed out that Kumar and Kuloor's model cannot be used to evaluate the bubble growth as a function of time. In fact, in Kumar and Kuloor's model the bubble growth can be evaluated by $V_b = Q^*t$ under constant flow conditions and by the related pressure equation under non-constant flow conditions. Lanauze et al's model[51], in which the end of the first stage of bubble growth was assumed to be when the base of bubble tangential contact with the orifice plate, is physically fallacious because the bubble base never reaches tangential contact with the orifice plate in practice due to the surface tension.

In conclusion, the mechanism of bubble formation proposed by Kumar and Kuloor (Model II of Figure 6.3) is reasonable except for the assumption of the detachment condition is when the base of the bubble has moved a distance equal to the bubble radius (r_{fb}) at lift-off. Many experimental studies have shown that the length of the bubble neck lies between the values of the orifice radius and the orifice diameter[48,53,55,56] . Thus, Kumar and Kuloor's model must be modified by considering the observed detachment condition.

For non-spherical bubble formation model, the main assumptions are that the pressure inside the bubble is uniform and the liquid pressure around the bubble is calculated by potential theory. Also the Bernoulli's equation doesn't account the time derivatives of potential function. They cannot be used to predict the bubble formation in viscid liquid. Although the non-spherical models can provide a better understanding of the bubble formation and can give better results in comparison with spherical models for the inviscous liquid since the moment of the detachment comes out naturally as the time when the neck attains zero width, they need complicated numerical calculation method such as finite difference.

6.6 CONCLUSIONS

1. Further research for bubble formation in a single orifice is required, particularly for the viscous liquid and liquid metals.

2. Since almost no research was done on the bubble formation in a multi-orifice or very narrow slot-shaped nozzle, any studies concerning the bubble formation and coalescence between bubbles at adjacent holes are interesting and important both from theoretical and practical points of view.

3. The note on bubble formation models by Lanauze et al. is incorrect.

4. The bubble formation mechanism of Kumar and Kuloor is reasonable except for the assumption of the detachment. The bubble formation models developed by Kumar et al. and by Wraith are different in concept although they give quite close expressions in the final bubble volume for the bubble formation dominated by inertial force.

CHAPTER 7

MODIFIED BUBBLE FORMATION MODEL WITH SURFACE TENSION AND INERTIAL FORCES

As concluded on page 93, although the mechanism of the bubble formation proposed by Kumar and Kuloor is reasonable, an improper detachment condition is used. In this chapter, a modified bubble formation model is proposed by considering a new detachment condition. In this model both surface tension force and inertia are considered.

Bubble formation under constant flow conditions is dominated by the surface tension force at extremely small flow rates (Equation (183)) and by the inertial force at higher flow rates. Between these two extremes is a range of flow rate where neither the inertial force nor the surface tension force can be neglected and the final bubble volume is highly sensitive to both. Similar to Kumar and Kuloor's two-stage model[47] of bubble formation dominated by inertia, i.e. Equation (186), the condition for the end of the first stage for bubble formation dominated by both inertial and surface tension forces can be expressed as:

$$V_{fb} \Delta \rho g = \frac{d}{dt_e}(M v_e) + 2 \pi r_o \sigma \cos(\theta_c) \tag{204}$$

Evaluation of Equation (204) by considering Equations (187) and (188) gives:

$$V_{fb} - 0.0474 \frac{Q^2}{g} V_{fb}^{-2/3} = \frac{2 \pi r_o \sigma \cos(\theta_c)}{\rho_l g} \tag{205}$$

The equation for the second stage of bubble growth is similar to Equation (184) except the surface tension term has been included, i.e.:

$$V_b \Delta \rho g = \frac{d}{dt}\left[V_b\left[\rho_g + \frac{11}{16}\rho_l\right]\frac{ds}{dt}\right] + 2\pi r_0 \sigma \cos(\theta_c) \tag{206}$$

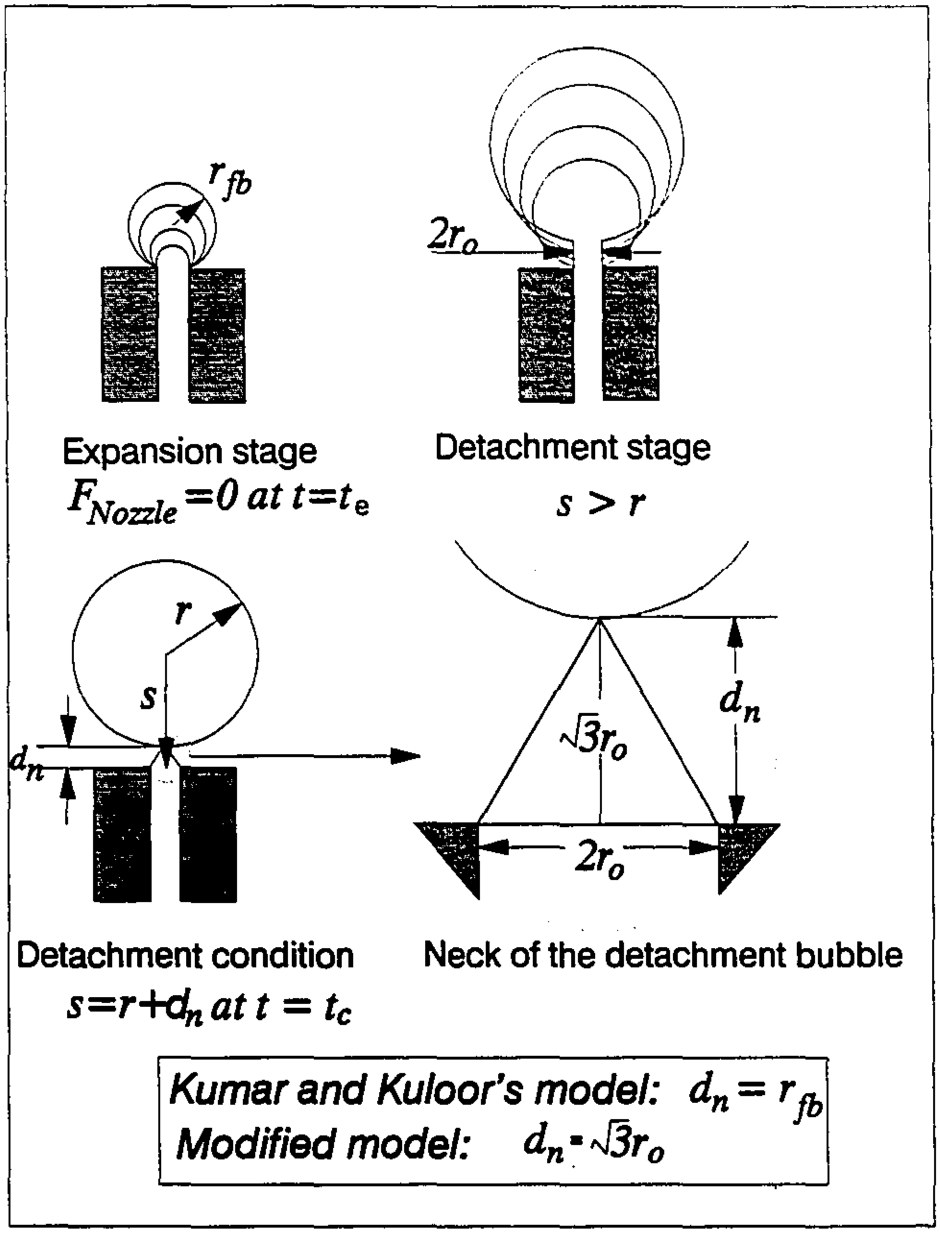

Figure 7.1 Geometrical assumption of modified bubble formation model.

The initial conditions for the second stage are: $t = 0$, $V_b = V_{fb}$, $r = s = r_{fb}$, $ds/dt = dr/dt = v_e$. If the end of the detachment stage is assumed to be when the length of the bubble neck is equal to d_n (Figure 7.1), i.e. $t = t_c$, $s = r + d_n$, the following expression for the final bubble volume can be obtained by the same mathematical procedure as used by Kumar and Kuloor[47].

$$
\begin{aligned}
d_n = {} & \frac{4g}{11Q^2}\left(V_f^2 - V_{fb}^2\right) - 0.62\left(V_f^{1/3} - V_{fb}^{1/3}\right) - \frac{32\pi r_o \sigma \cos(\theta_c)}{11 Q^2 \rho_l}\left(V_f - V_{fb}\right) \\
& + \frac{1}{Q}\left[\left\{\frac{32\pi r_o \sigma \cos(\theta_c)}{11 Q \rho_l} V_{fb} + 0.207\, Q\, V_{fb}^{1/3} - \frac{8g}{11Q} V_{fb}^2\right\}\right] \ln\left[\frac{V_f}{V_{fb}}\right]
\end{aligned}
\tag{207}
$$

Employing commercial software, TK-solver (see Appendix III), Equations (205) and (207) were simultaneously solved. It is obvious that if the neck length, d_n, is assumed to be equal to the bubble radius at the end of the first stage, Equation (207) is the expression of Kumar and Kuloor[37]. In our present analysis, d_n, is assumed to be $\sqrt{3}r_o$, by which the neck of the bubble looks like an equilateral triangle as shown in Figure 7.1. Obviously, $\sqrt{3}r_o$ lies between the orifice radius (r_o) and the orifice diameter ($2r_o$), which is consistent with experiment.

Figure 7.2 presents the predicted bubble volumes for various orifice diameters for water-air system using Kumar and Kuloor's model ($d_n = r_{fb}$) and the modified model ($d_n = \sqrt{3}r_o$). Kumar and Kuloor's model and the modified model give quite close predictions of bubble volumes for the orifice diameters between 0.5 and 2cm but result in a significant difference in the prediction of bubble volumes for very small orifice diameters (e.g. 0.01cm). As shown later, Kumar and Kuloor's model greatly overestimates the bubble volume for very small orifice sizes, because the neck length used by Kumar and Kuloor (r_{fb}) would be much larger than the diameter of orifice for small orifices. As mentioned before, many experimental studies have shown that the length of bubble neck is between the orifice radius and the orifice diameter. Thus, the modified model is expected to be reliable. Since most of the experimental work has been done for orifice diameters between 0.5 and 2 cm, it is to be anticipated that Kumar and Kuloor's model would give close predictions to the experimental data although an incorrect detachment condition was used in their model.

Figure 7.2 shows that at high flow rates where inertial force dominates bubble formation, Kumar and Kuloor's model converges for different orifice diameters. Since neck length depends on orifice size, different bubble sizes are predicted by the present modified

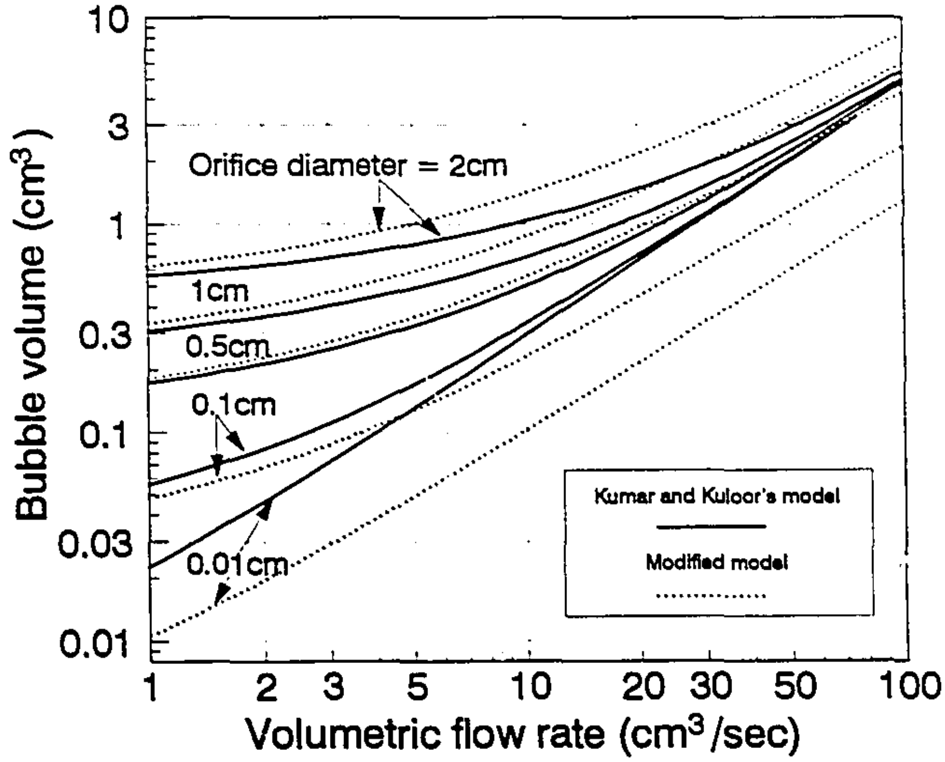

Figure 7.2 The comparison between Kumar and Kuloor's model and modified model for bubble formation dominated by both inertial and surface tension forces.

model even though inertial force dominates bubble formation. This was confirmed by the present experiments as shown in the next chapter. At very high flow rates, the bubble size predicted by the modified model becomes also independent of the size of the orifice because the neck of the bubble plays less role at very high flow rate.

CHAPTER 8

GAS INJECTION PHENOMENA THROUGH A VERY NARROW SLOT: EXPERIMENTAL

The apparatus employed for the study of bubble formation from a slot-shaped nozzle is illustrated schematically in Figure 8.1. It consisted of a square plexiglas vessel, containing deionized water or methyl alcohol at a fixed temperature (T = 20°C), a slot-shaped nozzle, a gas delivery system to supply compressed air and helium to the nozzle and a measuring and controlling system.

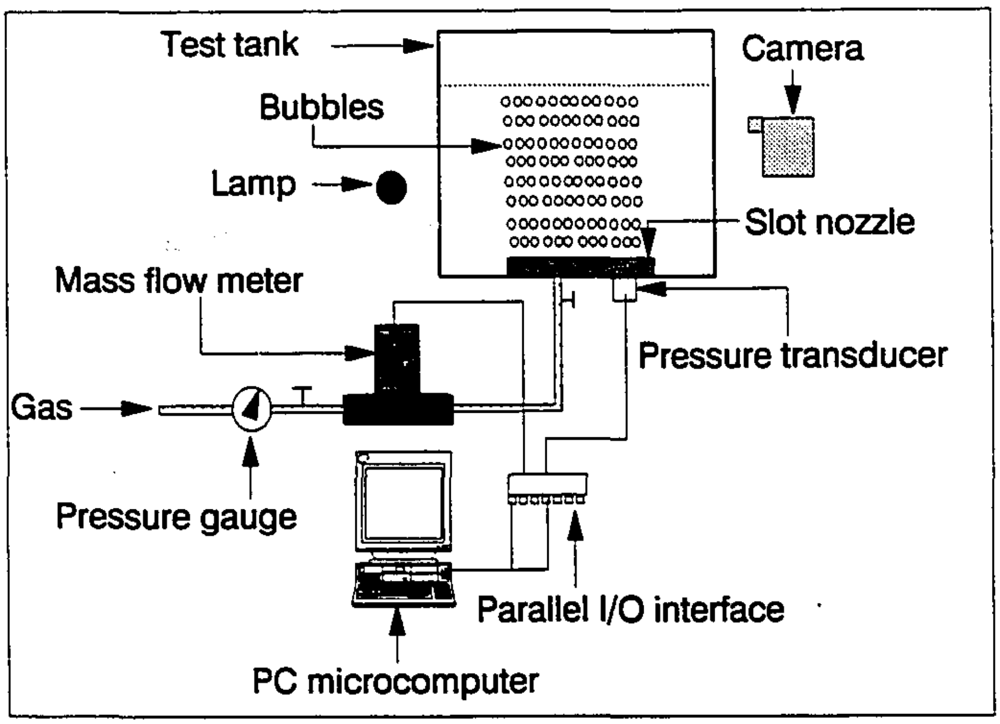

Figure 8.1 Schematic representation of the experimental system.

The flow rates of air or helium were measured by a mass flow meter with a range of 0-100 slpm at high gas flow rates and by two variable area flow meters with ranges of 0-1 slpm and 0-25 slpm at low gas flow rates. The pressure inside the nozzle chamber was measured by a pressure transducer.

Figure 8.2 Photograph of the stainless steel slot-nozzle.

Figure 8.2 is the photograph of the stainless steel slot-nozzle. Figure 8.3 presents the side view of the nozzle. Figure 8.4 shows the configuration of the slot-shaped nozzle. It consisted of two smooth stainless steel plates (2.54 cm in thickness). A sheet of thin (50-250μm) U-shaped polyester film was put between two stainless steel plates to make the slot. Thus, slot width was adjustable using different thicknesses of film.

Table 8.1 Some Related Experimental Parameters

L (cm)	W (μm)	V_c (mm^3)	h (cm)	H (cm)	T (K)
19.05	50-250	200	2	16	293

The dimensions of the slot and the experimental conditions are shown in Table 8.1, in which L is the length of the slot, W the slot width, h the length of the gas flow path within the slot nozzle, H the depth of liquid and T the temperature of the bath. Obviously, h is much larger than the slot spacing, W.

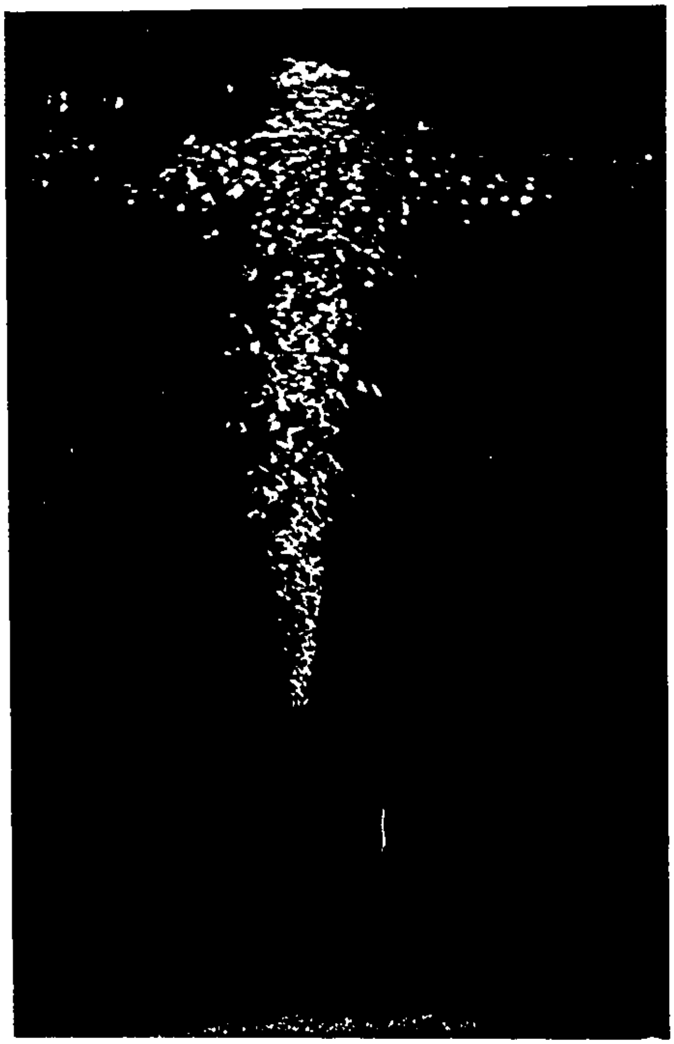

Figure 8.3 Side view of the slot-nozzle.

Gas was introduced into the slot through one side of the nozzle and, came out as individual bubbles along the top of the slot due to the Rayleigh-Taylor instability. The bubble formation was recorded by a high speed camera and/or a still frame camera. In order to measure the number of bubbles and the bubble size, negative black and white Kodak-Tmax professional films were used to record the bubble formation phenomena with an exposure time = 1/1000 sec using a still frame camera. After processing the films, slides were made so that high magnification (8 to 10) was achieved. The slides were then used to measure the number of bubbles and bubble volumes.

As summarized in Table 6.1, a number of system and operating variables affect the bubble formation from a nozzle. In the present research, small chamber volume of the slot-shaped nozzle (200 mm^3) and high pressure drop across nozzle were maintained so that the bubble formation could be considered as a constant flow condition. In order to investigate the effects of the densities and surface tensions of liquid and gas on the bubble formation, water and methyl alcohol were used as liquids and air and helium were used as gases.

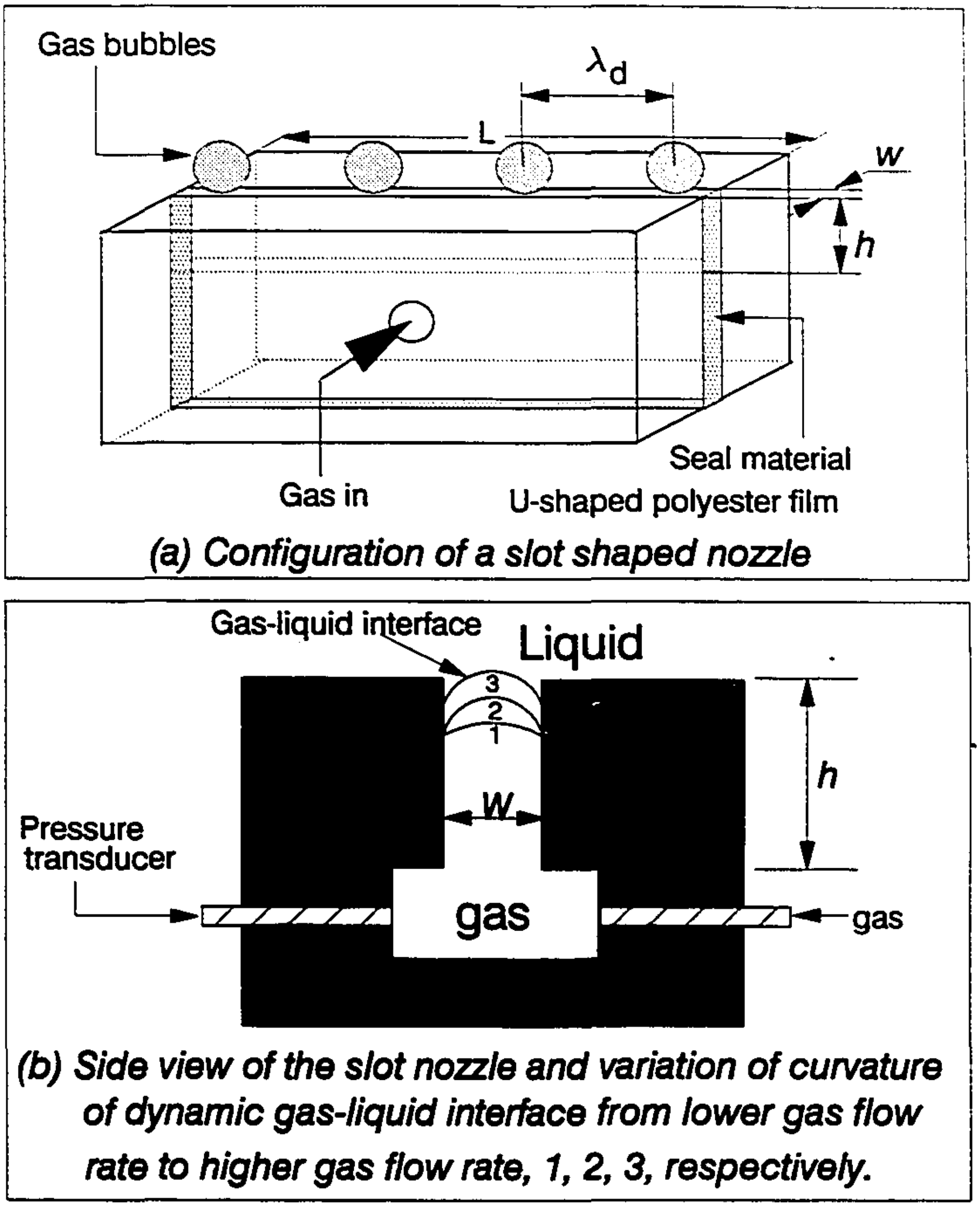

(a) Configuration of a slot shaped nozzle

(b) Side view of the slot nozzle and variation of curvature of dynamic gas-liquid interface from lower gas flow rate to higher gas flow rate, 1, 2, 3, respectively.

Figure 8.4 Configuration of a slot shaped nozzle and gas-liquid interface.

During experiments the slot width was changed from 50μm to 250μm while the length of the slot (L), the depth of the slot (h) and the liquid depth above the nozzle top surface (H)

were kept constant. Table 8.2 gives the experimental conditions.

Table 8.2 Experimental Conditions for Gas Injection Phenomena from a Slot Nozzle

Exp. No.	Slot Width, W (μm)	Gas	Liquid
1	125	Air	Water
2	125	Helium	Water
3	75	Air	Water
4	75	Helium	Water
5	75	Air	Methyl Alcohol
6	50	Air	Water
7	50	Air	Methyl Alcohol
8	50	Helium	Methyl Alcohol
9	250	Helium	Water
10	250	Air	Methyl Alcohol
11	250	Helium	Methyl Alcohol
12	175	Air	Methyl Alcohol
13	175	Helium	Methyl Alcohol
14	175	Air	Water
15	175	Helium	Water

Table 8.3 lists the properties of liquids and gases. Methyl alcohol, water, air and helium have very low viscosities so that the drag forces can be neglected during the analysis of the bubble formation. The surface tension of methyl alcohol is only one third of that of water. The density of air is seven times of that of helium. Consequently, the present liquid-gas system gives widely-distributed physical properties. However, no attempts were made to study the effects of viscosity and contact angle on the bubble

formation.

Table 8.3 Physical Properties of Liquids and Gases[80]

	Water	Methyl Alcohol	Air	Helium
Density (Kg/m^3)	1000	787	1.29	0.178
Surface tension (dyn/cm)*	72	23		
Viscosity (Kg/m/s)	1×10^{-3}	0.597×10^{-3}	2×10^{-5}	2×10^{-5}

When gas was injected into liquid through a slot-shaped nozzle, as the flow rate of gas was increased, three different bubbling regimes were found. They were: *regular bubble regime* at low flow rates, *coalescence bubble regime* at medium flow rates, and *gas globe regime* at high flow rates. As examples, Figure 8.5, Figure 8.6 and Figure 8.7 show the behaviour of different bubbling regimes when helium was injected into water through a $W = 125\mu m$ slot.

In the *regular bubble regime*, the regular bubbles were formed along the slot and the coalescence of the individual gas bubbles in the direction of slot was avoided as shown in Figure 8.5. The average number of sites (or bubble sources) along the slot, from which bubbles originate, increased with an increase in the gas flow rate, i.e., the distance between the bubble sources decreased with an increase of gas flow rate. Further increase of gas flow rate caused the bubble coalescence in the direction of slot before the individual bubbles detached from the nozzle. Thus, the second kind of bubble regime, i.e., *coalescence bubble regime,* was found at medium flow rates as shown in Figure 8.6. In this regime the coalescence between bubbles, which caused a considerable variation in the measured bubble radius, became significant with an increase in flow rate until finally a a continuous gas blanket extending the length of the slot[81] was reached. Because of the Rayleigh-Taylor instability of the liquid-gas interface, this blanket breaks into multiple bubbles at separate nodes with a characteristic wavelength $\lambda_{d,Taylor}$ (the distance between two nodes or two bubbles). This is the so-called *gas globe regime* at high flow rates and is

* It was found that the surface tension between liquid and helium was almost the same as that of liquid-air.

shown in Figure 8.7. As further examples, Figure 8.8-Figure 8.15 show some bubble formation phenomena in water and methyl alcohol.

In the present research, fifteen sets of experiments were done as shown in Table 8.2. For each of the experiments, the sizes of the bubbles in regular bubble regime and coalescence regime and the number of bubble sources were measured as a function of gas flow rate. The critical transformation condition between the regular bubble regime and the coalescence regime was also determined. The number of bubble sources in the regular bubble regime was measured by counting the number of bubbles inside a rectangle, the top line of which was parallel to the slot and was drawn a certain distance (i.e., 5mm) above the slot as shown in Figure 8.16. The number of the bubble sources were counted as shown in Figure 8.16.

During the determination of the bubble size, the bubbles were considered as ellipsoid with major and minor axis. The major and minor axis, a_i and b_i, of each bubble were measured, and the volumes of whole bubbles intersecting the top line of the rectangle were determined. Finally, the average bubble volume was calculated based on:

$$V_b = \frac{4\pi}{3}\frac{\Sigma a_i^2 b_i}{n_b} \tag{208}$$

The number of bubbles measured, n_b, depends on the experimental parameters (e.g., flow rate, slot spacing, liquid and gas properties) and varies from a few bubbles at low flow rates to almost a hundred bubbles at high gas flow rates. The original results for the fifteen experiments are given in Appendix II and are discussed in the next chapter.

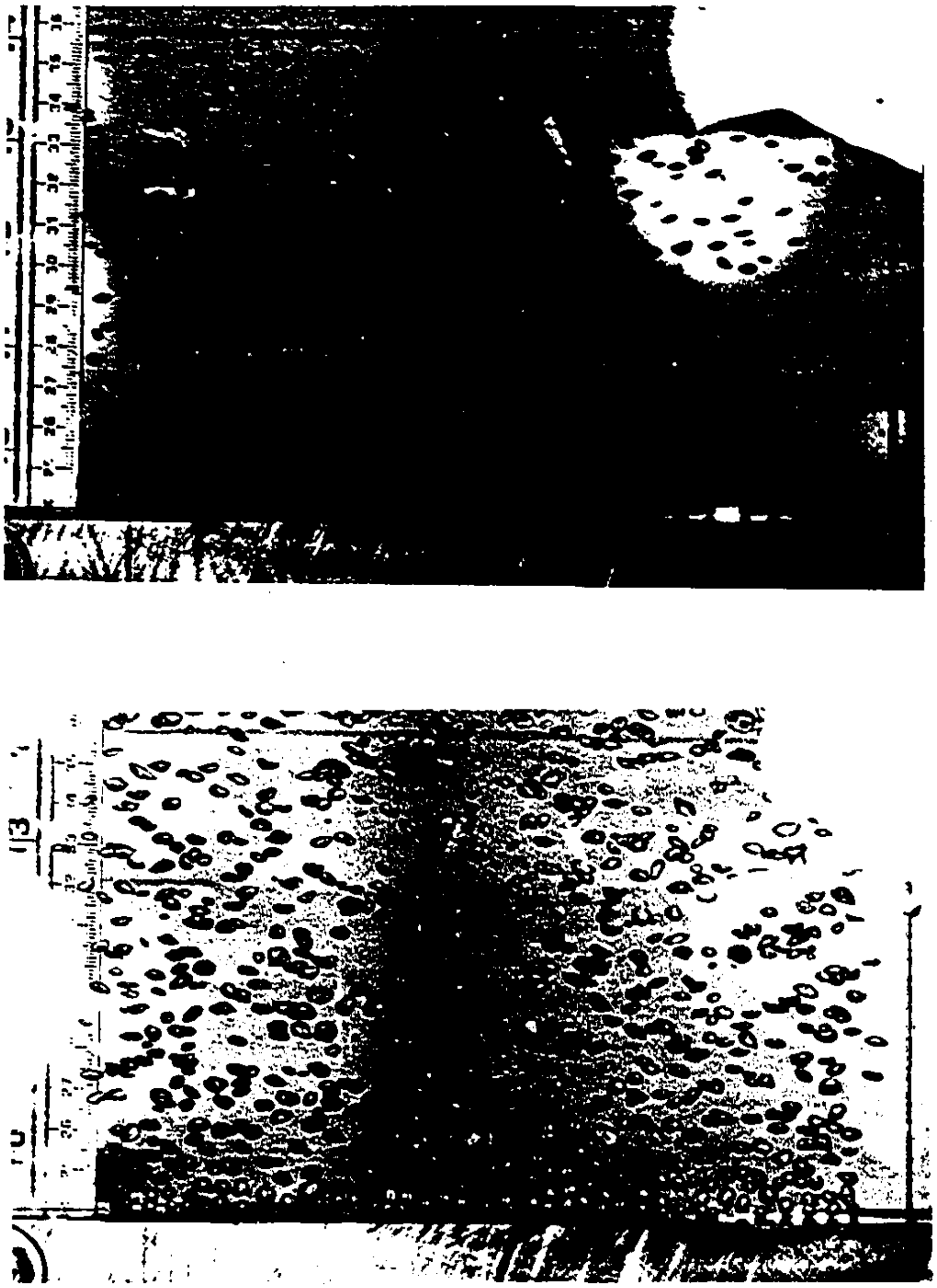

Figure 8.5 Regular bubble formation pattern when helium was injected into water through a slot with W=125μm at Q_t=1.502 slpm (top picture) and Q_t=4.575 slpm (bottom picture).

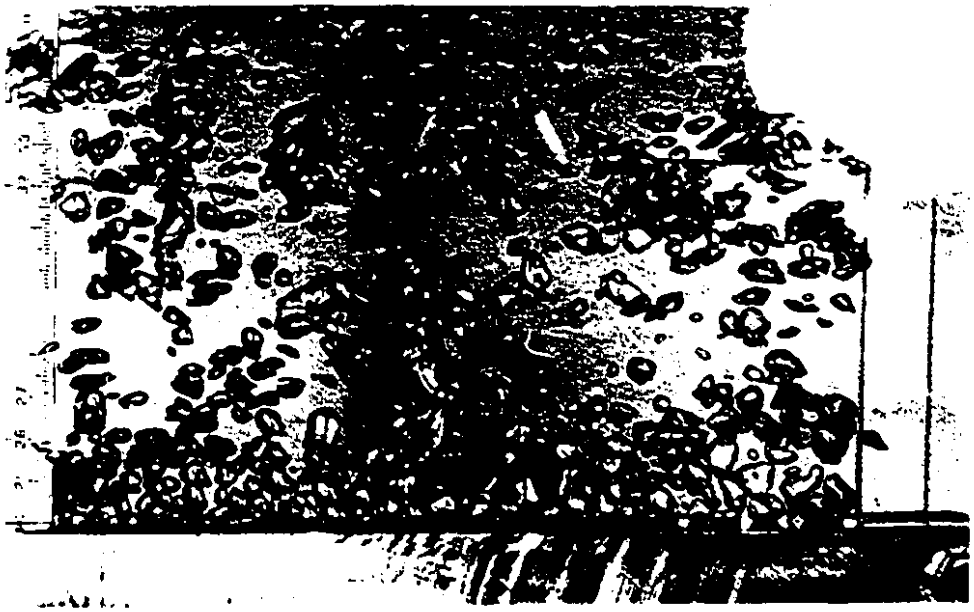

Figure 8.6 Coalescence bubble formation pattern when helium was injected into water through a slot with W=125μm at Q_t=15.16 slpm.

Figure 8.7 Gas globe formation pattern when helium was injected into water through a W=125μm slot at Q_t=65 slpm; N_{node}=5.

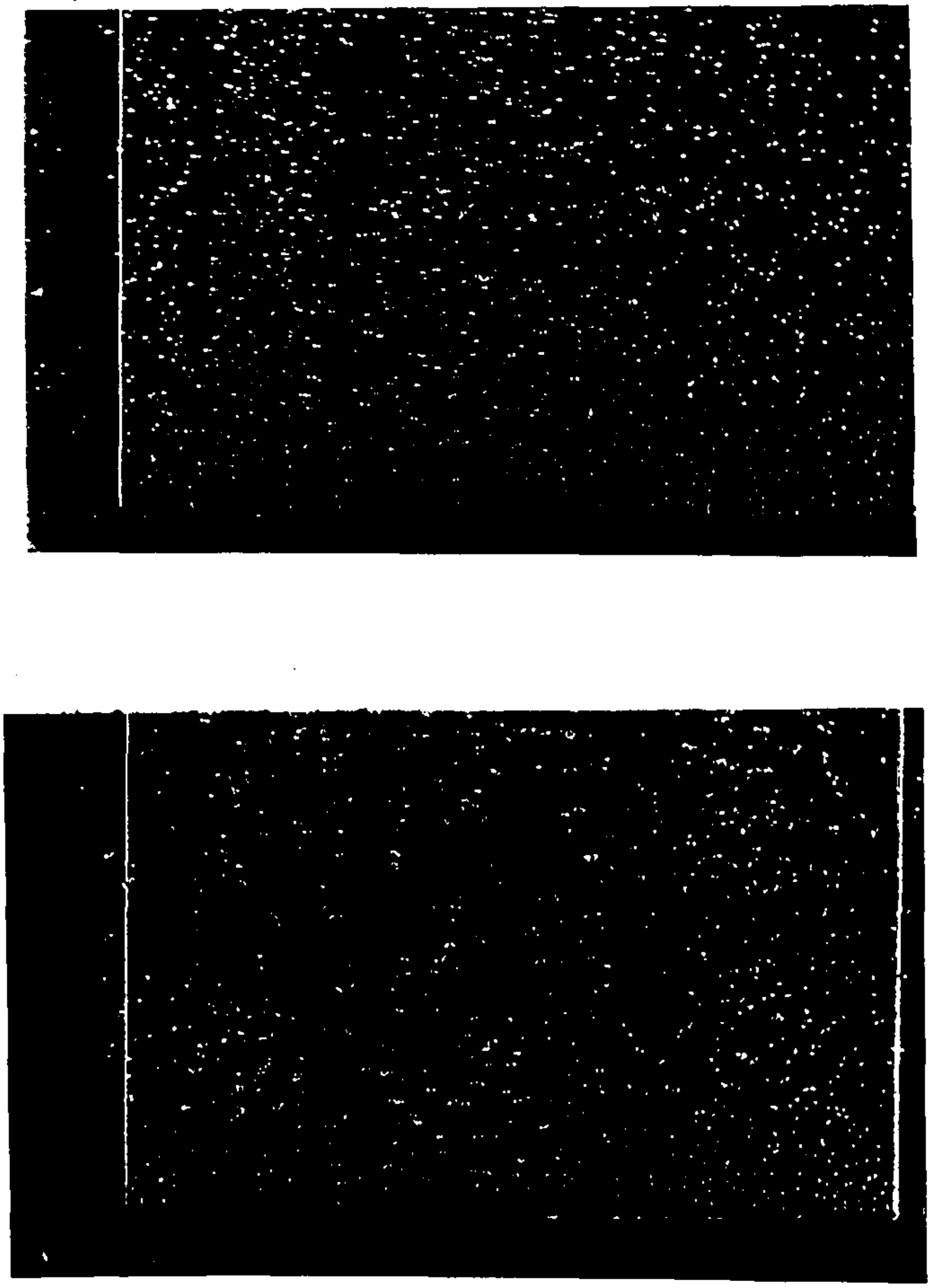

Figure 8.8 Regular bubble formation pattern when air was injected into water through a slot with W=50μm at Q_t=0.24 slpm (top picture) and Q_t=0.65 slpm (bottom picture).

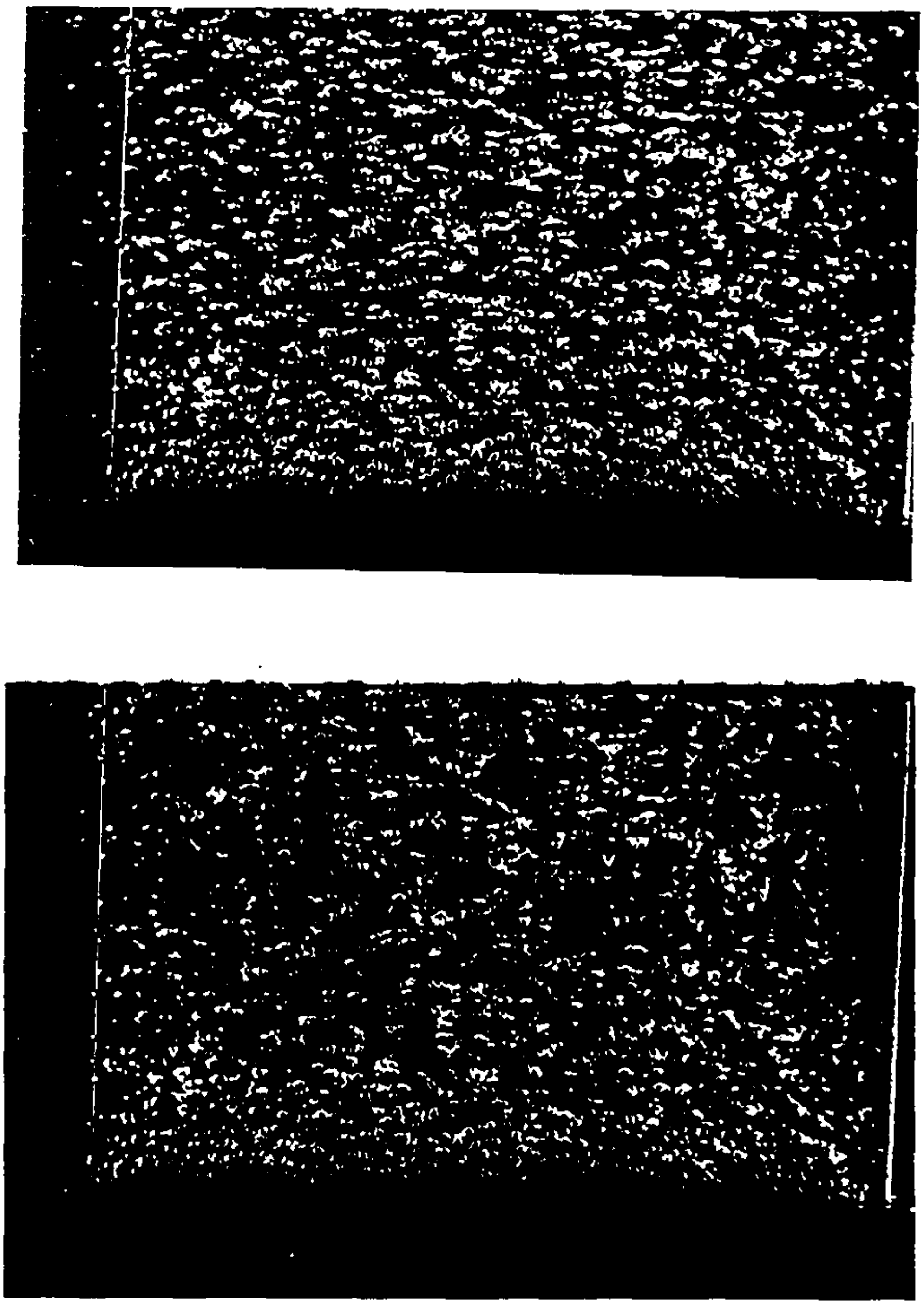

Figure 8.9 Coalescence bubble formation pattern when air was injected into water through a slot with W=50μm at Q_t=2.5 slpm (top picture) and Q_t=4 slpm (bottom picture).

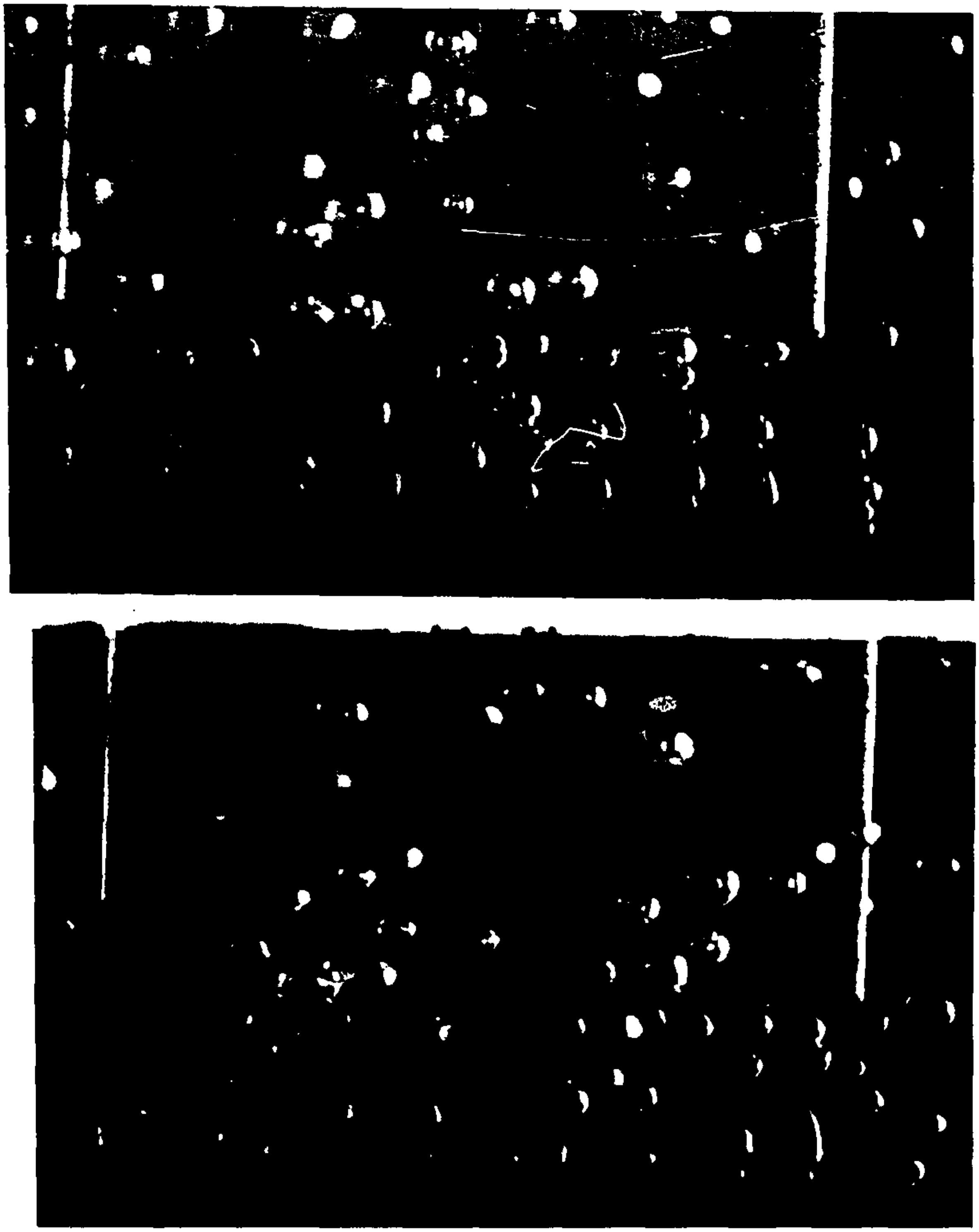

Figure 8.10 Bubble formation when air was injected into water with W=50μm at Q_t=0.65 slpm (top picture) and Q_t=0.9 slpm (bottom picture). These pictures show only a part of a slot.

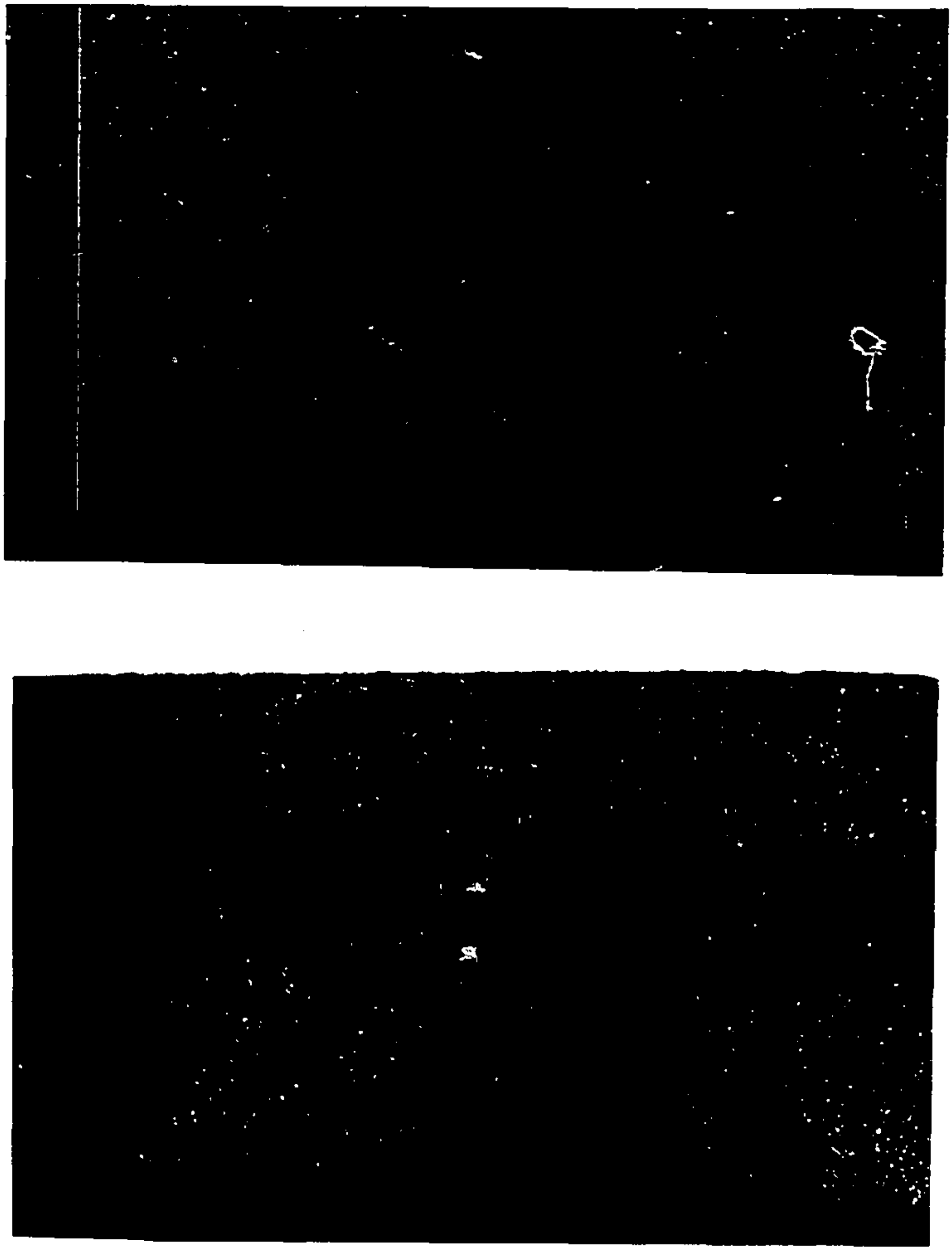

Figure 8.11 Regular bubble formation pattern when helium was injected into methyl alcohol through a slot with W=50μm at Q_t=0.07 slpm (top picture) and Q_t=0.88 slpm (bottom picture).

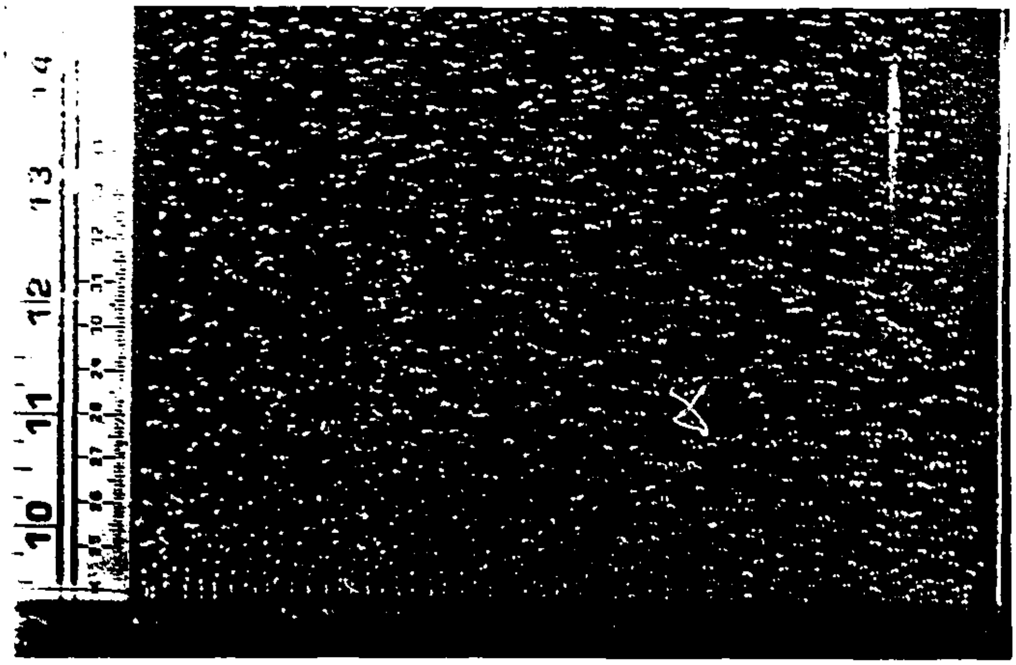

Figure 8.12 Regular bubble formation pattern when air was injected into methyl alcohol through a slot with W=75μm at Q_t=0.4slpm (top picture) and Q_t=0.8 slpm (bottom picture).

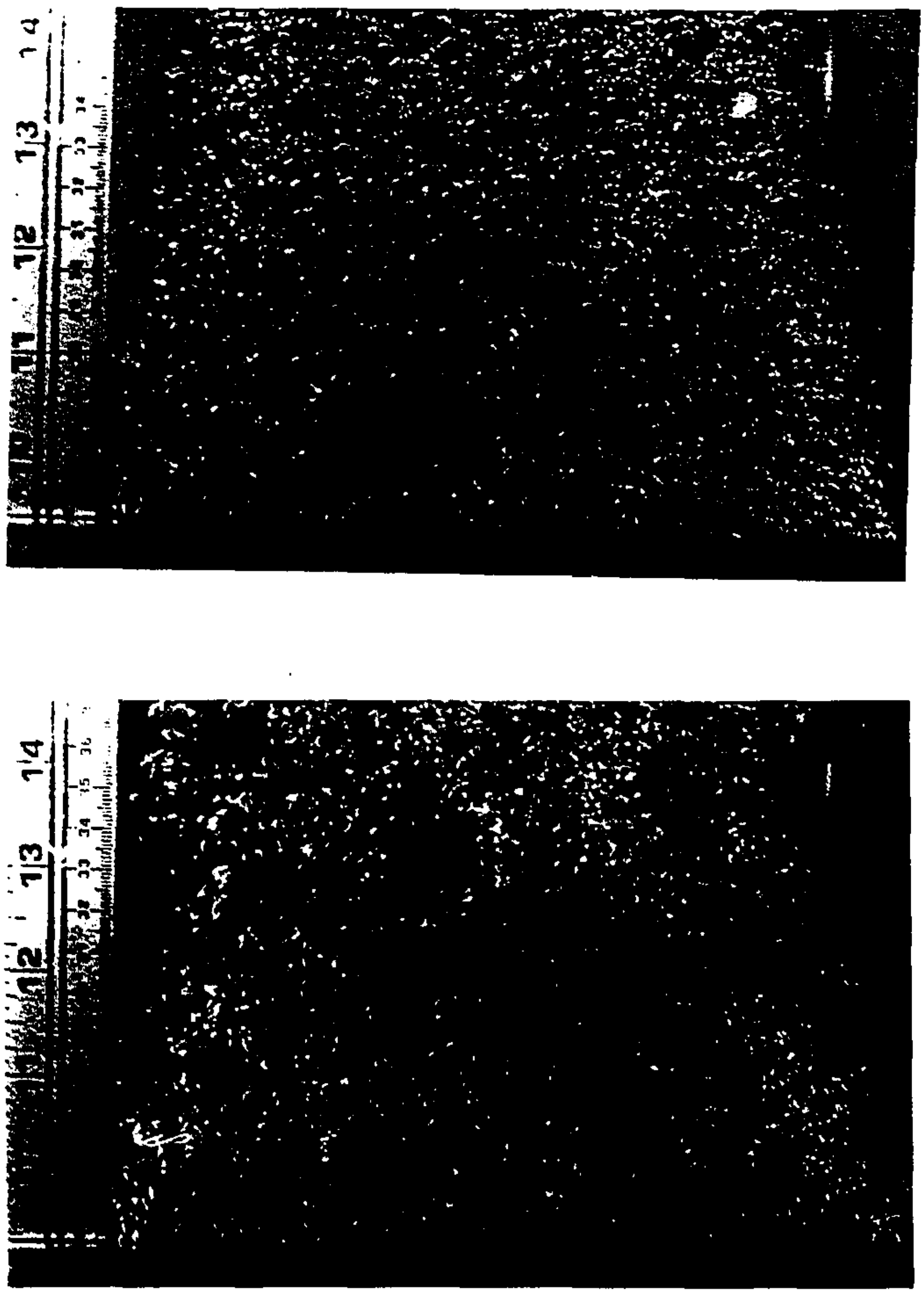

Figure 8.13 Coalescence bubble formation pattern when air was injected into methyl alcohol through a slot with W=75μm at Q_t=2.6slpm (top picture) and Q_t=5.4slpm (bottom picture).

Figure 8.14 Gas globe formation pattern when air was injected into methyl alcohol through a slot with $W=75\mu m$ at $Q_t=22.8$slpm; $N_{node}=10$.

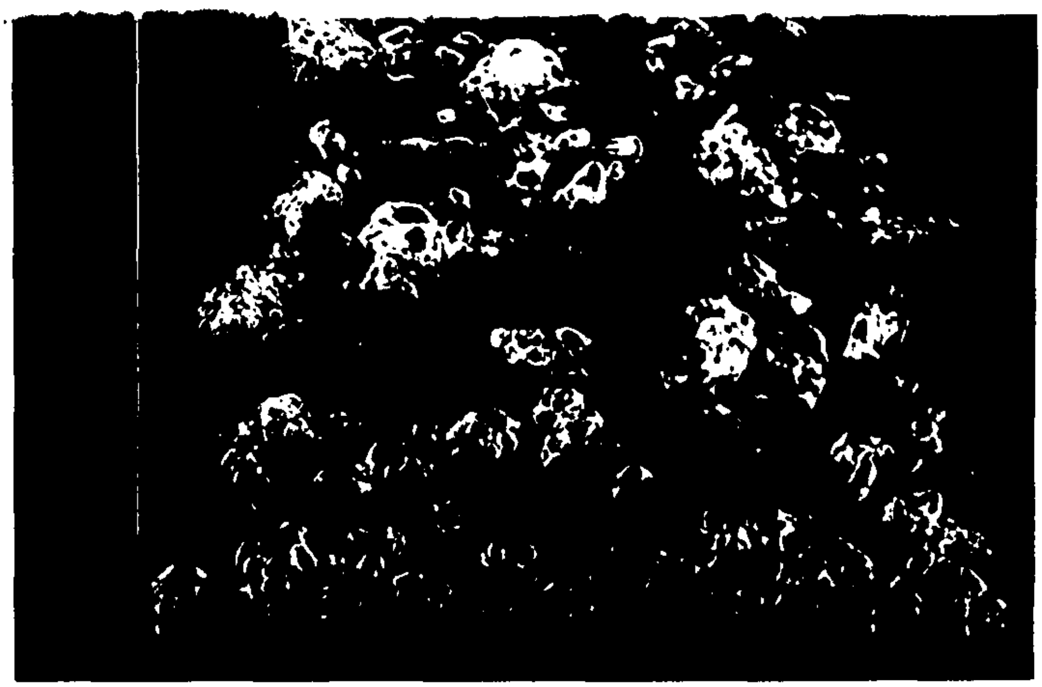

Figure 8.15 Bubble formation pattern in "*regular bubble region*" when helium was injected into methyl alcohol through a $W=250\mu m$ slot at $Q_t=7.6$ slpm.

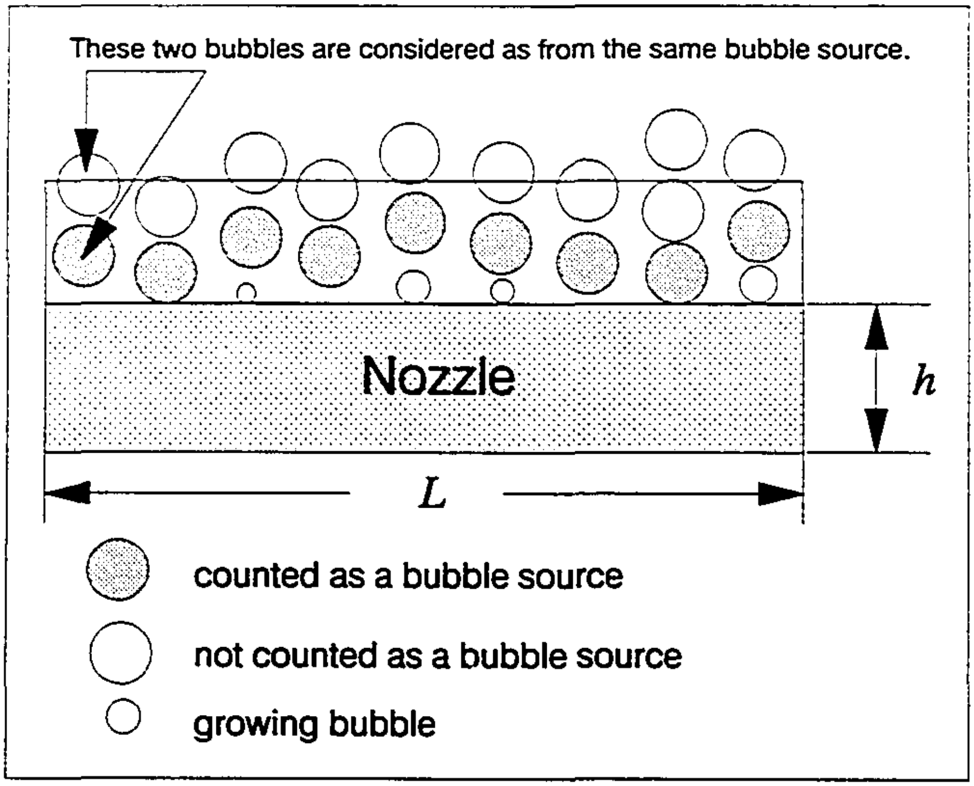

Figure 8.16 Schematic representation of measuring the number of bubble sources in the regular bubble region.

CHAPTER 9

GAS INJECTION PHENOMENA THROUGH A VERY NARROW SLOT: RESULTS AND ANALYSIS

9.1 PRESSURE DROP ACROSS A SLOT

Pressure drop across a nozzle is one of the most important parameters during gas injection, because it dominates the energy required to inject the gas. The relationship between the pressure drop and the gas superficial velocity depends on Reynolds number, *Re*. If the flow is the steady laminar flow ($Re < 2100$), the pressure drop across a narrow slot is proportional to the gas superficial velocity and is expressed as[82]:

$$\Delta P = \frac{12\, Q \mu_g h}{W^3 L} = \frac{12\, U_g \mu_g h}{W^2} \tag{209}$$

where μ_g is the viscosity of gas, Q the volumetric flow rate of gas, and U_g the superficial velocity of gas. Equation (209) is known as *Hagen-Poiseuille* law.

For a narrow slot, the force exerted on the solid surfaces by a fluid, F_k, is defined as:

$$F_k = (2Lh) \cdot (\frac{1}{2}\rho_g U_g^2) \cdot f \tag{210}$$

where $(2Lh)$ is the wetted surface, and $(\rho_g U_g^2/2)$ is the characteristic kinetic energy per unit volume. While the Reynolds Number, *Re*, is defined as:

$$Re = \frac{\rho_g W U_g}{\mu_g} \tag{211}$$

Furthermore, the friction factor is defined and expressed as:

$$f = \frac{F_k}{A_w \cdot \rho_g U_g^2} = \frac{\Delta P L W}{L h \rho_g U_g^2} \tag{212}$$

where $A_w = Lh$ is half of the wetted surface. From Equations (209)-(212) the relationship between the dimensionless friction factor and the dimensionless Reynolds Number is obtained:

$$f = \frac{12}{Re} \tag{213}$$

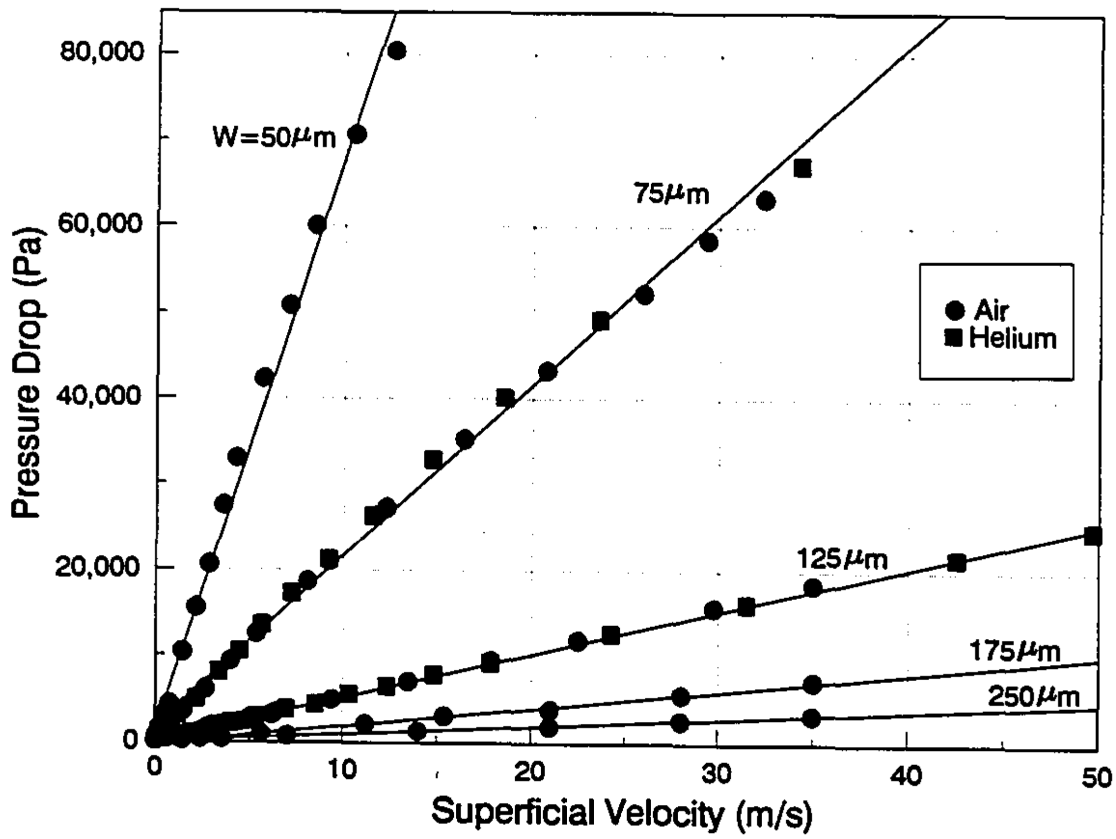

Figure 9.1 Measured pressure drop as a function of gas flow rate.

Figure 9.1 shows the relationship between the measured pressure drop across a slot and the gas superficial velocity. Clearly, the pressure drop is proportional to the gas velocity and both air and helium give the same pressure drop for the same gas superficial velocity. This means that gas density is unimportant for the pressure drop, which is consistent with *Hagen-Poiseuille* law.

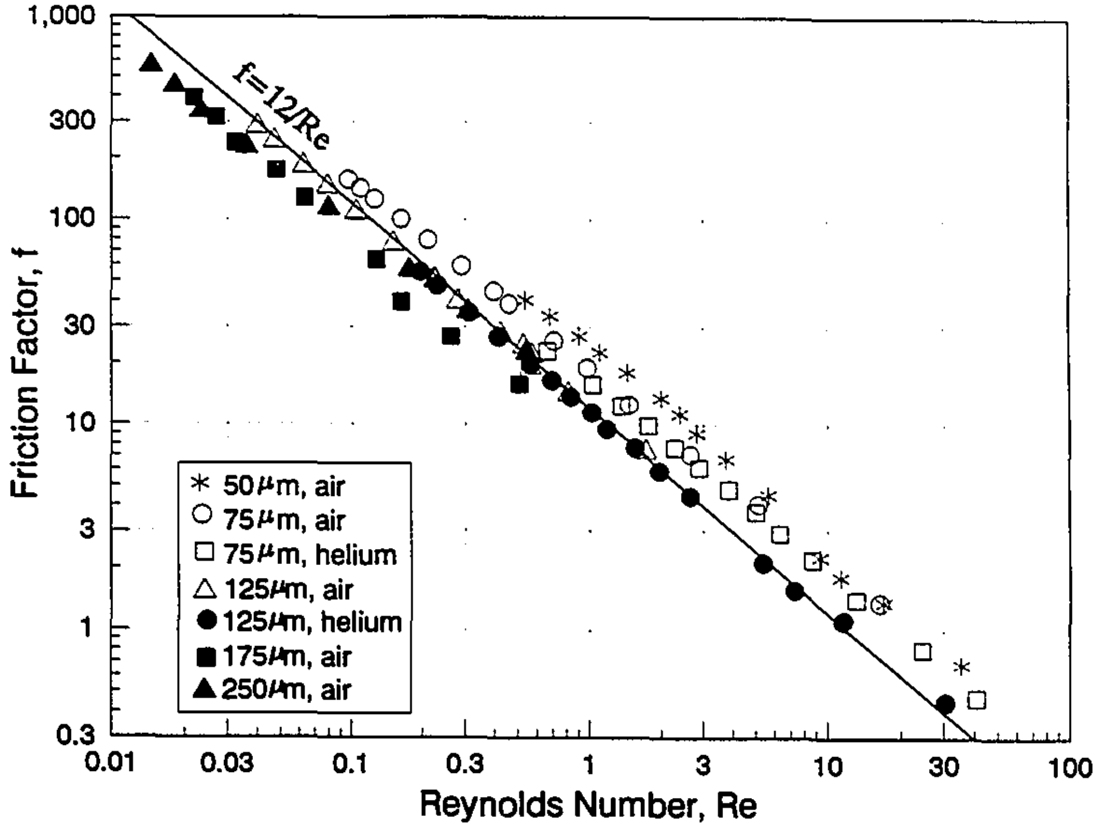

Figure 9.2 The relationship between fraction factor and Reynolds Number.

The measured pressure drop shown in Figure 9.1 can be represented by the relationship between the dimensionless fraction factor and the dimensionless Reynolds Number (Figure 9.2). The theoretical line predicted by Equation (213) is also presented in Figure 9.2. The agreement between the measured data and the theoretical prediction is excellent, which shows that the flow is laminar. In fact, the maximum Reynolds number shown in Figure 9.2 is 50, and is much less than 2100, the critical Reynolds Number for the transformation of a laminar flow to a turbulent flow.

9.2 BUBBLE FORMATION IN THE REGULAR BUBBLE REGIME

As mentioned above, in the *regular bubble regime* the regular bubbles were formed along the slot at separate locations which we refer to as bubble sources. There was no interaction between bubble sources. If the average number of the bubble sources is N when the inflowing total gas flow rate is Q_t, then each of the bubble sources can be considered as an independent one with gas flow rate Q_t/N. Since the bubble formation at low gas flow rates is dominated by surface tension, inertial and buoyancy forces, the theory of the bubble formation for a single circular orifice can be used to analyze the bubble formation through a very narrow slot. The only adjustment to be considered is the replacement of the surface tension term "$2\pi r_o$", the flow rate "Q" and the neck length of the bubble at detachment "d_n" of Equation (207) by $2W\sigma$, Q_t/N and $\sqrt{3}W/2$, respectively. Here, the wetted perimeter is assumed to be $2W$, that is, the bubble formed on a very narrow slot has a square "mouth". Since stainless steel is well wetted by both water and methyl alcohol, the contact angle is assumed to be zero for the present calculations.

Figure 9.3 to Figure 9.11 present the measured bubble volume as a function of gas flow rate for various slot widths. The predicted data, Equation (207), are also shown in these figures. In general, the agreement between measured and predicted results is good, which demonstrates that bubble formation from a very narrow slot is dominated by both surface tension and inertial forces. As a result, the bubble size is dependent on the slot spacing.

From Figure 9.6 and Figure 9.7, it is clear that Equation (207) overestimates the bubble size for the $W = 50\mu m$ slot. For this smallest slot width, both gas flow rate and bubble size are very small so that surface tension becomes very important in comparison with the inertial force. In Equation (207) the contact angle, θ_c, was assumed to be zero with the result that the surface tension force was overestimated. If the real contact angle which is larger than zero were considered in Equation (207), the calculated bubble volume would be smaller than that shown in Figure 9.6 and Figure 9.7, so that good agreement between calculated bubble volume and measured volume could be obtained.

In contrast to Figure 9.6 and Figure 9.7, it seems that Equation (207) underestimates the measured bubble volume for this largest width of slot (W=250μm) as shown in Figure 9.8 and Figure 9.9. In fact, the bubble formation through a wide slot is very unstable, and coalescence between bubbles occurs even in the so called "regular bubble regime" at low gas flow rates. As shown in Figure 8.15, the measurement of the bubble size becomes difficult due to the coalescence of bubbles and the measured bubble size is larger than that of a single bubble. In the present research, it was almost impossible to form regular bubbles from a slot with W > 250μm for water and methyl alcohol.

Figure 9.3 also shows the predictions of the Kumar and Kuloor's model. It is obvious that Kumar and Kuloor's model greatly overestimates the bubble volume.

As mentioned before and shown in Figure 8.5, Figure 8.8, Figure 8.10 and Figure 8.11, the number of bubble sources in the regular bubble regime increases with an increase in the gas flow rate. However, the reason for this behaviour is not immediately obvious, and there are no references in gas injection literature that are helpful on illuminating the physical background. The key problem for understanding the bubble formation from the slot-shaped nozzle in the regular bubble regime was to find a relationship between the average number of bubble sources, N, (or the distance between bubble sources) and the gas injection parameters, such as gas flow rate and slot width etc. In order to answer this question, we looked to the Rayleigh-Taylor instability.

As discussed in Part 1 of the thesis, an interface between two fluids of different densities is unstable when the light fluid is under the heavy fluid. When gas is injected vertically into water through a slot-shaped nozzle, the equilibrium gas-liquid interface can be imagined as a cylindrical one as shown in Figure 8.4. With an increase in the gas flow rate, the radius of the dynamic gas-liquid interface decreases. This interface is unstable since gas is pushing the liquid and produces nodal instabilities which disrupt the interface. Such nodes act as bubble sources along the slot. The distance between bubble sources is dominated by so called "most dangerous wavelength". Thus, the understanding of the gas bubble formation through a narrow slot relies on the analysis of the Rayleigh-Taylor instability of the hypothetical gas-liquid cylindrical interface, which was carried out in Part 1. From Equation (70) the relationship between the dangerous wavelength and the radius of the interface can be obtained. By using the dimensionless variables defined in Equations (74)-(77), the dispersion equation (70) becomes:

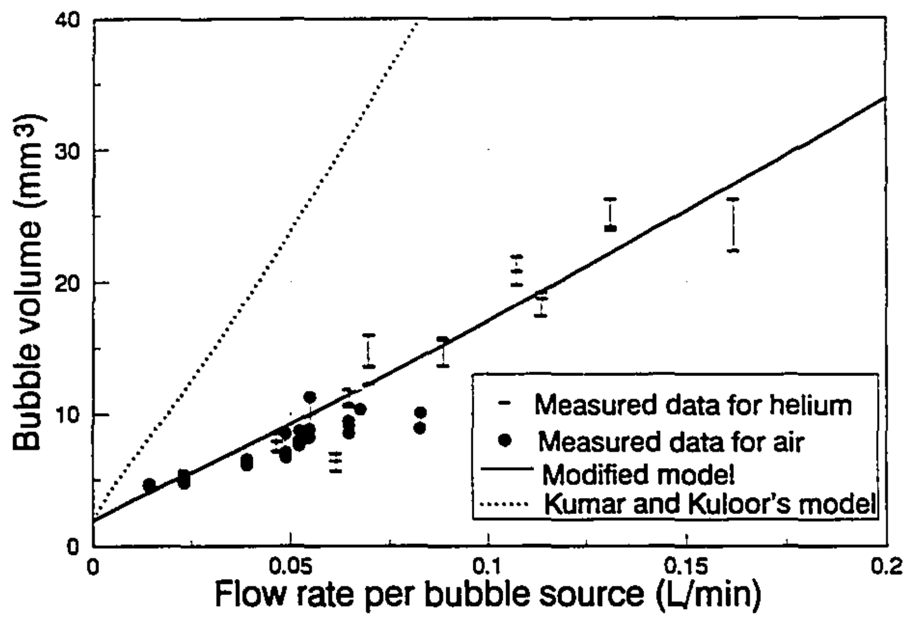

Figure 9.3 The predicted and measured bubble volume as a function of gas flow rate per bubble source for a $W=125\mu m$ slot submerged in water (from Tables A-1 and A-2).

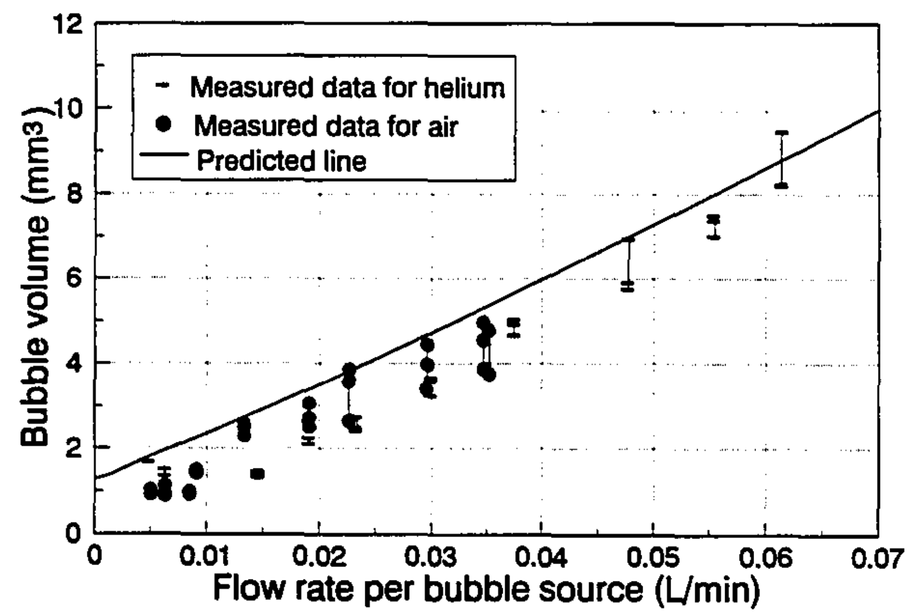

Figure 9.4 The predicted and measured bubble volume as a function of gas flow rate per bubble source for a $W=75\mu m$ slot submerged in water (from Tables A-3 and A-4).

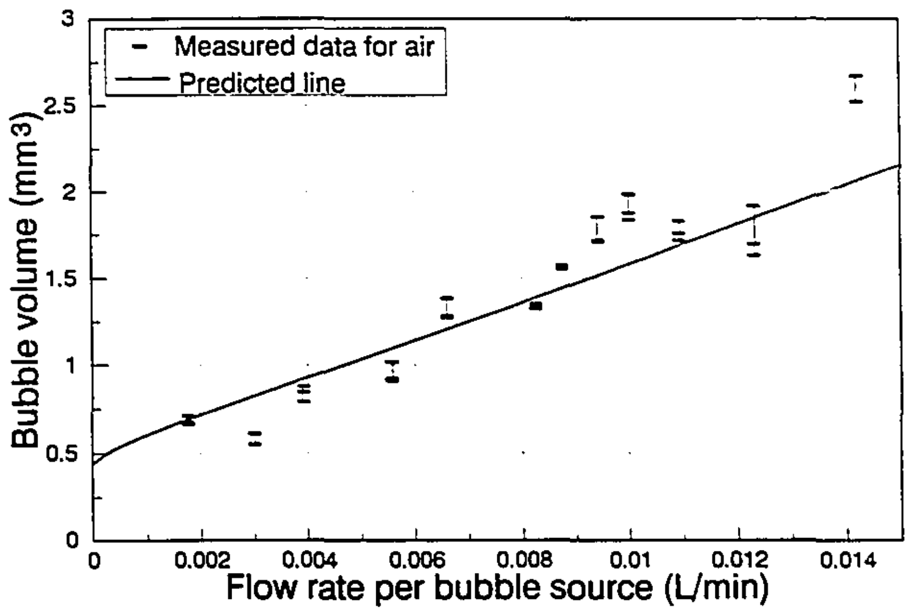

Figure 9.5 The predicted and measured bubble volume as a function of gas flow rate per bubble source for a W=75μm slot submerged in methyl alcohol (from Table A-5).

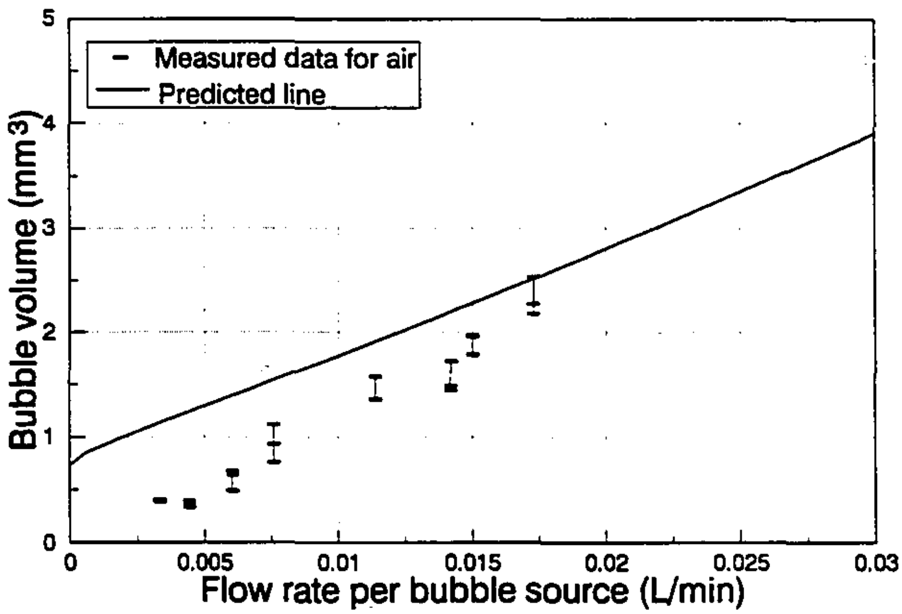

Figure 9.6 The predicted and measured bubble volume as a function of gas flow rate per bubble source for a W=50μm slot submerged in water (from Table A-6).

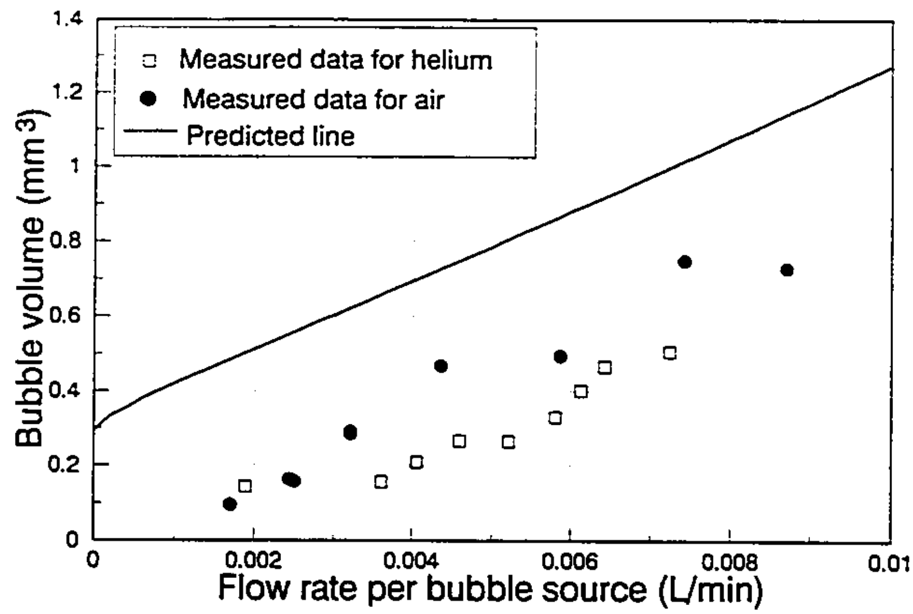

Figure 9.7 The predicted and measured bubble volume as a function of gas flow rate per bubble source for a W=50μm slot submerged in methyl alcohol (from Tables A-7 and A-8).

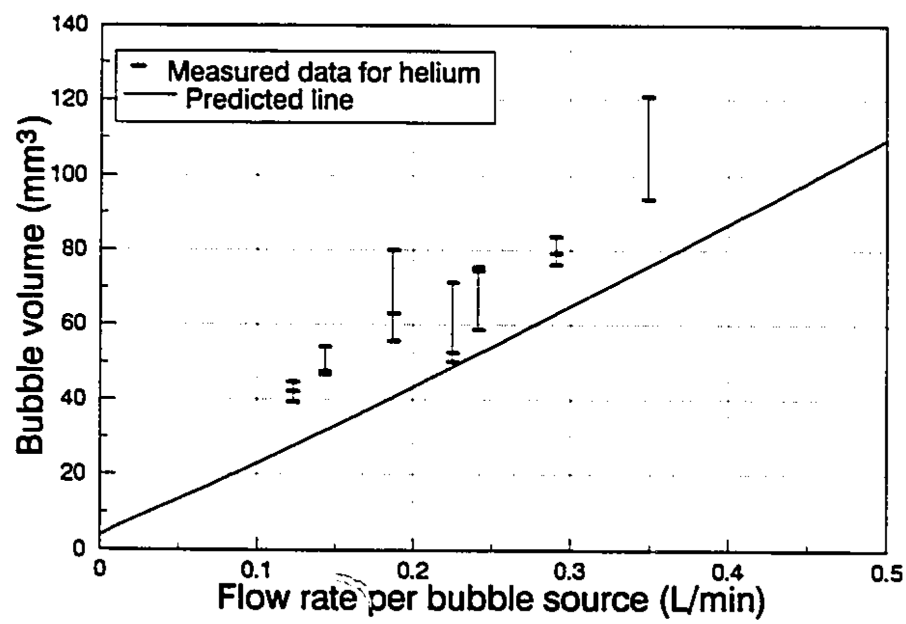

Figure 9.8 The predicted and measured bubble volume as a function of gas flow rate per bubble source for a W=250μm slot submerged in water (from Table A-9).

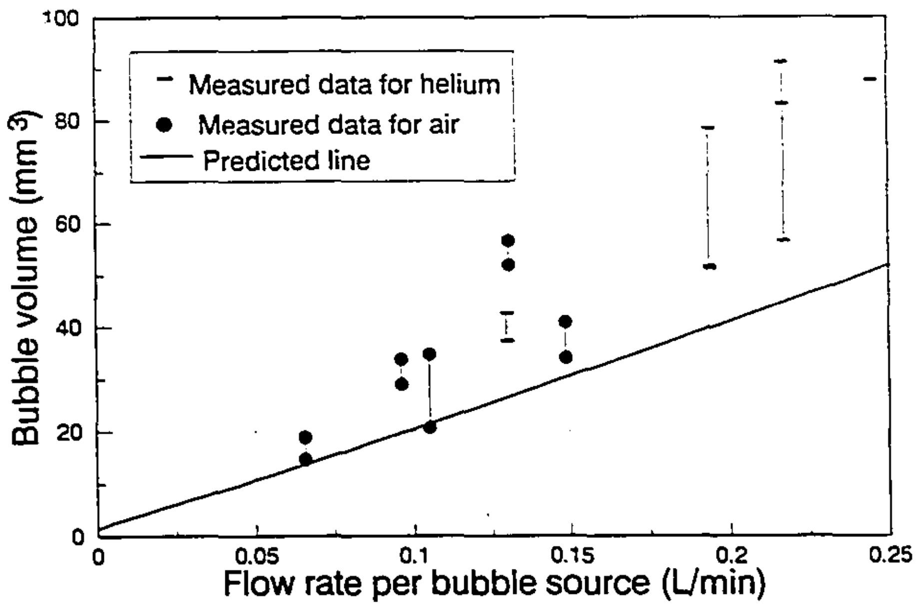

Figure 9.9 The predicted and measured bubble volume as a function of gas flow rate per bubble source for a W=250μm slot submerged in methyl alcohol (from Tables A-10 and A-11).

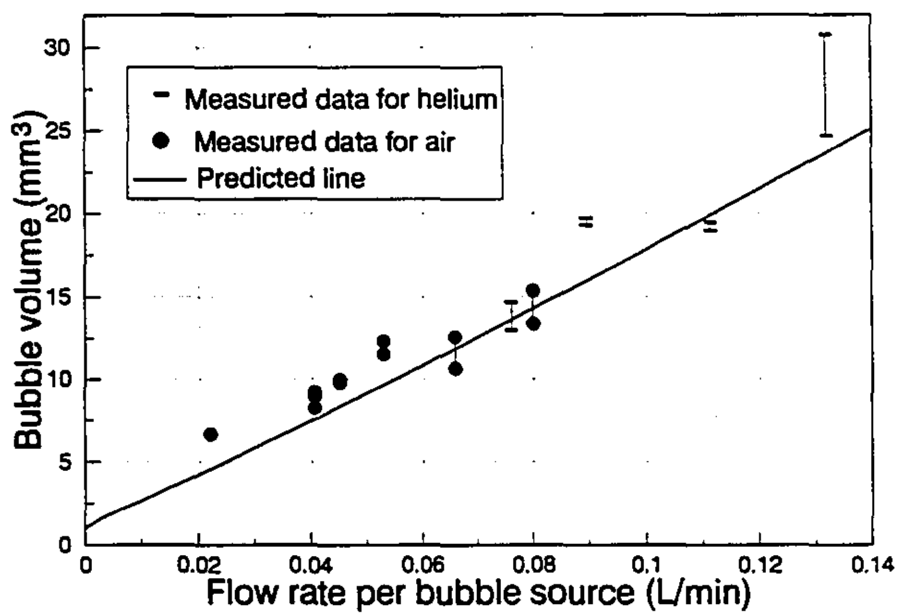

Figure 9.10 The predicted and measured bubble volume as a function of gas flow rate per bubble source for a W=175μm slot submerged in methyl alcohol (from Tables A-12 and A-13).

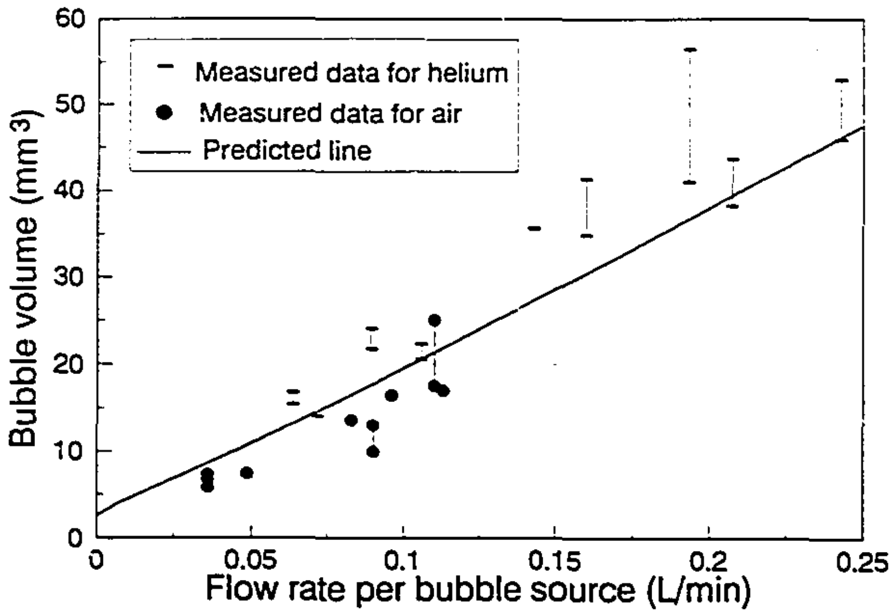

Figure 9.11 The predicted and measured bubble volume as a function of gas flow rate per bubble source for a $W = 175\mu m$ slot submerged in water (from Tables A-14 and A-15).

$$\Omega^2 = -\frac{1}{\alpha_2}\left[K^2 - \frac{1}{\Pi^2} - 1\right] K \tag{214}$$

which is similar to Equation (78) of film boiling. From Equation (214) the dimensionless critical wavelength is expressed as:

$$\Lambda_{c,bubble} = \frac{2\pi}{\left[1 + \frac{1}{\Pi^2}\right]^{1/2}} \tag{215}$$

and the dangerous wavelength can be calculated by using *Tk-Solver*. Figure 9.12 shows the numerically calculated ratio between dangerous wavelength and critical wavelength. It can be fitted well by Equation (216):

$$\frac{\Lambda_{d,bubble}}{\Lambda_{c,bubble}} = \frac{2.067 + \sqrt{3}\,0.3108\,\Pi^{1.434}}{1 + 0.3108\,\Pi^{1.434}} \tag{216}$$

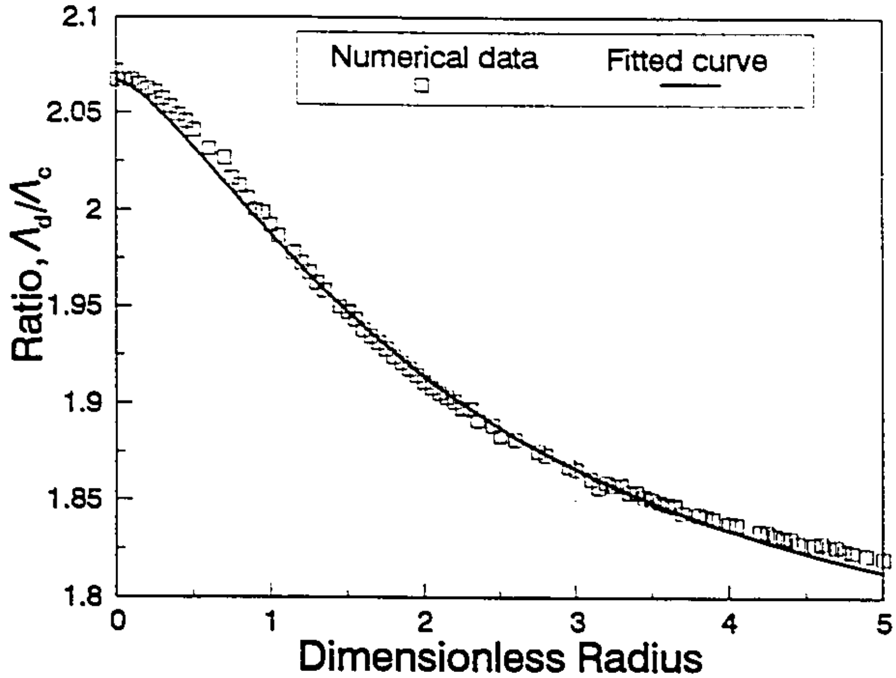

Figure 9.12 Calculated ratio between dangerous wavelength and critical wavelength as a function of dimensionless radius for an axisymmetrical cylindrical interface at $\theta=0$.

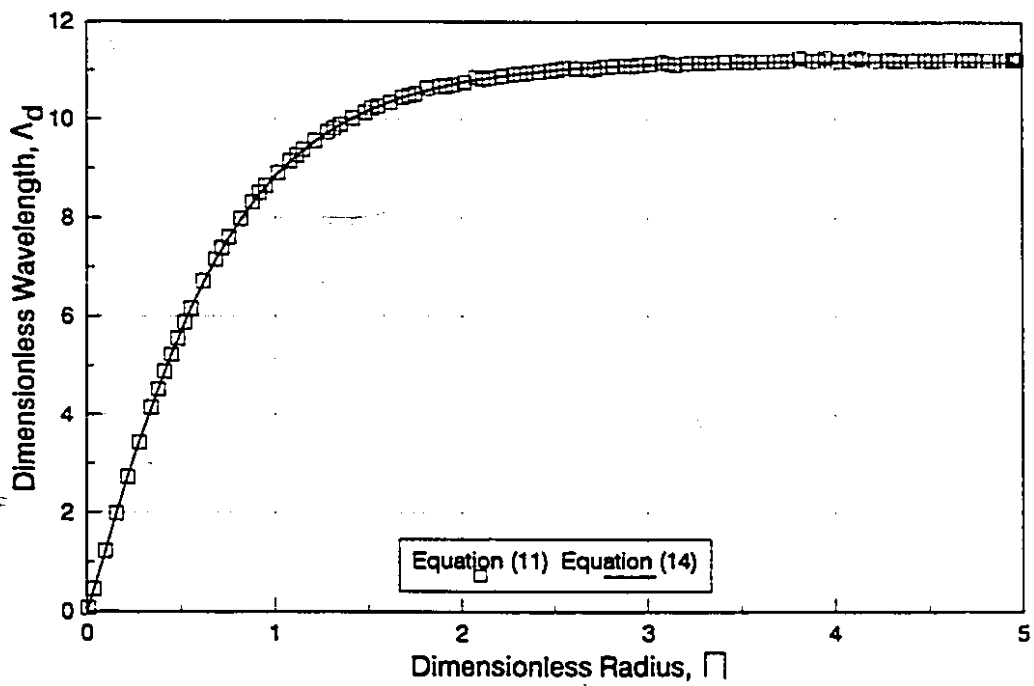

Figure 9.13 The relationship between the most dangerous wavelength and dimensionless radius of cylindrical interface.

Finally, the dimensionless dangerous wavelength is expressed explicitly as:

$$\Lambda_{d,bubble} = \frac{2.067 + \sqrt{3}\, 0.3108\, \Pi^{1.434}}{1 + 0.3108\, \Pi^{1.434}} \cdot \frac{2\pi}{\left[1 + \frac{1}{\Pi^2}\right]^{1/2}} \tag{217}$$

and is shown in Figure 9.13. From Figure 9.13, it is obvious that the dangerous wavelength decreases with a decrease in the cylindrical radius. For bubble formation through a very narrow slot, the radius of the hypothetical gas-liquid dynamic interface decreases with an increase in the gas flow rate. Therefore, the bubbles along the slot become close to one another as the flow rate is increased.

If the curvature of the dynamic gas-liquid interface could be correlated to the gas injection parameters (such as the gas flow rate, slot width, and the properties of liquid and gas), we would be able to predict the distance between bubble sources using Equation (217), and the gas bubble formation phenomena would be understood completely. Unfortunately, the curvature of the unstable dynamic gas-liquid interface can neither be measured nor predicted by previous existing theory. In fact, the research on a moving gas-liquid contact line and the interface shape in a liquid-gas system is one of the most important and difficult fields[83,84,85,86,87,88].

Although above analysis can not predict the number of bubble sources as a function of gas flow rate etc., it does provide us a physical picture or background on the bubble formation through a slot. The relationship between the number of the bubble sources and the gas injection parameters can be determined by experiments under the guidance of the dimensional analysis. For the bubble formation through a narrow slot under the constant flow condition, there are six variables, and the distance between bubble sources, λ_d, is expressed as:

$$\lambda_d = f(\rho_g, \rho_l, U_g, W, \sigma) \tag{218}$$

where g has been neglected because most of the experimental data are in shorter λ_d region (smaller R_o in Eq.(69)). Changing the orientation of the slot from vertical to horizontal verified that gravity g had very small effect on λ_d at very low gas flow rates and had no effect at high gas flow rates. The dimensions of each variable are listed in Table 9.1.

Table 9.1 Dimension of Each Variable

λ_d	ρ_g	ρ_l	U_g	W	σ
L	$M L^{-3}$	$M L^{-3}$	$L T^{-1}$	L	$M T^{-2}$

In Table 9.1, M, L and T represent the mass, the length and the time, respectively. According to Buckingham's pi theorem[89], Equation (218) can be reduced to a relation between three dimensionless variables because there are three of six variables which do not form a dimensionless variable, i.e., ρ_l, U_g and W. Then the three dimensionless groups are formed by power products of these three plus an additional variable, i.e.,

$$\begin{aligned} \Pi_1 &= \rho_l^a U_g^b W^c \rho_g = M^0 L^0 T^0 \\ \Pi_2 &= \rho_l^d U_g^e W^f \lambda_d = M^0 L^0 T^0 \\ \Pi_3 &= \rho_l^g U_g^h W^i \sigma = M^0 L^0 T^0 \end{aligned} \tag{219}$$

where a, b, c, d, e, f, g, h *and* i are constants and are determined by equating exponents of two sides of the dimensionless groups. Finally, the three dimensionless variables are expressed as:

$$\pi_1 = \frac{\rho_l}{\rho_g}, \quad \pi_2 = \frac{\lambda_d}{W}, \quad \pi_3 = \frac{\rho_l U_g^2 W}{\sigma} \tag{220}$$

where π_2 is called as dimensionless distance between bubble sources and is different from the dimensionless wavelength defined in Chapter 2, Λ. Clearly, dimensionless variable π_3 is called Weber number, and expressed by *We*.

The dimensionless analysis guarantees that the functional relationship of Equation (218) must be of the equivalent form:

$$\frac{\lambda_d}{W} = g\left(\frac{\rho_l}{\rho_g}, We\right) \tag{221}$$

The simplest form of function g is the power products of density ratio and Weber number, i.e.,

$$\frac{\lambda_d}{W} = c_1 \left[\frac{\rho_l}{\rho_g} \right]^{c_2} \cdot We^{c_3} = A \cdot We^{c_3} \tag{222}$$

or

$$\ln\left[\frac{\lambda_d}{W}\right] = \ln(c_1) + c_2 \ln\left[\frac{\rho_l}{\rho_g}\right] + c_3 \ln(We) \tag{223}$$

where c_1, c_2 and c_3 are constants and are determined by experiments, while A is expressed as:

$$A = c_1 \left[\frac{\rho_l}{\rho_g} \right]^{c_2} \tag{224}$$

From Equation (223) it is clear that the curve of the dimensionless distances (λ_d/W) verses dimensionless Weber number (We) should be linear in log-log coordinates if the function g assumed in Equation (221) is correct. The slope of the curve gives constant c_3, while the intercept represents the function $ln(A)=ln(c_1)+c_2 ln(\rho_l/\rho_g)$.

Figure 9.14 shows the experimental relationships between the dimensionless distance, λ_d/W, and dimensionless Weber number, We, for the first eight experiments, while the results of another seven experiments are shown in Figure 9.15. In general, $ln(\lambda_d/W)$ is really a linear function of $ln(We)$ and it seems that all of the curves have almost the same slope. The solid lines of Figure 9.14 and Figure 9.15 are based on fitted results. The slopes and intercepts of the fifteen curves are given in Table 9.2, from which the average value of constant c_3 is calculated to be -0.23. The intercepts, $ln(A)$, shown in Table 9.2 is a function of density ratio between liquid and gas and is represented in Figure 9.17. By fitting the experimental data, we get required constants, c_1=18.78 and c_2=0.15. Thus, the dimensionless distance between bubble sources is expressed as:

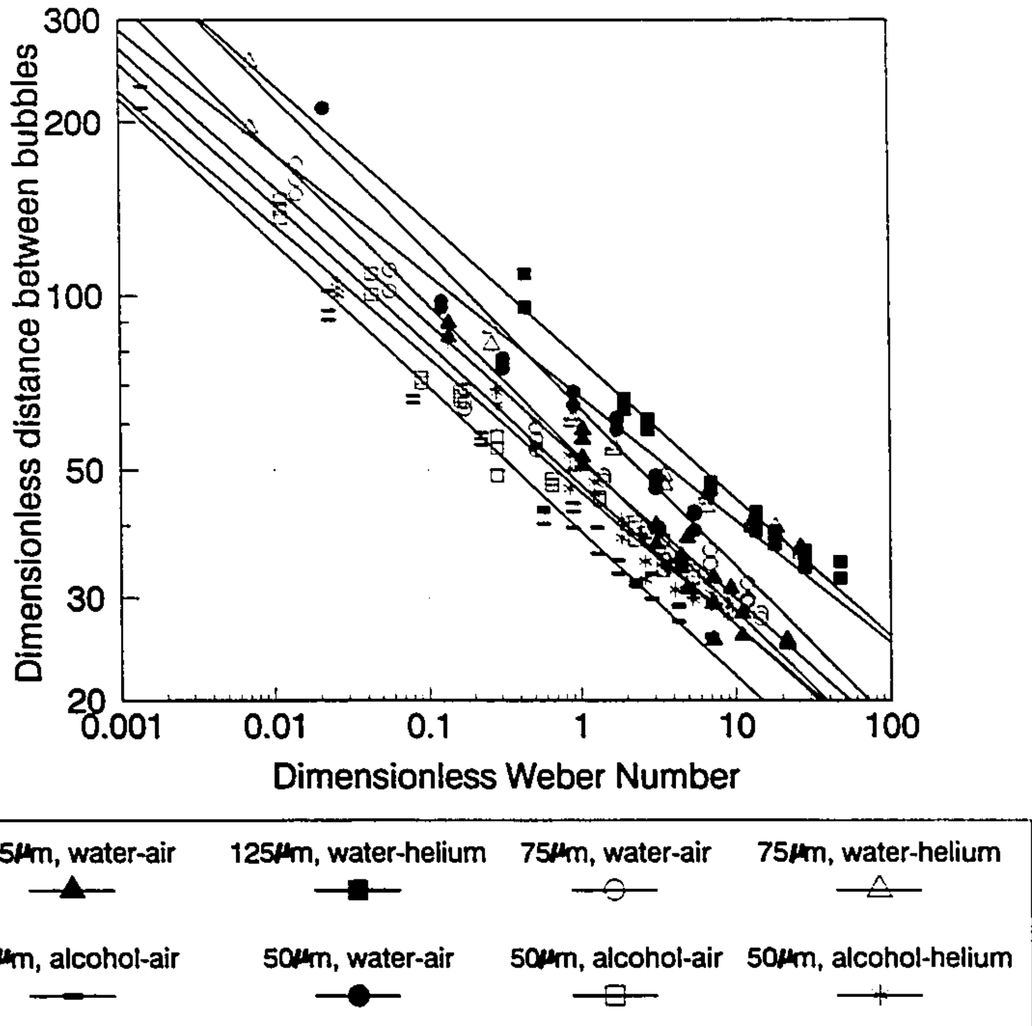

Figure 9.14 Measured dimensionless distance between bubbles as a function of Weber number for first eight experiments

$$\frac{\lambda_d}{W} = 18.78 \left[\frac{\rho_l}{\rho_g} \right]^{0.15} We^{-0.23} \tag{225}$$

Figure 9.16 shows the comparison of the dimensionless distances between measured and-predicted by empirical Equation (225). Clearly, very good agreement is obtained.

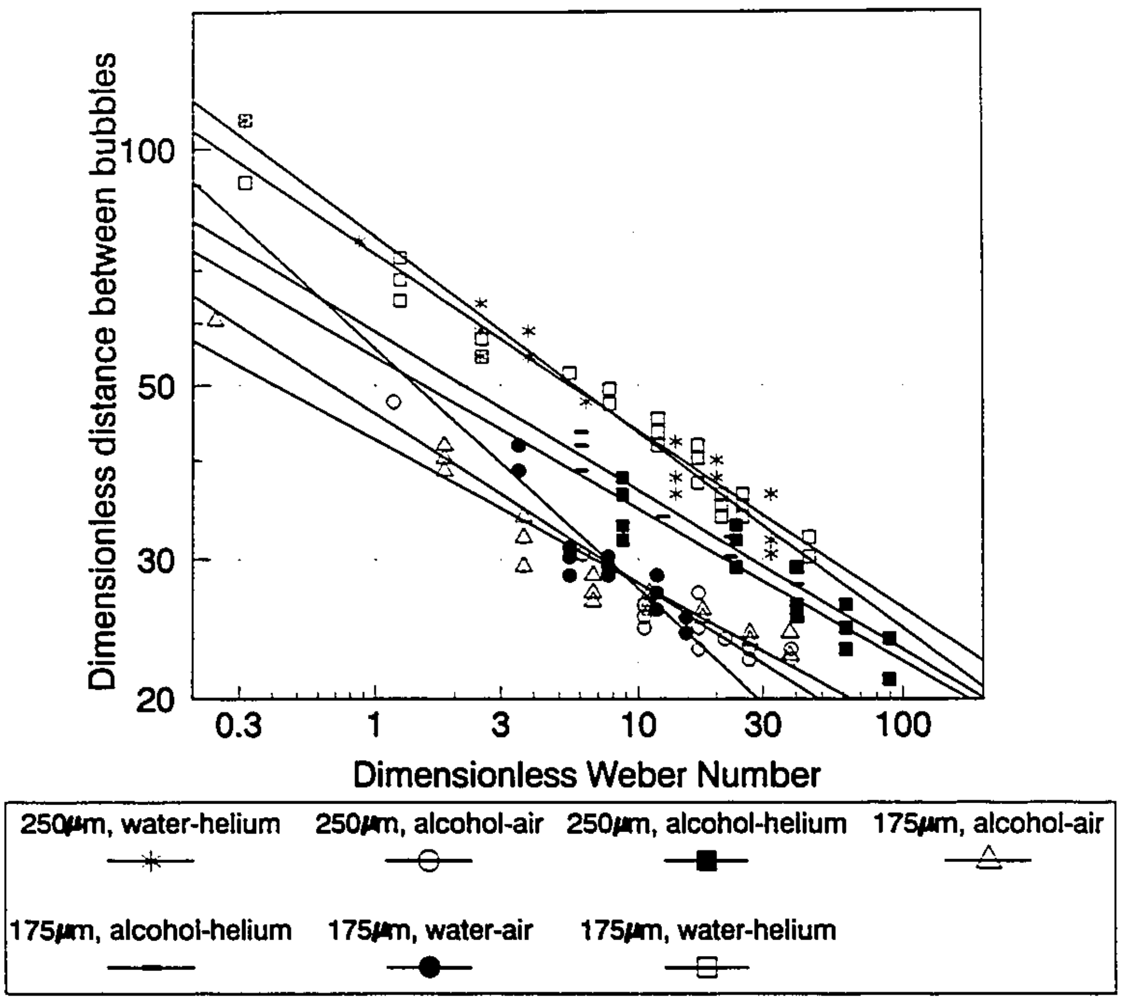

Figure 9.15 Measured dimensionless distance between bubbles as a function of Weber number for last seven experiments

Equation (225) can be rewritten, in dimensional form, by:

$$\lambda_d = 18.78 \frac{\sigma^{0.23} W^{0.77}}{\rho_g^{0.15} \rho_l^{0.089} U_g^{0.47}} \tag{226}$$

Based on Equations (225)-(226), the dimensionless distance between bubble sources (or the number of bubble sources) is dominated by Weber number and density ratio between liquid and gas. With an increase in the gas density, the number of bubble sources decreases, i.e., the number of bubble sources for helium is less than that for air under the same total gas flow rate. The reason is that the higher the gas density is, the smaller the

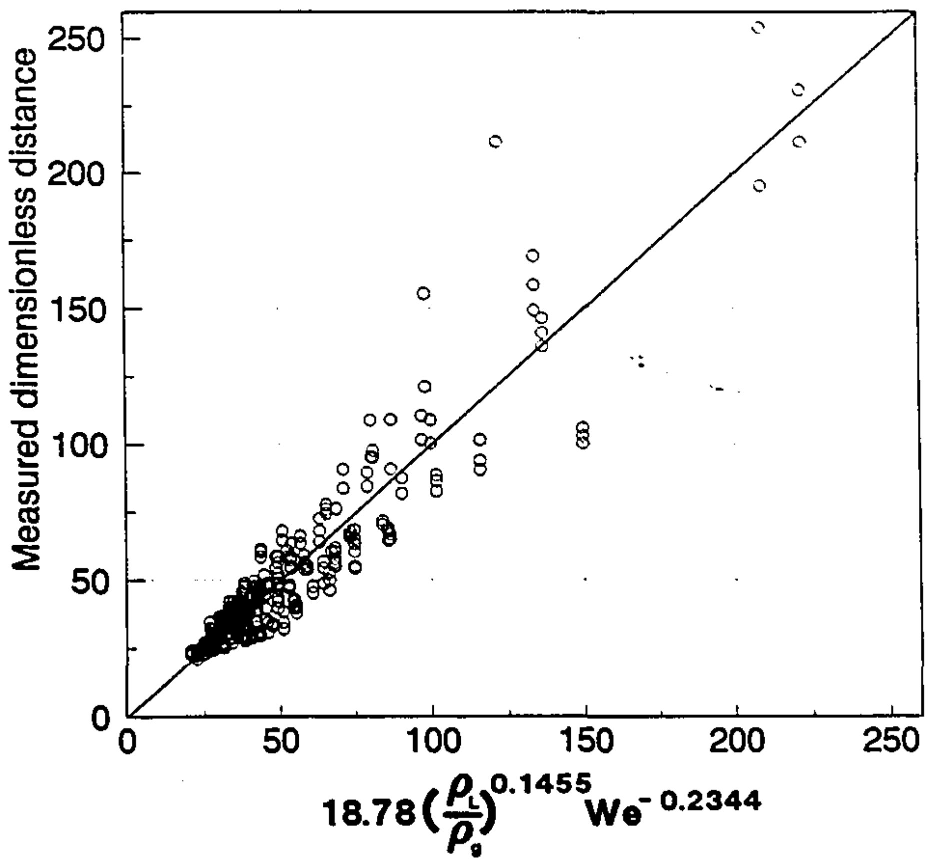

Figure 9.16 The comparison between the measured and predicted dimensionless distance between the bubbles.

radius of gas-liquid dynamic cylindrical interface due to the high gas momentum, and then the shorter the dangerous wavelength. From Equation (226) it is also clear that the distance between bubble sources increases as the decrease of the liquid density. The reason is that the interface becomes more unstable (shorter dangerous wavelength) as an increase in the liquid density. Of course, a decrease in the width of the slot and an increase in the gas velocity decrease the radius of the cylindrical interface so that the dangerous wavelength becomes shorter. Since the surface tension is always stabilizing the interface, any increase in the surface tension leads to a longer dangerous wavelength.

Table 9.2 Slopes and Intercepts of $ln(\lambda_d/W)$-$ln(We)$ Curves

Exp. No.	Regression coefficient	slope c_3	intercept $ln(c_1)+c_2 ln(\rho_l/\rho_g)$
1	0.965	-0.264	52.500
2	0.981	-0.239	77.500
3	0.974	-0.238	51.800
4	0.964	-0.212	66.700
5	0.988	-0.249	39.200
6	0.954	-0.271	63.700
7	0.963	-0.231	45.900
8	0.974	-0.243	47.200
9	0.974	-0.248	77.200
10	0.928	-0.215	46.000
11	0.849	-0.193	54.280
12	0.921	-0.182	42.600
13	0.928	-0.202	58.500
14	0.852	-0.304	55.600
15	0.973	-0.225	73.400

In a few words, the experimental results expressed by Equations (225)-(226) can be fully understood by the hydrodynamic instability theory presented in Part 1, i.e., the gas bubble formation along a slot is dominated by the Rayleigh-Taylor instability.

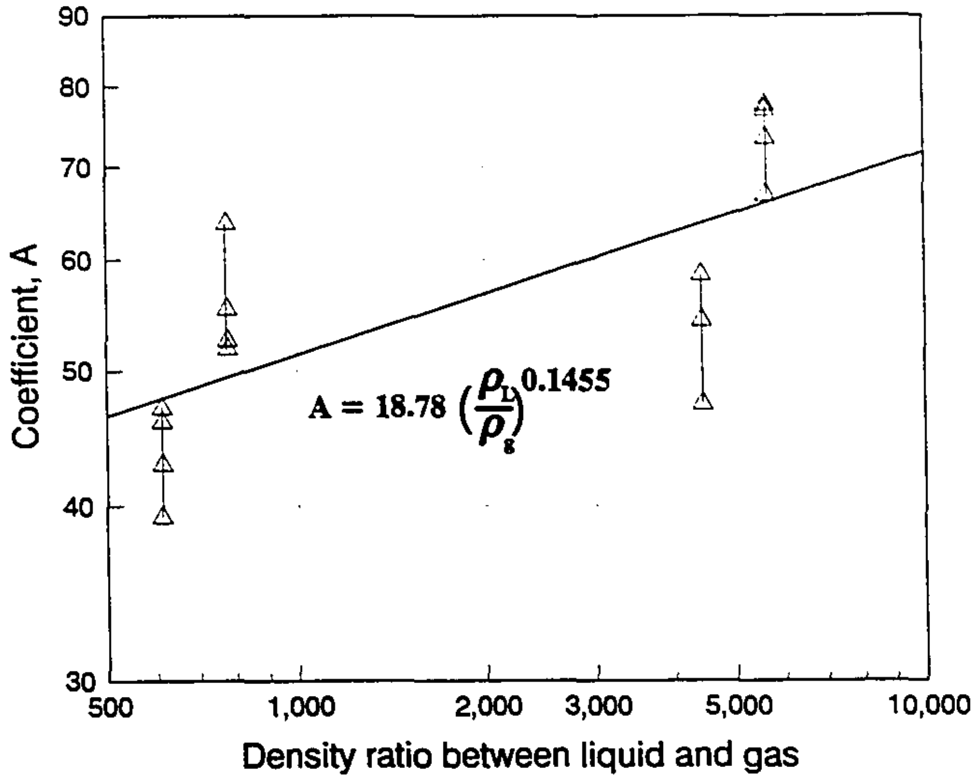

Figure 9.17 The relationship between coefficient, A, and the density ratio between liquid and gas, ρ_l/ρ_g.

9.3 BUBBLE FORMATION IN THE COALESCENCE BUBBLE REGIME

Because the number of bubble sources increases with an increase of gas flow rate, coalescence between bubbles occurs beyond certain gas flow rate as shown in Figure 8.6 and discussed before. In the coalescence bubble formation regime, each of the bubble sources can no longer be considered as an independent one due to the interaction between them so that a considerable deviation in the bubble size can be observed.

In this regime, bubble formation is dominated by inertia forces only because not only the gas flows are high but also the bubbles are formed after the interaction of the bubble sources so that the bubbles are detached from the interaction of the bubble sources rather than from the slot itself.

When the bubble formation is controlled by inertial force, the bubble volume is expressed as:

$$V_b = K_b \frac{Q_b^{6/5}}{g^{3/5}} = K_b \left[\frac{Q_t\, d_b}{L}\right]^{6/5} g^{-3/5} \tag{227}$$

where K_b is a constant with a value ≈ 1 (Equations (185) and (190)), d_b the diameter of the bubble, L the length of the slot, Q_t the total gas flow rate, Q_b the gas flow rate contributed to each of the bubbles and equal to $Q_t{*}d_b/L$. The evaluation of Equation (227) gives an expression for the bubble diameter:

$$d_b = \left[\frac{6\,K_b}{\pi}\right]^{5/9} \frac{Q_t^{2/3}}{g^{1/3}\,L^{2/3}} \tag{228}$$

The constant K_b is expressed as:

$$K_b = \frac{\pi\, L^{6/5}\, d_b^{9/5}\, g^{3/5}}{6\, Q_t^{6/5}} \tag{229}$$

From this equation, the measured bubble size in the coalescence bubble formation regime shown in Table A1-A15 of Appendix II can be used to evaluate the constant K_b, which is represented in Figure 9.18. The scatter of the K_b value is quite large because of the irregular bubble formation and the random of the bubble coalescence. But, nevertheless the K_b value ranges from 0.5 to 1.4 and the average value is 0.746 which is close to the theoretical analysis (Equations (185), (190) and (192)) and Hoefele's empirical data for water, 0.88[78].

Substituting the average value of K_b (0.746) into Equation (228), we get the final equation for predicting the bubble diameter in the coalescence bubble regime:

$$d_b = 1.217 \frac{Q_t^{2/3}}{g^{1/3}\,L^{2/3}} \tag{230}$$

Figure 9.19 presents the measured bubble size, d_b, as a function of total gas flow rate, Q_t, for the fifteen experiments along with the predicted data from Equation (230).

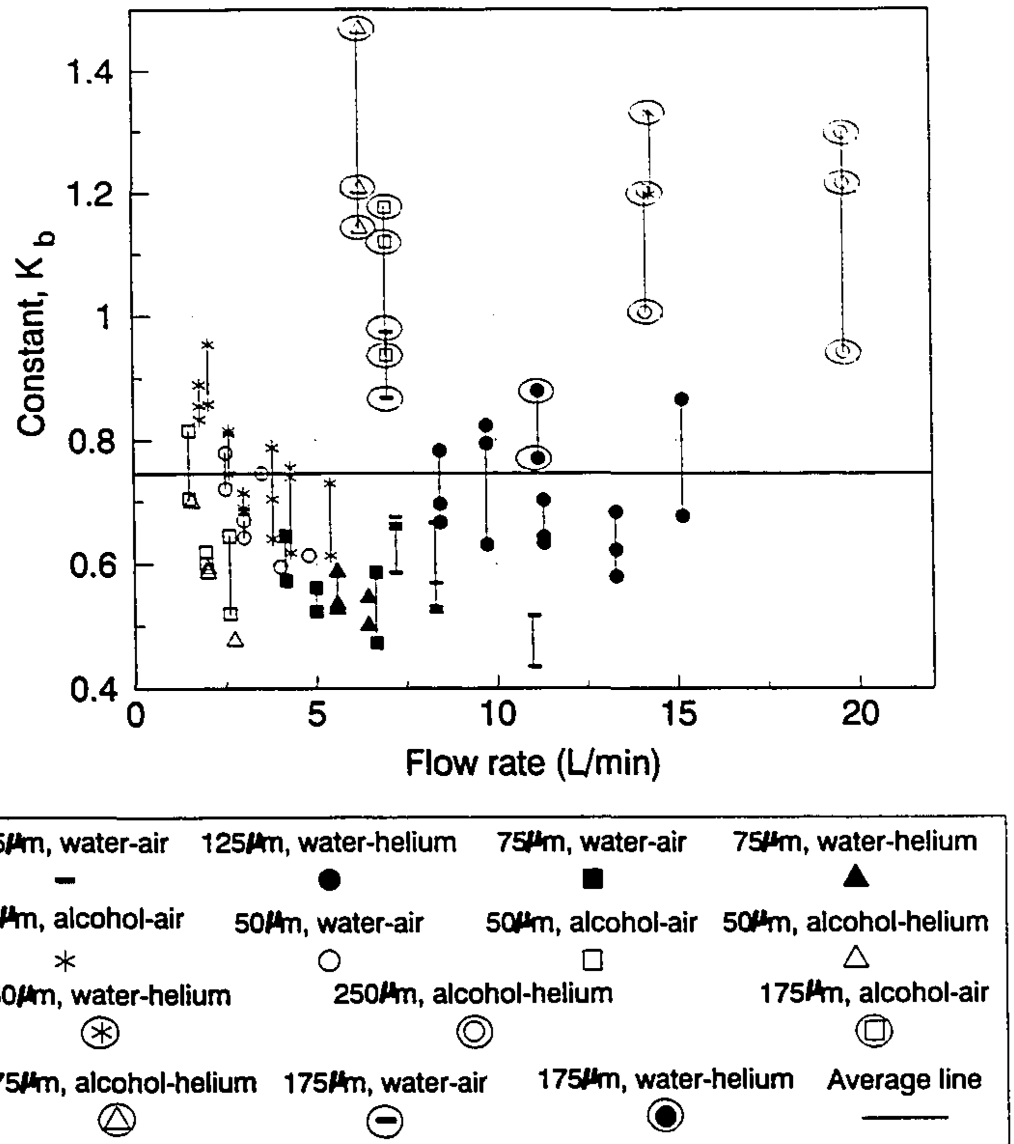

Figure 9.18 Measured K_b values for fifteen experiments

Evidently, Equation (230) closely represents the measured data.

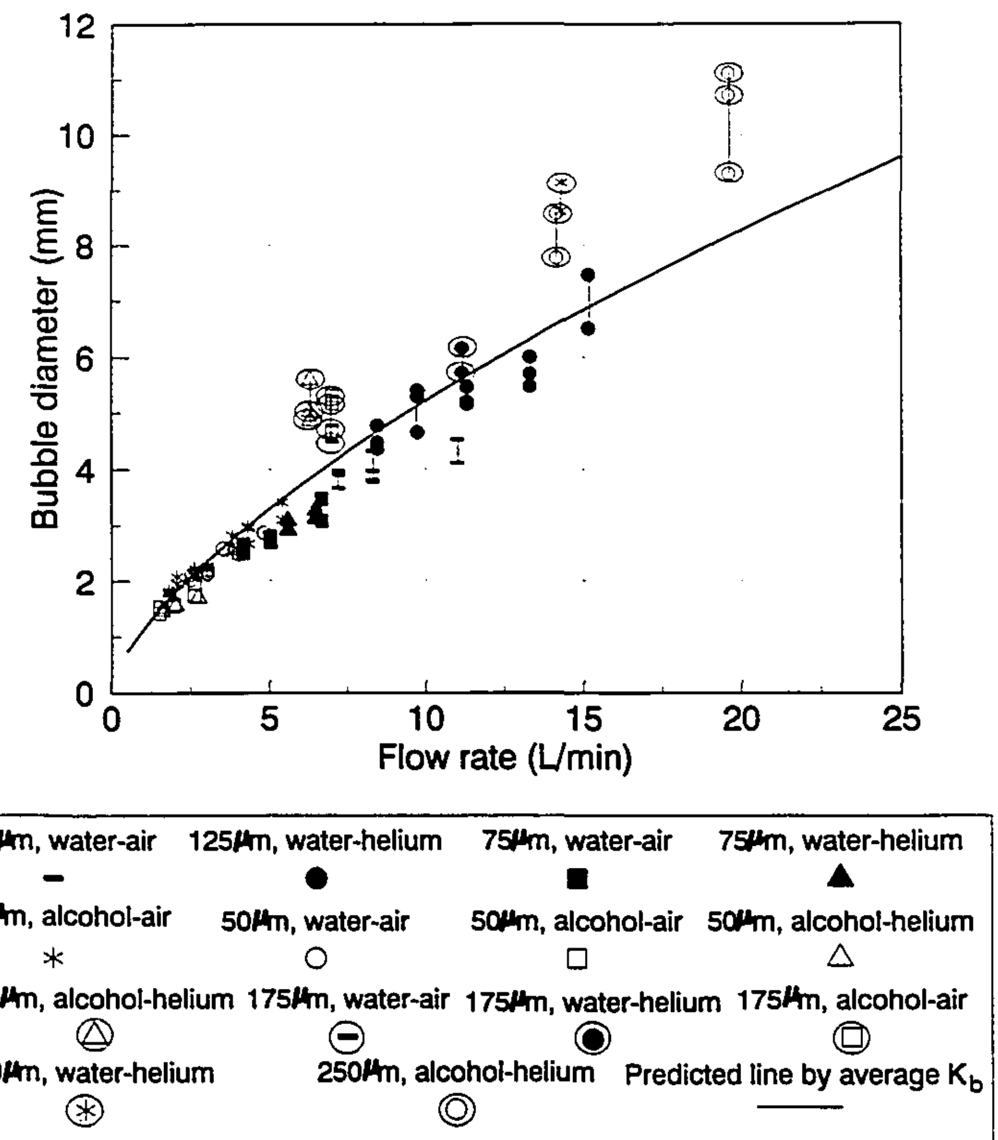

Figure 9.19 Measured bubble diameter as a function of total gas flow rate for the fifteen experiments.

9.4 CRITICAL TRANSITION CONDITION BETWEEN THE REGULAR BUBBLE REGIME AND THE COALESCENCE BUBBLE REGIME

The transition between the regular bubble formation and the coalescence bubble

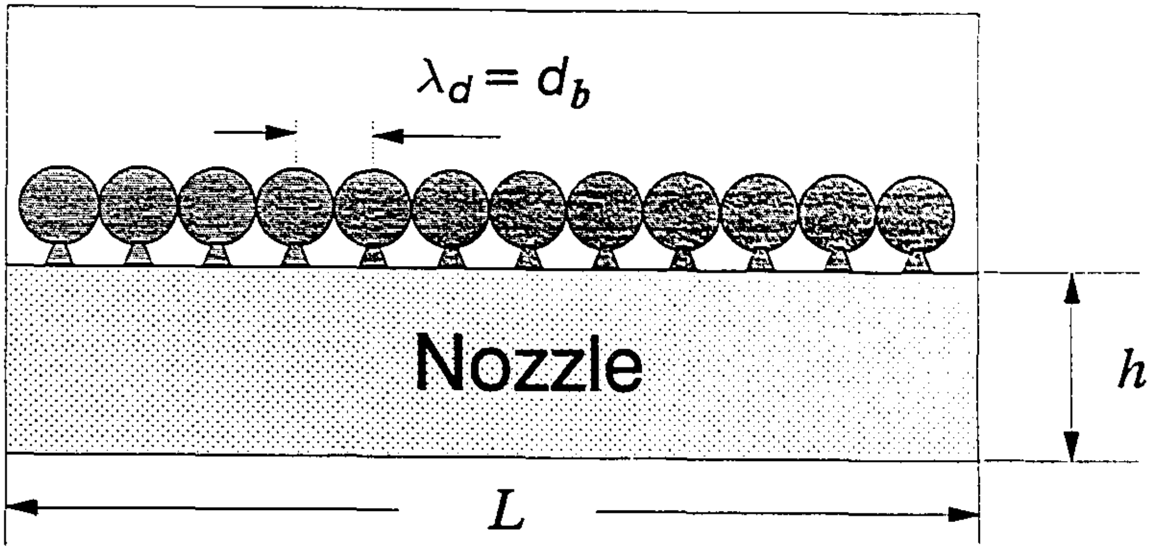

Figure 9.20 Schematic drawing of the critical transition condition between the regular bubble regime and the coalescence regime.

formation happens when the diameter of the bubble, d_b, times the number of bubble sources, N, is equal to the length of the slot L, i.e., the distance between the bubble sources (or dangerous wavelength) is equal to the diameter of the bubble, Figure 9.20. Thus, by equating the dangerous wavelength, λ_d, of Equation (225) to the diameter of the bubble, d_b, of Equation (230), we have following expression for the critical transformation condition:

$$Q_d = \frac{Q_t}{L\, W^{3/2}\, g^{1/2}} = 11.13 \left[\frac{\rho_l}{\rho_g}\right]^{0.13} \left[\frac{\sigma}{\rho_l\, W^2\, g}\right]^{0.21} \tag{231}$$

where Q_d is defined as dimensionless gas flow rate.

The comparison between measured and calculated dimensionless flow rate, Q_d, for the transformation between the regular and coalescence bubble formation for the fifteen experiments is presented in Figure 9.21. Clearly, Equation (231) is really an excellent representation for the critical transformation condition.

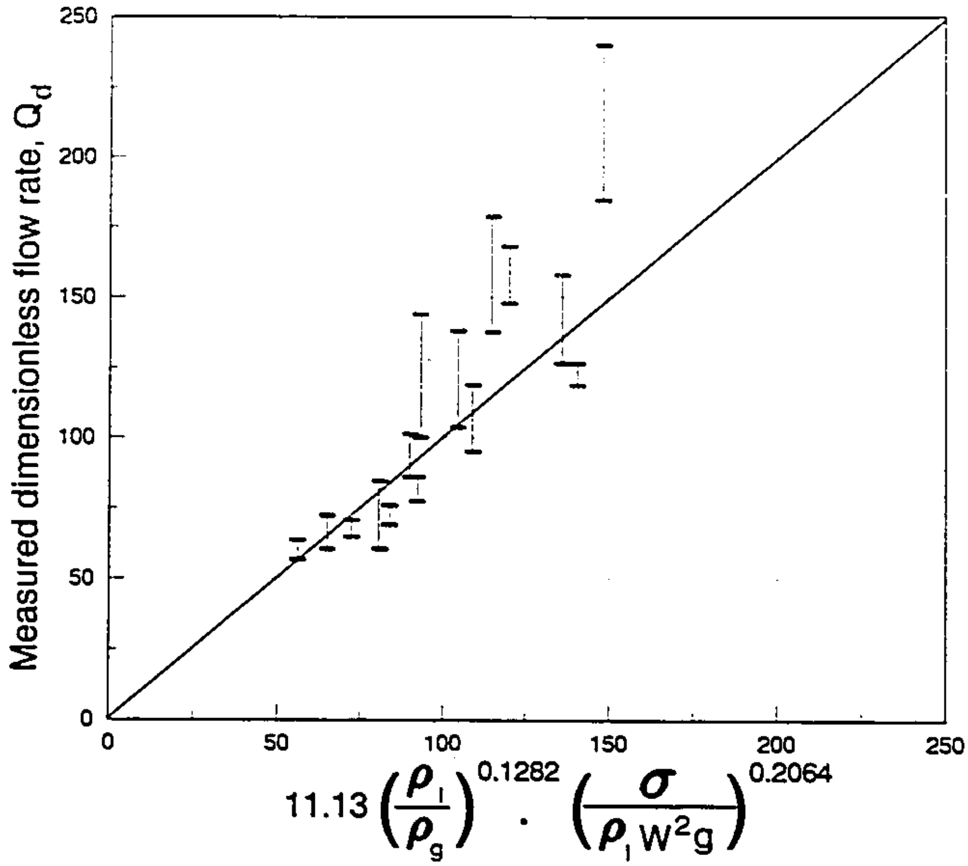

Figure 9.21 The comparison between measured and predicted critical transition condition.

9.5 BUBBLE FORMATION IN THE GAS GLOBE REGIME

In the coalescence bubble formation regime, although coalescence between bubbles happens, the bubble sources are still discontinuously distributed along the slot. As gas flow rate is increased, the bubble sources become closer to each other and the coalescence between the bubbles becomes significant. Finally at certain flow rate, a continuous gas-liquid blanket extending the length of the slot is formed; and gas globe regime is reached, Figure 9.22. This blanket is unstable from the Rayleigh-Taylor instability point of view. It breaks into multiple large gas bubbles at separate nodes with a characteristic wavelength $\lambda_{d,Taylor}$, Equation (30), which is 2.95cm for water-gas and 1.87cm for methyl alcohol-gas.

Since following relationship for the number of nodes, N_{node} should be hold:

$$\frac{L}{\lambda_{d,\,Taylor}} - 1 < N_{node} < \frac{L}{\lambda_{d,\,Taylor}} + 1 \tag{232}$$

it is expected that $5 \leq N_{node} \leq 7$ for water-gas and $9 \leq N_{node} \leq 11$ for methyl alcohol-gas for a $L = 19.05$cm slot. As shown in Figure 8.7 and Figure 8.14, the experiments really gave $N_{node}=5$ for water-gas and $N_{node}=10$ for methyl alcohol-gas. Experimental determined number of nodes (Table A-1 - Table A-15) for the fifteen experiments is listed in Table 9.3. Because the gas globe regime can be considered as the fully developed coalescence bubble formation regime, no attempts were made to obtain a critical transition condition between the coalescence regime and gas globe regime.

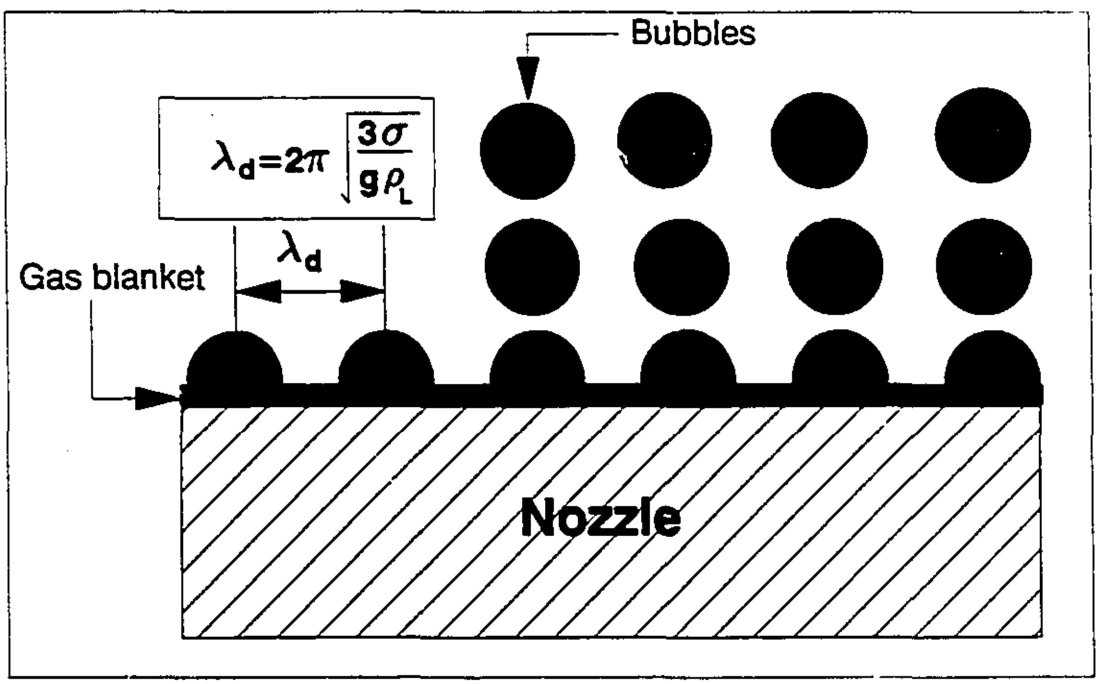

Figure 9.22 Schematic drawing of the gas globe regime.

Table 9.3 Experimental Determined Node Number for Gas Globe Regime

	Exp. No.	Flow Rate	N_{node}
water-gas	1	39.3	7
		50.7	6-8
	2	52.8	6-6
		64.4	5-6
	3	28.6	5-7
		24.6	6-6
	14	25	8-8
		50	6-7
Methyl alcohol-gas	6	14	8-8
		18	9-10
		22.8	7-10
		32.4	8
	7	10.5	8-8
		15	8-9
	10	28	6-7
		25	8
		20	7

Table 9.4 gives the most dangerous wavelengths of globe regime for several liquid metals according to Equation (30). Clearly, lead has the shortest wavelength because of highest density and lowest surface tension.

Table 9.4 Calculated Dangerous Wavelengths for Gas Globe Regime

	Density (g/cm^3)	Surface tension (dyn/cm)	λ_d (cm)	Node number for L=20cm $L/\lambda_d-1 < N_{node} < L/\lambda_d+1$
Methyl alcohol	0.786	23	1.87	9-11
Water	1	72	2.95	6-8
Lead	10.5	440	2.25	8-10
Aluminium	2.4	910	6.76	2-4
Nickel	7.9	1780	5.22	3-5
Iron	7.0	1900	5.73	3-5
Copper	8.0	1300	4.43	4-6

9.6 CONCLUSIONS

1. When gas was injected into liquid through a very narrow slot, three gas bubble formation regimes were observed. They were *regular bubble formation regime, coalescence bubble formation regime and gas globe regime*.

2. In the regular bubble formation regime, the bubble formation is dominated by surface tension and inertial forces. The bubble volume is predicted by Equation (207). The average number of the bubble sources increases with an increase in the gas flow rate. The dimensionless distance between the bubble sources is correlated to Equation (225).

3. In the coalescence bubble formation regime, the bubble formation is dominated by the inertial force only. The bubble diameter is predicted by Equation (230).

4. The critical transformation condition between the regular bubble formation regime and coalescence bubble formation is described by Equation (231).

5. In the gas globe regime, the node number is dominated by Rayleigh-Taylor instability, and is described by Equation (232).

6. The pressure drop across a slot can be described by Hagen-Poiseuille law.

CHAPTER 10

CONCLUSIONS AND SUGGESTIONS FOR FUTURE RESEARCH

10.1 CONCLUSIONS

10.1.1 HYDRODYNAMIC INSTABILITIES OF A CYLINDRICAL INTERFACE

1. The Rayleigh-Taylor instability of a cylindrical interface between two inviscid fluids was analyzed. A general dispersion equation, relating wavenumber, k, to growth rate, G, was derived:

$$G^2 = \frac{\sigma k \left[k^2 - \frac{1}{R_o^2} - \frac{(\rho_2 - \rho_1) g \, Cos(\theta)}{\sigma} \right]}{\rho_1 \alpha_1 + \rho_2 \alpha_2}$$

2. A mathematical model for predicting the dominated unstable wavelength during film boiling on a horizontal cylindrical heater was proposed:

$$\Lambda_{d,boiling} = \frac{2.16 + \sqrt{3}\, 0.4672\, \Pi^{1.491}}{1 + 0.4672\, \Pi^{1.491}} \cdot \frac{2\pi}{\left[1 + \frac{1}{2\Pi^2}\right]^{1/2}}$$

Excellent agreement between experimental results and predicted data was obtained.

3. Experiments and theoretical analysis were carried out to measure and to predict the dominated unstable wavelength during cylindrical liquid film breakup. It was found that the distance between the nodes decreases with a decrease in the radius of the test tube. The most dangerous wavelength is predicted successfully by a closed-form equation:

$$\Lambda_{d,droplet} = \frac{1.435 + 0.072\sqrt{3}\,\Pi^{1.877}}{1 + 0.072\,\Pi^{1.877}} \cdot \frac{2\pi}{\left[1 + \dfrac{1}{\Pi^2}\right]^{1/2}} \tag{235}$$

Therefore, Lee's experimental result and theoretical analysis were confirmed to be wrong.

4. The Rayleigh-Taylor instability of a cylindrical interface between two viscous fluids was analyzed. A general dispersion equation, relating wavenumber, k, to growth rate, G, was obtained with a successful application to film boiling on a cylindrical heater.

5. The Kelvin-Helmholtz instability of a cylindrical interface between two inviscid fluids was described mathematically. A general dispersion equation, relating wavenumber, k, to growth rate, G, was given:

$$\frac{G}{k} = -\frac{\rho_2\,\delta_2\,U_2 + \rho_1\,\delta_1\,U_1}{\rho_1\,\delta_1 + \rho_2\,\delta_2}$$

$$\pm\left[-\frac{\rho_1\rho_2\delta_1\delta_2(U_1-U_2)^2}{(\rho_1\delta_1+\rho_2\delta_2)^2} + \frac{\left[k^2-\dfrac{(1-n^2)}{R_o^2}-\dfrac{(\rho_2-\rho_1)g\cos(\theta)}{\sigma}\right]\sigma}{(\rho_1\delta_1+\rho_2\delta_2)k}\right]^{1/2}$$

The breakup of a liquid-in-air jet and an air-in-liquid jet were discussed. It was found that the dominated wavelength decreases rapidly with an increase in the jet velocity.

10.1.2 GAS INJECTION PHENOMENA THROUGH A VERY NARROW SLOT

1. A modified bubble formation model for the prediction of bubble size was proposed with considerations of surface force and inertial force. The bubble volume, V_f, was calculated from:

$$V_{fb} - 0.0474 \frac{Q^2}{g} V_{fb}^{-2/3} = \frac{2 \pi r_o \sigma \cos(\theta_c)}{\rho_l g}$$

and

$$\sqrt{3}\, r_o = \frac{4g}{11 Q^2}(V_f^2 - V_{fb}^2) - 0.62\,(V_f^{1/3} - V_{fb}^{1/3}) - \frac{32 \pi r_o \sigma \cos(\theta_c)}{11 Q^2 \rho_l}(V_f - V_{fb})$$
$$+ \frac{1}{Q}\left[\left[\frac{32 \pi r_o \sigma \cos(\theta_c)}{11 Q \rho_l} V_{fb} + 0.207\, Q\, V_{fb}^{1/3} - \frac{8g}{11Q} V_{fb}^2\right]\right] \ln\left[\frac{V_f}{V_{fb}}\right]$$

2. When gas was injected into liquid through a very narrow slot, three gas bubble formation regimes were observed. They were *regular bubble formation regime, coalescence bubble formation regime and gas globe regime.*

3. In the regular bubble formation regime, the bubble formation is dominated by both surface tension force and inertial force. The bubble volume was predicted successfully by a modified bubble formation model. The average number of the bubble sources increases with an increase in the gas flow rate. The dimensionless distance between the bubble sources was correlated by:

$$\frac{\lambda_d}{W} = 18.78 \left[\frac{\rho_l}{\rho_g}\right]^{0.15} We^{-0.23}$$

4. In the coalescence bubble formation regime, the bubble formation is

dominated by the inertial force only. The bubble diameter was predicted by:

$$d_b = 1.217 \frac{Q_t^{2/3}}{g^{1/3} L^{2/3}}$$

5. The critical transition condition between the regular bubble formation regime and coalescence bubble formation was described by:

$$Q_d = \frac{Q_t}{L\, W^{3/2} g^{1/2}} = 11.13 \left[\frac{\rho_l}{\rho_g} \right]^{0.13} \left[\frac{\sigma}{\rho_l W^2 g} \right]^{0.21}$$

6. In the gas globe regime, the node number is dominated by the most dangerous wavelength for the Rayleigh-Taylor instability of a plane interface, i.e.,

$$\frac{L}{\lambda_{d,\, Taylor}} - 1 < N_{node} < \frac{L}{\lambda_{d,\, Taylor}} + 1$$

7. The pressure drop across a slot followed the Hagen-Poiseuille law.

10.2 CLAIMS FOR ORIGINAL RESEARCH

This thesis covers fundamental theory, experiments and data analysis. Theoretical analysis of the hydrodynamic interfacial instabilities of cylindrical interfaces were first carried out with applications to boiling heat transfer, liquid film breakup and gas injection phenomena through a very narrow slot. Then, gas injection phenomena through a very narrow slot were comprehensively examined by means of experiments, dimensional analysis and mathematical modelling.

In particular, I claim the following original contributions accomplished during this study.

1. The Rayleigh-Taylor instability and Kelvin-Helmholtz instability of a ***cylindrical*** interface between two inviscid fluids or two viscous fluids were analyzed based on first principles (momentum and continuity equations). Dispersion equations, relating wavenumber, k, to growth rate, G, were derived for various conditions.

2. Mathematical models for predicting the dominant wavelengths during film boiling on a ***cylindrical*** heater and during the breakup of a liquid film around a ***cylindrical*** body were proposed for both inviscid and viscous fluids.

3. Experimental research confirmed that dominant unstable wavelength during ***cylindrical*** liquid film breakup on a ***cylindrical*** body decreases with a decrease in the radius of the cylindrical body.

4. A modified two-stage bubble formation model was proposed with considerations of surface tension and inertial forces to predict the bubble formation through a narrow slot.

5. Gas injection phenomena through a very narrow slot were extensively examined by means of experiments, mathematical modelling and dimensional analysis. Three different bubble formation regimes were described.

6. Mathematical description for each of the bubble formation regimes was developed.

7. Gas bubble formation through a very narrow slot is attributed to the Rayleigh-Taylor instability of a cylindrical interface.

10.3 SUGGESTIONS FOR FUTURE RESEARCH

1. Contact angle plays an important role in the bubble formation through a very narrow slot, especially for the regular bubble formation regime. Experiments should be carried out to clarify its effect.

2. The effect of liquid viscosity on the gas injection phenomena through a very narrow slot needs to be examined.

3. Gas injection phenomena through a very narrow slot should be explored in the liquid metal systems.

APPENDIX I

BESSEL FUNCTION

When n is an integer, the Bessel functions $I_n(X)$ and $K_n(X)$ can be expressed as:

$$I_n(X) = \sum_{m=0}^{\infty} \frac{\left(\frac{X}{2}\right)^{n+2m}}{m!\,(n+m)!} \tag{243}$$

$$K_o(X) = -\left[0.577216 + \ln\left(\frac{x}{2}\right)\right] I_o(x) + \sum_{m=1}^{\infty} \frac{1}{(m!)^2} \left(\frac{x}{2}\right)^{2m} \left[1 + \frac{1}{2} + \dots + \frac{1}{m}\right] \tag{244}$$

$$K_n(X) = (-1)^{n+1}\left[0.577216 + \ln\left(\frac{x}{2}\right)\right] I_n(x) + \frac{1}{2}\sum_{m=0}^{n-1} \frac{(-1)^m\,(n-m-1)!}{m!} \left(\frac{x}{2}\right)^{2m-n}$$
$$+ \frac{(-1)^n}{2} \sum_{m=0}^{\infty} \frac{\left(\frac{X}{2}\right)^{2m+n}}{m!\,(n+m)!} \left(\sum_{i=1}^{m} \frac{1}{i} + \sum_{i=1}^{m+n} \frac{1}{i}\right) \tag{245}$$

The relationships between Bessel functions and their differentials are

$$\frac{dI_n(X)}{dX} = \frac{I_{n-1}(X) + I_n(X)}{2} \quad , \quad \frac{dI_0(X)}{dX} = I_1(X) \tag{246}$$

$$\frac{dK_n(X)}{dX} = -\frac{K_{n-1}(X) + K_n(X)}{2} \quad , \quad \frac{dK_0(X)}{dX} = -K_1(X) \tag{247}$$

When X is larger (e.g. $X>7$ for n=0 or 1), the $I_n(X)$ and $K_n(X)$ can be approximately expressed as:

$$I_n(X) = \frac{\exp(X)}{\sqrt{2\pi X}} \left[1 - \frac{(4n^2-1)}{8X} + \frac{(4n^2-1)(4n^2-9)}{128X^2} \right] \tag{248}$$

$$K_n(X) = \frac{\sqrt{\dfrac{\pi}{2X}}}{\exp(X)} \left[1 + \frac{(4n^2-1)}{8X} + \frac{(4n^2-1)(4n^2-9)}{128X^2} \right] \tag{249}$$

APPENDIX II

EXPERIMENTAL RESULTS FOR GAS INJECTION

In this appendix the original experimental results for the fifteen experiments listed in Table 8.2 are given. In these tables Q_t is the total gas flow rate; d_{above} is the distance above the nozzle surface at which the size of the bubble was measured; N the measured number of bubble sources; N_{error} is the error for the measurements of the bubble sources; V_b is the measured bubble volume after Equation (208) ; d_d is the measured average bubble diameter; K_b is the estimated coefficient from measured bubble size in the coalescence bubble formation regime according to Equation (229); N_{node} is the measured node number in the gas globe regime.

Table A-1 Experimental Results for No.1 Experiment

Regular bubble formation regime					
Q_t (slpm)	Film No.	d_{above} (mm)	N	V_b (mm^3)	d_b (mm)
0.1	33	2	7	4.504	2.049
0.1	34	2	6	4.678	2.075
0.1	35	2	8	4.569	2.059
0.4	8	2	18	5.036	2.127
0.4	9	2	17	5.376	2.174
0.4	10	2	17	4.747	2.085
1.1	5	2	29	6.436	2.308
1.1	6	2	30	6.533	2.319
1.1	7	2	29	6.117	2.269

1.1	2-30	2	26	6.254	2.286
1.1	2-31	2	27		
1.9	11	2	41	7.049	2.379
1.9	12	2	38	6.676	2.336
1.9	13	2	38	8.487	2.531
2.3	2-36	2	45	8.737	2.555
2.3	2-37	2	43		
2.4	14	2	49	7.924	2.474
2.4	15	2	49	7.643	2.444
2.4	16	2	40	7.989	2.480
2.9	17	2	52	8.800	2.562
2.9	18	2	60	8.184	2.500
2.9	19	2	47	11.258	2.781
3.3	2-32	2	49		
3.3	2-33	2	49	10.326	2.702
3.6	20	2	59	8.507	2.533
3.6	21	2	54	9.422	2.620
3.6	22	2	54	9.091	2.589
5	23	2	61	8.858	2.567
5	24	2	60	10.042	2.677
Coalescence bubble formation regime					
			K_b value		
7.2	25	3	0.67478	32.468	3.958
7.2		5	0.657107	31.063	3.900
7.2	26	3	0.586218	25.621	3.660
7.2		5	0.664156	31.620	3.923
8.3	27	3	0.523355	28.249	3.779

8.3		5	0.530721	28.914	3.808
8.3	28	3	0.569323	32.504	3.960
8.3		5	0.66565	42.177	4.319
11	29	3	0.434732	36.420	4.113
11		5	0.516698	48.569	4.527
11	30	4	0.517932	48.763	4.533
Gas globe formation regime					
		N_{node}			
39.3	1-4	7			
50.7	1-37	8			
50.7	1-36	6			

Table A-2 Experimental Results for No.2 Experiment

Regular bubble formation regime					
Q_t (slpm)	Film No.	d_{above} (mm)	N	V_b (mm^3)	d_b (mm)
0.286	1	2	5	5.644	2.209
0.286	2	2	4	6.932	2.366
0.286	3	2	5	6.405	2.304
0.715	4	2	16	7.861	2.467
0.715	5	2	14	8.493	2.531
0.715	6	2	16	7.100	2.385
1.502	7	2	23	10.711	2.735
1.502	8	2	24	10.518	2.718
1.502	9	2	23	11.778	2.823
1.788	10	2	26	15.983	3.125
1.788	11	2	25	12.236	2.859
1.788	12	2	26	13.550	2.958

2.860	13	2	32	15.649	3.103
2.860	14	2	33	13.619	2.963
2.860	15	2	32	15.745	3.110
4.004	16	2	39	19.704	3.351
4.004	17	2	36	21.844	3.468
4.004	18	2	37	20.770	3.410
4.576	19	2	41	19.131	3.318
4.576	20	2	41	17.375	3.213
4.576	21	2	39	18.695	3.293
5.720	22	2	45	24.073	3.582
5.720	23	2	42	26.210	3.685
5.720	24	2	44	23.842	3.571
7.436	25	2	47	22.312	3.493
7.436	26	2	47	26.176	3.684
7.436	27	2	44		
Coalescence bubble formation regime					
			K_b value		
8.437	1-28	10	0.696	46.984	4.477
8.437	1-29	10	0.783	57.115	4.778
8.437	1-30	10	0.666	43.648	4.368
9.724	1-31	10	0.631	52.924	4.658
9.724	1-32	10	0.795	77.758	5.296
9.724	1-33	10	0.823	82.532	5.402
11.297	1-34	10	0.703	85.497	5.466
11.297	1-35	10	0.634	71.980	5.161
11.297	1-36	10	0.643	73.845	5.205
13.299	1-37	10	0.581	86.219	5.481

13.299	2-1	10	0.684	113.266	6.003
13.299	2-2	10	0.623	96.996	5.701
15.158	2-3	10	0.866	218.128	7.469
15.158	2-4	10	0.677	144.632	6.513
15.158	2-5	10			
Gas globe regime					
		N_{node}			
52.767	2-20	6			
52.767	2-21	6			
64.350	2-22	5			
64.350	2-23	6			

Table A-3 Experimental Results for No.3 Experiment

Regular bubble formation regime					
Q_t (slpm)	Film No.	d_{above} (mm)	N	V_b (mm^3)	d (mm)
0.015	4	2	3	1.019	1.249
0.015	5	2	3	0.921	1.207
0.100	6	2	16	1.124	1.290
0.100	7	2	17	0.888	1.193
0.100	8	2	15	0.936	1.214
0.200	1	2	23	0.928	1.210
0.200	2	2	25	0.993	1.238
0.200	3	2	23	0.982	1.233
0.350	9	2	40	1.473	1.412
0.350	10	2	39	1.502	1.421
0.350	11	2	37	1.424	1.396
0.600	12	2	43	2.296	1.637
0.600	13	2	47	2.581	1.702

0.600	14	2	45	2.508	1.686
1.000	15	2	52	2.507	1.686
1.000	16	2	53	2.737	1.735
1.000	17	2	52	3.075	1.804
1.500	18	2	65	2.649	1.717
1.500	19	2	64	3.856	1.946
1.500	20	2	70	3.585	1.899
2.200	21	2	79	3.407	1.867
2.200	22	2	70	4.445	2.040
2.200	23	2	74	3.982	1.967
2.900	24	2	80	4.960	2.116
2.900	25	2	86	4.547	2.055
2.900	26	2	85	3.871	1.948
3.200	27	2	90	4.775	2.089
3.200	28	2	92	3.754	1.928
Coalescence bubble formation regime					
			K_b value		
4.150	30	3	0.645	10.009	2.674
4.150	31	3	0.574	8.226	2.505
5.000	32	3	0.523	10.246	2.695
5.000	33	3	0.562	11.536	2.803
6.650	34	3	0.586	21.885	3.470
6.650	35	3	0.473	15.312	3.081

Table A-4 Experimental Results for No.4 Experiment

Regular bubble formation regime					
Q_t (slpm)	Film No.	d_{above} (mm)	N	V_b (mm^3)	d_b (mm)
0.014	5	2	3	1.674	1.473

0.072	3	2	10	1.506	1.422
0.072	4	2	13	1.352	1.372
0.429	6	2	29	1.456	1.406
0.429	7	2	31	1.401	1.388
0.429	8	2	29	1.326	1.363
0.787	9	2	42	2.641	1.715
0.787	10	2	41	2.251	1.626
0.787	11	2	41	2.124	1.595
1.073	12	2	46	2.422	1.666
1.073	13	2	47	2.748	1.738
1.073	14	2	46	2.493	1.682
1.573	15	2	52	3.602	1.902
1.573	16	2	52	3.655	1.911
1.573	17	2	54	3.253	1.838
2.145	19	2	59	5.021	2.125
2.145	20	2	57	4.917	2.110
2.145	21	2	56	4.652	2.071
3.003	22	2	64	6.939	2.366
3.003	23	2	63	5.910	2.243
3.003	24	2	62	5.759	2.224
3.575	25	2	66	7.380	2.416
3.575	26	2	64	7.496	2.428
3.575	27	2	64	7.009	2.374
4.290	28	2	71	9.453	2.623
4.290	29	2	69	8.203	2.502
4.290	30	2	70	8.240	2.506
Coalescence bubble formation regime					

			K_b		
5.577	32	3	0.587	15.451	3.090
5.577	33	3	0.527	12.903	2.910
5.577	34	3	0.535	13.216	2.933
6.435	35	3	0.546	18.212	3.264
6.435	36	3	0.501	15.805	3.114

Table A-5 Experimental Results for No.5 Experiment

Regular bubble formation regime					
Q_t (slpm)	Film No.	d_{above} (mm)	N	V_b (mm^3)	d_b (mm)
0.020	'1	2	12	0.666	1.083
0.020	'2	2	11	0.674	1.088
0.020	'3	2	11	0.711	1.107
0.080	1-7	2	28	0.549	1.016
0.080	1-8	2	27	0.612	1.053
0.080	1-9	2	25	0.612	1.053
0.150	1-10	2	38	0.848	1.174
0.150	1-11	2	39	0.792	1.148
0.150	1-12	2	38	0.880	1.189
0.250	1-4	2	46	0.922	1.208
0.250	1-5	2	44	1.021	1.249
0.250	1-6	2	45	0.911	1.203
0.400	1-1	2	59	1.384	1.383
0.400	1-2	2	60	1.273	1.345
0.400	1-3	2	63	1.283	1.348
0.500	1-16	2	60	1.340	1.368
0.500	1-17	2	64	1.325	1.363
0.500	1-18	2	58	1.355	1.373

0.600	1-13	2	71	1.555	1.437
0.600	1-14	2	71	1.576	1.444
0.600	1-15	2	64	1.559	1.439
0.700	1-19	2	73	1.708	1.483
0.700	1-20	2	73	1.718	1.486
0.700	1-21	2	77	1.855	1.524
0.800	1-22	2	81	1.984	1.559
0.800	1-23	2	80	1.837	1.520
0.800	1-24	2	79	1.877	1.531
0.900	1-25	2	85	1.757	1.497
0.900	1-26	2	85	1.719	1.486
0.900	1-27	2	77	1.831	1.518
1.100	1-28	2	93	1.915	1.541
1.100	1-29	2	87	1.696	1.480
1.100	1-30	2	88	1.631	1.460
1.400	1-31	2	98	2.526	1.690
1.400	1-32	2	99	2.672	1.722
Coalescence bubble formation regime					
			K_b		
1.800	1-33	6	0.834	2.890	1.767
1.800	1-34	6	0.856	3.016	1.793
1.800	1-35	6	0.890	3.219	1.832
2.050	1-36	6	0.955	4.692	2.077
2.050	1-37	6	0.858	3.929	1.958
2.600	2-1	6	0.810	5.743	2.222
2.600	2-2	6	0.745	4.993	2.121
2.600	2-3	6	0.815	5.799	2.229

3.000	2-4	6	0.714	6.191	2.278
3.000	2-5	6	0.685	5.785	2.227
3.000	2-6	6	0.691	5.858	2.237
3.800	2-7	6	0.787	11.695	2.816
3.800	2-8	6	0.640	8.283	2.510
3.800	2-9	6	0.704	9.703	2.646
4.300	2-10	6	0.740	13.491	2.954
4.300	2-11	6	0.619	10.016	2.674
4.300	2-12	6	0.755	13.958	2.987
5.400	2-13	6	0.729	20.783	3.411
5.400	2-14	6	0.613	15.573	3.098
Gas globe regime					
		N_{node}			
14.000	2-25	8			
14.000	2-26	8			
14.000	2-27	8			
18.000	2-28	9			
18.000	2-29	10			
18.000	2-30	9			
22.800	2-31	7			
22.800	2-32	9			
22.800	2-33	10			
32.400	2-34	8			

Table A-6 Experimental Results for No.6 Experiment

Regular bubble formation regime					
Q_t (slpm)	Film No.	d_{above} (mm)	N	V_b (mm^3)	d_b (mm)
0.650	1	2	56	1.581	1.445

0.650	2	2	56	1.361	1.375
0.650	3	2	59	1.358	1.374
0.020	13	2	6	0.388	0.905
0.020	14	2	6	0.406	0.919
0.020	15	2	6	0.406	0.919
0.080	10	2	18	0.339	0.865
0.080	11	2	18	0.368	0.889
0.080	12	2	18	0.396	0.911
0.240	7	2	40	0.488	0.977
0.240	8	2	39	0.675	1.088
0.240	9	2	40	0.638	1.068
0.380	4	2	50	1.121	1.289
0.380	5	2	49	0.934	1.213
0.380	6	2	51	0.759	1.132
0.900	16	2	65	1.450	1.404
0.900	17	2	63	1.487	1.416
0.900	18	2	62	1.726	1.488
1.200	19	2	80	1.971	1.556
1.200	20	2	78	1.960	1.553
1.200	21	2	82	1.786	1.505
1.600	22	2	91	2.270	1.631
1.600	23	2	97	2.526	1.690
1.600	24	2	90	2.175	1.608
Coalescence bubble formation regime					
			K_b		
2.500	28	6	0.721	4.373	2.029
2.500	29	6	0.780	4.979	2.119

3.000	30	6	0.670	5.569	2.199
3.000	31	6	0.643	5.196	2.149
3.500	32	6	0.746	9.059	2.586
4.000	33	6	0.596	8.138	2.496
4.800	34	6	0.614	12.315	2.865
Gas globe regime					
		N_{node}			
28.600	2-15	7			
28.600	2-14	5			
24.600	2-13	6			
24.600	2-12	6			

Table A-7 Experimental Results for No.7 Experiment

Regular bubble formation regime						
Q_t (slpm)	Film No.	d_{above} (slpm)	N	N_{error}	V_b (mm^3)	d_d (mm)
0.046	25	2	28	3	0.096	0.568
0.046	26	2	26	3		
0.046	27	2	27	3		
0.090	22	2	35	5	0.158	0.671
0.090	23	2	38	5		
0.090	24	2	35	5		
0.130	16	2	53	5	0.164	0.679
0.130	17	2	53	5		
0.130	18	2	54	5		
0.175	19	2	57	5		
0.175	20	2	56	5		
0.175	21	2	58	5		
0.230	13	2	78	20	0.285	0.817

0.230	14	2	67	10	0.291	0.823
0.230	15	2	70	10		
0.350	28	2	81	10	0.468	0.964
0.350	29	2	81	10		
0.350	30	2	79	10		
0.500	31	2	86	10	0.495	0.982
0.500	32	2	85	10		
0.500	33	2	85	10		
0.800	34	2	109	15	0.748	1.126
0.800	35	2	114	15		
0.800	36	2	101	15		
0.650	1	2	96	10		
0.650	2	2	101	10		
0.650	3	2	94	10		
0.700	37	2	98	10		
1.000	4	2	117	10	0.728	1.116
1.000	5	2	114	10		
1.000	6	2	114	10		
Coalescence bubble formation regime						
		K_b				
1.500	10	6 0.705			1.516	1.425
1.500	11	6 0.816			1.934	1.546
1.950	7	6 0.601			1.966	1.554
1.950	8	6 0.620			2.068	1.581
2.600	13	6 0.645			3.922	1.957
2.600	14	6 0.520			2.743	1.737
Gas globe formation regime						

		N_{node}			
10.500	1-17	8			
10.500	1-18	8			
15.000	1-19	9			
15.000	1-20	8			
15.000	1-21	8			

Table A-8 Experimental Results for No.8 Experiment

Regular bubble formation regime						
Q_t (slpm)	Film No.	d_{above} (mm)	N	N_{error}	V_b (mm^3)	d_d (mm)
0.070	25	2	37	3	0.143	0.649
0.070	26	2	38	3		
0.070	27	2	36	3		
0.160	28	2	43	2	0.156	0.668
0.160	29	2	44	2		
0.160	30	2	46	2		
0.230	31	2	56	5	0.209	0.736
0.230	32	2	59	5		
0.230	33	2	55	5		
0.310	22	2	69	5	0.267	0.799
0.310	23	2	63	5		
0.310	24	2	70	5		
0.400	34	2	72	10	0.265	0.797
0.400	35	2	76	10		
0.400	36	2	82	10		
0.480	37	2	80	10	0.330	0.857
0.480	1	2	84	10		
0.480	2	2	84	10		

0.590	3	2	96	10	0.402	0.916
0.590	4	2	100	10		
0.590	5	2	93	10		
0.700	6	2	99	10	0.467	0.963
0.700	7	2	118	10		
0.700	8	2	110	10		
0.820	9	2	114	10	0.506	0.989
0.820	10	2	112	10		
0.820	11	2	114	10		
0.880	12	2	109	10		
0.880	13	2	123	10		
0.880	14	2	110	10		
1.001	21	2	122	10		
1.001	22	2	128	10		
1.001	23	2	126	10		
1.144	24	2	131	10		
1.144	25	2	128	10		
1.144	26	2	125	10		
1.287	27	2	132	10		
1.287	28	2	128	10		
1.287	29	2	136	10		
Coalescence bubble formation regime						
			K_b			
1.573	18	6	0.699		1.642	1.464
2.002	30	6	0.587		1.988	1.560
2.002	31	6	0.593		2.026	1.570
2.717	33	6	0.476		2.585	1.703

Table A-9 Experimental Results for No.9 Experiment

Regular bubble formation regime						
Q_t (slpm)	Film No.	d_{above} (mm)	N	N_{error}	V_b (mm^3)	d_d (mm)
0.858	23	5	7	2	44.795	4.406
0.858	24	5	7	2	42.290	4.323
0.858	25	5	7	2	39.411	4.222
1.430	7(2)	5	10	2	46.713	4.468
1.430	8(2)	5	10	2	47.546	4.495
1.430	9(2)	5	10	2	54.176	4.695
2.431	1(2)	5	12	3	55.632	4.736
2.431	2(2)	5	13	3	80.024	5.347
2.431	3(2)	5	14	3	62.963	4.936
3.000	10(2)	5	13	3	71.199	5.142
3.000	11(2)	5	13	3	50.153	4.575
3.000	12(2)	5	14	3	52.596	4.649
3.861	35	5	16	3	58.735	4.823
3.861	36	5	16	3	74.456	5.220
3.861	37	5	16	3	75.370	5.241
5.720	26	5	20	3	76.076	5.257
5.720	27	5	21	3	83.730	5.428
5.720	28	5	18	3	79.119	5.326
6.864	32	5	19	3	120.985	6.136
6.864	33	5	20	3	93.813	5.638
6.864	34	5	20	3		
8.720	16(2)	5	21	5		
8.720	17(2)	5	25	3		
8.720	18(2)	5	24	5		
Coalescence bubble formation regime						

			K_b		
14.300	24(2)	15	1.198	333.174	8.601
14.300	25(2)	15	1.331	397.186	9.120

Table A-10 Experimental Results for No.10 Experiment

Regular bubble formation regime						
Q_t (slpm)	Film No.	d_{above} (mm)	N	N_{error}	V_b (mm^3)	d_d (mm)
1.050	18	5	16	2	18.816	3.300
1.050	19	5	16	2	14.630	3.034
2.400	13	5	25	3	33.719	4.008
2.400	14	5	25	3	28.998	3.812
2.400	15	5	25	3		
3.150	10	5	30	3		
3.150	11	5	29	3	34.680	4.046
3.150	12	5	31	3	20.728	3.408
4.000	7	5	33	3		
4.000	8	5	28	3	56.602	4.764
4.000	9	5	31	3	51.903	4.628
4.500	16	5	32	3		
5.000	4	5	33	3	40.829	4.272
5.000	5	5	34	3		
5.000	6	5	34	3	34.026	4.020
6.000	1	5	34	3		
6.000	2	5	33	3		
6.000	3	5	34	3		
Gas globe formation regime						
		N_{node}				
24	28	7				

25	28	6			
26	25	8			
27	20	7			

Table A-11 Experimental Results for No.11 Experiment

Regular bubble formation regime						
Q_t (slpm)	Film No.	d_{above} (mm)	N	N_{error}	V_b (mm^3)	d_d (mm)
2.860	16	5	21	3	42.651	4.335
2.860	17	5	20	3	37.362	4.148
2.860	18	5	23	3		
2.860	19	5	24	3		
4.720	31	5	26	3	51.794	4.625
4.720	32	5	24	3	51.261	4.609
4.720	33	5	23	3	78.410	5.310
6.150	37	5	29	5	83.126	5.415
6.150	1	5	30	5	56.514	4.761
6.150	2	5	26	5	91.191	5.585
7.600	3	5	33	5	87.745	5.513
7.600	4	5	31	5		
7.600	5	5	29	2		
9.152	34	5	32	5		
9.152	35	5	36	4		
9.152	36	5	36	5		
Coalescence bubble formation regime						
			K_b			
14.157	9	14	1.203		329.140	8.566
14.157	10	14	1.006		244.263	7.756

19.591	11	14	0.943	419.689	9.289
19.591	12	14	1.216	641.692	10.701
19.591	13	14	1.299	715.844	11.099

Table A-12 Experimental Results for No.12 Experiment

Regular bubble formation regime						
Q_t (slpm)	Film No.	d_{above} (mm)	N	N_{error}	V_b (mm^3)	d_d (mm)
0.400	4	5	18	3	6.680	2.337
1.100	1	5	28	5	9.198	2.600
1.100	2	5	27	5	8.937	2.575
1.100	3	5	26	5	8.231	2.505
1.550	35	5	32	5	9.978	2.671
1.550	36	5	37	5	9.779	2.653
1.550	37	5	34	5		
2.100	32	5	40	5	12.301	2.864
2.100	33	5	41	4	11.519	2.802
2.100	34	5	38	5		
2.700	29	5	41	5		
2.700	30	5	40	5	10.661	2.731
2.700	31	5	42	5	12.569	2.885
3.410	26	5	43	5	15.364	3.084
3.410	27	5	42	5	13.379	2.945
3.410	28	5	43	5		
4.200	23	5	45	5	15.674	3.105
4.200	24	5	46	5		
4.200	25	5	46	5	21.314	3.440
5.000	20	5	48	5	16.370	3.150
5.000	21	5	45	5		

5.000	22	5	45	5	23.603	3.559
Coalescence bubble formation regime						
			K_b			
7.000	6	1	1.121		71.534	5.150
7.000	7	1	1.177		77.567	5.291
7.000	8	1	0.937		53.037	4.662

Table A-13 Experimental Results for No.13 Experiment

Regular bubble formation regime						
Q_t (slpm)	Film No.	d_{above} (mm)	N	N_{error}	V_b (mm^3)	d_d (mm)
2.000	21	5	28	2	12.970	2.915
2.000	22	5	25	2	14.691	3.039
2.000	23	5	26	2		
2.860	15	5	32	4	19.738	3.353
2.860	16	5	32	4	19.315	3.329
2.860	17	5	32	5		
3.860	18	5	34	5		
3.860	19	5	36	5	19.460	3.337
3.860	20	5	34	5	18.968	3.309
5.150	12	5	39	5	30.795	3.889
5.150	13	5	41	5	24.705	3.614
5.150	14	5	37	5		
Coalescence bubble formation regime						
			K_b			
6.292	26	10	1.142		59.588	4.846
6.292	27	10	1.469		90.634	5.573
6.292	28	10	1.207		65.351	4.997

Table A-14 Experimental Results for No.14 Experiment

Regular bubble formation regime						
Q_t (slpm)	Film No.	d_{above} (mm)	N	N_{error}	V_b (mm^3)	d_d (mm)
0.300	16	5	7	1	6.838	2.355
0.300	17	5	9	2	7.348	2.412
0.300	18	5	9	2	5.855	2.236
0.600	13	5	12	1	7.423	2.420
0.600	14	5	12	1		
0.600	15	5	13	1		
2.400	10	5	26	3	13.027	2.919
2.400	11	5	28	3	9.953	2.669
2.400	12	5	26	3		
3.000	7	5	36	5	13.583	2.960
3.000	8	5	35	3		
3.000	9	5	38	5		
3.550	4	5	37	5		
3.550	5	5	36	5		
3.550	6	5	38	5	16.432	3.154
4.400	1	5	38	5	25.053	3.630
4.400	2	5	40	5	17.516	3.222
4.400	3	5	42	5		
5.000	19	5	45	5		
5.000	20	5	43	5	16.944	3.187
5.000	21	5	45	5		
Coalescence bubble formation regime						
			K_b			
7.000	22	10	0.869		46.746	4.469
7.000	23	10	0.974		56.624	4.764

Gas globe formation regime					
		N_{node}			
25.000	24	8			
25.000	25	8			
50.000	26	6			
50.000	27	7			

Table A-15 Experimental Results for No.15 Experiment

Regular bubble formation regime						
Q_t (slpm)	Film No.	d_{above} (mm)	N	N_{error}	V_b (mm^3)	d_d (mm)
0.286	12	5	4	2	14.039	2.993
0.286	13	5	4	2		
0.286	14	5	4	2		
0.720	9	5	10	1	16.792	3.177
0.720	10	5	12	1		
0.720	11	5	12	2	15.436	3.089
1.430	15	5	15	3	24.062	3.582
1.430	16	5	17	3	21.785	3.465
1.430	17	5	16	2		
2.045	6	5	19	1	20.600	3.401
2.045	7	5	20	1		
2.045	8	5	19	2	22.366	3.496
3.003	18	5	21	2	35.655	4.084
3.003	19	5	21	2	35.698	4.085
3.003	20	5	21	2		
3.575	3	5	23	2	41.379	4.291
3.575	4	5	22	2	34.890	4.054
3.575	5	5	22	2		

4.433	21	5	24	3		
4.433	22	5	25	2		
4.433	23	5	26	2		
5.291	34(1)	5	26	4	41.038	4.280
5.291	35(1)	5	27	4	56.510	4.761
5.291	36(1)	5	29	4		
5.863	29	5	32	3		
5.863	30	5	30	3		
5.863	31	5	31	3		
6.435	37(1)	5	32	5	43.724	4.371
6.435	1	5	30	5		
6.435	2	5	31	5	38.304	4.182
8.580	32	5	36	4	52.970	4.660
8.580	33	5	34	4		
8.580	34	5	36	4	45.928	4.443
Coalescence bubble formation regime						
			K_b			
11.154	32(1)	10	0.770		97.169	5.704
11.154	33(1)	10	0.880		121.298	6.142

APPENDIX III

TK-SOLVER PROGRAM FOR BUBBLE FORMATION THROUGH A NARROW SLOT

TK-SOLVER is a commercial software for solving various mathematical problems, such as non-linear equations, optimization and ordinary differential equations. All of the calculations made in the present thesis were done by TK-SOLVER. In TK-SOLVER there are eleven sheets; each sheet has a specific role and is furnished with tools that help accomplish the task. Some of the sheets are explained here:

- *Rule Sheet*

  The rule sheet contains the equations or rules for a model. Each row contains one rule and its status.

- *Variable Sheet*

  Each variable has its name and major attributes defined on one row of the variable sheet.

- *Unit Sheet*

  The unit sheet shows the relationships between different units.

- *Table Sheet*

  Table sheet shows the relationship between values of corresponding elements in different lists by displaying the values in columns and rows.

As an simple example, detailed TK-SOLVER programming of bubble formation model, Equations (205) and (207), is given in this appendix.

```
=================== RULE SHEET ==================== For Academic Use Only
S   Rule-----------------------------------------------------------------
*   dn=3^0.5/2*W
*   Vfb-0.0474*Q^2/g*Vfb^(-2/3)=2*W*SIGMA/RHOL/g
*   d=2*(3*Vfb/4/Pi())^(1/3)
*   11/4*dn*Q^2=TERM1+TERM2
*   TERM1=g*(Vf^2-Vfb^2)-1.705*Q^2*(Vf^(1/3)-Vfb^(1/3))-8*W*SIGMA/RHOL*(Vf-Vfb)
*   TERM2=(8*W*SIGMA/RHOL*Vfb+0.568*Q^2*Vfb^(1/3)-2*g*Vfb^2)*ln(Vf/Vfb)
*   df=2*(3*Vf/4/Pi())^(1/3)

=================== VARIABLE SHEET ================ For Academic Use Only
St  Input---- Name---- Output---- Unit-------- Comment------------------
L             Vfb      1.8376302  mm^3         Bubble volume during first stage
L   .001      Q                   L/min        Flow rate
    980       g                   cm/sec^2     Accelaration due to gravity
    125       W                   micromete    Spacing of the slot
    72        SIGMA               dyn/cm       Surface tension of liquid
    1         RHOL                g/cm^3       Density of liquid
L             d        1.5196836  mm           Bubble diameter of first stage
L   Vf                 2.1340683  mm^3         Final bubble volume
L   df                 1.5973616  mm           Final bubble diameter
    dn                 108.25318  micromete    Neck distance before bubble detac.
L   TERM1              -.0009835               1st part of bubble formation Equ.
L   TERM2              .00099177               2nd part of bubble formation Equ.

=================== UNIT SHEET ==================== For Academic Use Only
From------- To---------- Multiply By--- Add Offset---- Comment----------
cm          mm           10
cm^3        mm^3         1000
L/min       cm^3/sec     16.6666666667
cm          micromete    10000

=================== TABLE SHEET =================== For Academic Use Only
Name-------------------- Title------------------------------------------
bubble

=================== TABLE: bubble ================= For Academic Use Only
Screen or Printer:          Screen
Title:
Vertical or Horizontal:     Vertical
Row Separator:
Column Separator:
First Element:              1
Last Element:
List-------- Numeric Format---- Width---- Heading-----------------------
Q                                  10
Vf                                 10
df                                 10
```

TABLE: bubble — For Academic Use Only

Element	Q	Vf	df	
1	0	1.98440342		
2	.004	2.63971762	1.71469264	
3	.008	3.20883212	1.82999312	
4	.012	3.75429802	1.92830935	
5	.016	4.29833318	2.0172845	
6	.02	4.84770929	2.09980669	
7	.024	5.40459054	2.17731564	
8	.028	5.96942576	2.25066735	
9	.032	6.54199232	2.32044067	
10	.036	7.12182187	2.38706454	
11	.04	7.70838152	2.45087706	
12	.044	8.30114988	2.51215565	
13	.048	8.89964653	2.571134	
14	.052	9.50344057	2.62801242	
15	.056	10.1121501	2.68296472	
16	.06	10.7254383	2.73614311	
17	.064	11.3430077	2.78768181	
18	.068	11.9645958	2.83769993	
19	.072	12.5899694	2.88630365	
20	.076	13.2189212	2.93358807	
21	.08	13.8512654	2.97963872	
22	.084	14.4868355	3.02453282	
23	.088	15.125481	3.0683403	
24	.092	15.7670657	3.1111247	
25	.096	16.4114658	3.15294394	

GLOBAL SHEET — For Academic Use Only

Display Intermediate Values:	Yes
Stop on List Error:	No
Use Automatic Iteration:	Yes
Comparison Tolerance:	.000001
Typical Value:	1
Maximum Iteration Count:	10
Global Numeric Format:	
Append Variable Names:	Yes
Use Page Breaks:	No
Number Pages:	Yes
Form Length:	66
Printed Page Length:	60
Printed Page Width:	80
Left Margin:	0
Printer Setup String:	

REFERENCES

1. Lienhard J. H. and Witte L. C., "An historical review of the hydrodynamic theory of boiling", *Reviews in Chemical Engineering*, 1985, Vol.3, Nos.3 & 4, pp.187-280.

2. Whalley P. B., *Boiling, Condensation and Gas-Liquid Flow*, Oxford University Press, New York, 1990, pp.216-228.

3. Batchelor G. K., "The stability of a large gas bubble rising through Liquid", *J. Fluid Mech.*, 1987, Vol.184, pp.399-422.

4. Rayleigh Lord, "Investigation of the character of the equilibrium of an incompressible heavy fluid of variable density", *Scientific Papers*, Vol.II, Cambridge University Press, Cambridge, England, 1900, pp.200-207.

5. Taylor G., "The instability of liquid surface when accelerated in a direction perpendicular to their planes. I", *Proc. Roy. Soc.*, 1950, (A)201, pp.192-196.

6. Kelvin W., "Hydrokinetic solutions and Observations", *Phil. Mag.*, 1871, Vol.4, pp.374.

7. Helmholtz H., "Uber discontinuirliche Flüssigkeitsbewegungen", *Monatsber. Dtsch. Akad. Wiss. Berlin*, 1868, pp.215-228.

8. Lamb H., *Hydrodynamics*, American Edition, New York, Dovey Publication, 1945, pp.373 and pp.462.

9. Lee S.-L., "Taylor instability of a liquid film around a long, circular cylindrical body in still air", *J. Appl. Mech.*, Vol.30, *Trans. ASME*, Vol.85, Series E, 1963, September, pp.443-447.

10. Smarr L., Wilson J. R., Barton R. T. and Bowers R. L., "Rayleigh-Taylor overturn in supernova core collapse", *The Astrophysical Journal*, 1981, Vol.246, pp.515-525.

11. Norman M. L., Smarr L., Wilson J. R. and Smith M. D., "Hydrodynamic formation of twin-exhaust jets", *The Astrophysical Journal*, 1981, Vol.247, pp.52-58.

12. Emery M. H., Gardner J. H. and Boris J. P., "Rayleigh-Taylor and Kelvin-Helmholtz instabilities in targets accelerated by laser ablation", *Phys. Rev. Lett.*, 1982, Vol.48, pp.677-680.

13. Berenson P. J., "Film boiling heat transfer from a horizontal surface", *J. Heat Transfer*, 1961, Vol.83, pp.351-358.

14. Harrison W. J., "The influence of viscosity on the oscillations of superposed fluids", *Proc. London Math. Soc.*, 1908, Vol.6, pp.396-405.

15. Bellman R. and Pennington R. H., "Effects of surface tension and viscosity on Taylor instability", *Quart. Appl. Math.*, 1954, Vol.12, pp.151-162.

16. Rayleigh Lord, "On the stability of jets", *Proceedings of the London Mathematical Society*, 1878, Vol.10, pp.4-13.

17. Plesset M. S., "On the stability of fluid flows with spherical symmetry", *J. Appl. Phy.*, 1954, Vol.25, No.1, pp.96-98.

18. Birkhoff G., "Stability of spherical bubbles", *Quart. Appl. Math.*, 1956, Vol.13, pp.451-453.

19. Chandrasekhar S., *Hydrodynamic and Hydromagnetic Stability*, Oxford Univ. Press, New York, 1961, pp.428-513.

20. Leidenfrost J. G., "De aquae communis nonnullis qualitatibus tractatus", Duisburg; translated by C. Wares, 1966, *Int. J. Heat Mass Transfer*, 1756, Vol.15, pp.1153.

21. Chang Y. P., "A theoretical analysis of heat transfer in natural convection and in boiling", *Trans. ASME*, 1957, Vol.79, pp.1501-1513.

22. Chang Y. P., "Wave theory of heat transfer in film boiling", *J. Heat Transfer*, 1959, Vol.81, pp.1-12.

23. Zuber N., "On the stability of boiling heat transfer", *Trans. ASME*, 1958, Vol.80, pp.711-720.

24. Zuber N. and Tribus M., "Further remarks on the stability of boiling heat transfer", *UCLA Report No.58-5*, University of California, Los. Angeles, 1958.

25. Berenson P. J., "Film-boiling heat transfer from a horizontal surface", *J. Heat Transfer*, 1961, Vol.83, pp.351-358.

26. Lienhard J. H. and Wong P. T. Y., "The dominant unstable wavelength and minimum heat flux during film boiling on a horizontal cylinder", *J. Heat Transfer*, 1964, 88(2), pp.220-226.

27. Lienhard J. H. and Sun K. H., "Effect of gravity and size upon film boiling from horizontal cylinders", *J. Heat Transfer*, 1970, Vol.92, pp.292-298.

28. Dhir V. K. and Lienhard J. H., "Taylor instability of viscous fluids with application to film boiling", *Int. J. Heat Mass Transfer*, 1973, Vol.16, pp.2097-2109.

29. Bland D. R., *Solutions of Laplace's Equation*, By Routledge & Kegan Paul Ltd., London, 1965.

30. *Tk-Solver*, by Universal Technical Systems, Inc., Rockford, Illinois, U.S.A., 1989.

31. Basset A. B., *A treatise on hydrodynamics*, Vol.II, by Deighton, Bell and Company, 1888, pp.21-22.

32. Brimacombe J.K., Nakanishi K., Anagbo P.E. and Richards G.G., "Process dynamics: Gas-Liquid", *The Elliott Symposium*, June 10-13, Cambridge, MA, AIME, 1990, pp.304-372.

33. Aoki T., Masuda S., Hatono A. and Taga M., "Characteristics of submerged gas jets and a new type bottom blowing tuyeres", in *Injection Phenomena in Extraction and Refining, University of Newcastle Upon Tyne*, Ed. by A. E. Wraith, 1982, pp.A1-36.

34. Cheng Lin, Personal communication.

35. Lange K. W., "Reaction in combined blowing steelmaking", *Fifth International Iron and Steel Congress . Proceedings of the 6th Process Technology Conference*, Washington Meeting, April 6-9, 1986, Vol.6, pp.231-248.

36. Lange K. W., "Thermodynamic and kinetic aspects of secondary steelmaking processes", *International Materials Review*, 1988, Vol.33, No.2, pp.53-89.

37. Kumar R. and Kuloor N. R., "The formation of bubbles and drops", *Adv. Chem. Eng.*, 1970, Vol.8, pp.255-369.

38. Clift R., Grace J. R., and Weber M. E., *Bubbles, Drops, and Particles*, Academic press, INC. (London), 1978, pp.321-330.

39. Tsuge H., "Hydrodynamics of bubble formation from submerged orifices", *Encyclopedia of Fluid Mechanics*, 1986, Vol.3, pp.191-232, Gulf Publishing Co.

40. Szekely J., *Fluid Flow Phenomena in Metals Processing*, Academic Press, Inc., 1979.

41. Wraith A. E. and Kakutani T., "The pressure beneath a growing bubble", *Chem. Eng. Sci.*, 1974, Vol.29, pp.1-12.

42. Spell K. E. and Bakowski S., "A study of bubble formation at single slots submerged in water", *Trans. Inst. Chem. Eng. (London)*, 1950, Vol.28, pp.38-51.

43. Hughes R. R., Handlos A. E., Evans H. D. and Maycock R. L., "The formation of bubbles at simple orifices", *Chem. Eng. Progress*, 1955, Vol.51, No.12, pp.557-563.

44. Davidson J. F. and Schuler B. O. G., "Bubble formation at an orifice in a inviscous liquid", *Trans. Instn. Chem. Engrs*, 1960, Vol.38, pp.335-342.

45. Davidson J. F. and Schuler B. O. G., "Bubble formation at an orifice in a viscous liquid", *Trans. Instn. Chem. Engrs*, 1960, Vol.38, pp.144-154.

46. Davidson J. F. and Harrison H., *Fluidised Particles*, Cambridge University Press, Cambridge, 1963.

47. Kumar R. and Kuloor N. R., "Bubble formation in fluidised beds", *Chem. Tech.*, 1967, Vol.19, No.12, pp.733-737.

48. Wraith A. E., "Two stage bubble growth at a submerged plate orifice", *Chemical Engineering Science*, 1971, Vol.26, pp.1659-1671.

49. Hayes W. B., Hardy B. W. and Holland C. D., "Formation of gas bubbles at submerged orifices", *AIChE J.*, 1959, Vol.5, No.3, pp.319-324.

50. Satyanarayan A., Kumar R., And Kuloor N. R., "Studies in bubble formation. II. Bubble formation under constant pressure conditions", *Chem. Eng. Sci.*, 1969, Vol.24, 749-761.

51. Lanauze R. D. and Harris I. J., "On a model for formation of gas bubbles at a single submerged orifice under constant pressure conditions", *Chem. Eng. Sci.*, 1972, Vol.27, pp.2102-2105.

52. Khurana A. K. and Kumar R., "Studies in bubble formation-III", *Chem. Eng. Sci.*, 1969, Vol.24, pp.1711-1723.

53. Kupferberg A. and Jameson G. J., "Bubble formation at a submerged orifice above a gas chamber of finite volume", *Trans. Instn. Chem. Engrs*, 1969, Vol.47, pp.T241-250.

54. McCann D. J. and Prince G. H., "Bubble formation and weeping at a submerged orifice", *Chem. Eng. Sci.*, 1969, Vol.24, pp.801-814.

55. Lanauze R. D. and Harris I. J., "Gas bubble formation at elevated system pressure", *Trans. Instn. Chem. Engrs*, 1974, Vol.52, pp.337-348.

56. Tsuge H. and Hibino S.-I., "Bubble formation from a submerged single orifice accompanied by pressure fluctuations in gas chamber", *J. Chem. Eng. Japan*, 1978, Vol.11, No.3, pp.173-178.

57. Tsuge H. and Hibino S.-I., "Bubble formation from an orifice submerged in liquids", *Chem. Eng. Commun.*, 1983, Vol.22, pp.63-79.

58. Tsuge H., Tanaka Y. and Hibino S.-I., "Effect of the physical properties of gas on the volume of bubble formed from a submerged single orifice", *Canadian Journal of Chemical Engineering*, 1981, Vol.59, pp.569-572.

59. Marmur A. and Rubin E., " A theoretical model for bubble formation at an orifice submerged in an inviscid liquid", *Chem. Eng. Sci.*, 1976, Vol.31, pp.453-463.

60. Pinczewski W. V., "The formation and growth of bubbles at a submerged orifice", *Chem. Eng. Sci.*, 1981, Vol.36, pp.405-411.

61. Liow J.-L. and Gray N. B., "A model of bubble growth in wetting and non-wetting liquids", *Chem. Eng. Sci.*, 1988, Vol.43, No.12, pp.3129-3139.

62. Sahai Y. and Guthrie R. I. L., "The formation and role of bubbles in steelmaking operations", *International Symposium on model developments in steelmaking*, Jamshedpur, India, Paper 1.5, pp.1-24., 1981.

63. Engh T. A. and Nilmani M., "Bubbling at high flow rates in inviscid and viscous liquids (slags)", *Metall. Trans.*, 1988, Vol.19B, pp.83-94.

64. Milne-Thomson L. M., *Theoretical Hydrodynamics*, 2nd edn. Macmillan, London, 1949, P.405-16.

65. Kupferberg A. and Jameson G. J., "Pressure fluctuations in a bubbling system with special reference to sieve plates", *Trans. Istn. Chem. Engrs*, 1970, Vol.48, pp.T140-150.

66. Titomanlio G., Rizzo G., Acierno D., "Gas bubble formation from submerged orifices-'simultaneous bubbling' from two orifices", *Chem. Eng. Sci.*, 1976, Vol.31, pp.403-404.

67. Miyahara T., Matsuba Y., and Takahashi T., "The size of bubbles generated from perforated plates", *Int. Chem. Eng.*, 1983, Vol.23, No.3, pp.517-523.

68. Hobler T. and Pawelczyk, "Interfacial area in bubbling through a slot", *Brit. Chem. Eng. & Proc. Tech.*, 1972, Vol.17, No.7/8, pp.624-628.

69. Kozlowski M., and Wraith A. E., "Bubble and jet-cavity formation at slot-shaped tuyeres", CIM conference, Hamilton, Ontario, August 26-30, 1990.

70. Sano M., Fujita Y. and Mori K., "Formation of bubbles at single nonwetted nozzles in mercury", *Metall. Trans.*, 1976, Vol.7B, pp.300-301.

71. Sano M. and Mori K., "Bubble formation from single nozzles in liquid metals", *Trans. ISIJ*, 1976, Vol.17, pp.344-352.

72. Sano M., and Mori K., "Size of bubbles in energic gas injection into liquid metal", *Trans. ISIJ*, 1980, Vol.20, No.10, pp.675-681.

73. Mori K., Sano M., and Sato T., "Size of bubble formed at single nozzle immersed in molten iron", *Trans. ISIJ*, 1979, Vol.19, pp.553-558.

74. Andreini R. J., Foster J. S. and Callen R. W., "Characterization of gas bubbles injected into molten metals under laminar flow conditions", *Metall. Trans.*, 1977, Vol.8B, pp.625-631.

75. Irons G.A. and Guthrie R. I. L., "Bubble formation at nozzle in pig iron", *Metall. Trans.*, 1978, 9B, pp.101-110.

76. Irons G. A. and Guthrie R. I. L., "Bubbling behaviour in molten metals", *Canadian Metallurgical Quarterly*, 1981, Vol.19, No.4, pp.381-387.

77. Davis K. G., Irons G. A., and Guthrie R.I.L., "X-Ray cinematographic observations of gas injection into liquid metals", *Metall. Trans.*, 1978, Vol.9B, pp.721-722.

78. Hoefele E. O. and Brimacombe J. K., "Flow regimes in submerged gas injection", *Metall. Trans.*, 1979, Vol.10B, pp.631-648.

79. Lanauze R. D. and Harris I. J., "A note on gas bubble formation models", *Chem. Eng. Sci.*, 1974, Vol.29, pp.1663-1668;

80. Weast R. C., Astle M. J. and Beyer W. H., *CRC Handbook of Chemistry and Physics*, CRC Press Inc., Boca Raton, Florida, 1983-1984, 64th Edition, pp.(F-1)-(F-45).

81. S. M. Southern and A. E. Wraith, *Gas dispersion at diffuser sources for steelmaking*, 29th CIM conference, Hamilton, Ontario, August 26-30, 1990.

82. Bird R. B., Stewart W. E. and Lightfoot E. N., *Transport Phenomena*, John Wiley & Sons, 1960, pp.62 & 182.

83. Boender W., Chesters A. K., and Van Der Zanden A. J. J., " An approximate analytical solution of the hydrodynamic problem associated with an advancing liquid-gas contact line", *Int. J. Multiphase Flow*, 1991, Vol.5, pp.661-676.

84. Hoffman R. L., "A study of the advancing interface I. Interface shape in liquid-gas system", *Journal of Colloid and Interface Science*, 1975, Vol.50, No.2, pp.228-241.

85. Dussan V. E. B., "On the spreading of liquids and solids surfaces: static and dynamic contact lines", *Ann. Rev. Fluid and Mech.*, 1979, Vol.11, pp.371-400.

86. Dussan V. E. B. and Davis S. H., "On the motion of a fluid-fluid interface along a solid surface", *J. Fluid Mech.*, 1974, Vol.65, part 1, pp.71-95.

87. Dussan V. E. B., "Immiscible liquid displacement in a capillary tube: the moving contact line", *AIChE Journal*, 1977, Vol.23, No.1, pp.131-133.

88. Schwartz A. and Tejada S. B., "Studies of dynamic contact angles on solids", *Journal of Colloid and Interface Science*, 1975, Vol.38, No.2, pp.359-375.

89. Buckingham E., "On physically similar systems: Illustrations of the use of dimensional equations", *Phys. Rev.*, 1914, Vol.4, No.4, pp.345-376.